Processing and Characterisation of ZrC_xN_y Ceramics as a Function of Stoichiometry via Carbothermic Reduction-Nitridation

A Thesis submitted in partial fulfilment for the degree of Doctor of Philosophy

Robert Harrison

January 2015

Department of Materials
Imperial College London

To My Parents

Declaration I hereby declare that the work presented in this thesis is my own and other published works have been referenced appropriately.

The copyright of this thesis rests with the author and is made available under a Creative Commons Attribution Non-Commercial No Derivatives licence. Researchers are free to copy, distribute or transmit the thesis on the condition that they attribute it, that they do not use it for commercial purposes and that they do not alter, transform or build upon it. For any reuse or redistribution, researchers must make clear to others the licence terms of this work

Publications

- R. Harrison and W. E. Lee, Mechanism and kinetics of oxidation of ZrN ceramics, *Journal of the American Ceramic Society*, accepted Feb 2015, in Press.
- R. Harrison, O. Rapaud, N. Pradeilles, A. Maître, W. E. Lee, On the fabrication of ZrC_xN_y from ZrO_2 via two step carbothermic reduction-nitridation, *Journal of the European Ceramic Society*, 35 (2015) 1413-1421
- W. E. Lee, E. Giorgi, R. Harrison, A. Maître, O. Rapaud, Nuclear applications for ultra-high temperature ceramics and MAX phases, in *Ultra-High Temperature Ceramics*, W.G. Fahrenholtz, E.J, Wuchina, W.E. Lee, Y. Zhou. (Eds.), Wiley, 2014, 391-415
- R. Harrison, O. Ridd, D. D. Jayaseelan, W. E. Lee, Thermophysical characterisation of ZrC_xN_y ceramics fabricated via carbothermic reduction-nitridation, *Journal of Nuclear Materials*, 454 (1-3) (2014) 46-53

Presentations

- The Nuclear Materials (NuMat) conference, Florida, USA, Oct. 2014 (talk)
- Imperial College Department of Materials Postgraduate Research Day, London, UK, Mar. 2014 (talk)
- Imperial College Department of Materials 2^{nd} Year Postgraduate Seminar, London, UK, May 2013 (talk)
- Universities Nuclear Technology Forum (UNTF) conference, London, UK, Apr. 2013 (poster)
- The 5th International Workshop on Advanced Ceramics (IWAC05), London, UK, Sep. 2012 (poster)
- International Center for Materials Research (ICMR) Summer School on Inorganic Materials for Energy Conversion, Santa Barbara, USA, Aug. 2012 (poster)
- Imperial College Department of Materials Postgraduate Research Day, London, UK, Mar. 2012 (poster)

Abstract

Carbothermal reduction-nitridation of ZrO_2 has been studied in the context of application of non-oxide zirconium ceramics as fuel components in advanced nuclear fuels. Varying processing parameters of nitridation of ZrC_x (where $0.7 \leq x \leq 1$) powders revealed the rate increased with dwell time, dwell temperature and higher carbon content of the starting ZrC_x powders. A novel mechanism is reported whereby nucleation of small ($\leq$500 nm) ZrN containing crystals occurs on the surface of the ZrC_x powder particles, growing separate to the carbide particle and resulting in mixed phases. Sintering of the ZrC_xN_y powders by hot pressing resulted in higher densities than commercially-available ZrC powders suggesting nitrogen content improves the sinterability of ZrC containing ceramics.

Thermal and electrical conductivity of the ZrC_xN_y ceramics were all higher than the ceramics produced from commercially-available ZrC and ZrN powders. Room temperature thermal conductivities of the ZrC_xN_y ceramics were found to be 35 and 43 $Wm^{-1}K^{-1}$ for the lowest and highest N-containing ZrC_xN_y ceramics and increased with temperature to 45 and 55 $Wm^{-1}K^{-1}$ respectively at 2073 K. Electrical conductivities were in the range 250-450 $\times$ 10^4 $\Omega^{-1}m^{-1}$ for the ZrC_xN_y ceramics (at 298 K) and again increased with increasing nitrogen content. The increase in thermal conductivity of ZrC_xN_y with nitrogen content is due to the increase in electrical conductivity.

Oxidation studies of ZrN revealed oxidation begins at around 773 K with an initial destabilisation of ZrN occurring at around 673 K. A decrease in oxidation rate was observed between lower (973-1073 K) and higher temperatures (1173-1273 K). This is attributed to dense protective oxide scales forming at higher temperature (1173-1273 K) compared to porous oxide scales forming at lower temperature ($\leq$1073 K). However, this protective layer fails at higher temperature (1373 K), attributed to increased oxygen diffusion through the oxide layer.

Acknowledgments

I would like to thank the Engineering and Physical Sciences Research Council (grant EP/J500239/1), the sponsors of this research for the funding, along with the Armourers and Brasiers company for funding travel to international conferences to present this work.

I would like to thank my supervisor Prof. Bill Lee and the other academics of the Centre for Nuclear Engineering for their contribution of years of experience to this research and guidance of results in this work. I am also grateful for the opportunity for the degree of freedom given in this project, allowing me to explore avenues and areas of the research that were personally exciting. I also must thank Dr. Luc Vandeperre and Mr. Garry Stakalls who provided training and invaluable assistance with the thermal analysis equipment and help with the departments most temperamental machine, the hot press. I would also like to thank Dr. Doni Daniel for his help at the onset of the project and must thank Dr. Denis Horlait and Dr. Sam Humpry-Baker for always being willing to discuss experimental plans and results. I must also thank Dr. Mahmoud Ardakani and Mrs. Ecaterina Ware for their assistance on the SEM and TEM and Mr. Richard Sweeny on XRD. I would also like to thank Prof. Alexandre Maître, Dr. Olivier Rapaud and Dr. Nicolas Pradeilles for the opportunity to collaborate and travel to the European Ceramic Centre in Limoges, France and for their expertise, time and interest in this project. I am also very grateful to Dr. Salvatore Grasso for his help with the SPS experiments and Dr. Laura Cox for her help with the elemental analysis. I must also thank Edoardo Giorgi for his help in arranging the use of the chemical analysers at Horiba.

I would like to thanks my friends which I have made within the department, not only for their invaluable help learning the ropes but also for making my time at Imperial so enjoyable.

Lastly I would like to thank my parents, Bob and Louise Harrison. Although suffering their comments of 'having never left school' for the entirety of my postgraduate studies, they instilled in me the importance of education since a young age and have been resolute in their support of me throughout the entire of mine, and for that, I am unreservedly grateful.

List of Abbreviations

ADS	Accelerator driven system
AGR	Advanced gas cooled reactor
BCC	Body centered cubic
C_p	Heat capacity
CTE	Coefficient of thermal expansion
DC	Direct current
dpa	Displacements per atom
DSC	Differential scanning calorimetry
DTA	Differential thermal analysis
EDS	Energy dispersive spectroscopy
FB-CVD	Fluidised bed chemical vapour deposition
FCC	Face centered cubic
FEG	Field emission gun
FEM	Finite element models
FIB	Focussed ion beam
FP	Fission products
GFR	Gas cooled fast reactor

GIF	Generation IV international forum
HCP	Hexagonal close packed
HIP	Hot isostatic pressing
HM	Heavy metal
HP	Hot pressing
HRTEM	High resolution transmission electron microscope
HT-XRD	High temperature X-ray diffraction
ICDD	International centre for diffraction data
IMF	Inert matrix fuel
IR	Infra-red
LFR	Lead cooled fast reactor
LOCA	Loss of coolant accident
LWR	Light water reactor
MA	Minor actinides
MAGNOX	Magnesium non-oxidising
MSR	Molten salt reactor
NIST	National institute of standards and technology
NPP	Nuclear power plant
PDF	Powder diffraction file
PS	Pressureless sintering
PUREX	Plutonium uranium redox extraction
PWR	Pressurised water reactor

RT	Room temperature
SEM	Scanning electron microscope
SF	Spent fuel
SFR	Sodium cooled fast reactor
SPS	Spark plasma sintering
SWR	Supercritical-water reactor
TD	Theoretical density
TEM	Transmission electron microscope
TGA	Thermograviometric analysis
TRISO	Triple isotropic coated particle
UC	Uranium carbide
UN	Uranium nitride
VHTR	Very high temperature reactor
XRD	X-ray diffraction

Contents

Abstract **5**

Acknowledgments **6**

List of Abbreviations **7**

Contents **10**

List of Figures **13**

List of Tables **20**

1 Introduction **22**

2 Background **24**

2.1 Generation IV: A Nuclear Renaissance 24

2.1.1 Fast Reactors 25

2.1.2 The Gas Cooled Fast Reactor 27

2.1.3 Non-Oxide Fuel 28

2.1.4 Inert Matrix Fuel 31

2.1.5 Advanced Particle Fuel for GFR 32

2.1.6 Minor Actinide Management 35

2.1.7 Non-Oxide Fuel Processing 36

2.2 Zirconium Carbide and Zirconium Nitride Properties 43

2.2.1 Structure and Bonding 43

2.2.2 Phase Diagrams . . . 45
2.2.3 Thermal and Electrical Properties . . . 48
2.2.4 Mechanical Properties . . . 60
2.2.5 Fuel Fabrication Experience . . . 64
2.2.6 Oxidation Behaviour . . . 69
2.2.7 Irradiation Properties . . . 72
2.3 Outlook for Implementation . . . 77

3 Materials and Methods 78

3.1 Starting Powder Fabrication . . . 78
3.1.1 Carbothermal Reduction-Nitridation . . . 78
3.2 Pellet Production and Characterisation . . . 81
3.2.1 Density Measurements . . . 82
3.3 XRD . . . 82
3.4 SEM . . . 85
3.5 TEM Characterisation . . . 89
3.6 Thermophysical Characterisation . . . 91
3.6.1 Thermal Diffusivity . . . 91
3.6.2 Heat Capacity . . . 92
3.6.3 Thermal Conductivity . . . 94
3.6.4 Electrical Conductivity of Pellets . . . 95
3.7 Oxidation Studies . . . 96

4 Powder Fabrication 98

4.1 Powder Fabrication . . . 98
4.1.1 Development of Carbothermal Reduction . . . 98
4.1.2 Development of Nitridation . . . 103
4.1.3 Alteration of Nitridation Parameters . . . 114

4.2 Discussion . . . 121
4.2.1 Introduction . . . 121
4.2.2 Destabilisation of ZrC . . . 122
4.2.3 Nucleation and growth of ZrN rich phase . . . 123
4.2.4 Removal of carbon . . . 124
4.2.5 Reaction parameters . . . 125

5 Ceramic Production **127**
5.1 Densification . . . 128
5.1.1 Commercially-available ZrC and ZrN . . . 128
5.1.2 As-Fabricated ZrC_xN_y Powders . . . 134
5.2 Discussion . . . 143

6 Thermophysical Characterisation **145**
6.1 Results . . . 145
6.1.1 Thermal Properties . . . 145
6.1.2 Electrical Properties . . . 153
6.2 Discussion . . . 157
6.2.1 Thermal Properties . . . 157
6.2.2 Electrical properties . . . 159
6.3 Outlook . . . 162

7 Oxidation Behaviour **163**
7.1 Results . . . 163
7.1.1 Oxidation Behaviour and Kinetics . . . 163
7.1.2 Oxidation Layer Characterisation . . . 168
7.2 Discussion . . . 178

8 Conclusions and Further Work **181**

References **187**

List of Figures

2.1 Gas fast reactor schematic 27

2.2 Fuel element concepts for GFR 28

2.3 Rock-salt crystal structure, metal atoms = green spheres, non-metal (C or N) = red spheres 30

2.4 Neutron damage schematic 32

2.5 SEM image of cross section of a surrogate fuel particle 33

2.6 Proposed mechanism of nitridation of UO_2 microspheres 38

2.7 Schematic of carbothermic reduction of ZrO_2 40

2.8 Schematic of mechanism of nitridation of SiO_2 41

2.9 Molecular orbital formation of a diatomic molecule 44

2.10 Splitting of molecular orbital energies as a function of number of atomic orbitals 44

2.11 DOS of ZrC and ZrN (E_f= Fermi level) 45

2.12 Phase diagram for Zr-C system 46

2.13 Phase diagram for the Zr-N system 47

2.14 Phase diagram for Zr-C-N system at 1423K 48

2.15 Heat capacities of ZrC as a function of temperature 50

2.16 Heat capacity of ZrN as a function of temperature 51

2.17 Heat capacity of some zirconium carbonitrides as a function of temperature 52

2.18 Thermal conductivity of ZrC as a function of temperature 54

2.19 Thermal conductivity of ZrN as a function of temperature 54

2.20 Thermal conductivities of ZrC_xN_y phases as a function of temperature 55
2.21 Electrical conductivity of ZrC and ZrN as a function of temperature . 57
2.22 Electrical conductivities of ZrC_xN_yphases at room temperature as a function of [C]/[C]+[N] ratio 57
2.23 Elongation with respect to length at 298 K of ZrC as a function of temperature 59
2.24 Elongation with respect to length at 298 K of ZrN as a function of temperature 59
2.25 Young's modulus of ZrC as a function of temperature 61
2.26 Hardness of ZrC as a function of temperature 63

3.1 Bragg's law 84
3.2 Basic schematic of an SEM 86
3.3 Depiction of two beam-grain orientation interactions 87
3.4 Typical BSE image from channelling contrast 88
3.5 Interaction of TEM incident beam with specimen 90
3.6 Schematic of laser flash apparatus 92
3.7 Heat capacity of alumina standard as a function of temperature with manufacturers reference 93
3.8 Heat capacities as a function of temperature for ZrC_xN_y phases calculated from NIST data 94
3.9 Schematic of electrical conductivity measurement on bar samples . . . 96

4.1 TGA-DTA analysis of 1Zr-3C sample ($\sim$ 150 mg) to 1873 K (10 K/ min) under argon (60 ml/min) 99
4.2 XRD of powders from TGA-DTA experiments 99
4.3 XRD of 1Zr-3C and 1Zr-2.7C after carbothermic reduction 101
4.4 a) SEI of $ZrC_{1.0}$ powder from carbothermic reduction, b) EDS spectra of $ZrC_{1.0}$ powder 102
4.5 SEI of $ZrC_{1.0}$ powder from carbothermic reduction after milling small particles (1-2μm) showing agglomerates ($\sim$5μm) 103

4.6 XRD showing progression of nitridation iterations of $ZrC_{1.00}$ samples 106

4.7 XRD showing progression of nitridation iterations of $ZrC_{0.9}$ samples . 107

4.8 SEI of powders from iteration 2 of $ZrC_{0.9}$ powder (dwell time 8 h, dwell temperature 1873 K) $ZrC_{0.67}N_{0.33}$ a) region with ledges and terraces, b) region showing small spherical particles 108

4.9 a) BF-TEM image of $ZrC_{0.9}$ after nitridation iteration 2 (dwell time 8h, dwell temperature 1873K) $ZrC_{0.67}N_{0.33}$, b) higher magnification showing external layer, c) SADP of area shown in b 109

4.10 a) BF-TEM image of $ZrC_{0.9}$ after nitridation (dwell time 8h, dwell temperature 1873K) $ZrC_{0.67}N_{0.33}$,b) higher magnification image showing external layer, c) SADP of area shown in b 110

4.11 a) BF-TEM image of $ZrC_{0.9}$ after nitridation (dwell time 8h, dwell temperature 1873K) $ZrC_{0.67}N_{0.33}$, b) SADP of area shown in a 110

4.12 Types of crystal surfaces, F - flat face, S - stepped face and K - kinked face, according to TLK formation [147] 111

4.13 SEI of nitrided powders from iteration 4, starting composition $ZrC_{0.9}$ (dwell time 24h, dwell temperature 1800K) $ZrC_{0.43}N_{0.52}$, a) shows regions of ledge and terraces, b) reveals small spherical particles . . . 112

4.14 SEI of nitrided powders from iteration 4, starting composition $ZrC_{1.00}$ (dwell time 24h, dwell temperature 1800K) $ZrC_{0.25}N_{0.7}$ 112

4.15 a) BF-TEM image of powder from iteration 5, nitridation of $ZrC_{0.9}$ (dwell time 24h, dwell temperature 1873K) $ZrC_{0.3}N_{0.65}$ b) higher magnification showing external layer, c) SADP of area shown in b 113

4.16 a) BF-TEM image of powder from iteration 5 - nitridation of $ZrC_{0.9}$ (dwell time 24h, dwell temperature 1873K) $ZrC_{0.3}N_{0.65}$, b) higher magnification showing external layer, c) SADP of area shown in b . . 114

4.17 XRD of powder from one step carbothermic reduction-nitridation reaction (dwell temperature 1873 K, dwell time 4h) 115

4.18 XRD of powders reacted in 0%, 1% and 10% hydrogen doped nitrogen atmospheres for 2h at 1873 K 116

4.19 Change in wt% carbon as a function of time for nitridation reaction a) reaction temperature 1800 K b) reaction temperature 1873 K (lines to guide eyes only) 117

4.20 XRD pattern of $ZrC_{1.0}$ powder reacted for 2-4 h under 10% H_2 . . . 118

4.21 Peak resolution of XRD patterns from Figure 4.20, a) peak resolution of 2 h nitridation, b) peak resolution of 4 h nitridation. Baselines in both graphs indicate no unresolved peaks 119

4.22 SEI of powder after 2 h nitridation reaction at 1873 K 119

4.23 SEI of powder after 4 h nitridation reaction 1873 K 120

4.24 XRD pattern of annealed $ZrC_{0.67}N_{0.33}$ powder 121

4.25 Schematic diagram of the mechanism of nitridation of ZrC particles . 125

5.1 XRD pattern of commercially-available ZrC and ZrN powder 128

5.2 SEIs of SPS-ZrN-1 (dwell time 10 min, dwell temperature 2373 K, 50 MPa) a) after polishing, b) after thermal etching 132

5.3 BSE images of polished, unetched SPS-ZrC-1 (dwell time 12 min, dwell temperature 2373 K, 50 MPa) a) low magnification to show grain boundary size distribution, b) higher magnification showing pore distribution 132

5.4 BSE image of polished, unetched HP-ZrN-1 (dwell time 60 min, dwell temperature 2273 K, 50 MPa, a) higher magnification, b) lower magnification 133

5.5 BSE image of polished, unetched HP-ZrC-1 (dwell time 60 min, dwell temperature 2273 K, 50 MPa) 133

5.6 SEI of ZrC_xN_y powders after milling a) $ZrC_{0.55}N_{0.4}$ b) $ZrC_{0.4}N_{0.55}$ c) $ZrC_{0.33}N_{0.6}$ and d) $ZrC_{0.12}N_{0.78}$. 135

5.7 Excerpts of XRD patterns of ZrC_xN_y powders before sintering 137

5.8 Excerpts of XRD patterns of ZrC_xN_y after sintering at 2273 K for 1 hour under 50 MPa uniaxial pressure 138

5.9 Lattice parameters of ZrC, ZrN and ZrC_xN_y ceramics as a function of [C]/[C]+[N] 138

5.10 Photograph of 10 mm ceramic pellets a) commercial ZrC, b) $ZrC_{0.4}N_{0.55}$, c) $ZrC_{0.33}N_{0.6}$, d) $ZrC_{0.12}N_{0.78}$ and e) commercial ZrN 139

5.11 BS electron images of $ZrC_{0.55}N_{0.4}$ ceramic pellet, a) low magnification revealing uniform density and grain size, b) higher magnification showing more detailed grain boundaries (line features due to residual scratches) 140

5.12 SEM images of $ZrC_{0.4}N_{0.55}$, a) SEI revealing surface microstructure, b) BSE image which reveals grains and pore distribution in bulk (line features due to residual scratches) 140

5.13 SEM images of $ZrC_{0.33}N_{0.6}$, a) SEI revealing surface microstructure, b) BSE image which reveals grains and pore distribution in bulk . . . 141

5.14 BS electron images of $ZrC_{0.12}N_{0.78}$ ceramic pellet, a) BSE image revealing bulk grain sizes, b) BSE image at higher magnification showing more detailed grain boundaries (line features due to residual scratches) 141

5.15 a) HRTEM image of grain boundary in $ZrC_{0.12}N_{0.78}$ ceramic showing crystalline lattice fringes in both grains, b) SAED pattern of grain A showing a cubic single phase 142

6.1 Thermal diffusivity of ZrC and ZrN ceramics derived from commercially-available powders by SPS and HP 146

6.2 Thermal diffusivity as a function of temperature for ZrC_xN_y ceramics 147

6.3 Heat capacity as a function of temperature of ZrC ceramic produced from commercially-available powder and ZrC_xN_y ceramics 148

6.4 Lattice parameter as a function of temperature for ZrC_xN_y ceramics ZrC and ZrN ceramics derived from commercially-available powders . 149

6.5 Linear CTE's as a function of temperature for ZrC_xN_yceramics and ZrC and ZrN ceramics derived from commercially-available powders . 150

6.6 Thermal conductivities as a function of temperature of HP and SPS for ceramic samples made from commercially available powders (corrected for porosity using Equation 2.15) 151

6.7 Thermal conductivities as a function of temperature of ZrC_xN_y ceramics (corrected for porosity using Equation 2.15) 152

6.8 Temperature dependence of electrical conductivity of ZrC, ZrN ceramics produced from commercially available powders and ZrC_xN_y ceramics produced from as-fabricated powders 153

6.9 Temperature dependence of the electrical contribution to thermal conductivity (K_{el}) of ZrC, ZrN ceramics produced from commercially available powders and ZrC_xN_y ceramics produced from as-fabricated powders 154

6.10 Temperature dependence of electrical and phonon contribution to thermal conductivities of ZrC_xN_y ceramics produced from as-fabricated powders 155

6.11 Thermal conductivity as a function of stoichiometry for ZrC 159

6.12 Room temperature electrical conductivity of ZrC as a function of C/Zr ratio 161

7.1 HT-XRD of ZrN powder with scans at every 100 K to 1023 K under static air 164

7.2 Excerpt of HT-XRD showing destabilisation of ZrN with temperature 165

7.3 TGA-DTA results of isothermal oxidation of ZrN sample at 1173 K . 166

7.4 Change in mass (ΔW) per unit surface area (A) as a function of time for each oxidation temperature 167

7.5 Square of the change in mass per unit surface area as a function of time for each oxidation temperature 167

7.6 Parabolic rate constants (k_p) as a function of temperature 168

7.7 SEIs of oxide layer of ZrN sample heated to 973 K for 5 h, a) shows fragmented oxide layer, b) shows grains revealed near to oxide layer . 169

7.8 SEIs of oxide layer of ZrN sample heated to 1073 K for 5 h, a) shows cracks present in bulk ZrN, b) shows cracks in oxide layer 170

7.9 SEIs of oxide layer of ZrN sample heated to 1173 K for 5 h, a) shows region of where intermediate layer is penetrated by oxide scale (rectangle shows FIB section) b) shows cracks in the oxide layer 171

7.10 SEIs of oxide layer of ZrN sample heated to 1273 K for 5 h, a) shows region where grains revealed deep into bulk, b) shows cracks in oxide scale and region of EDS from grain in the bulk 172

7.11 SEIs of oxide layer of ZrN sample heated to 1373 K for 5 h, a) shows depth of oxidation of grain boundaries into the ZrN bulk, b) shows ZrN grain close to oxide scale with oxygen content in grain boundaries (area shown in rectangle represents FIB section) 173

7.12 XRD of ZrN sample oxidised at 1373 K for 5 h revealing ZrN and monoclinic ZrO_2 174

7.13 a) TEM image of FIB section (area represented by rectangle in Figure 7.9a), taken from intermediate layer of sample oxidised at 1173 K for 5 h, b) [001]ZrN SADP of bulk region, c and d) [001] and [103] c-ZrO_2 SADP patterns of intermediate layer grains 175

7.14 a) BF-TEM image of FIB section (area represented by rectangle in Figure 7.11b) taken from grain boundary of sample oxidised at 1373 K for 5 h, b) [$1\bar{1}0$]c-ZrO_2 SADP of area indicated by circle 176

7.15 Phase diagram for the Zr-N-O system at 1273 K 177

7.16 Schematic diagram of proposed mechanisms of oxidation of ZrN at low and higher temperatures 180

8.1 Zr-N phase diagram, highlighting metal rich liquidus sintering region 183

List of Tables

2.1 Overview of Generation IV systems 25

2.2 Fuel requirements for the GFR 28

2.3 Comparison of typical properties between oxide, metallic and nitride fuel for fast reactors 29

2.4 IMF candidates 31

2.5 Reference design for advanced coated fuel particles for GFR 34

2.6 Chemical analysis and densities for ZrN and TiN containing pellets compared with PuN pellets 64

2.7 Sintering parameters for SPS of inert matrix pellets 66

3.1 Composition of zirconia and carbon mixtures 78

3.2 Nitridation reaction parameters 80

3.3 PDFs used to index XRD data from ICDD 84

4.1 Carbon and nitrogen analysis by oxidation technique of powders fabricated by carbothermal reduction (2073 K, 4h) 101

4.2 Carbon analysis by combustion of powders fabricated by carbothermic reduction (2073 K, 4 h) 102

4.3 Carbon and nitrogen analysis using oxidation analysis of nitrided powders using different starting C/Zr ratios, dwell times and dwell temperatures 104

4.4 Chemical analyses of reacted powders using oxidation technique . . . 118

4.5 Mole fractions of gaseous species present during nitridation of ZrC powder at 1873 K under flowing H_2(10%) - N_2 gas calculated using FactSage 122

5.1 Carbon and nitrogen analysis of commercial powders using the oxidation technique 129

5.2 Carbon, nitrogen and oxygen analysis of commercial powders using the combustion technique 129

5.3 SPS parameters and bulk properties of ceramics 130

5.4 HP sintering (dwell temperature 2273 K) program and bulk properties of ceramics produced 131

5.5 Carbon, nitrogen and oxygen chemical analysis of nitrided powders [1)] Crushed pellet analysed, [2)] Powder analysed, [a)] combustion analysis results [b)] oxidation analysis results 136

5.6 Bulk properties of hot pressed ceramic pellets, [a]- Determined from combustion analysis [b]- Determined from oxidation analysis [c]- Measured by SEM 142

1 Introduction

Non-oxide ceramics such as the carbides and nitrides of group IV transition metal elements have an interesting mixture of ionic, covalent and metallic bonding. This combination of bonding gives the materials an unusual mixture of advantageous properties such as high hardness ($\sim$25 GPa) and very high melting temperatures ($\geq$ 3000K) along with good thermal and electrical conductivity ($\geq$ 10 $Wm^{-1}K^{-1}$and $\sim 200\times10^{4}\Omega^{-1}m^{-1}$ respectively).[1] As a result of these properties the carbide and nitride of zirconium are receiving increased attention for use in advanced nuclear power plants (NPP). They have been proposed as candidates for use as fuel cladding and inert matrix fuel (IMF) materials or as coatings for advanced nuclear fuel particles for the Gas Cooled Fast Reactor (GFR)[2], which is one of the six reactors proposed as part of the next generation of NPP; so called Generation IV reactors.[3] In particular, the materials are of interest for use as IMF's whereby a fissile phase is dispersed in an inert phase, in this case ZrN. The inert matrix aids heat transfer from the fission reactions to the coolant, reduces the build-up of hot-spots and as it is neutron transparent, reduces the amount of waste produced via transmutation of materials in the core. These materials have been used extensively as coatings for drill tips and cutting tools, however, studies into bulk processing routes, thermophysical characterisation and irradiation studies are in their early stages.

Materials used in fuel elements in next generation NPP are expected to be more efficient than previous materials and are also expected to be subject to harsher thermal and radiation environments. A thorough knowledge of how the structure and bonding of the materials gives rise to the high hardness, melting temperature and thermophysical properties will be advantageous in their processing and production and for predicting their evolution during the fuels lifetime.

This thesis aims to enhance understanding of the processing and fabrication of nitride materials and to contribute to knowledge of their thermal and electrical conductivities, investigating the effects of impurities and defects on them. As will

be shown the results provide an understanding of the production of ZrN as well as a thorough set of thermophysical properties as a function of stoichiometry. This aims to reduce the large scatter in these data currently present in the literature. The work in this thesis is presented in eight chapters. The second chapter details the background and technological issues with the advancement to the next generation of NPP along with a review of literature on the fabrication of non-oxide fuel materials and the properties of ZrC, ZrCN and ZrN. The third chapter describes the materials, methods and experimental techniques used in this work. Chapter four presents the results of the fabrication of ZrC_xN_y ceramic powders via a two-step carbothermal reduction and nitridation of ZrO_2 and densification of them is presented in the fifth chapter. The sixth chapter details the thermophysical properties of the ZrC_xN_y ceramic as a function of stoichiometry. Chapter seven presents preliminary results on the oxidation behaviour of commercially-produced ZrN ceramics. Chapter eight concludes the major findings of this work and future work and recommendations are presented.

2 Background

This chapter introduces the next generation of NPP and the technological challenges facing their implementation. A review of the shortcomings of traditional fuels is presented and the benefits of non-oxide materials are highlighted. Current understanding of processing and thermophysical properties of these non-oxide materials are reviewed before entering into a more in depth look at ZrC and ZrN, two of the more researched candidate non-oxide materials for use as IMF materials and the motivation for this work.

2.1 Generation IV: A Nuclear Renaissance

Supporting energy demands for an increasing population, whilst addressing the depletion of fossil fuels and meeting greenhouse gas regulations has led to a renewed interest worldwide in nuclear power. Currently, 15% of the world's electricity is generated by nuclear energy with 3000 TWh being produced each year, the largest supply by any non-greenhouse gas emitting resource.[2]

Six systems (Table 2.1) have been selected by the Generation IV International forum (GIF). GIF was initiated in 2001 with the aim of establishing and identifying targets for a new fleet of reactors. The current goals for Generation IV nuclear energy system include;[2]

- Increasing the sustainability of nuclear power by maximising energy production from fuel and cutting waste
- Increased safety through intrinsic and passive autonomous systems
- Reducing proliferation risk by reducing the ease of theft of weapons grade materials.

The six power plant concepts are the Very High Temperature Reactor (VHTR), Supercritical-Water Reactor (SWR), Gas Cooled Fast Reactor (GFR), Lead Cooled

Fast Reactor (LFR), Sodium cooled Fast Reactor (SFR) and the Molten Salt Reactor (MSR).

System	Fuel	Neutron spectrum	Operating temperature/ K	Fuel cycle	Coolant
VHTR	UO_2	Thermal	1173-1273	Open	Helium
SWR	UO_2	Thermal	773-898	Open/closed	Water
GFR	(U,Pu)C/ (U,Pu)N	Fast	1123	Closed	Helium
LFR	(U,Pu)C/ (U,Pu)N	Fast	773-1073	Closed	Lead
SFR	U-Pu-Zr	Fast	823	Closed	Sodium
MSR	Salt	Thermal	973-1073	Closed	Fluoride Salts

Table 2.1: Overview of Generation IV systems [2]

This renewed interest in nuclear technology has led to a vast increase in the global output of research into materials that will be able to meet the requirements of Generation IV NPP. Much research was performed on exotic fuel's in the 1960's and in recent years several reviews, technical reports and textbook chapters have collated and summarised the challenges and advancements in the field.[4–8]

2.1.1 Fast Reactors

Thermal reactors use neutrons that have been slowed to 'thermal' speeds (typically having kinetic energy < 1 eV) by moderators to induce fission in ^{235}U, shown in Equation 2.1

$$_{92}U^{235} +_0 n^1 \longrightarrow_{92} U^{236} \longrightarrow_{56} Ba^{139} +_{36} Kr^{94} + 3_0n^1 + Energy \qquad (2.1)$$

Natural uranium consists of 0.7% ^{235}U, with the majority being ^{238}U which has a low thermal neutron capture cross section meaning it typically does not undergo fission in a thermal spectrum. Due to the low amount of the fissionable isotope, the uranium

density in the reactor core needs to be sufficient to achieve a chain reaction. In older reactors such as MAGNOX (named from the magnesium non-oxidising, MAGNOX alloy used to clad the fuel) this was achieved by using uranium metal which has a density of 19.1 g cm^{-3} providing enough ^{235}U for a chain reaction. In light water reactors (LWR) and advanced gas cooled reactors (AGR) higher temperatures precluded the use of metallic uranium due to its low melting point (1330 K [7]). Instead UO_2 is employed (with a melting temperature of 3000 K [7]), with an isotopic enrichment of ^{235}U to between 3.5-4.9%.

Fast reactors operate without neutron moderators and so neutron energies retain the energy from fission reactions (typically having a kinetic energy > 1 MeV). At these energies a ^{238}U nucleus can capture a neutron, transmuting it to fissionable ^{239}Pu, thus the reactor breeds its own fuel, shown in Equation 2.2. The ^{239}Pu produced can then undergo fission, to produce energy and more neutrons for further breeding.

$$_{92}U^{238} +_0 n^1 \longrightarrow_{92} U^{239} \longrightarrow_{93} Np^{239} +_{-1} e^0 \longrightarrow_{94} Pu^{239} + _{-1}e^0 \tag{2.2}$$

The breeding performance of a fuel depends on properties such as heavy metal density and light nuclei content, and is given by the conversion ratio;

$$CR = \frac{M(fissile\,produced)}{M(fissile\,consumed)} \tag{2.3}$$

For a $CR = 1$ the system is self-sustaining, if <1 then the system is a termed a burner as it depletes fissile material in the core. If the CR is >1 then the system is a breeder, as it produces fissile material in the core. CR is dependent upon the neutron spectrum of the reactor and the density of the fuel. The more energetic or harder the spectrum is the higher the CR, this can be achieved by avoiding light nuclei in the fuel (such as oxygen) or using fast neutron transparent coolants (such as He, Pb). The latter helps prevent the loss of neutrons from the core and so improves the neutron economy of the system. Due to the presence of only one light atom per fissile atom, actinide monocarbides and mononitrides could give better breeding performance over oxide fuels under fast neutron spectra with regards to fuel breeding.

2.1.2 The Gas Cooled Fast Reactor

The GFR concept (Figure 2.1) combines the advantages of high temperature gas reactors with a fast neutron spectrum that offers higher sustainability of breeding and the burning of actinide wastes. The heat released from fission will be transferred to gaseous helium with an anticipated output temperature of 853-1273 K. Compared to other coolants such as molten salt, gas coolants are advantageous as they are compatible with water, non corrosive and have negligible activation, reducing handling and disposal costs. They are also optically transparent allowing remote visual inspection of the core and negligible coolant void allowing a greater fuel loading.[9, 10]

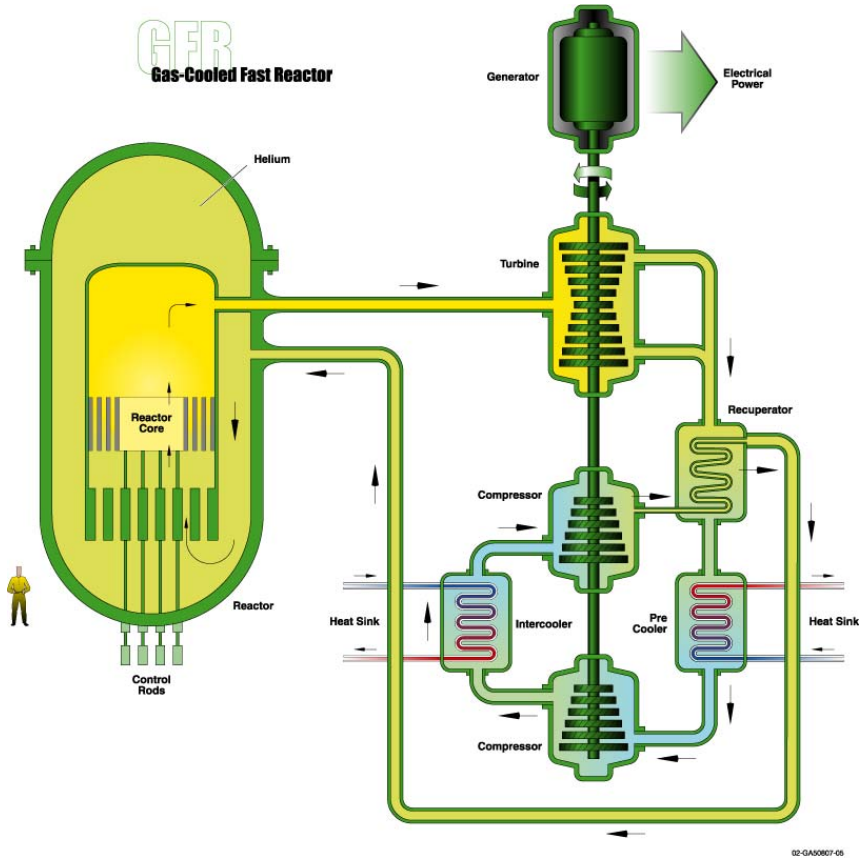


Figure 2.1: Gas fast reactor schematic [2]

One concept fuel for the GFR is a ceramic-ceramic dispersion fuel based on a balance between thermal conductivity and high temperature capability.[11] Current fuel concepts are shown in Figure 2.2, these include dispersion fuels, in the form

of cylindrical or hexagonal sticks or spherical particles in an inert matrix block or plate. Anticipated requirements for the GFR fuel material are given in Table 2.2, these values have been taken as reference, or blueprint requirements of fuel materials in the GFR.[3]

Requirement	Reference Value
Melting/decomposition temperature	>2200 K
Radiation induced swelling	<2 vol% over service life
Thermal conductivity	>10 W/mK
Neutronic properties	Materials allow low core heavy metal inventory and maintain good safety

Table 2.2: Fuel requirements for the GFR [12]

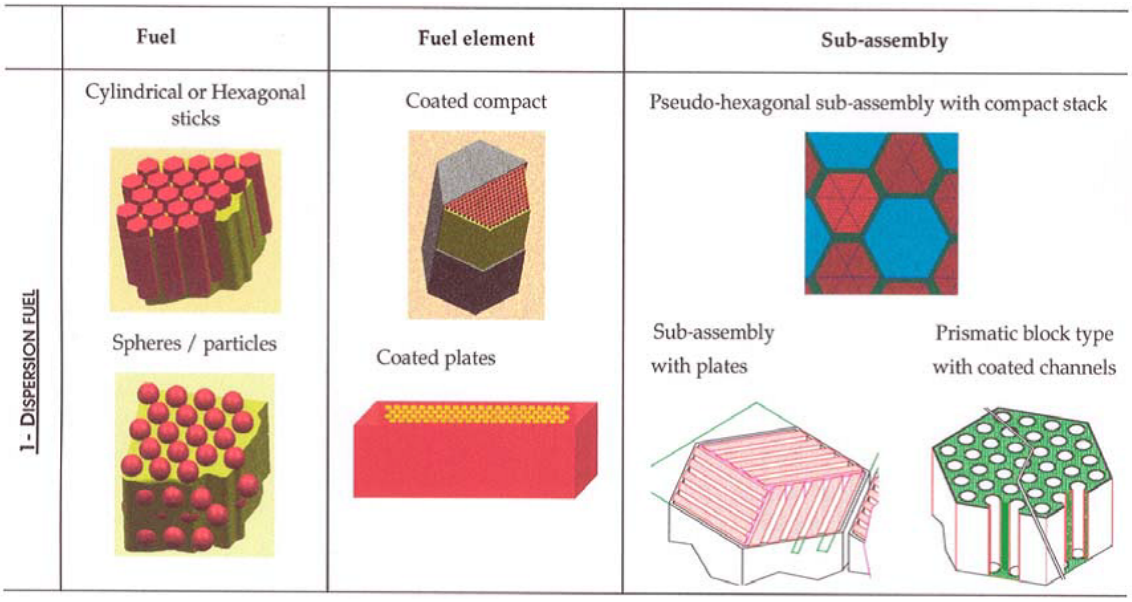


Figure 2.2: Fuel element concepts for GFR[12]

2.1.3 Non-Oxide Fuel

Metallic fuels offer advantages of high heavy metal density but suffer disadvantages, such as anisotropic crystal swelling, low melting temperature and high fission product (FP) induced swelling with regards to application in a fast reactor. The refractory metals tungsten, tantalum, molybdenum, niobium and rhenium also have poor neutronic properties such that the materials would slow the neutrons adversely

affecting the hard neutron spectrum. Oxide fuel can overcome some of the flaws of metallic fuels such as melting temperature, but suffer low thermal conductivities, poor neutronic properties and low conversion ratios for breeding fuel.

Irradiation tests performed on oxide IMF's (such as MgO, $MgAl_2O_4$, $Y_2O_3$and CeO_2) with UO_2 revealed extensive matrix cracking leading to unacceptable amounts of fission gas release.[13, 14] The results have been attributed to differences in thermal expansion between the fissile and inert phases. These results along with fuel requirements for GFR eliminate the use of metals and oxides as fuels. Uranium carbide (UC) and uranium nitride (UN) have been identified as candidate fuels for fast reactors over uranium oxide due to their high heavy metal density, high thermal conductivity and minimal impact on neutron spectrum with properties summarised in Table 2.3. Carbide and nitride fuels combine both the advantages of metallic and oxide fuel.[6, 7]

	Oxide fuel	Metallic fuel	Carbide fuel	Nitride Fuel
Chemical composition	$(U_{0.8}Pu_{0.2})O_2$	U-19Pu-10Zr (wt.%)	$(U_{0.8}Pu_{0.2})C$	$(U_{0.8}Pu_{0.2})N$
Theoretical density / g cm^{-3}	11.1	15.9	13.6	14.3
Fissile and fertile metal atom density / g cm^{-3}	9.75	14.3	-	13.5
Thermal conductivity / $Wm^{-1}K^{-1}$ at 1000K	2.6	40	18.8	15.8
Thermal conductivity / $Wm^{-1}K^{-1}$ at 1200K	2.4	-	21.2	20.1
Melting temperature / K	3083	1330	3296	3053

Table 2.3: Comparison of typical properties between oxide, metallic and nitride fuel for fast reactors [6, 7]

Ceramics based on binary monocarbides and mononitrides all have the rock salt structure and belong to the space group $Fm\bar{3}m$ with a B1 structure (B denotes there are equal amounts of two types of atoms and the 1 denotes the specific type of arrangement of atoms within the B group) where metal atoms occupying the face centered cubic (FCC) sites and carbon or nitrogen the octahedral interstitial sites (Figure 2.3).[15]

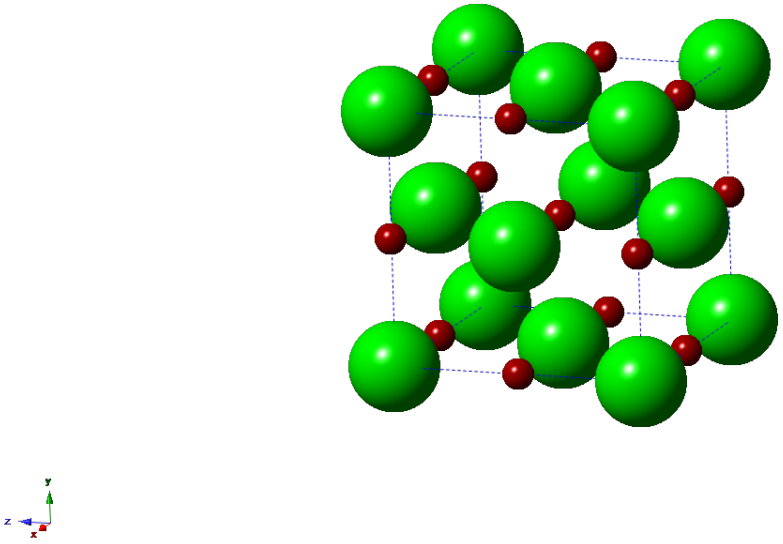


Figure 2.3: Rock-salt crystal structure, metal atoms = green spheres, non-metal (C or N) = red spheres

Although carbides and nitrides have similar density and thermophysical properties, the nitride fuels have advantages over the carbides. The nitrides are not as pyrophoric and can be handled in commercially available inert gases as compared to the carbides which require ultra high purity.[16] In general, actinide nitride fuels are easier to prepare as a single phase with plutonium only forming the mononitride and the sesquinitrides of uranium (UN_2 and U_2N_3) being unstable, while uranium and plutonium have stable higher carbides (Pu_2C_3, PuC_2, U_2C_3, UC_2). Nitrides have slightly higher density, show reduced swelling under irradiation, better retention of FP and dissolve easier in HNO_3 which makes them more viable to reprocess via the Plutonium Uranium Redox EXtraction (PUREX) process.[16] However, a potential issue for nitrides is the production of large amounts of radiotoxic ^{14}C via

the neutron capture reaction of ^{14}N (Equation 2.4). To prevent this, enriched ^{15}N may be employed, however this would add expense to the fuel fabrication process.

$$ {}_7N^{14} +_0 n^1 \longrightarrow_6 C^{14} +_1 P^1 \tag{2.4} $$

2.1.4 Inert Matrix Fuel

IMF's consist of fissile material diluted in a non-fissile material which has a low neutron capture cross section. This concept offers increased safety by reducing the maximum fuel temperature that would be reached by having pure fissile material in the core, whilst producing no further transuranic waste material due to the inert phase having a low activation. Another proposed benefit of these inert phases is that they should have increased retention of FP's. Neutron transparent oxide and non-oxide matrices are listed along with compatible fertile phases in Table 2.4.[11]

Matrix type	Inert Matrix	Fertile Matrix
Oxide	BeO, MgO, Y_2O_3, ZrO_2, CeO_2	ThO_2, UO_2
Binary oxide	$MgAl_2O_4$, $Y_3Al_5O_{12}$, $ZrSiO_4$	ThO_2, UO_2
Oxide solid solution	$Mg_{(1-x)}Al_{(2+x)}O_{(4-x)}$	(U,Th)O_2, (Pu,U)O_2
Carbide	SiC, TiC, ZrC	ThC2, ThC, UC, PuC
Nitride	AlN, TiN, ZrN, CeN	ThN, UN, PuN

Table 2.4: IMF candidates [11]

Dispersion fuels may consist of a distribution of either fine or discrete fuel particles embedded in a metal or ceramic matrix. [12] The fuel designs can be classed as either Cer-Cer, in which the ceramic fissile phase is embedded in a ceramic matrix or a Cer-Met where the inert matrix is a metal. Two current concepts for these dispersion fuels exist, the first is macrodispersion which employs relatively large fuel particles (500-1000 μm) widely distributed in the matrix. The second is microdispersion, which incorporates a fine dispersion of the fissile phase (40-100 μm) into the inert matrix. Although this process is more convenient due to experience with this type of ceramic processing, fission related damage will occur over a larger volume of the matrix affecting thermal conductivity and structural integrity of the matrix.

The inert phases of the fuel will be placed under extreme operating conditions with radiation damage occurring from neutrons, alpha decay (producing ~5 MeV alpha

particles and ~100 keV daughter nuclei) and FP (70-100 MeV). Chauvin et al. [17] reviewed the effects of this damage on dispersion and solid-solution fuels. Due to the range of particles and energies the damage mechanisms in the inert phases will be different. Alpha particles cause isolated displacements as far as a range of 20 μm, with their recoil atoms causing short dense collision cascades of 25 nm. In general, however, it is the FP tracks that cause the most atomic displacements with two fragments emitted in opposite directions having fission tracks of ~ 8-10 μm. A schematic diagram of these damage pathways in the matrix is shown in Figure 2.4.

In a solid solution fuel this means damage will occur homogeneously, however in a dispersion fuel the damage may be isolated to one phase depending on the size of the inclusions of the dispersed phase. Annealing effects observed at the operating temperature of the reactor however may allow the materials to distribute the point defects produced by radiation damage.

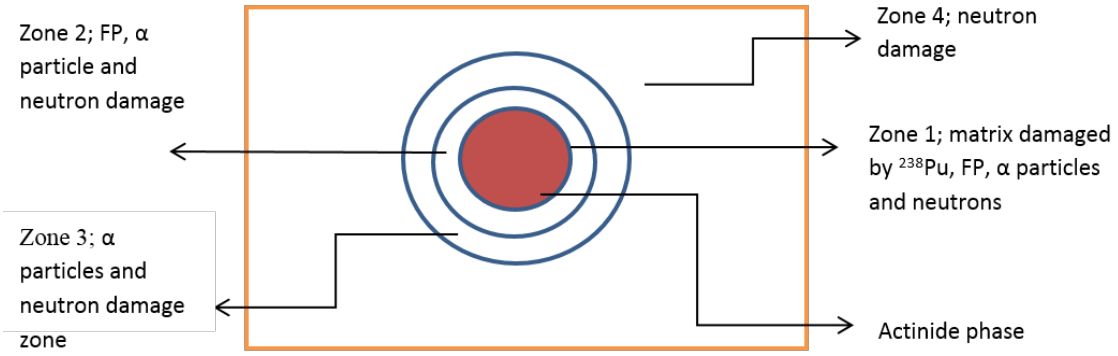


Figure 2.4: Neutron damage schematic reproduced from Chauvin et al. [17]

Spherical fuel particles dispersed in an inert matrix block may be produced using a sol-gel type process to fabricate the particles and then dispersing within the inert matrix. Calculations performed by Chauvin et al.[17] give the optimal diameter of the particle fuel between 50 and 300 μm, with a porosity of 10% as this would supply a fission gas plenum (pores where gases released from fission can gather during fuel burn-up) without compromising thermal conductivity.

2.1.5 Advanced Particle Fuel for GFR

Due to safety concerns associated with increased matrix swelling, macrodispersions are currently the preferred fuel form concept for application in the GFR. The

simplest design of this fuel consists of an un-buffered fuel particle embedded in the matrix, with particles containing about 15% porosity to act as the fission gas plenum. A more intricate fuel form consists of fissile kernels coated with non-fissile material, similar to the VHTR (TRISO) particles, shown in Figure 2.5.[12] However, the use of particle coatings decreases heavy metal (HM) density in the core and so the coating layers will need to be kept to a minimum. Reference concepts consist of particles coated with a porous buffer layer acting as the fission gas plenum and a dense outer layer, providing a barrier to fission gas release.

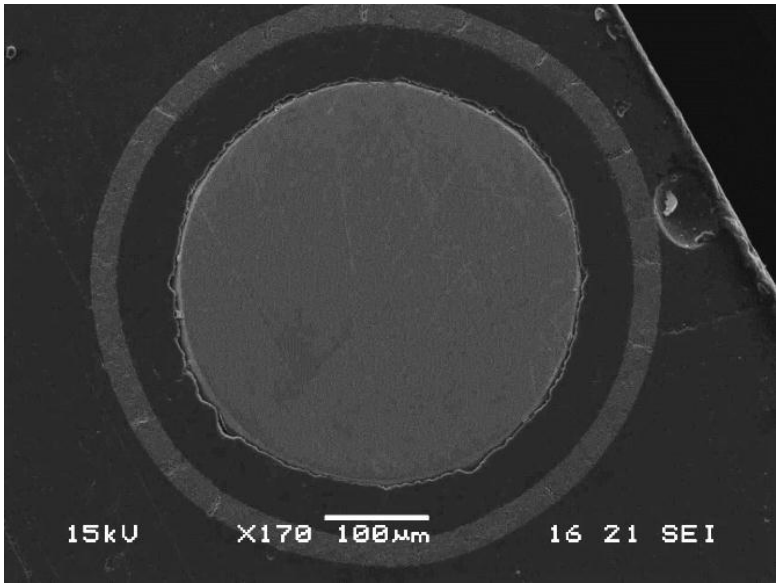


Figure 2.5: SEM image of cross section of a surrogate advanced fuel particle, zirconia kernel produced by the sol-gel coated with carbon (inner layer) and titanium nitride (outer layer), deposited by fluidised bead chemical vapour deposition (FB-CVD), sample courtesy of Dr T. Besmann, Oak Ridge National Laboratory (ORNL)

Meyer et al. [12] in their review of development of GFR fuel based initial fuel screening criteria on the parameters of a melting temperature greater than 2273 K, an actinide metal (or HM)) density greater than 5 g/cm^{-3} and a fuel burn-up potential greater than 5% HM. Reference parameters of fuel particles including diameter, coating layer thickness and density are given in Table 2.5.

Parameter	Large particles	Small particles
(U,Pu)C fuel kernel diameter	1.40 mm	410 μm
SiC buffer coating thickness ($\leq$30% TD)	~58μm	~18μm
SiC outer coating thickness	~61μm	~18μm
Heavy metal (HM) density	6 g cm^{-3} HM, 75% particle loading	5 g cm^{-3} HM, 63% particle loading
Matrix	Dense SiC	Dense SiC

Table 2.5: Reference design for advanced coated fuel particles for GFR [12]

Fast neutron environments eliminate the use of high quantities of light elements as they slow neutrons. Although carbon and nitrogen are light elements, if UC or UN monoliths are used the light element content has been halved compared to UO_2. This also restricts the use of TRISO-coated particles which contain large quantities of pyrolytic carbon (PyC). Reduction of light element content will be needed to make these particles suitable for use in a fast reactor. Carbide fuel kernels have better fuel densities and thermophysical properties than oxide fuels, however the fabrication of monocarbide fuels is more difficult due to the high temperatures required along with high vapour pressures of some of the transuranics such as plutonium and americium.[16]

In this instance coating layers for the nitride kernel need to be selected on the basis of compatibility with the neutron environment, fuel kernel and other structural material such as the matrix. FB-CVD was developed in the 1950's with the specific aim for use in coating uranium thorium carbide microspheres with layers of PyC and silicon carbide for use in high temperature gas cooled reactors.[18]

Little has been published on fabricating coated fuel particles for GFR's. The use of methylsilane (CH_3SiH_3) as a non-halide precursor using FB-CVD to fabricate surrogate fuel particles coated with porous and dense layers of SiC was studied by Slaga.[19] However, use of SiC would be unfavourable with a UN fuel kernel as reaction between UN and SiC is thermodynamically favourable above 823 K.[12] This makes nitrides such as ZrN and TiN interesting candidates for coatings due to their chemical compatibility, thermal and neutronic properties.

Nosek et al. [20] performed thermomechanical simulations of GFR fuel particles con-

sisting of a UC or UN kernel surrounded by two coatings of TiC, SiC, ZrC, TiN and ZrN. Finite element models (FEM) were used to determine the stresses produced in the particles from thermal expansion, fission gas release, swelling and creep over the life time of the particle from fabrication and through reactor operation. The authors found that the potential coatings must have melting points >2273 K, thermal conductivities >10 $Wm^{-1}K^{-1}$ and swellings of <2% over service life (~80 displacements per atom, dpa) due to irradiation.

2.1.6 Minor Actinide Management

Typical Pressurised Water Reactor (PWR) Spent Fuel (SF) mass is composed mostly of UO_2 (, ∼98.5 wt%) and short-lived FP's from the splitting of a uranium nucleus which present no long term radiotoxicity hazard. Around 0.4 wt% of SF is made up of long-lived FP's such as ^{127}Cs, ^{90}Sr, ^{99}Tc and ^{129}I. However, it is plutonium and minor actinides (MA) notably ^{241}Am, ^{243}Cm and ^{237}Np which pose the main long-term radiotoxicity and heat load issues, as well as proliferation risks.[11] Although they only make up a small per cent (~1.0 wt%) of the SF.

If fuel is operated on a once-through cycle the resulting SF will take over 100,000 years for radioactivity to fall to the same level as uranium ore. If the PUREX method is employed to remove and reprocessed plutonium and uranium isotopes this radiotoxic lifetime falls to 10,000 years. However, if MAs can be separated and then placed into a reactor to undergo fission or transmutation to a more stable and short lived (half life ≤30 years) isotopes the SF will only consist of FP's, meaning the radiotoxic lifetime falls to ~500 years. Although this is desirable, issues with handling and fabrication of fuels that incorporate these MAs will prove difficult due to radiotoxicity. If carbide or nitride fuel is employed, the vaporisation of some of these MAs, as well as the pyrophoricity of the materials will provide difficult challenges.[21]

The concept of U, Pu and MA reprocessing is generally referred to as Partitioning and transmutation (P+T). In such a route, once separated from the SF the actinides will be incorporated into an IMF (eg. (U,Am,Zr)N) and placed into a fast reactor for transmutation either undergoing fission, leaving shorter-lived FP or transmuting to more stable isotopes .

2.1.7 Non-Oxide Fuel Processing

Synthesis of carbides and nitride materials generally involves direct reaction with the metal, the metal hydride or the metal oxide, with the metal oxide route being the main precursor from spent fuel reprocessing. Other techniques have been examined including self-propagated high temperature synthesis [22, 23] as well as chemical vapour deposition techniques.[24–26]

As the majority of the existing SF exists as oxide fuel, carbothermic reduction of oxide powders is the most economically attractive route for the large scale production of non-oxide fuels.[27] Methods of carbothermal reduction and nitridation of oxides generally use similar processing parameters, [7, 16] mixing of oxide powder with a carbon source, heat treatment to between 1873 and 2373 K under inert atmosphere and then further heat treatment in a hydrogen doped nitrogen atmosphere to complete the reaction and remove excess carbon. The basic mechanism of carbothermic reduction and nitridation is (Equation 2.5 and Equation 2.6);

$$MO_2 + 3C \longrightarrow MC + 2CO \tag{2.5}$$

$$MC + \frac{1}{2}N_2 + 2H_2 \longrightarrow MN + CH_4 \tag{2.6}$$

2.1.7.1 Studies of Carbothermal Reduction and Nitridation

U and Pu Systems

Pautasso et al. [28] examined the reaction of uranium and plutonium oxide with carbon and nitrogen using thermogravimetry. Experiments were carried out at 1650-1870 K under nitrogen followed by a hydrogen doped-nitrogen atmosphere to remove carbon. A first order rate equation with an activation energy of 307 kJ/mol was determined, no detailed mechanism is provided however the authors propose the reaction proceeds by the formation of the carbonitride and then the removal of carbon to leave only the nitride stating the carbon diffusion through the product layer is the rate limiting step. The authors found that to ensure a low oxygen product, free carbon levels in excess in the starting product should be used. However, for all samples excess carbon was present both as free and bound (U,Pu)C_xN_y.

The kinetics of the carbothermal reduction and nitridation of carbon doped uranium oxide microspheres (3-10 μm) have been examined by Mukerjee et al.[29] Uranium oxide microspheres were produced via a sol-gel route and heated at 1623, 1723 and 1826 K under a flow of nitrogen gas. The dwell samples were held at temperatures anywhere between 2 and 24 h. Effluent CO gas produced from the removal of carbon and oxygen was oxidised further using a copper catalyst and the resulting CO_2 trapped in a NaOH solution. Reaction rate was calculated by weight of CO liberated at time t/total CO expected as per reaction (Equation 2.7);

$$UO_2 + 2C + \frac{1}{2}N_2 \longrightarrow UN + 2CO \tag{2.7}$$

C, N and O analysis of the samples showed that oxygen and carbon contents decreased with increasing dwell times. Higher nitridation advancement was observed when using a hydrogen doped (8%) nitrogen atmosphere. The mechanism (shown in Figure 2.6) proposed by Mukerjee et al. [29] shows that the there is an immediate formation of a UC_xN_y phase on the surface of the particle and diffusion of N_2 present at the surface of the particle to the UC_xN_y/UO_2 interface. Free carbon present in the UC_xN_y phase then dissolves and diffuses to the UC_xN_y/UO_2 interface forming further UC_xN_y phases with dissolved oxygen, which then diffuse out of the UC_xN_y phase. The oxygen then reacts with free carbon forming gaseous CO which then diffuses out of the microsphere. Mukerjee et al. [29] concluded from their kinetic results that the reaction follows a first order rate equation, with an activation energy of 365.7 $\pm$ 14.9 kJ/mol and is controlled by CO diffusion through the UC_xN_y layer. The rate of reaction is dependent on the value of y in UC_xN_y, where y is dependent on the N_2 pressure/ flow rate, with higher pressures giving higher y values, the rate of reaction increased with increasing carbon content, agreeing well with Pautasso et al.[28]

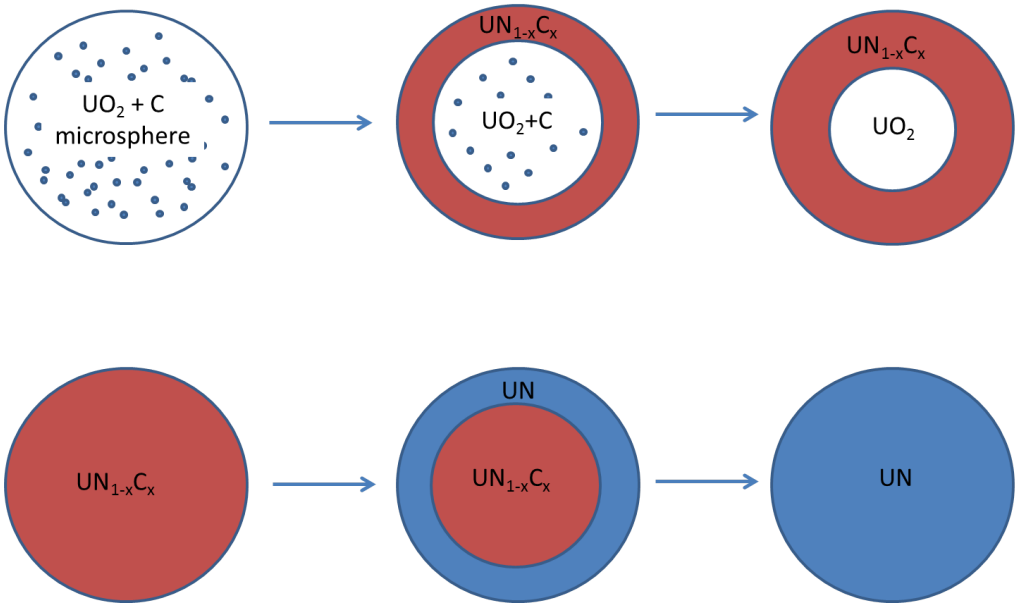


Figure 2.6: Adapted schematic of proposed mechanism of nitridation of UO_2 microspheres with a C/UO_2 mol ratio ≥ 2 by Mukerjee et al. under nitrogen atmosphere at 1673 K [29]

Bardelle and Warin [30] examined the mechanism and kinetics of uranium and plutonium mononitrides synthesis at 1823 K for 15 h under nitrogen atmosphere followed by a hydrogen doped nitrogen atmosphere, before cooling in a hydrogen doped argon atmosphere to prevent sesquinitride formation. The authors proposed a longer dwell under the hydrogen doped nitrogen atmosphere as previous authors had noticed an increase in N wt% after using hydrogen doped nitrogen gas at the end of a reaction.[28, 29, 31] However with previous work focusing on CO release,[28, 31] Bardelle and Warin [30] used mass spectrometry of the exhaust gas and report the detection of HCN gas, which behaves as a reactive agent for removing carbon, proposing the following mechanism (Equation 2.8);

$$(U_{0.8}Pu_{0.2})O_2 + 2HCN \longrightarrow (U_{0.8}Pu_{0.2})N + 2CO + H_2 + \frac{1}{2}N_2 \qquad (2.8)$$

Unlike Bardelle and Warin, Nakagawa et al.[32] noticed a peak in the partial pressure of CH_4 using gas chromatography during the reaction of UC and CeC_2 with NH_3 between 5 and 15h at 1133K. The authors compare the rate of reaction between using an NH_3 flow (200 mL/min) and N_2(50 mL/min) + H_2(150 mL/min) gas mix, noting the NH_3 promotes the removal of carbon, and therefore rate of nitridation

by shifting the rate of reaction (Equation 2.9) to the right.

$$C_{(s)} + \frac{4}{3}NH_{3(g)} \rightleftharpoons CH_{4(g)} + \frac{2}{3}N_{2(g)} \tag{2.9}$$

Streit et al.[33, 34] produced (U,Zr)N and (Pu,Zr)N microspheres by the sol-gel method followed by carbothermic reduction. However, nitridation is assumed by loss of mass using a TGA/DTA under nitrogen atmospheres without any hydrogen doping atmosphere at any point of the reaction is used unlike previous studies ([29, 30, 32]). From this it would be difficult to observe the reaction by TGA alone as there will be a competing process with weight loss from the oxide to either the carbide or nitride and weight gain from the carbide to the nitride. Carbon and nitrogen also have very similar molecular weights, weight loss from forming the carbide or nitride from the oxide would be very difficult to observe and comment on this forming the nitride instead of the carbide by TGA.

Zr System

The mechanism of carbothermal reduction of ZrO_2 and TiO_2 which are a similar system to U/PuO_2 have been examined by Berger at al.[35] The authors propose the mechanism for $ZrO_2 + x$C begins with CO formation from the solid state reactions of oxide and carbon particles. The increased number of lattice defects arising from their formation in the sub-stoichiometric ZrO_{2-x} allows incorporation of carbon into the vacancies leading to a ZrC_xO_y phase. The authors state the reactions rates of oxygen loss and carbide formation are not equal which leads to substoichiometric oxycarbides. The substitution of oxygen for carbon proceeds via the same mechanism of oxygen removal of O by CO to give CO_2 and the incorporation of C into the vacancies left behind. This would be a similar mechanism to that reported by Pautasso et al. [28] and Mukerjee et al. [29] whereby C and N occupy vacancies left from oxygen removal.

TEM studies of the carbothermal reduction of zirconia to assess the reaction mechanisms have been reported by David et al.[36] Samples of ZrO_2 and C (carbon black) with a C/Zr molar ratio of 2.89 were heated at temperatures of 1873 and 2023 K for dwells of 0 to 8 h. TEM studies on powders that had undergone minimal reaction showed that ZrC_xO_y is not observed on ZrO_2 particles, but located in the vicinity of them. The authors state the mechanism begins with destabilisation of carbon black

and zirconia, with oxidation of carbon leading to $CO_{(g)}$ and the removal of oxygen from zirconia giving a $ZrO_{2-x(s)}$ phase. This destabilisation of zirconia continues until a layer of Zr exists on an underlying Zr-O phase which the authors state can then exist as gaseous $Zr_{(g)}$ and $ZrO_{(g)}$. Nucleation and growth of the oxycarbide phase was observed by TEM to occur within carbon black agglomerates, which may arise from condensation of $ZrO_{(g)}$ and $CO_{(g)}$ followed by solid state diffusion to $ZrC_xO_{y(s)}$. The oxycarbide is then further reduced by contact with $CO_{(g)}$ leading to a more carbon enriched particle until eventually the carbide is formed, a schematic of the mechanism is shown in Figure 2.7.

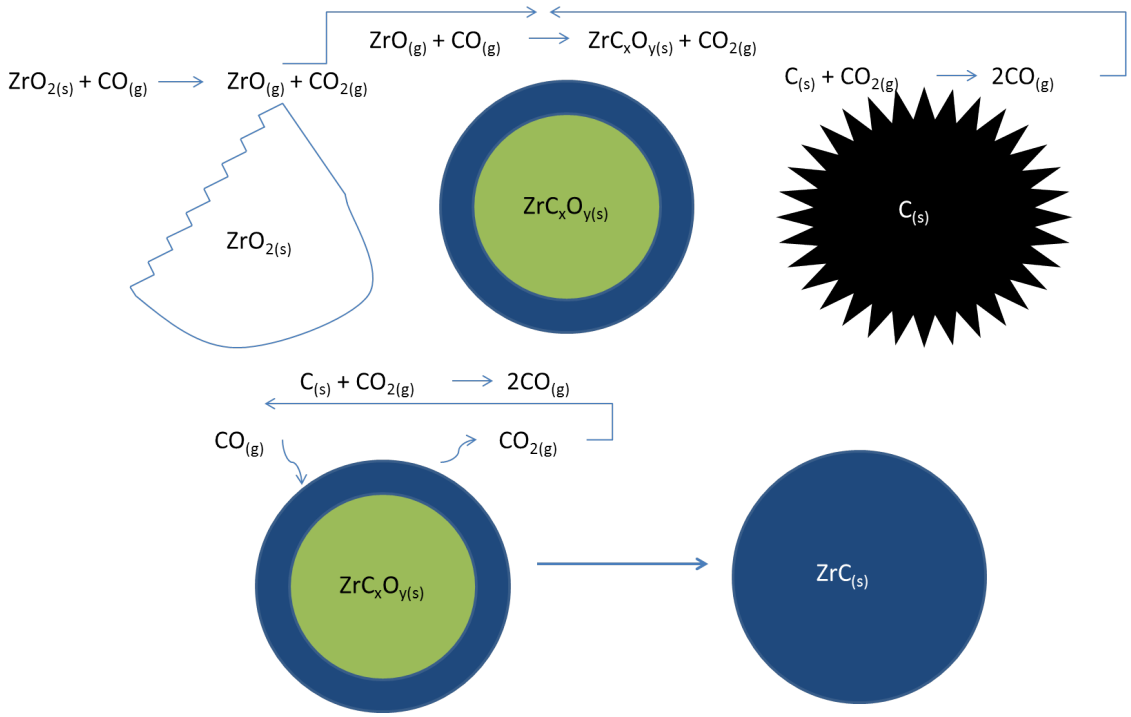


Figure 2.7: Schematic of carbothermic reduction of ZrO_2 reproduced from David et al.[36]

No studies into the mechanism of carbothermal reduction and nitridation of ZrO_2 are available in the literature as far as the author is aware. However, there have been studies on the silicon nitride system, which although existing over a broader range of stoichiometries than ZrN is prepared in by the same method.

Si System

Weimer et al. [37] studied the mechanism and kinetics of the carbothermal nitridation of Si_3N_4 using TEM studies. SiO_2 was mixed with carbon black to achieve 50-150% excess carbon according to the reaction (Equation 2.10) ;

$$3SiO_2 + 6C + 2N_2 \longrightarrow Si_3N_4 + 6CO \tag{2.10}$$

Mixed powders were then heated to 1648-1698 K for dwell times of 1 to 5h. The reaction mechanism begins with a solid-solid reaction where deoxygenation of the SiO_2 crystal via the carbon to produce $CO_{(g)}$ and $SiO_{(g)}$ occurs whereby more $SiO_{(g)}$ is produced by the reaction of $CO_{(g)}$ with SiO_2, generating $CO_{2(g)}$ similar to the ZrO_2 mechanism proposed by David et al. [36] Nucleation of $Si_3N_{4(s)}$ occurs in the free carbon agglomerates where the complete removal of oxygen from $SiO_{(g)}$ by $CO_{(g)}$ allows the $Si_3N_{4(s)}$ phase to form. The nitride then grows via repeating gas phase reactions of $SiO_{(g)}$ with $CO_{(g)}$ and $N_{2(g)}$(schematic shown in Figure 2.8). The authors suggest that the gas phase reaction between $SiO_{(g)}$ and $CO_{(g)}$ is likely to be the rate limiting step which can be envisaged as a low chance of co-condensation of the two gas phase. An activation energy of 457 $\pm$ 55 kJ/mol for the overall reaction was reported.

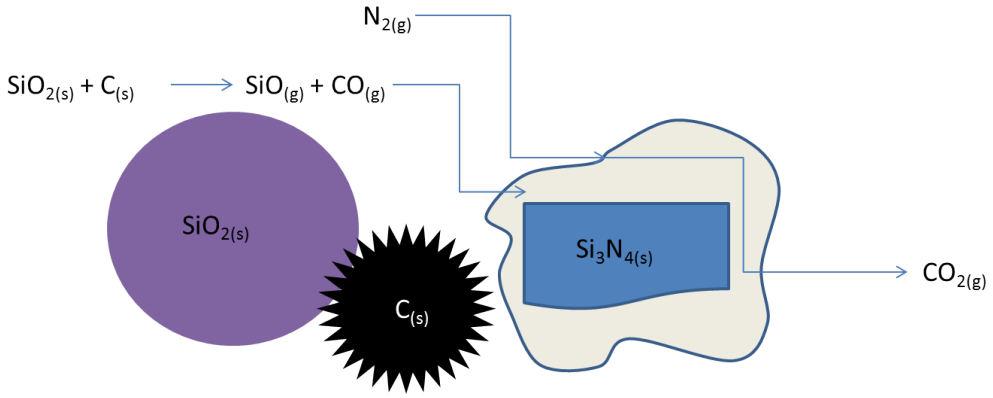


Figure 2.8: Schematic of mechanism of nitridation of SiO_2 reproduced by Weimer at al.[37]

Sample controlled reaction temperature was used by Ortega et al. to study the kinetics and diffusion mechanism on the carbothermal synthesis of Si_3N_4.[38] Silica and carbon were mixed in a molar ratio C/SiO_2 of 5.5, a 5% hydrogen doped nitrogen

atmosphere was used as the reaction atmosphere at 2073 K. The authors assume the reaction occurs at the silica and carbon grains, with the formation of $SiO_{(g)}$ vapour through contact of silica and carbon via Equation 2.11;

$$SiO_{2(s)} + C_{(s)} \longrightarrow SiO_{(g)} + CO_{(g)} \tag{2.11}$$

Once the SiO vapour is formed it continues to react with carbon and nitrogen to produce Si_3N_4 ribbons, with more $SiO_{(g)}$ and nitrogen gas diffusing to the nucleation point resulting in growth of the Si_3N_4 layer. With the layer thickness increasing, gas diffusion rate to the growth site decreases and this becomes the rate limiting step. Ortega et al. [38] describe the reaction by a two-dimensional diffusion kinetic model as the chemical reaction at the site of nucleation is faster than the vapour diffusion through the advancing Si_3N_4 skin. The reaction has an overall activation energy of 306 kJ/mol which is lower than that reported by Wiemer et al.[37] but agrees well with the observation of Bardelle and Warin's observation [30] that the activation energy of the carbothermic reduction-nitridation reaction decreases with the use of a hydrogen doped atmosphere.

2.2 Zirconium Carbide and Zirconium Nitride Properties

2.2.1 Structure and Bonding

Zirconium carbide and zirconium nitride are both crystalline face centered cubic, rock salt structure ($Fm\bar{3}m$ space group) whereby the carbon and nitrogen atoms occupy the interstitial octahedral sites. Their bonding is a complex mixture of ionic, covalent and metallic, conferring certain desirable characteristics in both materials. Strong covalent and ionic bonds give them high melting points ($\geq$ 3000 K) and hardness (20-25 GPa), whereas metallic bonding gives them high thermal ($\geq$ 10 $Wm^{-1}K^{-1}$) and electrical conductivities (200-500 $\times 10^4$ $\Omega^{-1}m^{-1}$).[1]

Zirconium contains the electronic structure $[Kr]5s^24d^2$, carbon and nitrogen have the structure, $[He]2s^22p^2$ and $[He]2s^22p^3$ respectively. Carbon and nitrogen are more electronegative due to their increased ability to attract electron density arising from poor electron shielding of their nucleus. Nitrogen is one of the most electronegative atoms due to increased pull on its outer electrons arising from an extra proton in the nucleus. This difference of electronegativity between the metal and the non-metal is what gives rise to the ionic character of the bonds.

Both the carbide and nitride show a degree of covalent bonding which arises from interactions between the 2p state of the non metal and 4d state of zirconium, resulting in metal-non-metal as well as metal-metal bonding, but essentially with no non-metal to non-metal bonding. Metallic bonding arises when atoms are ionised, leaving the positive metal atoms and the delocalised electrons which move freely through the lattice. Electrostatic forces between the delocalised electrons and the positive metal atoms give rise to the bonds. The high thermal and electrical conductivity of metals (and the carbides and nitrides of some transition metals) arise from the ability of the delocalised electrons to move through the lattice. The formation of these bands can be described using molecular orbital theory shown in Figure 2.9 where a diatomic molecule combines two atomic orbitals to form two molecular orbitals. In metals the electrons in the higher energy states are delocalised over the whole crystal. As more molecular orbitals are formed, from the enormous amount of atomic orbitals in a metal lattice, the energy difference between adjacent molecular orbitals decreases (Figure 2.10).[39] The gap between bonding and antibonding orbitals, in the case

of metals, also decreases leading to a continuum level. A density of electron states arises from the overlap of bonding and antibonding orbitals from the non-metal 2p orbital and the d metal orbital., which has been reported to be just under the Fermi level for the carbide.[40] The Fermi level for metals corresponds to the energy of the highest occupied molecular orbital (HOMO) at T=0 K while for semi-conductors it is defined as the energy level which has 50% occupation probability of a material and lies in the band gap at T=0 K. Thus for a metal or material with no band gap, at non-zero temperatures electrons close to the Fermi level will have enough energy to be promoted to the conductance band (Figure 2.10).

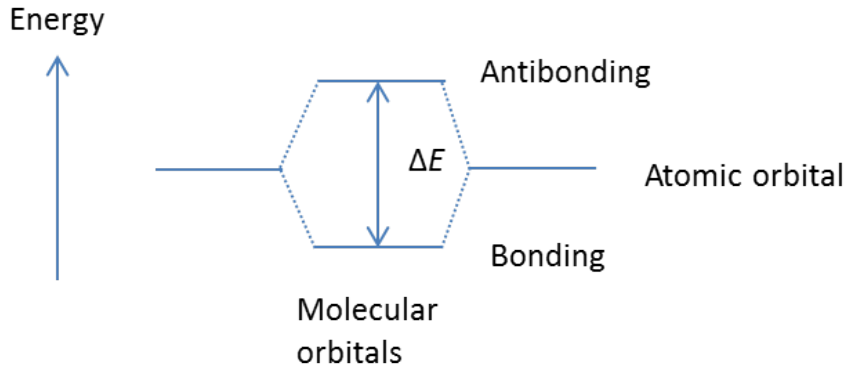


Figure 2.9: Molecular orbital formation of a diatomic molecule

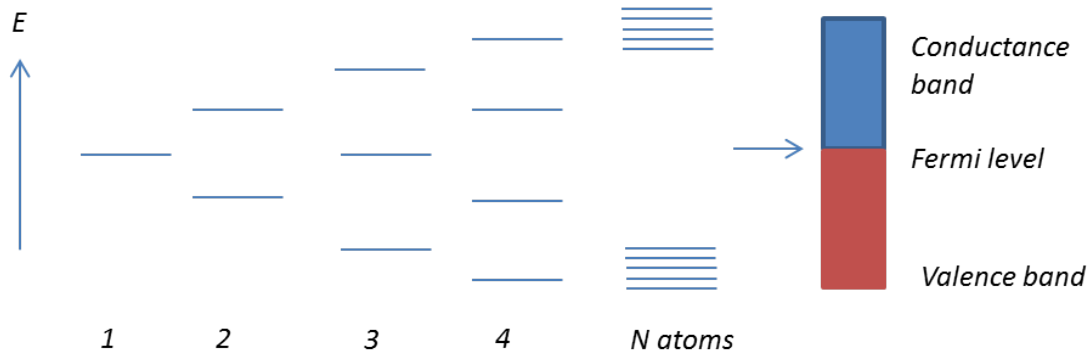


Figure 2.10: Splitting of molecular orbital energies as a function of number of atomic orbitals

The band structure of the carbides and nitrides contains a non-metal 2s, a non-metal 2p to zirconium d,s and zirconium 4d,5s,5p states. There is a minimum in the density

of states (DOS) at the Fermi level when there are 8 electrons in the valence band, also known as a valence electron concentration (VEC). at a VEC of 8 the Fermi level is found between the non-metal p to metal d and d-like bands.[1] With a VEC of more than 8 then there are a higher number of DOS at the Fermi level,[41] which is located in the low energy region of the metallic band. Schwarz et al. [42] calculated the DOS of ZrC and ZrN using augmented plane wave (APW) calculations and are shown in Figure 2.11.

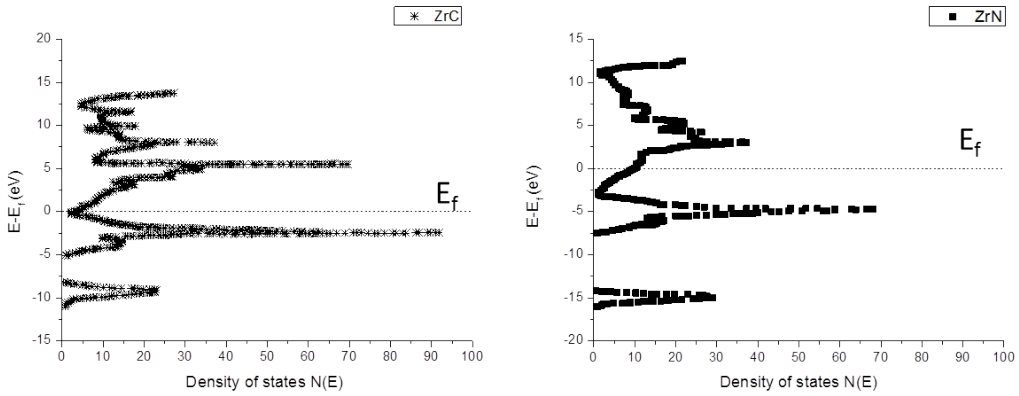


Figure 2.11: DOS of ZrC (left) and ZrN (right) (E_f= Fermi level) reproduced from Schwarz et al.[42] showing a higher DOS at E_f for ZrN

2.2.2 Phase Diagrams

The carbide and nitride can accommodate non-metal vacancies and are generally written with the non-stoichiometric formula ZrC_{1-x} or ZrN_{1-x}. The phase diagrams for ZrC an ZrN are shown in Figure 2.12 and Figure 2.13 respectively.[43, 44]

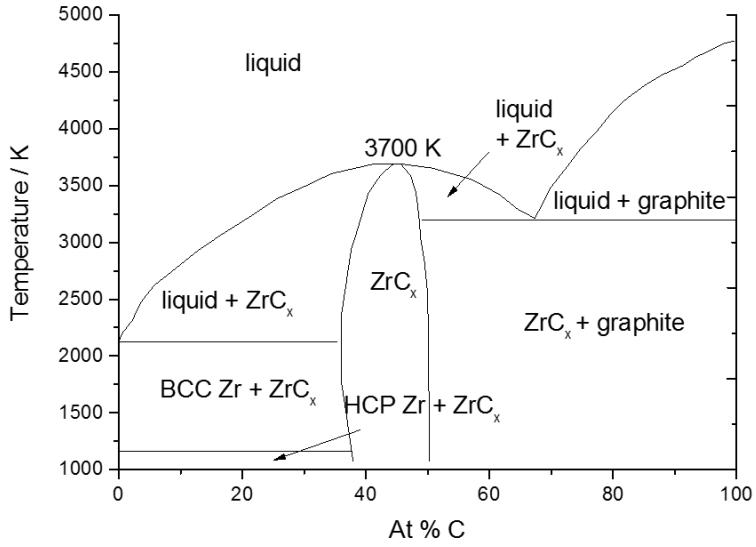


Figure 2.12: Calculated phase diagram for Zr-C system. Reproduced from Fernandez-Guillermet [43]

Figure 2.12 reveals the existence of the ZrC_x phase between around 37.5 and 49.5 at% C, where x is between 0.6 and 0.98, with the congruent melting of the ZrC_x phase (roughly around $ZrC_{0.85}$) at 3700 K. Below roughly 37.5 at% C a hexagonal close packed (HCP) Zr and ZrC_x two phase-field exists until around 1200 K where the Zr metal becomes body centered cubic (BCC), this phase begins melting at around 2127 K, resulting in liquid Zr and solid ZrC_x. It is also important to note there is no existence of a ZrC_x phase where x is greater than 1, instead ZrC_x + C phases form at carbon contents above 49.5 at%.

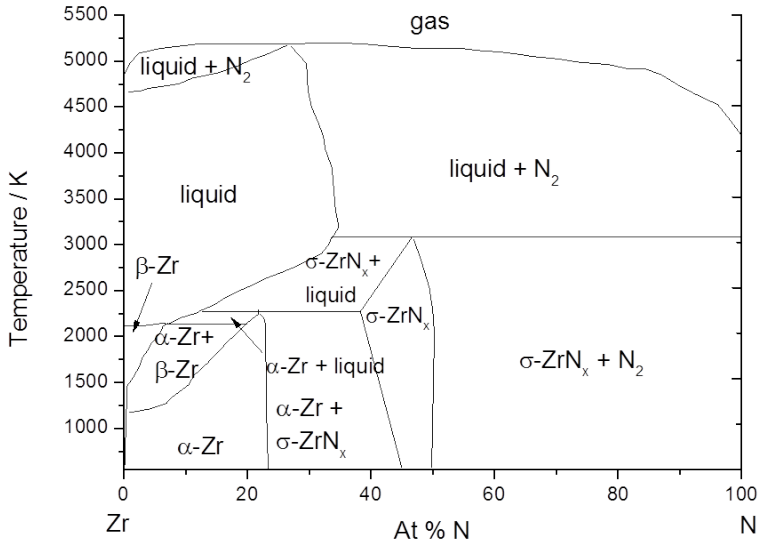


Figure 2.13: Calculated phase diagram for the Zr-N system. Reproduced from Gribaudo et al. [44]

The Zr-N phase diagram (Figure 2.13) reveals a gas phase, a liquid phase, the solution of nitrogen in BCC-Zr (β-Zr) and the solution of nitrogen in HCP-Zr (α-Zr) as well as the non-stoichiometric FCC $\sigma-ZrN_x$ phase where $x \leq 1$ at N at% less that 50. Ma et al. [45] reported a ZrN_4 phase in the region of the single phase $\sigma-ZrN_x$, however Lengauer [41] stated the zirconium nitrogen system consisted of one nitride phase of σ-ZrN_{1-x}, similar to the carbide, where the N/Zr ratio $\leq$1. Gribaudo et al. [44] also state the σ-ZrN_xphase exists where x=0.5-1 below 50 at% N similar to the Zr-C system, however above 50 at% N a solid ZrN phase and N_2 gas phase exists with no higher nitrides.

The ZrN_x phase at the Zr-rich boundary has been examined using several techniques, such as metallography, X-ray diffraction (XRD), hardness and electrical resistivity. Eron'yan et al. [46] used vapour pressures and XRD to determine congruent melting of the ZrN_x phase at close to stoichiometry took place above 3673 K under a partial pressure of N_2 of around 6 MPa.

Binder et. al. [47] also reported a tentative Zr-C-N ternary diagram for the carbonitride at 1423K using microprobe and metallographic analysis of Zr-C-N samples prepared from mixing commercially-available ZrC and ZrN powders to achieve desired stoichiometries (Figure 2.14).

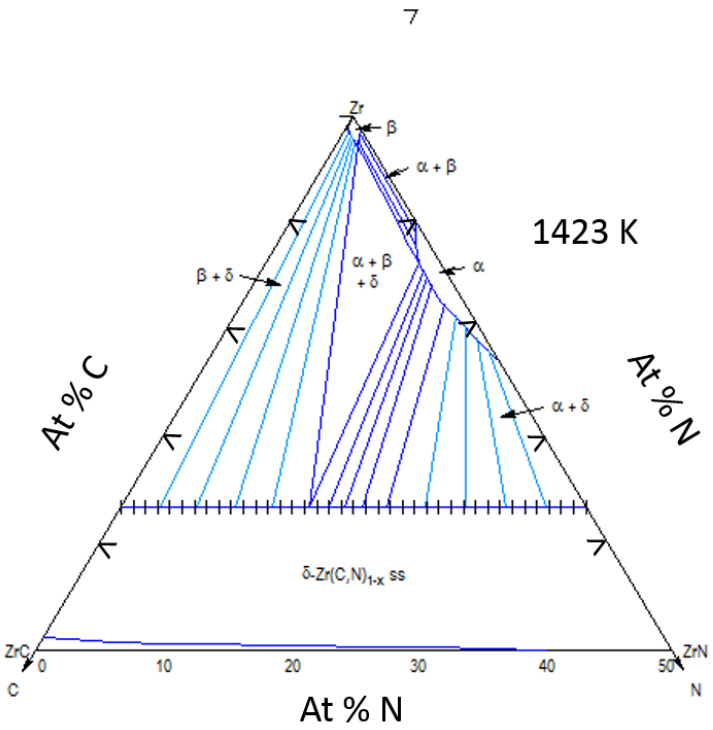


Figure 2.14: Phase diagram for Zr-C-N system at 1423K [47]

Figure 2.14 indicates that at 1423 K the carbonitride has a quasi-binary solid solution which is due to the carbon and nitrogen atoms occupying the octahedral interstitial sites randomly denoted in Figure 2.14 as the δ phase, whereby δ-Zr(C,N)$_{1-x(ss)}$ denotes the solid solution carbonitride with this B1 rocksalt structure ($Fm\bar{3}m$, space group 225). The metal rich boundary is essentially a straight line dividing the δ-Zr(C,N)1-x phase and the HCP α(ZrC,N) and BCC β(ZrC,N) phases. A three phase equilibrium triangle of δ+α+β also exists with a higher nitride composition of the Zr(C_xN_{1-x})$_y$ phase.

2.2.3 Thermal and Electrical Properties

2.2.3.1 Enthalpy of Formation

Standard enthalpy of formation (Δ_fH) for ZrC and ZrN at near stoichiometry is -196.65 and -365.26 kJ/mol respectively.[1, 48] Toth [49] summarised the heat of

formations for ZrC_x phases with increasing carbon vacancies having to be less negative which can be explained as the ZrC bond strength decreasing resulting in less stable compositions. This difference in enthalpy of formation between ZrC and ZrN matches well with Piersons' [1] comments that the ZrN bond is stronger due to the increased electronegativity difference between nitrogen and carbon. However, Lengauer [41] states the nitride bond is weaker than the carbide due to the extra electron in the nitrogen 2p orbital occupying an antibonding orbital. Lengauer [41] also explained the more negative the heat of formation for the nitrides, the lower the equilibrium nitrogen pressure is, which determines the phases obtained and if the pressure is high enough this leads to a non-metal/metal ratio greater than 1. However, ZrN_x metastable phases with $x > 1$ (such as Zr_3N_4) are usually only produced using magnetron sputtering or chemical vapour deposition techniques to produce thin films where observation of metastable phases is possible.[24–26, 50]

2.2.3.2 Heat Capacity

Heat capacity (C_p) corresponds to the ratio of heat energy added to a material to the resulting temperature change and shows how much energy is required to heat a mole of material by 1 K. Heat capacities for ZrC plotted as a function of temperature are shown in Figure 2.15.[51–55] Heat capacities of ZrC were measured by Neel et al. [54] and Levinson [53] using high temperature drop calorimetry. Scatter in the literature is due to authors reporting different stoichiometries of ZrC_x where x can be between 0.92 and 0.96. Chase [48] reported the function of C_p against temperature by (where C_p is heat capacity in J mol^{-1} K^{-1} and T is the absolute temperature) by Equation 2.12.

$$C_pZrC = 51.027 + 3.685T - 0.199T^2 + 0.028T^3 - 1.304/T^2 \tag{2.12}$$

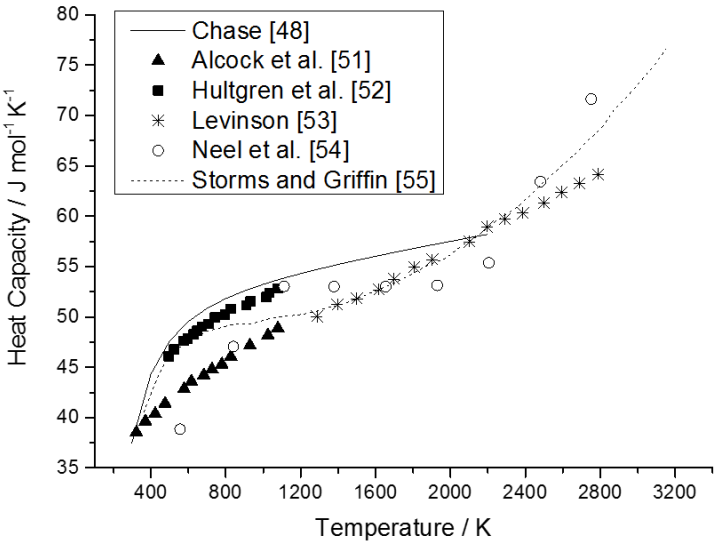


Figure 2.15: Heat capacities of ZrC as a function of temperature [48, 51–55]

Molar heat capacities for ZrN and some zirconium carbonitride phases are shown in Figure 2.16 and Figure 2.17.[54, 56–59]. Differential scanning calorimetry (DSC) was used to measure heat capacity of ZrN by Basini [56], Ciriello [59] and Muta [58] and by drop calorimetry by Hedge [57] and Neel. et al.[54]. Chase [48] reported the function of C_p against temperature in Equation 2.13.

$$C_pZrN = 46.4587 + 7.0063T - 0.0077T^2 + 0.0007T^3 - 0.7205/T^2 \qquad (2.13)$$

Both the carbide and nitride show a sharp increase in C_p at low temperatures to about 600 K, then plateauing until 1500 K where it begins to increase again. Nitrides generally show a slightly higher heat capacity than the carbide, however with experimental room temperature (RT) values of around 42 J mol^{-1} K^{-1} compared to 38 J mol^{-1} K^{-1} for ZrN and ZrC respectively the differences can fall within experimental error and so can be considered negligible.

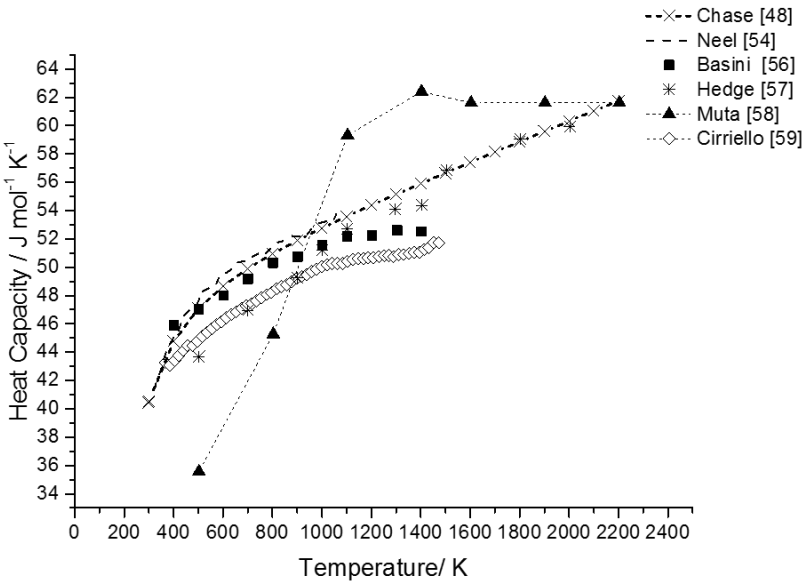


Figure 2.16: Heat capacity of ZrN as a function of temperature [48, 54, 56–59]

Lengauer et al. [60] measured the heat capacities of some carbonitrides of zirconium using DSC up to 1100 K, again, C_p increased with increasing nitrogen content.[60] Einstein's formula for predicting molar heat capacity is derived from the oscillation of the bonds of a molecule, explaining that as T approaches 0 K, heat capacity also reaches zero and the plateaus of C_p observed in materials at higher temperatures arise from saturation of oscillating bonds with energy. From this the explanation the higher C_p's of the higher nitrogen containing carbonitrides arises from the nitride containing more occupied antibonding orbitals giving longer, weaker bonds which are less stiff. This results in the vibrational energy levels being closer together, therefore when a quantity of energy arrives as heat there is little change in the distribution in the population of the energy levels (according to the Boltzmann distribution) and corresponds to a material with a higher heat capacity.

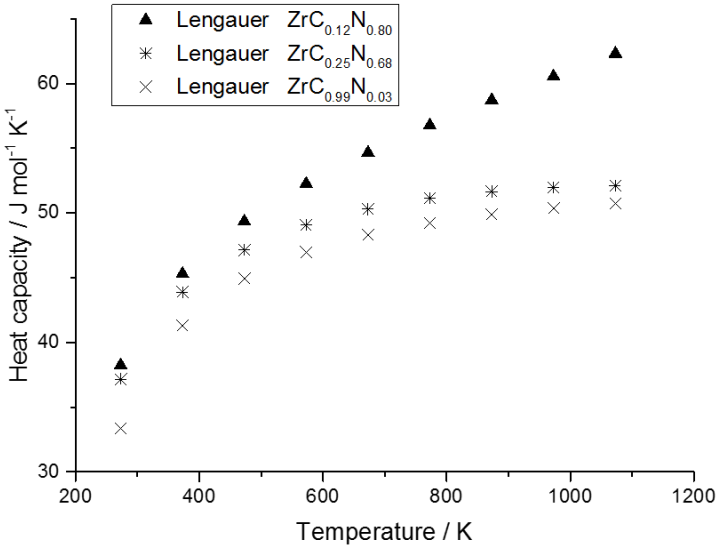


Figure 2.17: Heat capacity of some zirconium carbonitrides as a function of temperature from Lengauer et al. [60]

2.2.3.3 Thermal Conductivity

Thermal properties, such as thermal conductivity are an important property for nuclear fuel elements. The desire for increased efficiency for Generation IV reactors necessitates high thermal conductivity to increase the rate of heat transfer from the fissile phase to the coolant. Safety is another paramount concern for all materials being evaluated for use in Generation IV NPP. IMF's must reduce the potential for the build-up of hot spots within the reactor core where fission events and their daughter decay events will cause concentrated hot spots in the event of a loss of coolant accident (LOCA) event.

Thermal conductivity ($Wm^{-1}K^{-1}$) is the product of the thermal diffusivity (α, m^2 s^{-1}), density (ρ, kg m^{-3}) and heat capacity (C_p, J kg^{-1} K^{-1}) of a material, given by Equation 2.14.

$$K = \alpha \rho C_p \tag{2.14}$$

Thermal conductivities can be corrected to represent the thermal conductivity of a material having 100% theoretical density using the Maxwell-Eucken equation

(Equation 2.15), where P is the porosity, Kp is the measured thermal conductivity and K_{TD} is the corrected thermal conductivity for a fully dense material.[61]

$$Kp = \frac{(1-P)}{(1+P)} K_{TD} \tag{2.15}$$

Thermal conductivity of ZrC and ZrN as a function of temperature have been studied extensively (Figure 2.18 and Figure 2.19).[41, 54, 56–59, 62–66] All values in Figure 2.18 and Figure 2.19 have been corrected to 100 %TD for ease of comparison, however the experimental values obtained by Basini et al.[56] for a 70% TD ZrN sample are shown as they match quite well with literature and extrapolation to a fully dense material using Equation 2.15 may be inappropriate for such a large porosity.[56] A positive trend is seen for both the carbide and nitride which is evidence for metallic bonding. Thermal conduction in ceramics is a contribution of phonon and electron conduction. In defect free materials, phonon conduction increases with increasing temperature as phonon-phonon collisions are rare, until a point where lattice vibrations become anharmonic causing scattering of the phonons and reducing thermal conductivity. It is therefore expected, if the thermal conductivities of ZrC and ZrN were wholly dominated by phonon conduction that there would be a decrease at higher temperatures, however this is not observed in Figure 2.18 and Figure 2.19. With the exception of some work on ZrN reported by Basini et al. [56] Hedge et al. [57] and Neel et al. [54] which decreases at higher temperatures.

The carbide and nitride of zirconium can accommodate vacancies, particularly on the non-metal site, with regards to thermal properties, vacancies are points of defects where phonons and electrons can be scattered which decrease thermal conductivity. The effect of non-stoichiometry on the thermal conductivity of ZrC has received attention with the thermal conductivity falling rapidly to around 10 $Wm^{-1}K^{-1}$ for $ZrC_{0.5}$-$ZrC_{0.85}$ [67, 68] However, no study of the effect of thermal conductivity as a function of nitrogen vacancies exists for the nitride. This may be the reason for the large amount of scatter in the literature as vacancies, impurities and porosity will all adversely affect thermal conductivity with the stoichiometry rarely being reported in the literature.

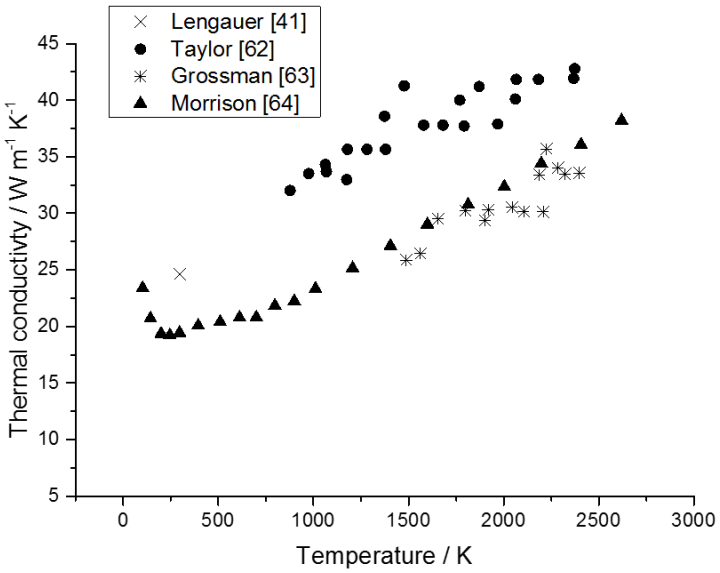


Figure 2.18: Thermal conductivity of ZrC as a function of temperature [41, 62–64]

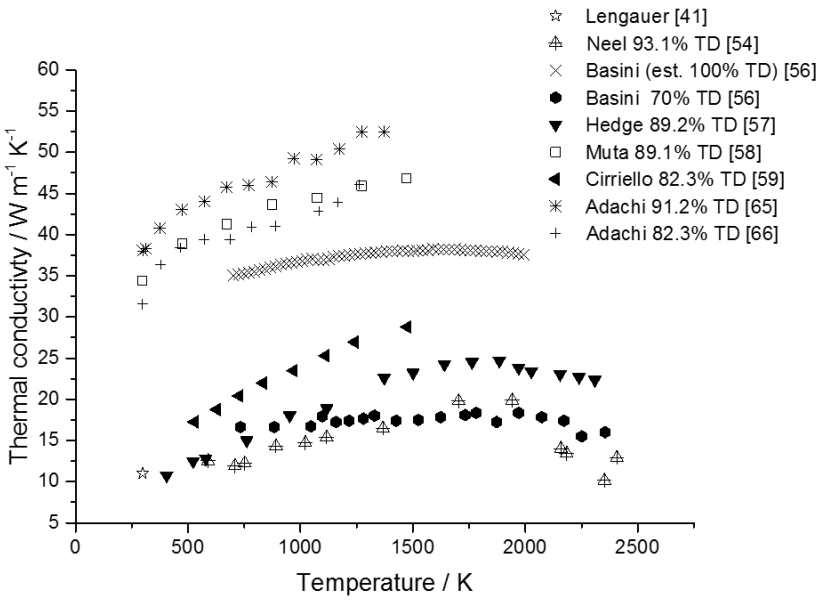


Figure 2.19: Thermal conductivity of ZrN as a function of temperature [41, 54, 56–59, 65, 66]

Lengauer et. al.[60] reported the thermal conductivities of several ZrC_xN_y ceramics to 1100 K shown in Figure 2.20. The authors produced the desired compositions by

mixing of commercially-available ZrC and ZrN powders and chemical analysis was performed by combustion gas analysis. The trend in increasing thermal conductivity with increasing nitrogen content was attributed to a higher number of electrons contributing to thermal conductivity with increasing nitrogen content as determined by electrical conductivity measurements (presented in the the following section).

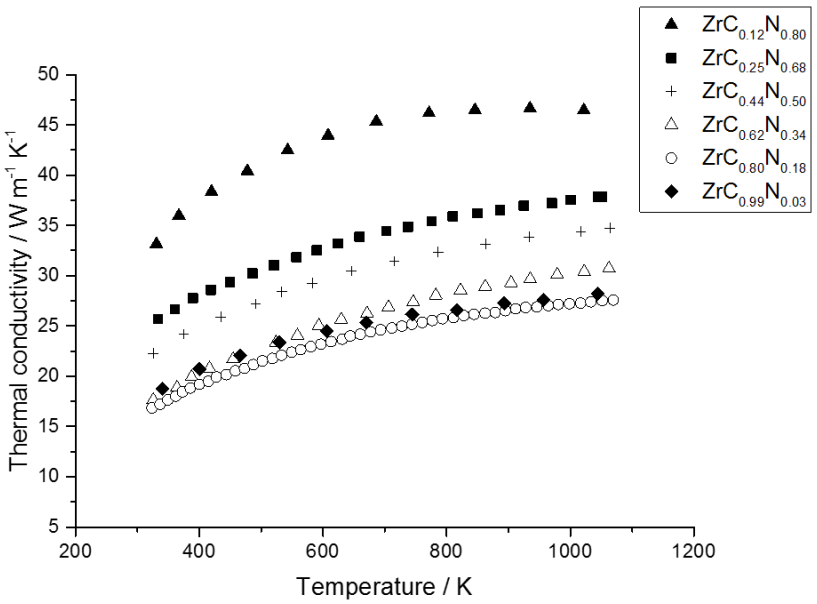


Figure 2.20: Thermal conductivities of ZrC_xN_y phases as a function of temperature from Lengauer et al. [60]

2.2.3.4 Electrical Conductivity

Thermal conductivity is a sum of the electron and phonon conduction of a material expressed in Equation 2.16, where K_{Tot} ($Wm^{-1}K^{-1}$) is the total thermal conductivity, K_{el} ($Wm^{-1}K^{-1}$) is the electron contribution and K_{lat} ($Wm^{-1}K^{-1}$) is the phonon contribution to thermal conductivity. The electronic contribution can be determined using the Wiedemann-Franz-Loranz equation (Equation 2.17), where L is the Lorenz number, widely accepted as 2.44×10^{-8} $W\Omega K^{-2}$, σ is the electrical conductivity ($\Omega^{-1}m^{-1}$) and T is the absolute temperature (K).[66]

$$K_{Tot} = K_{lat} + K_{el} \tag{2.16}$$

$$K_{el} = L\sigma T \tag{2.17}$$

The Wiedemann-Franz law states that for metals, the ratio of thermal conductivity to electrical conductivity is proportional to temperature (Equation 2.18) and is a constant.[69] Morgan [70] reported that the electrical contribution to thermal conductivity of good electrically conductive ($\geq 10^3\ \Omega^{-1}\mathrm{m}^{-1} \leq 10^5\ \Omega^{-1}\mathrm{m}^{-1}$) ceramics obey this law of proportionality and their electrical heat conduction can be determined using the Wiedemann-Franz-Lorenz equation (Equation 2.19). Due to the phonon conduction still being an important factor in these materials the Wiedemann-Franz-Lorenz equation corresponds only to the K_{el} contribution of K_{tot}. Lorenz demonstrated this constant to be L (Equation 2.19) calculated from Equation 2.20, where k_b is the Boltzmann constant (J K^{-1}) and e is the charge of an electron (C). In the case of metals, their thermal conductivity is completely dominated by electrical heat conduction so the Wiedemann-Franz-Lorenz equation $\sim \mathrm{K}_{Tot}$.

$$\frac{K}{\sigma} \propto T \tag{2.18}$$

$$\frac{K}{\sigma} = LT \tag{2.19}$$

$$L = (\frac{\pi^2}{3})(\frac{k_b}{e})^2 \tag{2.20}$$

Electrical conductivities of ZrC and ZrN as a function of temperature are presented in Figure 2.21.[63, 65, 66, 71–74] The electrical conductivities of some zirconium carbonitride phases are shown in Figure 2.22, although no values for the monolithic phases were presented in the same work.[60] ZrC and ZrN both show metallic behaviour, with an inverse relationship to temperature. Factors such as porosity, impurities, vacancy concentration and microstructure will affect the electrical conductivity of the samples, which is again the cause of scatter in the literature, mainly for the ZrN samples. However, no detailed work has been reported on how defects, oxygen and carbon impurities and microstructure affect conductivity.

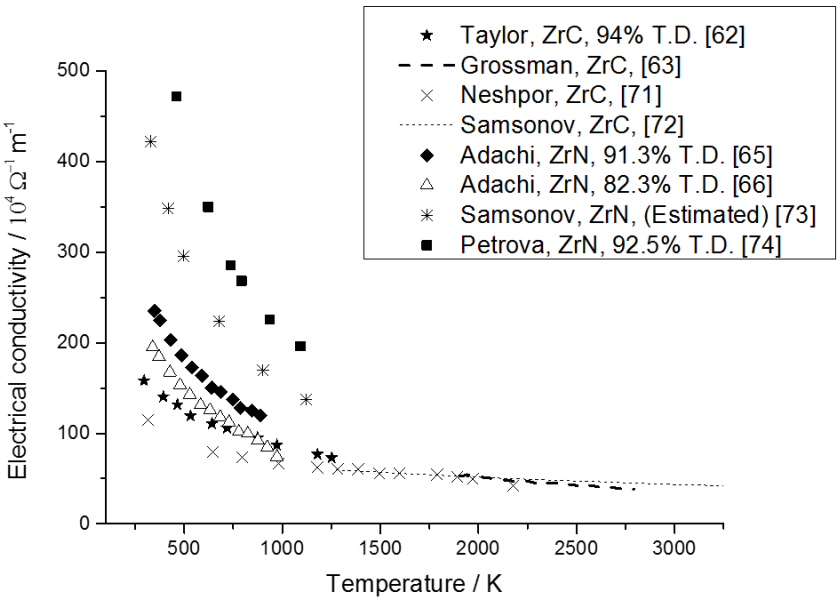


Figure 2.21: Electrical conductivity of ZrC and ZrN as a function of temperature [62, 63, 65, 66, 71–74]

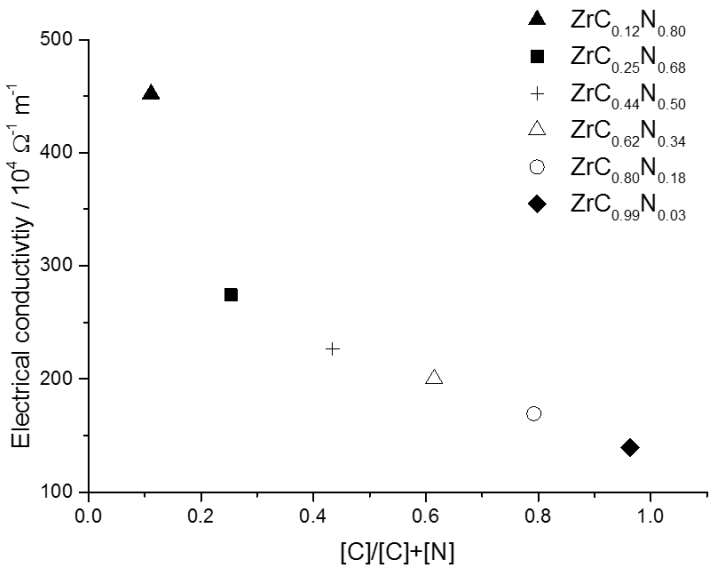


Figure 2.22: Electrical conductivities of ZrC_xN_yphases at room temperature as a function of [C]/[C]+[N] ratio from Lengauer et al. [60]

Adachi et al. [66] measured the electrical conductivity of ZrN samples containing around 10-18% porosity, determining nitrogen content using chemical analysis to

give a stoichiometry of $ZrN_{0.935}$, however no oxygen or carbon analysis is presented. Vacancies and impurities are an important factor in conduction as defects create a scatter point for phonons and electrons, reducing the electrical conductivity. Adachi et al.[66] also reported the electron contribution to thermal conductivity (Equation 2.17) as 16 and 20 $Wm^{-1}K^{-1}$ for the 18% and 10% porous samples respectively, which amounts to two thirds of the total conductivity reported. Petrova et al. [74] reported the room temperature electrical conductivity of ZrN as $\sim$450 $\times$ $10^4\Omega^{-1}m^{-1}$using samples produced by precipitation of $ZrCl_4$ with N_2/H_2 gas achieving stoichiometries of between $ZrN_{0.97-1.00}$ and sample densities very close to theoretical density, stating that this preparation route seems to lead to high purity materials however no experimental technique for elemental analyses is presented.

It can be seen from Figure 2.21 and Figure 2.22 that the nitride has a higher electrical conductivity than the carbide, and for the carbonitride electrical conductivity increases with increasing nitrogen content. Lengauer [41] attributed this increase in conductivity to the nitride having a higher DOS at the Fermi Level (Figure 2.11)[42], due to the nitrogen's extra valence electron resulting in an antibonding state the symmetry of the p-d non-metal to metal bond changes allowing increased metal d-d bonding, resulting in this increased DOS at the Fermi Level.

2.2.3.5 Thermal Expansion

Interatomic spaces between metal and non-metal atoms can vary as a function of temperature, due to increased energy exciting the atoms into higher energy states. This causes higher amounts of vibration, which results in them moving further apart from each other due to anharmonic behaviour when oscillating. The degree of bonding strength affects the extent to which the atoms can move away from each other, with stronger bonds reducing thermal expansion and weaker bonds showing the opposite effect. Thermal expansion is an important character of a composite fuel material, such as UN dispersed in ZrN. If the two materials expand by different amounts on heating there is a thermal expansion mismatch, which can result in the ceramics cracking. This is a potential issue for advanced nuclear fuels, as cracking can lead to the release of FP from the pellet. The thermal expansion of ZrC and ZrN measured by neutron diffraction,[75] high temperature X-ray diffraction [76, 77] and dilatometry [54, 65, 66, 78] and are presented in Figure 2.23 and Figure 2.24.

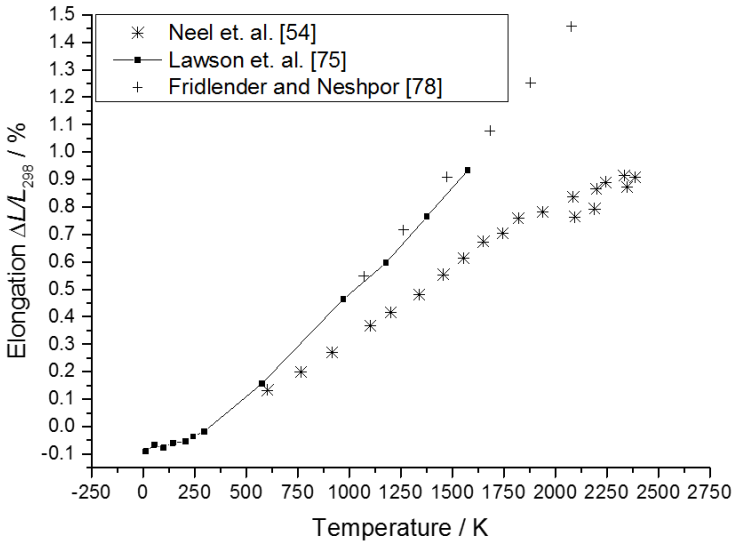


Figure 2.23: Elongation with respect to length at 298 K of ZrC as a function of temperature [54, 75, 78]

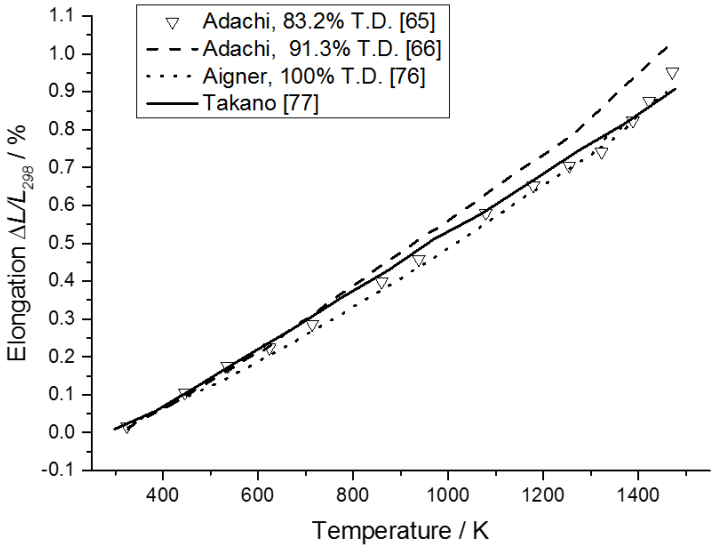


Figure 2.24: Elongation with respect to length at 298 K of ZrN as a function of temperature [65, 66, 76, 77]

Adachi et. al. [65] explained that thermal expansion is not affected by porosity and grain size, accounting for the similar results for their porous samples with previous

work. For these materials the expansion in length, which can be expressed as the coefficient of thermal expansion (CTE). The CTE represents the degree of expansion, ΔL, as a function of temperature and has the unit K^{-1}. The carbides and nitrides presented in Figure 2.23 and Figure 2.24 all have CTEs in the range of 2 to 8 $\times$ 10^{-6} $K^{-1}$from RT-1273 K and is similar to other ceramics such as alumina and zirconia. Aigner et al. [76] measured the variance in thermal expansion of zirconium carbonitrides using high temperature XRD, giving the CTEs (α av) in Equation 2.21.

$$\alpha_{av} = (7.8 + 0.3(\frac{[C]}{[C]+[N]})) - 0.6(\frac{[C]}{[C]+[N]}) \times 10^{-6} \tag{2.21}$$

2.2.4 Mechanical Properties

ZrC and ZrN have received extensive use as coatings for cutting tools and abrasives due to their high hardness and melting points. As a consequence, the majority of work regarding the mechanical properties of ZrN and ZrC, such as Young's modulus and hardness has been performed on thin films and coatings.[79–88]

2.2.4.1 Young's Modulus

Young's modulus is a measure of stiffness of a material and represents a constant of elasticity between the stress and strain of material that linearly deforms with force, known as a linear elastic material. The most popular method of determining elastic constants in materials with high values of Young's modulus is by measuring the velocity of ultra sonic waves passed through a material, measuring the vibration of the materials (dynamic resonance) or can be measured by applying a static load and measuring the resulting strain (static method).

Young's modulus of ZrC as a function of temperature was measured by dynamic methods by Baranov et al. [86] and Travushkin et al. [87] and by 4 point bend method by Zubarev et al. [89](Figure 2.25). Measuring strain in materials with high Young's modulus values (GPa) with high tensile strengths (MPa) via static methods is difficult due to the low values strains thus measurements from vibrational data Figure 2.25 is likely more accurate than the bending data.

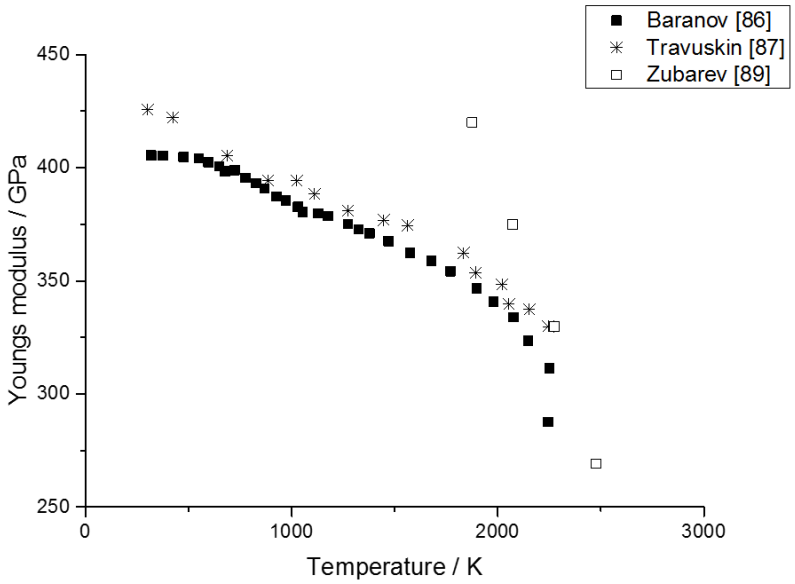


Figure 2.25: Young's modulus of ZrC as a function of temperature [86, 87, 89]

Alexandre and Desmaison-Brut [90] measured the Young's modulus of ZrN which was produced using hot isostatic pressing (HIP) at 2223 K under 195 MPa of pressure for between 1-2 hours. Elasticity measurements were made by the disc vibration technique and reported as a function of porosity, with highly dense (1% porosity) samples having a Young's modulus of around 390 GPa, decreasing to 290 GPa with increasing porosity (8% porosity). Adachi et al. [91] measured the Young's modulus of ZrN ceramics prepared by spark plasma sintering (SPS) using ultrasonic pulse echo method. Samples of varying porosity (7-18%) were measured giving a values of 288 GPa for the 8% porous sample and 156 GPa for the 18% sample.

2.2.4.2 Hardness

Hardness is defined as the resistance of a material to the formation of a permanent impression on its surface by an indenter.[92] A variety of shapes are used for the indenter, in the Vickers hardness test a square pyramid is used, the Knoop hardness test is similar except that the pyramid is elongated. Dislocations are line defects in a material, such as an extra or missing half plane of atoms (edge dislocation), or two offset planes (screw dislocation). Movement of these dislocations provide a mechanism for plastic deformation. Slip (dislocation motion) can be defined by

atom position in the crystal structure, giving the slip plane (denoted with ( ) for specific and {} for groups of planes) and the direction of slip (denoted with [ ] for specific and < > for groups of planes)

ZrC has received many more hardness studies than the nitride (Figure 2.26), with indentation being used to study bulk hardness and preferred slip systems.[93] The covalent bonding in ZrC means that in closer packed planes the bonds will be stronger than in a metal giving a harder material.

Hardness as a function of temperature has been studied by Kohlstedt [94] on single crystals of $ZrC_{0.94}$ around 1273 K. Discs of 10 mm in diameter and 0.5 mm in height were orientated in the (001) plane and placed under a load of 500 g at a rate of 10 μm/sec. Kohlstedt [94] noted that at lower temperatures, the highly directional covalent bonds on the close-packed {111} planes inhibit slip and reduce dislocation mobility. However, at higher temperatures sharp decreases in hardness were explained due to the increasing mobility of s electrons with temperature screening the bonding orbitals which reduces the directionality of the covalent bonds, thereby reducing the hardness to that similar of a metal. However, this may be described more simply by the fact dislocations can only move if they overcome resistance of the lattice which will have to overcome an activation barrier which is normally not very high, thus thermal energy, kT, can have a significant impact.[95]

Kumashiro et al. [96] measured the micro-hardness of single crystals of $ZrC_{0.9}$, $NbC_{0.9}$ and $TaC_{0.83}$ using a load of 100 g for varying loading times (1-100 sec), with the indentation orientation in the {100} plane in the <001> direction. $ZrC_{0.92}$ was found to be the softest, being justified as ZrC having a larger lattice parameter than the other carbides, reflecting the metal carbide bond being longer and therefore weaker. Thermal softening was observed as it was by with Kohlstedt which was attributed to lattice vibration increasing, resulting in a bond lengthening and weakening.

Gridneva et al. [97] measured the Vickers hardness (H_v) of single crystal ZrC on the (100) plane under a load of 115 g to a temperature of 1200 K. The authors noted the sharp fall in microcracks around the point of indentation at 1123 K, at which temperature ZrC can be deformed plastically. Cracks produced from indentations spread in the <100> direction, with the {111} <110> and {110} <110> slip systems being active.

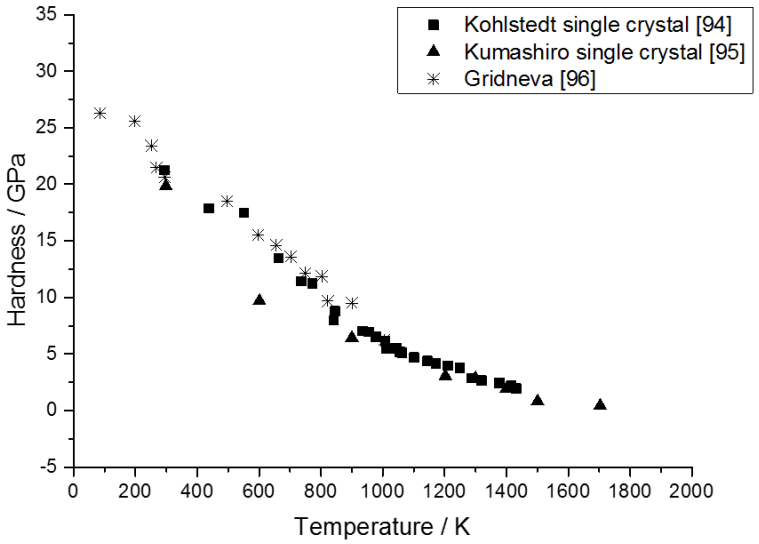


Figure 2.26: Hardness of ZrC as a function of temperature [94, 96, 97]

Microhardness of ZrN produced by SPS was measured by Adachi et al. [91] using an H_v tester at room temperature, with loads between 0.98 and 9.8 N being applied for 15 s. H_v was characterised as a function of porosity, with denser samples of 8% porosity having a H_v of between 10 and 11 GPa (depending on load), which decreased to between 5-8 GPa for more porous samples (18%). Results were extrapolated to a fully dense sample, estimating a H_v of around 15 GPa for the samples.

Lengauer et al. [60] measured the room temperature H_v of some ZrC_xN_y phases using a load of 0.98N. H_v was found to decrease with nitrogen content, from a value of 23 GPa for ZrC to around 18 GPa for $ZrC_{0.25}N_{0.75}$. The effects of nitrogen on the hardness of the materials were explained as the result of increased antibonding states in the nitride arising from its extra valance electron. Although the nitride will have more antibonding states occupied than the carbide, decreasing the covalent nature of it's bonding, the nitride bond is also electrostatically stronger due to nitrogen being more electronegative than carbon.

2.2.5 Fuel Fabrication Experience

2.2.5.1 Mixed Nitride Systems

The Japanese Atomic Energy Agency (JAEA) has also proposed ZrN and TiN as diluent materials for the Accelerator Driven System (ADS). Arai and Nakajima [98] and Minato et al. [27] prepared PuN pellets containing ZrN and TiN as inert matrices. The mixtures used carbothermal-reduced PuO_2 powder and commercial ZrN and TiN. PuN was prepared by mixing PuO_2 and graphite in a C/PuO_2 molar ratio of 2.2, the powders were then compacted into discs at 100 MPa and heated in an N_2 atmosphere at 1823 K for a dwell time of 10 h, then heated at 1723 K for a dwell time of 20 h using a hydrogen doped nitrogen atmosphere. The powders of PuN and ZrN were mixed in a Pu:Zr ratio of 40:60 wt% respectively and a 50:50 wt% mixture of Pu:Ti. The mixed powders were compacted into discs again (and heated under a hydrogen doped nitrogen atmosphere for 5 h for homogenisation of the respective nitrides). This step was repeated three times, then the discs were ground and compacted into green pellets at 300 MPa and sintered under argon at 2003 K for 5 h followed by heating in a hydrogen doped nitrogen atmosphere at 1673 K to control stoichiometry resulting in a lengthy processing time. Nitrogen, carbon and oxygen quantities were determined by combustion gas chromatography, inert gas fusion coulometry and high frequency heating coulometry, respectively, Table 2.6 shows chemical analysis and sintered density results (wt% have been converted to at% for comparison).

Sample	Pu content/ at%	Nitrogen/ at%	Oxygen/ at%	Carbon/ at%	Bulk density / %TD
PuN + ZrN	11.4	45.4	4.2	1.4	95
PuN + ZrN	18.9	51.0	2.1	1.5	90
PuN + TiN	10.9	45.4	2.5	1.0	75
PuN	49.7	49.7	0.3	0.3	96

Table 2.6: Chemical analysis and densities for ZrN and TiN containing pellets compared with PuN pellets [98]

XRD revealed the Pu, Zr, N system existed as one FCC phase except for a small amount (<1 wt%) of oxide phases present, while the TiN pellets consisted of a composite of PuN + TiN. Lattice parameters of the ZrN pellets were in good agreement

with parameters assumed by Vegards law, again suggesting a solid solution was formed giving pellets of single phase (Pu,Zr)N. Lattice parameters for the TiN containing samples did not change from those of PuN and TiN separately, supporting the co-existence of the two phases. Arai and Nakajima [98] suggest it may be possible to increase the solubility by increasing the sintering temperature or reducing particle sizes. A single phase ceramic is not a strict requirement but control of the microstructure becomes more important if the composite exists as two phases, density of these two phases will also be important as higher densities will give structural stability and increase thermal conductivity.

Initial fabrication of carbide and nitride fuel has been focused on processing routes to the non-oxide material and sintering techniques to achieve dense ceramics of the refractory carbides and nitrides with some initial thermophysical properties also being measured. Thermophysical properties of $(Pu_{0.25},Zr_{0.75})N$ solid solutions have been reported by Basini et al. [56] No details of the experimental pressing procedure is given however the authors report the density of the $(Pu_{0.25},Zr_{0.75})N$ samples to be 89% of the theoretical density (TD) which is much higher than the 70% TD for the ZrN pellets reported in subsubsection 2.2.3.3. Basini et al. [56] report the scarcity of thermal conductivity data with the few available results not being reproducible. They give the thermal conductivity of $(Pu_{0.25},Zr_{0.75})N$ between 700 and 2300 K as between 10-20 $Wm^{-1}K^{-1}$. Conductivities were then corrected to fully dense materials using the Maxwell-Eucken correlation (Equation 2.15). With these corrections the thermal conductivities were 15-25 $Wm^{-1}K^{-1}$ over the same temperature range.

Thermal properties of ZrN and PuN have been also been reported by Ciriello et al. [59] including the specific heat, thermal diffusivity and thermal conductivity. (Pu,Zr)N samples were prepared using a sol get method to precipitate a mixture of $(Pu_{0.25},Zr_{0.75})O_2$ which was mixed with carbon black and then underwent carbothermic reduction under nitrogen atmosphere at a dwell time of 12 h and a temperature of 1673 K. After the 12h dwell the atmosphere was changed to an 8% hydrogen/nitrogen atmosphere for 16 h. XRD revealed an oxide phase and thermal conductivity measurements of the $(Pu_{0.25}Zr_{0.75})N$ pellet were 10-20 $Wm^{-1}K^{-1}$ from 500-1500 K, the low values reported may be caused by the oxide impurities revealed by XRD from the processing and porosity of both the pellets as a result of the green body sintering technique.

Thermophysical properties of TiN, ZrN, DyN, UN pellets by made by SPS have been determined by Muta et al.[58] Powders were fabricated from their oxides by carbothermic reduction and sintered under a flow of nitrogen gas under a pressure of 100 MPa with a dwell time of 5 min. Fabricated powders and their composites were produced using SPS with sintering parameter shown in Table 2.7.

Sample	SPS temperature / K	Sintering time /min	Relative density/ %TD	Thermal conductivity (298-1600 K)/ $Wm^{-1}K^{-1}$
TiN	2073	21	95.7	40-55
ZrN	2073	21	89.1	35-42
UN	1773	18	89.9	15-21
TiN+DyN (6Ti:4Dy)	1873	19	93.8	25-25
TiN + UN (6Ti:4Dy)	1873	19	95.5	28-36
$Zr_{0.6}Dy_{0.4}N$	1873	19	102	22-30
$Zr_{0.6}U_{0.4}N$	1873	19	96.3	10-24

Table 2.7: Sintering parameters for SPS of inert matrix pellets [58]

Again restriction of grain growth in all samples was reported with grains in the region of ∼1-5 μm. Thermal conductivities of all samples prepared by SPS (Table 2.7) increased compared to conventionally prepared samples (sintered at 2073 K for 8-28 h). The increase in thermal conductivity was attributed to the build-up of local high temperature regions on the particles surface during sintering which removes thin impurity regions on the particle, reducing the scattering of impurity-phonons. It would be expected however, that smaller grains may give an increase in phonon scattering. However, Lee et al. [99] measured the effect of grain size on thermal conductivity of HP SiC samples with average grain sizes of 0.7, 1.3 and 1.5 μm which had RT thermal conductivities of 82, 106 and 112 $Wm^{-1}K^{-1}$ respectively, showing a plateau in thermal conductivity above grains 1 μm. The observation by Muta et al. [58] of increased thermal conductivity arising from less impurity scattering of phonons is therefore plausible.

2.2.5.2 Sintering

The driving force for densification is reduction of the surface area which are regions of high energy due to atoms at the surface having fewer neighbors than atoms in the bulk. Sintering occurs by several mechanisms which include densifying mechanisms;

- Grain boundary diffusion
- Lattice diffusion from the grain boundary
- Plastic flow

Non-densifying mechanisms include;

- Surface diffusion
- Lattice diffusion from the surface
- Vapour transport

After initial stages of sintering where rapid neck formation occurs, the porous phase still exists as a continuous phase. Plastic flow or grain boundary diffusion to the pore results shrinkage of the pore and therefore densification, opposed to surface or vapour diffusion. This pinches off the continuous porosity and forming discontinuous pores. Vapour and surface diffusion also lead to grain coarsening whereby grains become larger however porosity is not removed (non-densifying). In the densification of non-oxide materials, surface oxides on the surface of the non-oxide particles have been attributed to poor densification by enhancing grain coarsening.[100]

SPS has been increasingly used to prepare dense samples of nitrides. SPS, which is also referred to as pulsed electric current sintering or field assisted sintering involves the passing of a pulsed DC current through the graphite die and sample inside heating via rapid Joule heating along with uniaxial pressing to compact powders.[58, 101] A review by Munir et al. [102] reports the success of SPS in achieving cleaner grain boundaries, improved mechanical and thermoelectric properties, densities close to TD, low grain growth and improved oxidation and corrosion resistances.

SPS offers the advantages of sintering materials in a matter of minutes as opposed to the hours needed using other conventional densification techniques such as hot pressing (HP) or pressureless sintering (PS). It is generally well established that rapid Joule heating and current effects in materials with good conductivity are mechanisms that operate during the sintering process. Hulbert et al. [103] recently studied the mechanism of 'a momentarily-generated' spark plasma between particles.

Plasma is a state of matter similar to gas in which a certain proportion of the particles are ionised. However, the authors noted the absence of plasma generation and suggest the enhanced densification of SPS lies in other factors such as the rapid heating rates.

Sintering behaviour and microstructures of the IMF carbides and nitrides have been studied by Ryu et al. [101] who used SPS to fabricate IMF pellets of actinide oxide phases in carbides and nitrides. Dy_2O_3 was used to simulate MA oxides. When comparing the sintering behaviour of the monolithic carbide and nitrides with the Dy_2O_3 dispersion mixture Ryu et al. [101] found the sintering onset temperature was lower for the simulated actinide containing composite. Density measurements were performed using the water immersion method with the monolithic carbides and nitrides having densities of 63 and 65 % TD respectively with addition of 20 wt% Dy_2O_3 the TD for ZrC and ZrN achieved was 68 and 74% TD respectively, perhaps other factors were causing the high porosity of the materials, such as particle size or sintering program, as these value are less than observed elsewhere without oxide doping.[58, 66, 67] This reduction in porosity was attributed to the removal of oxide surface and enhanced diffusion as observed by others.[104, 105] Sakai and Iwata [104] noted the self-diffusion coefficient of AlN increases with oxygen content due to cation vacancies introduced in AlN crystals by oxygen doping. Korh et al. [105] reported that addition of Sm_2O_3 to AlN enhances AlN diffusion due to the formation of a liquid phase in Sm_2O_3-Al_2O_3-AlN system and this liquid phase increases mass transport.

Hollmer [106] reports the manufacturing methods for (U, Zr)N fuels by SPS using both commercially available and laboratory produced powders synthesised from pure metal starting materials. Individual powders of UN and ZrN were produced by a hydriding-nitriding of metal ingots followed by mixing and SPS. Pellets of 99.7% TD were achieved using laboratory-fabricated powders, compared with 89.7% TD using commercially-available ZrN. Heating rates and dwell temperatures were kept the same to compare densification (sintering parameters of 50 or 100 K/min and holding temperature of 1473 or 1923 K). Hollmer [106] attributes this observation to the high oxygen impurities of the commercial powder (7.697 wt% compared with 0.734 wt% for the produced powders), although no experimental technique for chemical analysis is given and no errors reported. Therefore it is not appropriate to discuss the results from the commercial powder as a nitride due to almost equivalent amounts of N and O are present (composition of 31.1 at% N, 23.7 at% O and 45.2 at% Zr assuming

no presence of other elements). However, high densities (99.7% TD) were achieved using the as-fabricated powders suggesting a small amount of oxygen contamination (∼0.7 wt%) has little effect on the achievable density.

Dysprosium nitride (used as a U/MA surrogate) and zirconium nitride composites have been fabricated by Pukari and Takano [107] by the hydrogenation-nitridation of Dy and Zr metal ingots. Oxygen concentrations up to 1.2 wt% were added using ZrO_2 or by increasing milling times to deliberately increase O content as to assess the effect on the processing of these materials. Powders were pressed into green bodies at 300 MPa and then pressureless sintered at 1923 or 1973 K for 6 h. Pukari and Takano [107] conclude that oxygen content that has dissolved into the nitride phase increases the achievable densities of ZrN and (Dy,Zr)N. Densities of ZrN increased from 89.6 to 91.6 TD for 0.20 and 0.8 wt% O respectively, and (Dy,Zr)N increased from 93.1 to 94.5 TD for 0.26 and 0.59 wt% O respectively. However, no error ranges on the density measurements are given and only geometrical densities are reported and these details would be necessary to asses the significance of these changes.

The observations of increasing density with oxygen content by Pukari and Takano [107] agrees well with the high densities achieved by Hollmer.[106] Low concentrations of oxides that can be further oxidised on may act as oxygen getters, reducing oxygen contaminatino of the non-oxide particel surface, reducing the mechanism of grain coarsening allowing increased solid-state sintering.[100] However, the formation of secondary phase oxides will occur and the effects on thermal properties may be detrimental.

2.2.6 Oxidation Behaviour

Diffusion of atoms in a material is theoretically governed by the existence of a atomic concentration gradient whereby atoms diffuse from an area of high concentration to low concentration. Ideal diffusion, such as that of a gas through a porous solid can be described by Ficks first law (Equation 2.22), where F is the flux of atoms, D is the diffusion coefficient and dn/dx represents the change in gradient in concentration in the x direction.

$$F = -D\frac{dn}{dx} \tag{2.22}$$

However, another constraint that becomes important in the diffusion of atoms in

a solid is the energy needed for that atom to move, known as the activation energy, E_a. According to the Boltzmann distribution, the distribution of atoms that populate higher energy states decreases exponentially and so is proportional to $exp(-\triangle E/kT)$, where $\triangle E$ (J) is the energy difference between two states, k is the Boltzmann constant (1.381×10^{-23} J K^{-1}) and T is the temperature (K). The diffusion coefficient, D (m^2/s) is related to this activation energy by Equation 2.23, where D_0 is a constant for that system and corresponds to the y-intercept on a plot of lnD vs. $1/T$ ($T = \infty$).

$$D = D_0 exp(-E_a/kT) \tag{2.23}$$

The standard enthalpy of formation ($\Delta_f H^0$) of ZrO_2 is -1097.46 kJ/mol as compared to -196.65 and -365.26 kJ mol^{-1} for ZrC and ZrN respectively.[1, 48] With little change between the entropy (S) of the oxide, carbide and nitride (between 33-50 J mol^{-1} K^{-1}[48]) the reaction is driven by this large decrease in enthalpy. Therefore there is a large decrease in the free energy of the system according to Equation 2.24, where G is the Gibbs free energy, H is the enthalpy, T is absolute temperature and S is the entropy.

$$\triangle G = \triangle H - T\triangle S \tag{2.24}$$

Grain boundaries in polycrystalline materials provide regions of high disorder and crystalline defects (such as vacancies and impurities) due to lattice mismatch and the width of the grain boundary can be assumed to be 1-2 atomic diameters thick.[108] This provides a diffusion pathway which requires less energy than moving through the lattice due to the lower activation energy needed. The rate of grain boundary diffusion is also dependent on the grain size, with smaller grains having a larger grain boundary to grain size ratio which would increase the rate of diffusion via grain boundary diffusion. Another pathway for diffusion is the surface of the solid as it contains high energy surfaces due to the surface atoms having fewer neighbours than in the bulk. It is therefore often reported that the rate of diffusion is fastest for surface diffusion, followed by grain boundary diffusion and slowest for lattice diffusion.[109] With regards to oxidation it can be envisaged that surface oxidation would be rapid and this followed by rapid attack of the grain boundaries by oxygen.

Zirconium Nitride

The majority of oxidation studies of ZrN have been performed on thin films due to the extensive use of ZrN as a hard coatings of tools [110–112]. Krusin-Elbaum and Wittmer [111] studied the oxidation kinetics of ZrN thin films reporting the activation energy of oxidation to be 241 ± 10 kJ mol^{-1} in the temperature range of 748-923 K with the oxide layer comprising of monoclinic and cubic ZrO_2. The authors oxidised thin films with a thickness of between 60 nm - 1 μm under flowing O_2. Krusin-Elbaum and Wittmer [111] found non-linear kinetics with parabolic rate behaviours being observed and state the diffusion of oxygen through the oxide layer is the rate limiting step. Cubic zirconia was determined to be present as well as monoclinic using glancing angle XRD, however no comment is made of the existence of this cubic polymorph or the effect it may have on oxidation rate.

Panjan et al. [112] studied the oxidation of several metal nitride thin films (between 300 nm and 3 μm) under flowing O_2 between 773-1123 K. The authors showed the oxidation of ZrN coatings to have an activation energy of 229 kJ mol^{-1} and also obey a parabolic rate law, agreeing well with Krusin-Elbaum and Wittmer.[111] Both studies show a plateau region after initial oxidation and Krusin-Elbaum and Wittmer [111] suggest the diffusion of oxygen through the oxide layer is the rate limiting step. Electrical resistivity measurements were performed on CrN thin films which showed a rapid increase in resistivity which the authors attributed to oxidation of grain boundaries during the initial stage of oxidation. Typical grain sizes of the nitride thin films were 20-40 nm and so it would be plausible that oxidation of grain boundaries would results in increased electron scattering, however no comment or comparison of the electrical resistivity increase of thin films with temperature is given.

Caillet et al. [113] studied the oxidation of 30 μm ZrN coatings in the range of 823-973 K observing linear kinetics, contrary to Krusin-Elbaum and Wittmer [111] and Panjan et al. [112] suggesting oxygen diffusion through the oxide layer does not affect the rate, however a significant mass loss was observed around 823 K. The authors propose nitrogen is initially lost forming HCP-Zr at the surface prior to oxidation of ZrO_2. The oxide layer was comprised of monoclinic and cubic ZrO_2 and the authors propose the mechanism begins by destabilisation of ZrN resulting in a Zr rich phase which then becomes a saturated α-Zr layer before forming an oxide scale.

Zirconium Carbide

ZrC has similar chemical properties and crystal structure to ZrN and it's oxidation kinetics and mechanism in the bulk are better understood [67, 93, 114–116] with onset of oxidation occurring between 653-750 K [93] similar to that of ZrN.[111] The mechanism of oxidation of ZrC at temperatures above 743 K is explained with the following steps; [114]

- Formation of a ZrO_xC_y phase surface, which proceeds to form amorphous ZrO_2 and C.
- Crystallites of cubic zirconia (c-ZrO_2) nucleate which form a dense oxide layer with free carbon stabilising the c-ZrO_2 polymorph (via substitution of $O^{2-}$with C^{3-}ions, creating oxygen vacancies).
- Oxygen then diffuses through this oxide layer to the free carbon producing CO_2 which diffuses out via any existing cracks or pores leaving behind voids and pores in the zirconia layer, which with very little carbon left to stabilise transforms to monoclinic zirconia (m-ZrO_2), along with small amounts of tetragonal polymorph (t-ZrO_2). [93]

The oxygen diffusion through ZrO_2 has been reported as around $\sim 10^{-10} m^2/s$ [117] at 1723 K, which is around 10 times faster than for SiO_2 at similar temperatures [118] and so the effectiveness of the dense ZrO_2 layer is expected to be limited.[119]

2.2.7 Irradiation Properties

To meet the requirements of Generation IV fuels, inert phase candidates for IMF's must have a low neutron capture cross section, thus reducing the possibility for transmutation in the reactor to form radioactive waste. Zirconium alloys have long been used as structural components in Light Water Reactors (LWR's) due to their very low capture cross section for thermal neutrons.[120]

Irradiation damage during use in reactors is mainly due to the elastic interaction between neutrons and the atoms, causing displacements and eventually point defects. These atomic displacements also cause further displacements from the movement of the atom initially displaced losing the transferred kinetic energy from the neutron collision. Inelastic collisions also occur, whereby energy is lost through some other form than kinetic and is a cause of transmutation. A main effect of radiation damage

in materials is the formation of dislocation loops, whereby the vacancies formed from atomic displacements migrate to the same plane causing a distortion of the neighbouring planes resulting in a vacancy loop. Little work has been performed on the irradiation properties of ZrC and ZrN, with initial studies focusing on heavy atom and proton irradiation.

Gosset et al. [121] performed heavy ion irradiation experiments on hot pressed ZrC samples under 4 MeV Au ions with a fluence of ~10^{11}-5 $\times$ 10^{15} Au/cm^2. Irradiation defects produces small faulted dislocation loops with increases in lattice parameters of 0.03-2% for the different fluences up to 1 $\times$ 10^{14} Au/cm^2. A secondary phase of tetragonal ZrO_2 is observed by TEM after irradiation with the cause being attributed to oxygen contamination of the starting powders and the sensitive nature of ZrC to oxidation.

Yang et al. [122] performed TEM and irradiation hardening characterisation of ZrN ceramics using 2.6 MeV protons, produced by hot pressing commercial powders. The authors noted a Zr_yO_x phases using SEM-EDS. Samples were given two irradiation doses of 0.35 and 0.75 displacements per atom (dpa) at 1073 K. At lower dpa irradiation's no change in lattice parameter was detected, however during the 0.75 dpa irradiation a lattice increase of about 0.07% was observed. Dislocation loops and point defects, showing some vacancy type loops were observed by high resolution TEM (HRTEM), with increased hardening after irradiation being attributed to the formation of point defects in the sample. No irradiation induced amorpharisation or precipitation occurred at the dpa doses, however TEM showed aligned bubbles perpendicular to the proton beam.

Gan et al. [123, 124] studied the microstructural effect of proton irradiation of SiC, ZrC and ZrN samples using 1MeV Kr irradiation and 2.6 MeV protons. Commercial samples were hot pressed under vacuum and TEM discs were irradiated at 1073 K to a dpa of around 700 dpa using Kr ions and under a fluence of 2.75 $\times$ 10^{19} protons/cm^2 giving a dpa of around 0.7 for the proton irradiation. The authors explain the proton irradiation experiments, however, are more akin to the core of a GFR reactors for displacement dose. In the ZrC samples, faulted loops were observed using TEM in the proton irradiated samples compared with no observation of this in the Kr ion irradiation, however Kr ion irradiation induced amorpharisation. No significant change in lattice parameter was observed in High Order Laue Zone (HOLZ) patterns. ZrN was observed to show the least microstructural change under

the proton irradiation as compared to ZrC and SiC.

Nanostructured zirconium nitride layers have been irradiated with Xe (167 MeV), Kr (250 MeV) and Bi (695 MeV) ions in the fluence ranges of ~10^{12} and 10^{15} ions/cm^2 for Xe and ~10^{12}-10^{13} ions/cm^2 for Kr and Bi to simulate FP bombardments by Vuuren et al.[125] Layers were produced using vacuum arc-vapour deposition to achieve thickness's of 0.1, 3, 10 and 20 μm. No changes in phase were observed by XRD after irradiation. A lattice parameter (~0.3%) increase was observed for Xe and Bi ions with the 3 and 10μm layers at the highest fluence and this is attributed to the accommodation of Xe in the ZrN lattice. HRTEM showed no changes to the nanocrystalline natures of the ZrN samples and no amorpharisation is observed. Hardness was measured using nanoindentation with no hardening observed after irradiation, contrary to Yang et al. [122] which is attributed to the different behaviour of nanostructured ceramics compared to microstructured materials, a possible mechanism for this is that reduced grain size in nanostructured materials proving harder materials.

Irradiation effects on thermophysical properties of ZrC and ZrN is an important factor when considering these materials for use as inert matrices and under high irradiation environments. Irradiation damage and heavy ion bombardment from fission fragments will cause defects and voids within the lattice, which will increase scatter points for electrons and phonons, hence decreasing thermal and electrical conductivities. However, there is little work on the irradiation effects on thermophysical properties of ZrC and ZrN.

Andrievskii et al. [126]examined the effect of irradiation damage on electrical properties of ZrC with compositions ranging from $ZrC_{0.7}$ to $ZrC_{0.94}$ using a fast neutron fluence of 1.5×10^{20} n/cm^2 at temperatures of 423 and 1373 K. The authors found that, compared with unirradiated ZrC which has an electrical resistivity of 43$\mu\Omega$cm that there was a 481% increase at 423 K and a 51% increase at 1373 K. The increase in resistivity is attributed to defect formation, the lower increase at higher temperatures may be an effect of annealing reducing stresses on the lattice. Thermal conductivity of ZrC_x decreases with increasing vacancy concentration,[67, 127] the same is true for electrical resistivity, with resistance increasing with vacancy concentration. Andrievskii et al. [128] also found a difference between samples with varying C/Zr ratio, with only a 6% increase in resistivity for $ZrC_{0.7}$ versus a 213% increase for $ZrC_{0.94}$. This is further evidence for ZrC_x with higher vacancy concentra-

tions showing more radiation tolerance due to reduced point defect formation.[127] However, it is prudent when comparing percentage increases to note that the initial resistivity of $ZrC_{0.94}$ is around 3 times lower than $ZrC_{0.7}$.[67]

David et al. [129] characterised the effects of heavy ion irradiation on the thermal conductivity of TiN, TiC and ZrN. Irradiation was carried out using 8 MeV Kr ions at a fluence of 1 and 6 $\times$ 10^{16} ions/cm^2 on sintered ceramics obtained from isostatic pressing. Inelastic and elastic collisions were stated to occur at different depths, with inelastic collisions occurring when the ions had high energy at the surface and second, elastic collisions when the Kr ion energy decreases. Inelastic collisions were calculated to occur in the first 3.3μm of the sample with elastic collisions occurring a further 1.4 μm after the inelastic collision depth. Modulated thermoreflectance microscopy (MTRM) was used to characterise thermal conductivity at the two collision areas. The authors noted an increased amount of thermal degradation in the elastic collision region, with a decrease from 20 Wm^{-1}K^{-1} in the unirradiated sample to 1 Wm^{-1}K^{-1} after both fluences. The elastic collisions were deemed to be more damaging to thermal conduction due to displacement cascades being more degrading than point defect formation of inelastic collisions. Inelastic collisions reduced thermal conductivity from 20 Wm^{-1}K^{-1} to 10 and 5 Wm^{-1}K^{-1} under fluences of 1 and 6 $\times$ 10^{16} ions/cm^2 respectively.

The effects of fast neutron irradiation has recently been studied be Snead et al. [130] with a dose of 1-10 $\times$ 10^{25} n/cm^2 and temperature of 908-1753 K on 98% TD rods of $ZrC_{0.87}$. For all irradiation doses and temperatures, no swelling was observed with all lattice parameter increases being <0.2% and within the errors of the unirradiated samples. Non-irradiated samples had a room temperature thermal conductivity in the range of 12 to 16 Wm^{-1}K^{-1} and irradiated samples having values of 11-15 Wm^{-1}K^{-1}, with higher amounts of thermal conductivity degradation being observed for lower irradiation temperatures, agreeing well with Andrievskii et al.[128] Snead et al. [130] states that the electrical conductivity of the sample does not change appreciably after irradiation, although no details or results are given and they attribute the degradation of thermal conductivity to increased phonon scattering from point defects formed after irradiation.

Jensen et al. [131] measured the change in thermal conductivity of ZrC samples irradiated to 1.75 dpa using 2.6 MeV proton radiation. Hot pressed commercially available ZrC with 99% TD was characterised by scanning thermal microscopy, lock

in infrared thermography and photothermal radiometry to measure the thermal conductivity of the surface layer ($\sim 52 \pm 2\mu m$). The thermal conductivity of the material decreased from an virgin sample value of 26.7±1 $Wm^{-1}K^{-1}$to 11.9±0.5 $Wm^{-1}K^{-1}$ for the irradiated sample. Optical microscopy revealed cracking in the unirradiated portion of the sample and not in the irradiated volume, the authors theorise that small voids may have been pushed by the proton beam to the damaged/undamaged interface causing the cracking, however no evidence for damage or amorpharisation was seen in the irradiated layer and the authors state the cause of thermal conductivity degradation to be due to loop defects as reported by Yang et al.[122]

2.3 Outlook for Implementation

Carbide and nitride fuels possess the desired thermophysical, neutronic and mechanical properties desired for use in advanced NPP. However, fabrication processes to non-oxide ceramics via carbothermic reduction-nitridation are predominantly from decades ago with renewed efforts in the last decade in their infancy. The mechanism of carbothermic reduction has been studied, however there is much confusion as to the exact mechanism with fewer studies available for the nitridation reaction. It's prudent that these mechanisms be fully understood in order to best exploit the reaction for the fabrication of non-oxide fuel from the large stockpiles of mixed oxide fuel left from reprocessing of SF.

ZrC and ZrN are both promising candidates for use in next generation fuels due to their high melting temperatures, superior thermal conductivity, good mechanical properties and increasing positive irradiation results with both materials being studied by academic and industry research for use in these applications. However, this review has highlighted some areas where data are largely scattered or limited, with impurities, vacancies and microstructure all affecting reported values. Fabrication experience of powders is limited with the majority of thermal, mechanical and irradiation properties being carried out on commercially available ZrC and ZrN powders with quantitative analysis of ceramics rarely reported. It is clear that production of dense, pure and stoichiometric ceramics is not yet fully achieved, hindering the reporting of accurate thermophysical data.

Irradiation properties of ZrC are limited with initial studies of defect formation, swelling, mechanical and thermal properties being reported. ZrN has received fewer studies than the carbide, characterising only defect formation, swelling and mechanical properties of irradiated samples. Firstly a consistent best practice method to the fabrication and processing of ZrN needs to be developed to reduce scatter of thermophysical properties of ZrN across the literature, this will then allow for irradiation effects on thermal properties of ZrN to be studied, to build a robust knowledge base of the effects of radiation on the thermophysical properties.

3 Materials and Methods

The aims of experiments described in this chapter were to fabricate ZrN and ZrC_xN_y powders through a two-step carbothermic reduction-nitridation processing route and to produce dense ceramics. The ceramics were then characterised to examine their microstructure and thermophysical properties, such as thermal conductivity, heat capacity and electrical properties as a function of stoichiometry and impurities (such as carbon and oxygen). The experimental techniques used throughout this work are described in detail here.

3.1 Starting Powder Fabrication

3.1.1 Carbothermal Reduction-Nitridation

3.1.1.1 Development of Carbothermic Reduction

Powders of monoclinic ZrO_2 (99%, 1-5μm, Sigma Aldrich, Gillingham, UK) and carbon black (∼40 nm, ABCR, Karlsruhe, Germany) were mixed in a ratio as to achieve a ZrC powder with a C/Zr mole ratio of 1 and 0.7 (sample names 1Zr-3C and 1Zr-2.7C respectively, Table 3.1) according to the Equation 3.1; (where x is equal to 0 or 0.3 for the samples 1Zr-3C and 1Zr-2.7C respectively).

$$ZrO_2 + (3 - x)C \longrightarrow ZrC_{1-x} + 2CO \tag{3.1}$$

Sample	Mass of ZrO_2 / g	Mass of C / g	Theoretical stoichiometry
1Zr-3C	20.000±0.001	5.854±0.001	$ZrC_{1.00}$
1Zr-2.7C	20.000±0.001	5.073±0.001	$ZrC_{0.70}$

Table 3.1: Composition of zirconia and carbon mixtures

The powders were homogenised by forming a non-aqueous slurry using acetone for the ease of removal due to its low boiling point and then ball milled for 12 h using ZrO_2 milling media and dried to completeness at 373 K.

Thermograviometric analysis and differential thermal analysis (TGA/DTA) were performed to determine the reaction onset temperature to be used for the carbothermal reduction process. TGA/DTA measures the change in weight of a sample using a microbalance during a thermal cycle. As well as the weight change the temperature difference between the sample and reference crucibles under identical heat flow is measured, providing detail on any exothermic or endothermic processes occurring during the thermal cycle. In this work a Netzsch STA 449F1 was used under flowing argon (100 ml/min). The mixed ZrO_2 and carbon powder (60 mg) was placed in the alumina crucible in TGA/DTA and then heated to 1773 and 1873 K. Resulting powders from the TGA/DTA experiments were analysed by XRD and a temperature of 1873 K was chosen. Powders were then subjected to a 4 h dwell at 1873 K (+10 K/min) under Ar in a graphite furnace (FCT systeme GmbH, Frankenblick, Germany) to produce the corresponding carbides by carbothermal reduction.

3.1.1.2 Development of Nitridation

The resulting powders from the carbothermal reduction were further wet ball milled for 12 h in acetone using ZrO_2 milling media and dried as before at 373 K. Nitridations of dried powders ($\leq 1\ \mu m$, agglomerates 1-5 μm) were carried out for 4-24h at a temperature between 1800-1873 K (+35 K/min) under a flowing atmosphere of 10% hydrogen-90% nitrogen in a tube furnace (Lenton, Derbyshire, UK). The reaction parameters are given in Table 3.2. Powders from all reactions were stored in a vacuum desiccator.

Iteration	Starting powder	Starting C/Zr ratio	Dwell Temperature / K	Dwell time / h
1	1Zr-3C	3	1873	4
2	1Zr-3C	3	1800	8
2	1Zr-2.7C	2.7	1800	8
3	1Zr-3C	3	1873	8
3	1Zr-2.7C	2.7	1873	8
4	1Zr-3C	3	1800	24
4	1Zr-2.7C	2.7	1800	24
5	1Zr-3C	3	1873	24
5	1Zr-2.7C	2.7	1873	24

Table 3.2: Nitridation reaction parameters

The as-fabricated ZrC (3 g) powders were placed in Al_2O_3 crucibles in the tube furnace, the working tube had an internal diameter of 50 mm and a length of 1200 mm. Flowing argon (0.5 L/min) was used to purge the tube for 1h (argon was chosen as it is heavier than air) before reaction, the gas was then changed to the hydrogen doped nitrogen gas (10% H_2-90% N_2, 0.5 L/min) and the heating programme started. After nitridation the powders were wet ball milled for 12 h in acetone using ZrO_2 milling media and dried as before at 373 K.

3.1.1.3 Powder Chemical Analysis

Quantitative chemical analyses of the powders were carried out via combustion and oxidation analysis techniques.

Combustion analysis of carbon content was performed using combustion and infrared (IR) detection of the resulting CO/CO_2 gas (Horiba, EMIA-V2 series, Palaiseau, France) at the University of Limoges and Horiba. Standards of non-ferrous steel with varying carbon contents, from 0.044 to 4.44 wt% were used to generate a calibration curve. Samples of 0.5-1 g were placed in an alumina crucible with tungsten and tin as a combustion accelerator (due to the carbide and nitrides having very high melting and combustion temperatures) and heated to 3273 K in O_2.

Oxygen and nitrogen content were measured using a separate instrument (Horiba, EMGA-930) at Horiba Europe research centre (Horiba, Jobin Yvon SAS, Palaiseau, France), steel standards of 0.0425 and 0.0023 wt% O and 0.0009 and 0.0018 wt% N

were used for calibration. Powders (∼30 mg) were weighed into a nickel crucible and then crushed before heating to 3273 K under He. Nitrogen and oxygen gases were separated by gas chromatography. Oxygen was reduced to CO/CO_2 and detected by two non-dispersive IR detectors and nitrogen detected as N_2 by a thermal conductivity cell.

For the oxidation analysis technique the samples were oxidised at 1173 K in oxygen and the resultant gases detected by quantitative IR spectroscopy and thermal conductivity (FlashEA 1112, Thermofisher, Loughborough, UK) at Queen Mary University, however oxygen was not detected. Samples of around 3 mg were weighed into a tin crucible and carbon and nitrogen content is determined by conversion into N_2 and CO_2 which are then separated in a gas chromatography column. An aspartic acid standard was used to generate a calibration curve using 5 standard measurements of increasing weight (1-5 mg).

For both techniques each sample was repeated 3 times for reproducibility and the results are given as an average of the 3 measurements and the error as the standard deviation of those 3 measurements, error in the measurements can also arise from air trapped between the powders.

3.1.1.4 FactSage

FactSage software (Ver. 6.2) was used to calculate gaseous species under the nitridation reaction conditions. The software uses thermodynamic databases of pure compounds to calculate changes in enthalpy, entropy, heat capacity and Gibbs energy of the compounds input to the calculation under definable parameters such as pressure and temperature. The calculation uses a Gibbs energy minimisation algorithm and so the results correspond to the lowest possible Gibbs energy for the particular chemical reaction or equilibrium and the specified conditions.[132]

3.2 Pellet Production and Characterisation

Densification was performed using both SPS and HP. For SPS commercially available ZrC (Sigma Aldrich, 5 μm, $\geq$ 99.95%) and ZrN (Sigma Aldrich, 1-2 μm, $\geq$ 99.0%) were densified using the SPS unit at Queen Mary University (HP D/25/1, FCT systeme GmbH, Gewerbepark 11, Rauenstein, Germany) in a 20 mm graphite die

lined with graphite paper, under vacuum (0.5 mbar, 50 Pa). Sintering was performed at 2373 K (+100 K/min) under 50 MPa uniaxial pressure for a dwell time of 10 minutes. SPS uses a pulsed direct current (DC) current to rapidly heat samples, which requires a sample of good electrical conductivity and good contact between the sample, graphite foil and graphite die.

The as fabricated ZrC_xN_y powders and commercially available ZrC (Sigma Aldrich, 5 μm, $\geq$ 99.95%) and ZrN (Sigma Aldrich, 1-2 μm, $\geq$ 99.0%) were densified using hot pressing (HP W/25/1, FCT systeme GmbH, Gewerbepark 11, Rauenstein, Germany) in a graphite die (20mm diameter) lined with graphite foil, under argon (30 mbar above atmospheric pressure). Sintering was carried out for 1 h at 2273 K (+10 K/min) under 50 MPa uniaxial pressure. During hot pressing, a uniaxial pressure was applied at high temperatures which results in denser ceramics compared to pressureless pellet sintering routes whereby a green body pellet is cold pressed and then sintered.

3.2.1 Density Measurements

Density (g cm^{-3}) measurements were made according to the Archimedes method using a Sartorious YDK01 (Sartorious mechatronics UK Ltd. Surrey, UK). Samples were first weighed in air and then the sample submerged in water to record buoyancy. The equation used to calculate density is shown below, Equation 3.2, where ρ is the density, W_a is the weight in air, ρ_{fl} is the density of the fluid (in this case water) and G is the buoyancy. The value of 0.0012 accounts for the density of air. Density values are reported as the average of three measurements and the error as the standard deviation of those measurements. The systematic error of the instrument is given as $\pm$0.2% which is smaller than the errors given from standard deviation.

$$\rho = \frac{(W_a[\rho_{fl} - 0.0012])}{0.99983G} + 0.0012 \tag{3.2}$$

3.3 XRD

Phase analysis of the powders and pellets was performed using X-ray diffraction (XRD) (Pananalytical, The Netherlands) at 40 kV and 40 mA, using Ni-filtered

CuKα radiation. Samples were scanned between 20-120° 2θ. Lattice parameter was calculated using the interplanar spacing d_{hkl} of 5 highest reflections using Bragg's law (Equation 3.3), where $\lambda = 1.5406$ Å, for a cubic unit cell the lattice parameter a, is given in Equation 3.4. Figure 3.1 shows the derivation of Bragg's law, it can be seen that $sin\theta_{hkl}$ is equal to $\lambda/2d_{hkl}$, which rearranges to Equation 3.3. Systematic error was accounted for using the Nelson-Riley function (Equation 3.5). Plotting lattice parameter, a against $cos^2\theta$ for angles approaching 2θ =180° allows regression with the intercept of the resulting extrapolation being equal to $cos^2\theta = 0$. Equation 3.5 reveals that as $cos^2\theta$ tends towards 0, the first term $cos^2\theta/sin\theta$ also tends towards 0 and the second term, $cos^2\theta/\theta$ becomes ≈0/90, resulting in $\delta\theta \approx 0$. Bulk samples were mounted on a sample holder and a press used to align the top of the pellet with the sample holder ensuring all samples were measured at the same height. Peak positions are accurate to 0.02° giving an uncertainty in lattice parameter calculations of ±0.001 Å.

$$\lambda = 2d_{hkl}sin\theta \tag{3.3}$$

$$a = d\sqrt{h^2 + k^2 + l^2} \tag{3.4}$$

$$\delta\theta = \frac{cos^2\theta}{sin\theta} + \frac{cos^2\,\theta}{\theta} \tag{3.5}$$

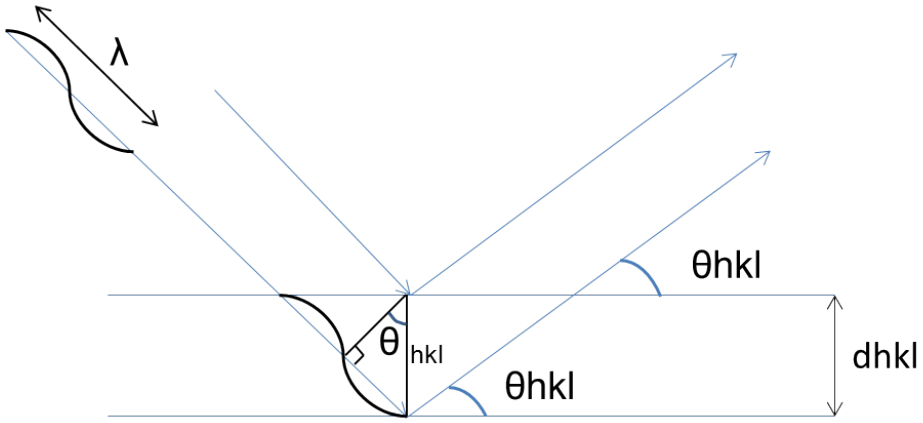


Figure 3.1: Bragg's law

Phases determined by XRD were indexed using International Centre for Diffraction Data (ICDD) Powder Diffraction Files (PDF) which are shown in Table 3.3. Peak resolution was performed by fitting Gaussian functions (in the form e^{-x^2}) using eXPFit (Ver. 1.5).

Phase	Space group	Crystal system	PDF reference code
m-ZrO_2	$P2_1/C$	Monoclinic	001-0750[133]
t-ZrO_2	$P4_2/nmc$	Tetragonal	027-0997[134]
c-ZrO_2	$Fm\bar{3}m$	Cubic	035-0784[135]
ZrC	Fm3m	Cubic	035-0784[136]
ZrN	Fm3m	Cubic	031-1493[137]

Table 3.3: PDFs used to index XRD data from ICDD

Thermal expansion of crystalline cubic structures occurs isotropically as the lengths of the unit cell are all equal, $a = b = c$ and the angles are all right angles, $\alpha = \beta = \gamma = 90°$. Due to this, thermal expansion of the materials can be measured either from change in lattice parameter with temperature or linear expansion using dilatometry. As thermal energy is supplied to the lattice, atoms in the crystal vibrate with greater amplitude causing an expansion of the bond and therefore the lattice. High temperature XRD (HT-XRD) was used for the determination of thermal expansion and the investigation of phase changes as a function of temperature. For measurement of thermal expansion of the ceramic pellets the samples were crushed to a powder and HT-XRD (Pananalytical, The Netherlands) was performed at 40 kV and 40 mA, using Ni-filtered CuKα radiation under vacuum (10^{-4}Pa). Samples

were scanned between 20-120° 2θ up to a temperature of 1273 K (60 K/min) with a scan performed at each 100 K. Lattice parameter was calculated using the interplanar spacing d_{hkl} of 5 reflections using Bragg's law (Equation 3.3), where $\lambda =$ 1.5406 Å, and the coefficients of thermal expansion, α calculated by Equation 3.6 where $\triangle L$ is the change in length, L_o is the initial length and $\triangle T$ is the change in temperature.

$$\frac{\Delta L}{L_o} = \alpha \triangle T \tag{3.6}$$

HT-XRD analysis was also used to study the oxidation of ZrN powders. Commercially available ZrN powder (Sigma Aldrich, 1-2 m, $\geq$ 99.0%) was heated under static air in a high temperature furnace using a Pt heating strip (HDK 2.4, Buhler, Tubingen, Germany) at 40 kV and 40 mA,using Ni-filtered CuK radiation between room temperature and 1023 K, with scans performed every 12 K between 673-1023 K.

3.4 SEM

Scanning electron microscopes (SEM) generate an image by producing and accelerating a beam of electrons towards a sample surface which leads to signals arising from interactions with the solid. These signals include secondary electrons which are released from the sample surface and back scattered electrons which are from the incident beam.[138] The electron gun produces the source of electrons by excitation of a tungsten or LaB_6 tip using thermionic emission or field emission from a single crystal tungsten sharpened to a 100 nm tip (field emission fun, FEG). Electrons are accelerated from the filament which is a cathode to an anode plate with a gap. This allows a fraction of the electrons to carry on down the column to the sample; this is known as the beam current. Electromagnetic lenses then focus the beam into a small spot, called demagnification and this beam raster's, or scans a selected area of the sample surface. Two pairs of scanning coils are used to control the raster of the beam by deflecting the beam off-axis and then back on-axis. The resolution of the image can be improved by varying the working distance of the sample, accelerating

voltage, beam current and spot size. A basic schematic of an SEM is shown below (Figure 3.2).

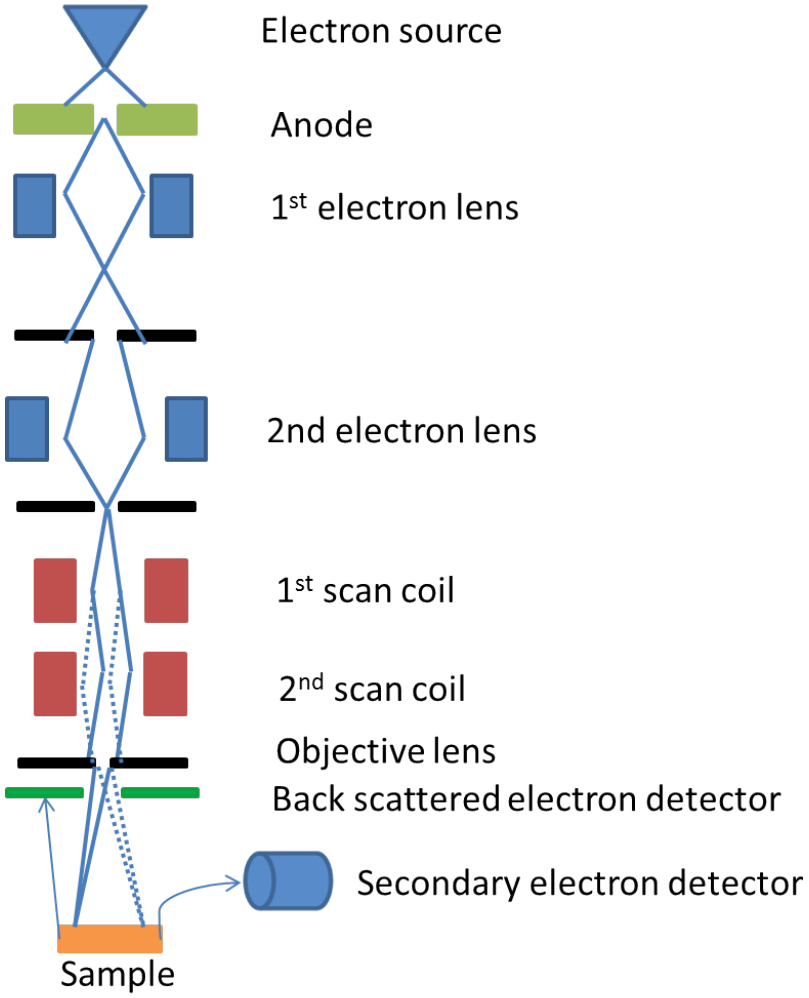


Figure 3.2: Basic schematic of an SEM

The electrons can interact with the sample either via inelastic collisions, whereby energy is transferred to electrons in the surface of the material, producing secondary electrons or via elastic collisions where no energy is transferred and the electrons from the incident beam are scattered back to the detectors, producing back scattered electrons. Back scattering increases with increasing atomic number leading to contrast between different atoms, known as Z contrast. Contrast in secondary electrons is generally dominated by the surface of the sample. Channelling contrast is an effect whereby grains in a certain orientation line up with the incoming electrons,

allowing further penetration of these electrons into the gaps, or channels between the atoms in the lattice. Back scattered electrons that penetrate further will have a lower back scattering coefficient and therefore have different contrast from electrons that do not penetrate as far into the sample. Figure 3.3 shows two crystal structures of grains at slightly different orientations. Therefore there are two beam-crystal orientations with the channels in the left crystal matching more with the direction of the beam allowing further penetration of the electrons and a reduced coefficient of back scattering.[139] A typical image from channelling contrast for examining grain sizes is shown in Figure 3.4.

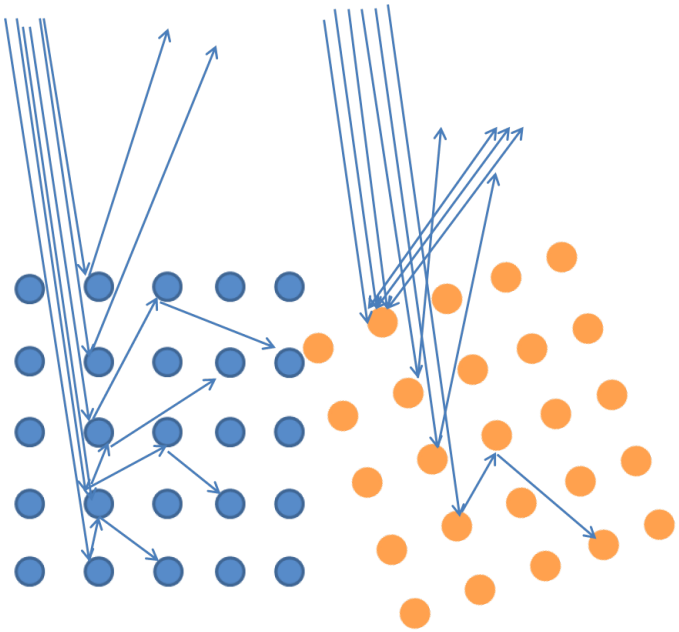


Figure 3.3: Depiction of two beam-grain orientation interactions

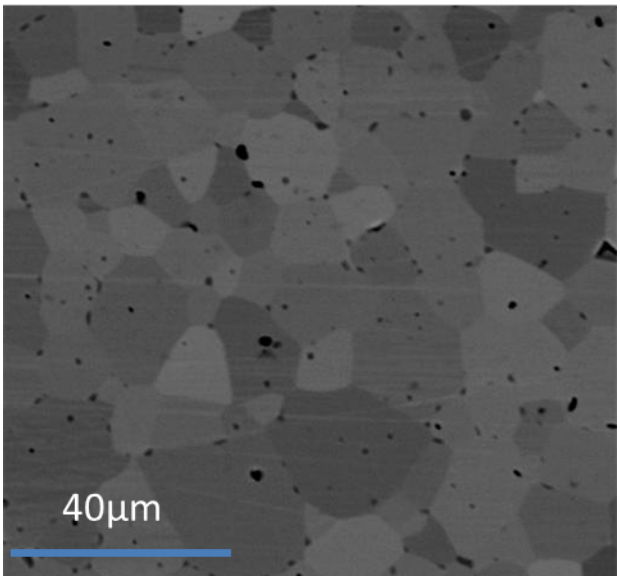


Figure 3.4: Typical BSE image from channelling contrast

Energy dispersive spectroscopy (EDS) can be used to qualitatively analyse chemical composition of the samples. EDS relies on the inelastic scattering of the incident electron beam whereby there is ionization of an inner shell electron of the specimen, resulting in a characteristic X-ray on relaxation of the electron. This characteristic X-ray has a discrete energy that is unique to the atom it has come from, allowing the technique to be used qualitatively. This is different to a Bremsstrahlung X-ray which is caused by deceleration of the incident electron from the Coulombic field of the atoms in the specimen, resulting in an X-ray being emitted.

Microstructure characterisation of the sintered and polished pellets were performed using back scattered electron imaging (SEM, JSM 6400, JEOL, Tokyo, Japan) using an accelerating voltage of 20 kV and a working distance of 15 mm. EDS was carried out using an INCA polymer ultra-thin window detector at 20 kV, with peak positions and intensities calibrated with a Co standard. SEM analysis of the powders was performed by depositing the powder onto carbon tape and imaged using secondary electron imaging at 5-15 kV (SEM, JSM 5610, JEOL, Tokyo, Japan and FIB-SEM, Auriga, Zeiss, Germany).

3.5 TEM Characterisation

As with the scanning electron microscope the electrons in a transmission electron microscope (TEM) are released from the LaB_6 by thermionic emission or by field emission gun (FEG) in newer models and the filament is again used as a cathode. A small negative bias is applied to a Wehnelt cylinder which the electrons accelerate through towards the anode, which has a hole in its center allowing some of the electron beam to pass though producing the beam. Again, as with the SEM the electron beam in the TEM is manipulated with electromagnetic lenses towards the sample, which needs to be thin enough for the electron beam to pass through ($\leq$100 μm) and onto the viewing screen. The electron beam can interact elastically or in-elastically with electrons or nuclei of the sample.[140] Contrast is proportional to atomic number with atoms with higher Z numbers giving darker images, however there is also contrast due to thickness of the sample, with thicker regions being darker than thinner regions. In HRTEM contrast arises from interference with the electron wave, called phase contrast (depending on the phase of the electron wave). This produces regions of contrast known as lattice fringes, which give information about the atomic structure of the sample in the image. Electron diffraction patterns can also be generated using TEM via selected area electron diffraction (SAED). An intermediate, or diffraction aperture is inserted into the back focal plane (BFP) of the objective lens and the objective aperture is removed, then focused on the objective lens BFP.[141] If the electrons are scattered from a crystalline region and satisfy the Bragg's equation (Equation 3.3) a diffraction pattern is formed whereby spots are produced due to positive interference of the scattered electrons (Figure 3.5). The distance from the incident beam to the spots relates to the d spacing of the lattice and the symmetry of the diffraction spots give information about the symmetry of the lattice cell.

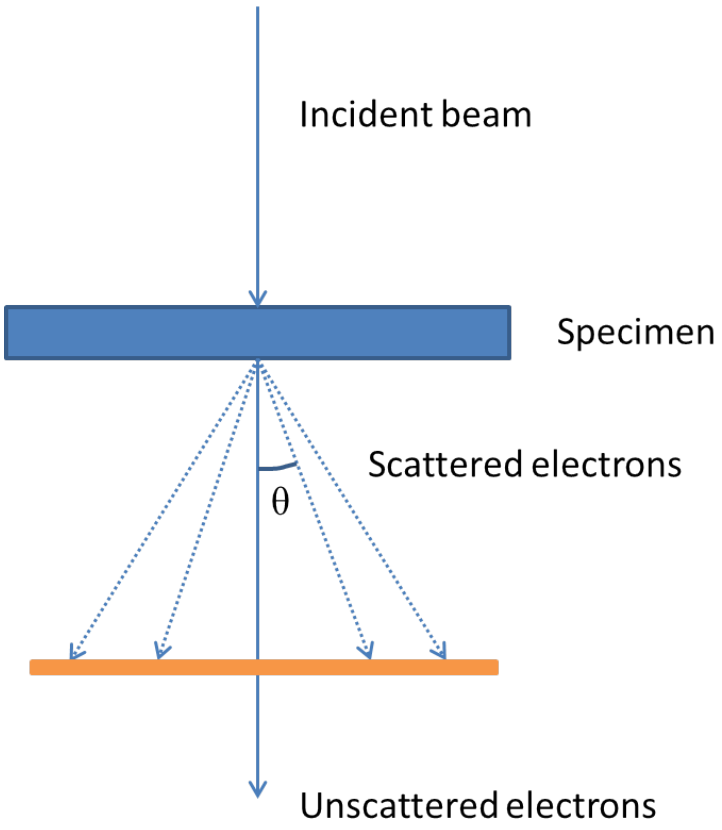


Figure 3.5: Interaction of TEM incident beam with specimen

TEM samples of the powders were prepared by grinding in a mortar with a pestle, suspended in water and a layer of supernatant particles near the surface of the suspension was pipetted onto a Cu grid as to select the lightest, smallest particles and dried under a lamp. Pellets were prepared by grinding 3 mm diameter samples to a thickness of $\sim$100μm using 1200 grit silicon carbide paper. The samples were then dimple ground using 3 and 1 μm polishing wheels (Gatan dimple grinder) to achieve a sample thickness of $\sim$30 μm before ion milling using a Gatan precision ion polishing system (PIPS) at 2-4.5 KeV. HRTEM analysis was performed on the pellet slices (HRTEM FX2100, JEOL, Tokyo, Japan), the electron source is a LaB_6 filament and an accelerating voltage of 200 kV was used. SAEDs were indexed by matching with calculated patterns using SingleCrystal software package (Ver. 2.2.9)

Focused ion beam (FIB, FEI, Helios Nanolab 600, OR, USA) was also used to prepare samples from oxidation studies and transmission electron microscope analysis performed on the oxidised ceramics (TEM FX2000, JEOL, Tokyo, Japan). The FIB

instrument uses Ga^+ ions to mill trenches either side of the lamella with a length of around 10 μm. A Pt layer is then deposited to protect the lamella from Ga^+milling and then the section, around 10×10 μm in dimension is milled, attached to a support grid and removed from the trench.

3.6 Thermophysical Characterisation

3.6.1 Thermal Diffusivity

Thermal diffusivity was measured using laser flash technique (LFA-427, Netzsch GmbH, Wolverhampton, UK) from room temperature to 2073 K under high purity Ar (99.99%). Samples of the sintered pellets with a 10mm diameter and a thickness of between 1 to 2 mm were characterised. The technique uses a laser pulse (voltage: 450 V for 0.8 ms) which is shot onto the front face of the sample. An IR detector is then used to measure the temperature from the sample rear face giving a temperature rise of the surface area as a function of time (cm^2/s) (Figure 3.6). Temperature points of 298, 773, 1173, 1473, 1773 and 2073 K were chosen. Three laser pulses were performed at each selected temperature; the values of thermal diffusivity are reported as an average of these three values with the error reported as the standard deviation.

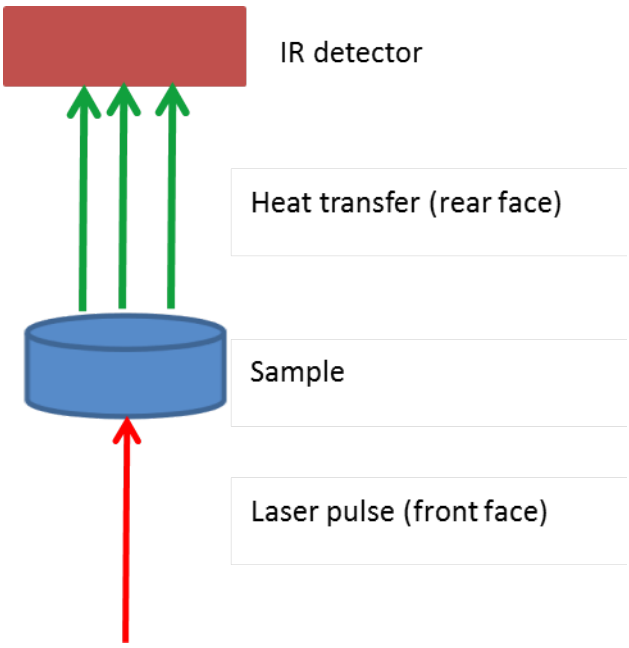


Figure 3.6: Schematic of laser flash apparatus

3.6.2 Heat Capacity

Heat capacity was measured using differential scanning calorimetry (STA449-C, Netzsch) from room temperature to 1273 K (+20 K/min, 50 ml/min) under argon atmosphere (99.99% pure) using an zirconium metal ring as an oxygen trap system in the furnace. The samples were cylindrical pellets with a diameter of 5 mm and height of around 1 mm. Sapphire (αAl_2O_3) and Al_2O_3 (polycrystalline) reference standards were used to check the accuracy (Figure 3.7). DSC works in a similar fashion to DTA, with the samples being placed into a sample Pt crucible and a reference Pt crucible being left empty. The DSC curve gives the amount of energy required to keep the two crucibles at the same temperature throughout the heating programme, with the sample crucible requiring more energy due to it containing a non-zero mass. To begin each run the furnace was evacuated and back filled with argon three times to ensure minimal oxygen content. For each sample, a blank run was performed to account for the energy needed to heat two empty crucibles, then a sapphire standard and finally the samples were ran. The heat capacity of the sample is then calculated using a ratio method compared to the sapphire standard. The manufacturer quotes the systematic error of the instrument as ±3%.

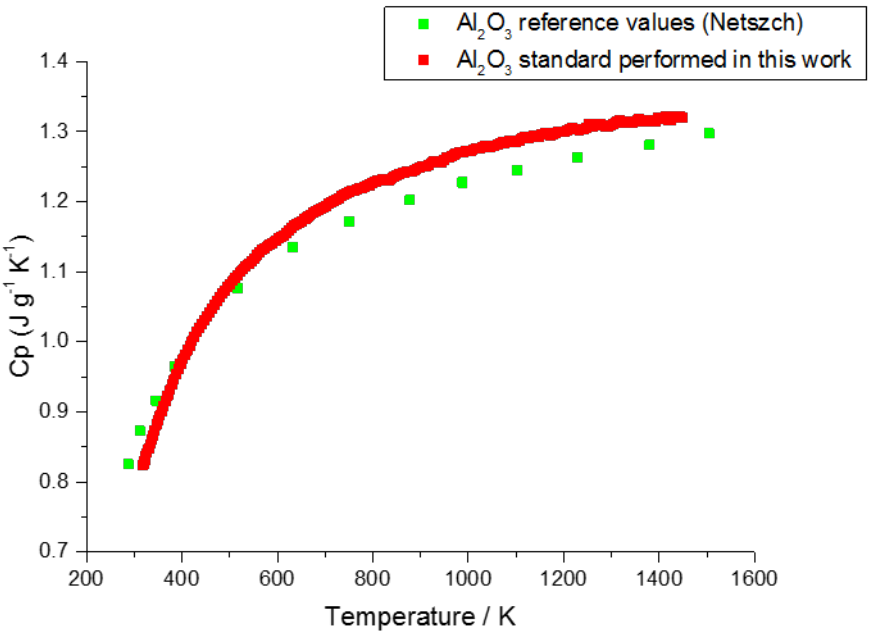


Figure 3.7: Heat capacity of alumina standard as a function of temperature with manufacturers reference

Heat capacities were also calculated using the rule of mixtures of C_p values for monolithic ZrC and ZrN from the National Institute of Standards and Technology (NIST).[48] Heat capacity was calculated using the Shomate equation (Equation 3.7) were C_p is heat capacity and T is temperature (K)/1000, along with constants A, B, C, D and E from Chase.[48]

$$C_p = A + BT - CT^2 + DT^3 - E/T^2 \tag{3.7}$$

Heat capacity can be reported with the units of J $g^{-1}K^{-1}$ or J $mol^{-1}K^{-1}$. The ratio of wt% carbon to wt% nitrogen as determined from chemical analysis was assumed as the ratio of ZrC and ZrN in the mixed ZrC_xN_y phases and this ratio used to calculate the mixed C_p values from the NIST data in J $g^{-1}K^{-1}$ according to Equation 3.8. Stoichiometries of the samples did not equal 1 (x+y≠1) and this was taken into account as can been seen in Figure 3.8 where the calculated C_p values at some points are not a mixture of monolithic ZrC and ZrN but are lower than them. An error of ±3% was added to the calculated values which ensures the calculated

values fall within the small difference ($\leq$0.05 J g^{-1}K^{-1}) between monolithic ZrC and ZrN literature values (Figure 3.8).

$$(\frac{wt\%N}{wt\%N + wt\%C} \times C_pZrN) + (\frac{wt\%C}{wt\%N + wt\%C} \times C_pZrC) = C_pZrC_xN_y \quad (3.8)$$

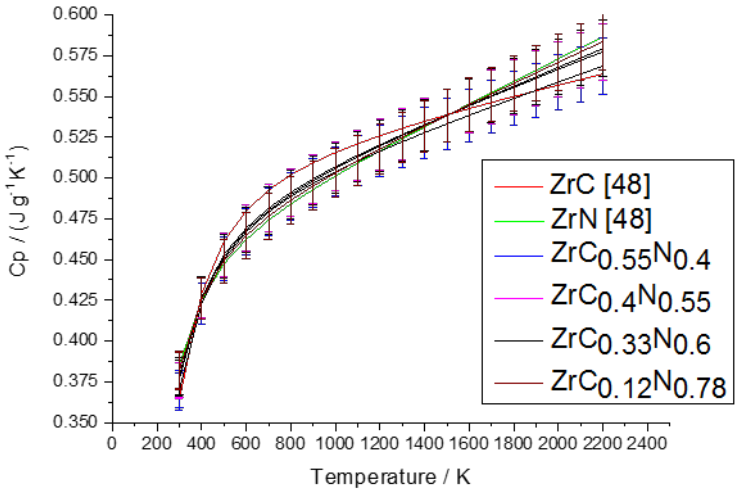


Figure 3.8: Heat capacities as a function of temperature for ZrC_xN_y phases calculated from NIST data [48]

3.6.3 Thermal Conductivity

Thermal conductivity was calculated from the experimental values obtained for the thermal diffusivity and density along with the calculated C_p values (Equation 3.8) using Equation 3.9;

$$K = \alpha\rho C_p \quad (3.9)$$

where K is the thermal conductivity (W m^{-1} K^{-1}), α is the thermal diffusivity (m^2 s^{-1}), ρ is the density (kg m^{-3}) and C_p is the heat capacity (J kg^{-1} K^{-1}). Reported

thermal conductivity values are calculated from the averaged measurements from thermal diffusivity and densities, with the error being propagated from the individual errors of each separate measurement.

3.6.4 Electrical Conductivity of Pellets

Electrical conductivity was measured using four point DC between 273-1023 K under flowing high purity argon (99.99% pure, 50 mL/min) using platinum electrodes. Samples were in a bar shape with dimensions ∼15 × 5 × 3 mm, four notches were ground into the sample for an improved connection with the Pt electrodes and to reduce movement during the measurement (Figure 3.9). A current was applied through the two exterior electrodes with the voltage across the sample measured between the two interior electrodes. For the calculation of electrical conductivity the samples need to obey Ohms law, which states that the current measured between the two points is directly proportional to the voltage applied, shown in Equation 3.10, where V is voltage (V), I is the current (A) and R is the resistance (Ω);

$$V = IR \tag{3.10}$$

To ascertain that the sample obeyed Ohms law, currents in the range of +100 mV to -100 mV were passed and the voltage measured plotted as I vs V with a straight line showing direct proportionality. Alternative current (+100 and -100 mV) was applied as to ensure good agreement when switching the direction of current through the sample. Electrical conductivity ($\Omega^{-1}m^{-1}$) was calculated from the inverse of R_o. R_o (Ωm) was determined using Equation 3.11, where V is the measured voltage (V), I is the applied current (A), A is the cross sectional area of the sample (cm^2) and L is the length between the voltage electrodes (cm) (Equation 3.11). The electrical contribution to thermal conductivity was calculated using the Wiedemann-Franz-Loranz Equation 2.19, where L has the value of 2.55×10^{-8} $W\Omega K^{-2}$.[66]

$$R_o = \frac{V}{I} \times \frac{A}{L} \tag{3.11}$$

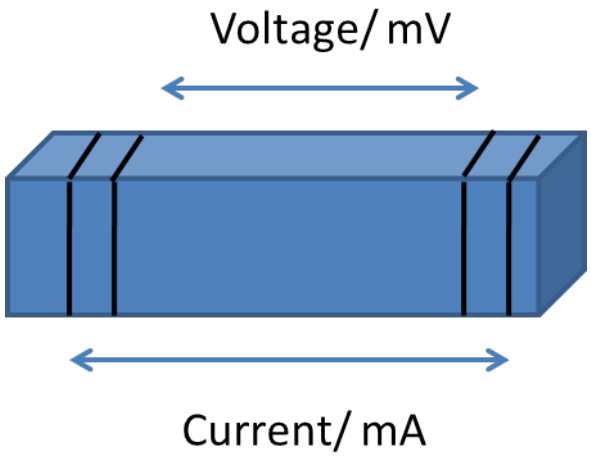


Figure 3.9: Schematic of electrical conductivity measurement on bar samples

3.7 Oxidation Studies

ZrN pellets prepared from commercially available powders were used for oxidation studies and had a sintered density of 7.13 ± 0.01 g/cm^3 and a theoretical density of 97.7 ± 0.1% (sample name SPS-ZrN-1 Table 5.3).

Cubic samples with dimensions ∼3 × 3 × 3 mm were prepared by electrical discharge machining and polished to give a uniform surface. These samples were oxidised under static air using thermograviometric analysis coupled differential thermal analysis (TGA/DTA) (STA-449-F1, Netzsch GmbH, Selb, Germany) at 5 temperatures; 973, 1073, 1173, 1273 and 1373 K (+20 K/min) for a dwell time of 5 h continually recording weight change at 0, 1, 2, 3, 4, and 5 h time points. Rate constants for each isothermal step were determined according to Equation 3.12, Equation 3.13 and Equation 3.14, where $\triangle W$ is the change in weight (mg) A is the area of the pellet (cm^2), k_L, k_p and k_c are the linear, parabolic and cubic rate constants respectively and t is the time (s).[142] Errors of $\triangle W/A$ are given as the percentage error of the TGA/DTA instrument compounded with the error from the area measurements of the pellets.

$$(\frac{\triangle W}{A}) = k_L t \tag{3.12}$$

$$(\frac{\triangle W}{A})^2 = k_p t \tag{3.13}$$

$$(\frac{\triangle W}{A})^3 = k_c t \tag{3.14}$$

4 Powder Fabrication

This chapter discusses fabrication of ZrC_xN_y powders from ZrO_2 via a two step carbothermic reduction-nitridation route and the production of dense ceramics from these powders. Processing parameters such as starting composition, dwell times, dwell temperatures and atmospheres were varied to develop optimal processing routes. Possible mechanisms of nitridation consistent with the experimental results and characterisation are evaluated.

4.1 Powder Fabrication

4.1.1 Development of Carbothermal Reduction

To assess the onset of reaction of carbothermic reduction, TGA-DTA was used to measure the weight change and differential temperature of 1Zr-3C reaction mixture (described in subsubsection 3.1.1.1) as a function of temperature and to ascertain the onset temperate of carbothermic reduction. Figure 4.1 shows the TGA-DTA curves from the powders heated to 1873 K. The endotherm around 400 K is likely due to the driving off of moisture and organics (such as the ethanol used in milling) and the DTA signal increases with temperature after 400 K as the differential temperature between the sample and reference crucibles increases. The endothermic peak at around 1464 K in the DTA trace corresponds to the monoclinic to tetragonal phase change as there is no change in mass associated with the transition and the monoclinic to tetragonal transition is usually reported at 1443 K.[143] Another endothermic peak is present between 1663-1673 K along with a vast change in mass, which corresponds to the loss of carbon via CO evolution. XRD of the starting zirconia powder and the reacted products from the TGA-DTA is shown in Figure 4.2 which reveals that the monoclinic ZrO_2 peaks decrease with higher dwell temperature and the ZrC peaks increase concomitantly.

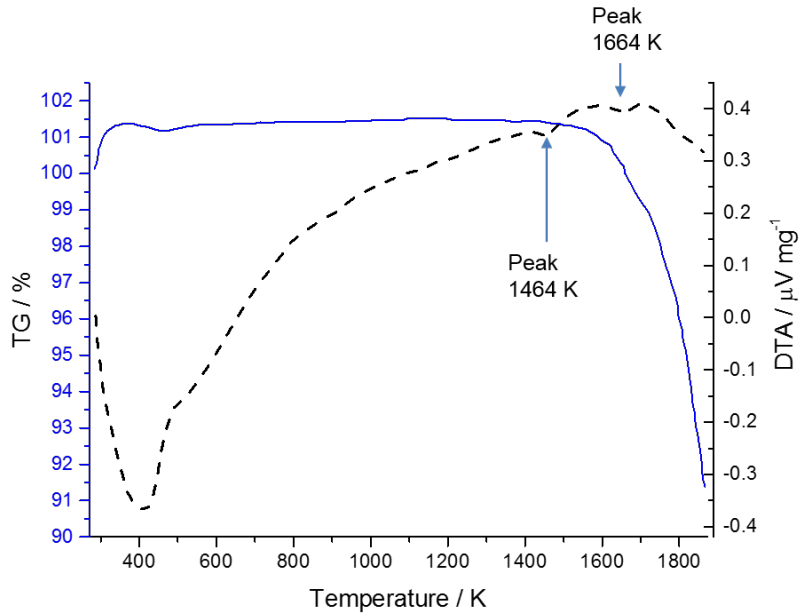


Figure 4.1: TGA-DTA analysis of 1Zr-3C sample (∼ 150 mg) to 1873 K (10 K/ min) under argon (60 ml/min)

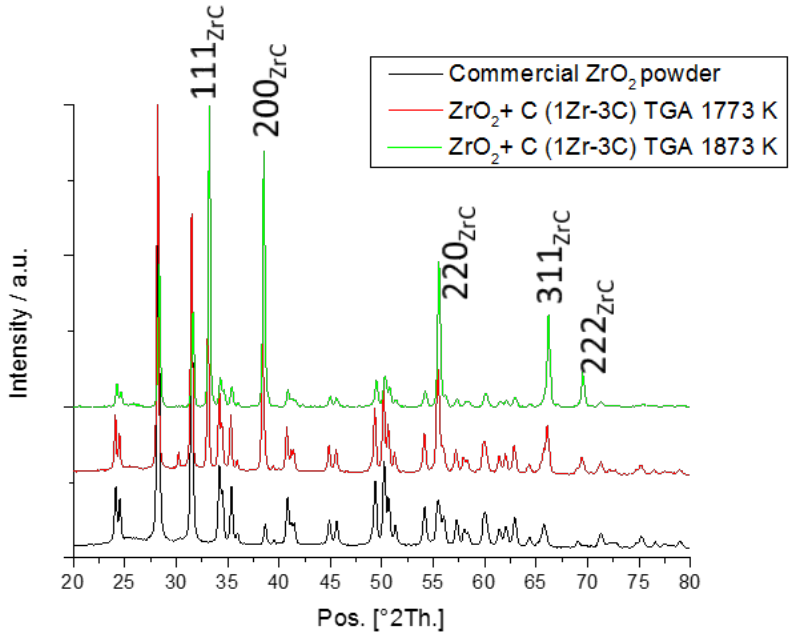


Figure 4.2: XRD of powders from TGA-DTA experiments

To assess the formation of ZrN_x from nitridation of substoichiometric ZrC_{1-x} powders,

two different starting compositions (described in Table 3.1) were fabricated in a graphite furnace as described in subsubsection 3.1.1.1. XRD analysis of the powders reacted via this carbothermic reduction process is shown in Figure 4.3. The XRD pattern of the 1Zr-3C mixture is consistent with a single crystalline phase of ZrC (PDF 00-035-0784[144]), however, the 1Zr-2.7C shows a slight shoulder indicating presence of a minor phase.

XRD (Figure 4.3) reveals a shift in peak position between the two carbothermally reduced powders with different carbon content. The peaks for the 1Zr-3C powder occurring at lower 2θ angles corresponding to an increased lattice parameter compared to the 1Zr-2.7C sample. This change in lattice parameter between the two compositions is evidence for the different amounts of carbon in the lattice as reported by several authors.[55, 63, 64, 67] As carbon is removed from the near stoichiometric $ZrC_{1.00}$ lattice, the covalent bond strength that gives ZrC its strong bonds decreases. This decrease in bond strength is associated with a lengthening of the bond increasing the lattice parameter from 4.696 Å to a maximum value of 4.702 Å at a stoichiometry of $\sim ZrC_{0.9}$. Continuing removal of carbon then decreases the lattice parameter as the interstitial space the carbon atoms previously occupied is now free and the Zr metal lattice shrinks to a minimum of 4.687 Å at around $ZrC_{0.55}$.[67] The lattice parameter of the two samples calculated from XRD (as described in section 3.3) patterns (Table 4.1) showed 1Zr-3C samples had a larger unit cell than the 1Zr-2.7C (by $\sim$0.010 Å) samples in agreement with the trend between lattice parameter and carbon vacancy concentration. However, the lattice parameter is smaller than the value for $ZrC_{0.55}$. The asymmetry of the peaks in 1Zr-2.7C also suggests the existence of two crystal phases, such as a carbon-rich and carbon-poor phase.

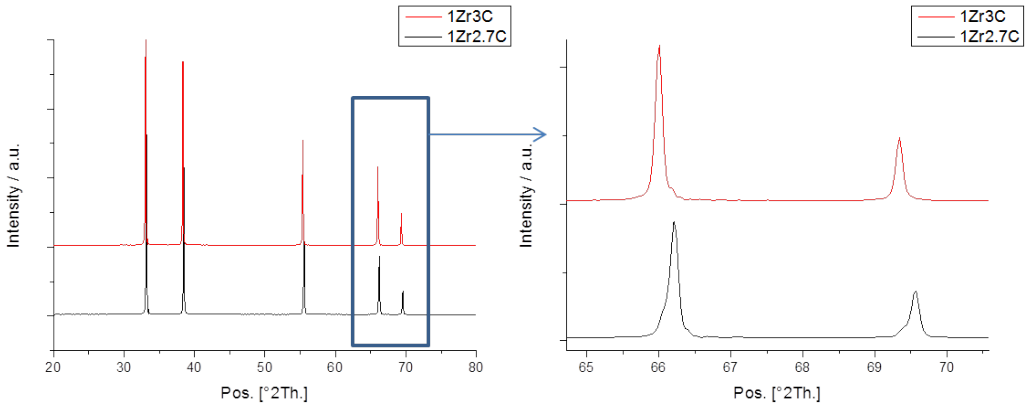


Figure 4.3: XRD of 1Zr-3C and 1Zr-2.7C after carbothermic reduction

Chemical analyses of the powders were performed by oxidation and combustion techniques as described in subsubsection 3.1.1.3 and the results are shown in Table 4.1 and Table 4.2 respectively. It can be seen from the stoichiometries that both techniques are in good agreement with each other. However, at stoichiometries corresponding to $ZrC_{1.0}$ and $ZrC_{0.9}$ an increase in lattice parameter would be expected, as the maximum unit cell size is found at $\sim ZrC_{0.9}$. The increased carbon content in 1Zr-2.7C samples could arise from contamination from un-reacted free carbon which would not affect the lattice parameter determined by XRD. Gendre et al.[145] have shown that the lattice size of ZrC in mixed ZrC_xO_y phases decreases to a minimum of 4.680 Å at stoichiometries around $ZrC_{0.79}O_{0.13}$ which agrees well with the expected stoichiometry from the lattice parameter in this work.

Sample	Starting C/Zr mol ratio	at% C	at% N	Stoichiometry	a / Å
1Zr-2.7C	2.7	44.42±1.82	2.42 ±0.39	$ZrC_{0.89}N_{0.04}$	4.6834
1Zr-3C	3	49.76±6.06	1.99 ±0.57	$ZrC_{1.00}N_{0.04}$	4.6933

Table 4.1: Carbon and nitrogen analysis by oxidation technique of powders fabricated by carbothermal reduction (2073 K, 4h)

Sample	at% C	at% N	at% O	Stoichiometry
1Zr-2.7C	46.78 ±0.80	0.66 ±0.02	2.24 ± 0.07	$ZrC_{0.93}$
1Zr-3C	51.47 ±0.87	0.62 ±0.01	3.07 ± 0.02	$ZrC_{1.02}$

Table 4.2: Carbon analysis by combustion of powders fabricated by carbothermic reduction (2073 K, 4 h)

EDS was performed on the powders after the reaction, revealing the presence of carbon and zirconium. There is no peak at immediate higher energies to the carbon peak in the EDS spectra, which is where the corresponding oxygen peak would occur, showing that there is little if any oxygen present in the sample. Although EDS is a rapid way to determine elemental composition it is semi quantitative at best and it can also be difficult to differentiate between light elements due to their characteristic X-rays being at similar energies.

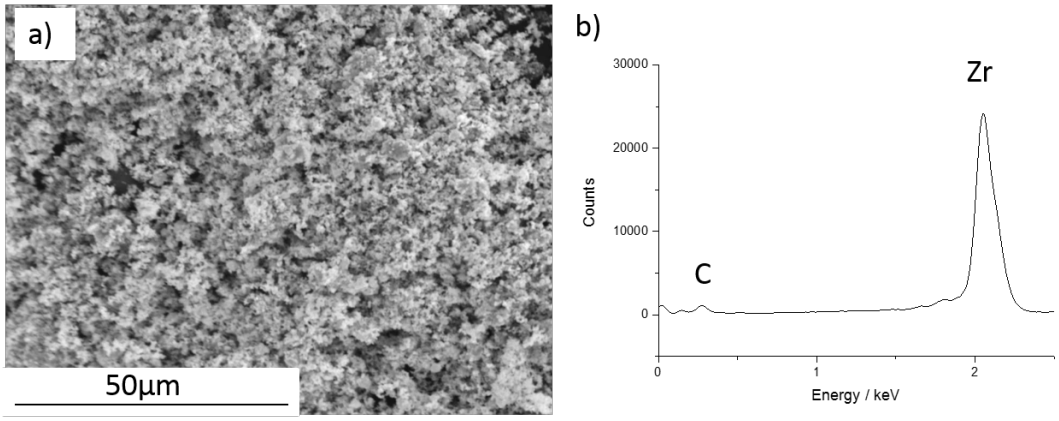


Figure 4.4: a) SEI of $ZrC_{1.0}$ powder from carbothermic reduction, b) EDS spectra of $ZrC_{1.0}$ powder

The samples were then wet milled as described in subsubsection 3.1.1.2 to maximise powder surface area to ensure a higher rate of nitridation of the powders. The milled powders were examined by SEM to assess their particle sizes and are shown in Figure 4.5. The average particle sizes were around 1-2 μm with the particles forming agglomerates of around 5 μm.

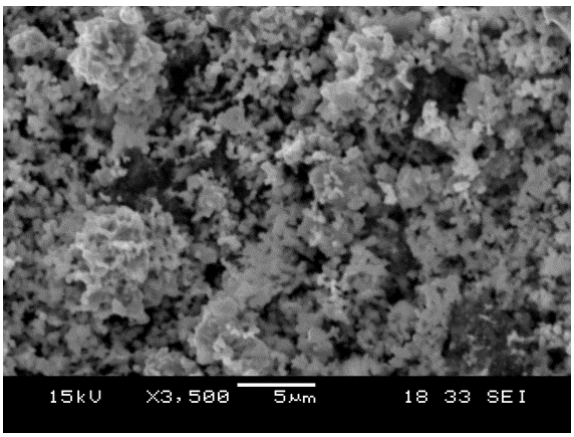


Figure 4.5: SEI of $ZrC_{1.0}$ powder from carbothermic reduction after milling small particles (1-2μm) showing agglomerates ($\sim$5μm)

4.1.2 Development of Nitridation

Nitridation reactions were performed on the $Zr_{1.0}$ and $ZrC_{0.9}$ samples. These initial reactions evolved through a series of experiments with increasing dwell times and dwell temperatures to increase the nitrogen content of the final products. Nitridation parameters, starting ZrC_x composition and elemental analysis of resulting powders (performed by the oxidation technique) are shown in Table 4.3.

Iteration	Starting C/Zr mol ratio	Dwell time / h	Dwell temperature / K	at% C	at% N	Stoichiometry
1	3	4	1873	33.54 ±0.47	13.76 ±1.29	$ZrC_{0.68}N_{0.28}$
2	3	8	1800	25.15 ±0.43	24.20 ±0.58	$ZrC_{0.50}N_{0.48}$
2	2.7	8	1800	33.50 ±0.14	16.30 ±0.34	$ZrC_{0.67}N_{0.33}$
3	3	8	1873	28.52 ±0.78	18.00 ±0.29	$ZrC_{0.36}N_{0.57}$
3	2.7	8	1873	25.03± 0.23	20.72 ±0.42	$ZrC_{0.5}N_{0.45}$
4	3.0	24	1800	12.09 ±0.49	34.86 ±0.02	$ZrC_{0.25}N_{0.7}$
4	2.7	24	1800	21.25 ±0.35	26.23 ±0.06	$ZrC_{0.43}N_{0.52}$
5	3.0	24	1873	6.04 ±0.25	39.23 ±0.22	$ZrC_{0.12}N_{0.78}$
5	2.7	24	1873	14.81 ±0.75	32.26 ±0.37	$ZrC_{0.3}N_{0.65}$

Table 4.3: Carbon and nitrogen analysis using oxidation analysis of nitrided powders using different starting C/Zr ratios, dwell times and dwell temperatures

For the first nitridation iteration (subsubsection 3.1.1.2, dwell temperature 1873 K, dwell time 4 h) only $ZrC_{1.0}$ was tested to assess the initial progress of the reaction under these parameters. XRD (Figure 4.6) shows this sample was crystalline with a cubic structure, however, each reflection was split into two main components, suggesting to a multiphasic system. Comparing 2θ reflection values from the PDF files for ZrC and ZrN [136, 137] to the XRD patterns shown in Figure 4.6 and Figure 4.7 reveals the peaks have shifted from their corresponding positions for the monolithic phase. In monolithic ZrC the (311) reflection occurs at 65.969° 2θ with the ZrN (311) reflection at 67.917° 2θ whereas in the first nitridation iteration the (311) reflection peak has two maxima, one at 66.4927 and the other at 66.8887° 2θ. This suggests that although the peaks split, indicating the existence of two phases, the peaks also shift, with the ZrC-like peaks occurring at higher 2θ [136] suggesting the size of the ZrC lattice size is decreasing as well as the ZrN-like peaks occur at lower 2θ angles than the reflections for ZrN,[137] suggesting the nitrides lattice size is larger than the monolithic phase.

For the second iteration (dwell temperature 1800 K, dwell time 8 h) both $ZrC_{1.00}$ and $ZrC_{0.9}$ were subject to nitridation. XRD reveals a two phase system with each reflection having two maxima, however the relative intensities of the peaks between the samples from iteration 2 and iteration 1 are different. The $(311)_{ZrN}$ and $(222)_{ZrN}$ peak is more intense in sample nitrided for longer (iteration 2, 1800 K, dwell time 8 h) compared with iteration 1 (1873 K, dwell time 4 h). The $(311)_{ZrC}$ and $(222)_{ZrC}$ peaks are less intense in the sample with a higher initial carbon content (Figure 4.6) and compared to the $ZrC_{0.9}$ sample (Figure 4.7) suggesting this has undergone more nitridation. XRD also reveals there is no definite separation between the 2 peak maxima for the (311) and (222) reflections suggesting that although the bulk of material is a composite there may exist a range of x and y values in the ZrC_xN_y phase at the reaction interface.

XRD from powders after iteration 4 (dwell temperature 1800 K, 24 h) again reveals the reaction has progressed further with no visible ZrC peak splitting being observed, although a slight shoulder is still present to the left of the main peaks in $ZrC_{0.9}$ samples (Figure 4.7) indicating the presence of the ZrC phase. It could be assumed from the single maximum peaks of iteration 4 (dwell temperature 1800 K, 24 h) in the XRD (Figure 4.6) that the $ZrC_{1.00}$ sample has undergone an almost complete reaction, however slight peak asymmetry still suggests a ZrN-rich phase with a low amount of crystalline ZrC present.

From the XRD of iteration 5 (dwell temperature 1873 K, dwell time 24 h) it can be seen that the $(311)_{ZrC}$ and $(222)_{ZrC}$ peaks in figures Figure 4.6 and Figure 4.7 are not visible, suggesting an almost complete reaction, however, the peaks are still asymmetric suggesting the presence of minor phases that are close in lattice size.

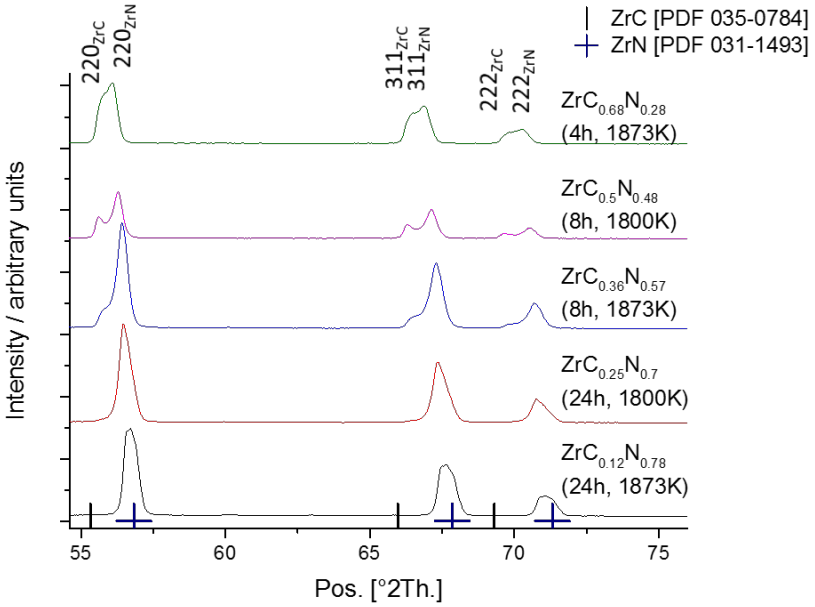


Figure 4.6: XRD patterns showing progression of nitridation iterations of $ZrC_{1.00}$ samples [136, 137]

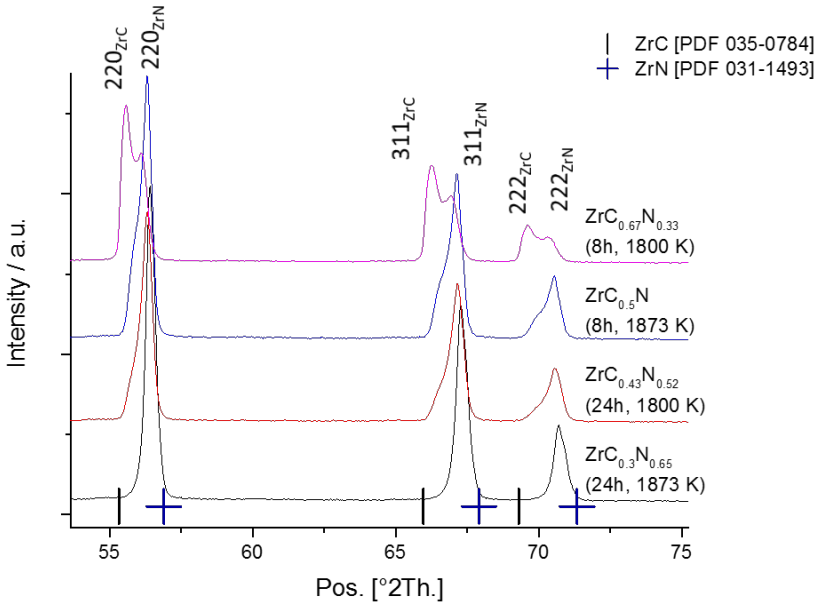


Figure 4.7: XRD patterns showing progression of nitridation iterations of $ZrC_{0.9}$ samples [136, 137]

SEIs for all nitrided powders revealed submicron ultimate particles after the nitridation but with larger 1-5 μm agglomerates. Figure 4.8 shows powder $ZrC_{0.67}N_{0.33}$ from iteration 2 using $ZrC_{0.9}$ powder after carbothermic reduction. On most particles, ledges and terraces can be seen. Small spherical particles can be seen on the surface of the larger particles which may be the nucleation of ZrC_xN_y or ZrN on the surface of the bulk particles, consistent with the observation of a mixed phase revealed by XRD (Figure 4.6 and Figure 4.7).

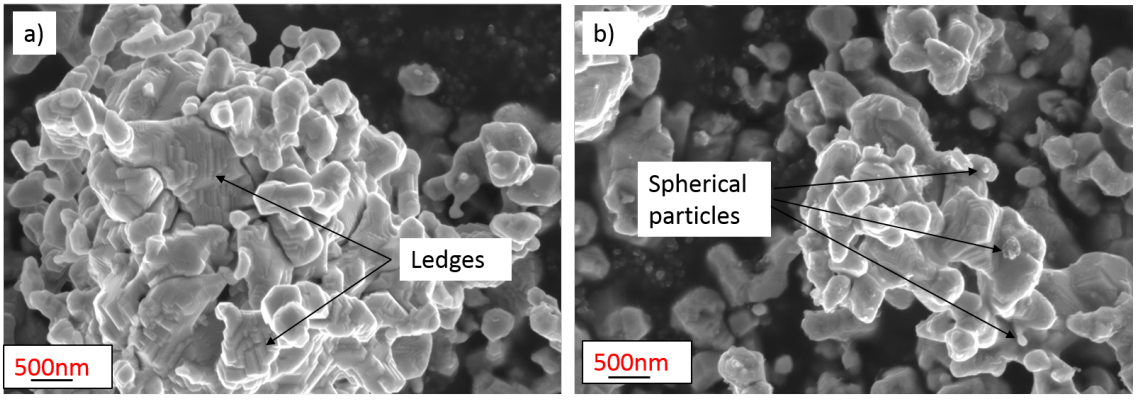


Figure 4.8: SEI of powders from iteration 2 of $ZrC_{0.9}$ powder (dwell time 8 h, dwell temperature 1873 K) $ZrC_{0.67}N_{0.33}$ a) region with ledges and terraces, b) region showing small spherical particles

BF-TEM of the $ZrC_{0.67}N_{0.33}$ powder after nitridation (Figure 4.9a) shows the ledges of the particle and increased magnification of the region reveals a core-rim particle structure (Figure 4.9b). The SAED pattern of the particle (Figure 4.9c) reveals a crystalline pattern and indexed well with ZrN ([112] zone axis) along with double diffraction streaks and a calculated lattice parameter of 4.624 Å which is slightly higher than the literature value for of 4.579 Å [137]. Double diffraction spots were also seen for another region shown in Figure 4.10 although the SAED from Figure 4.10c indexed well with ZrC ([200] zone axis) as would be expected as the bulk of the particle is the carbide, however the calculated lattice parameter from the SAED was 4.678 Å which is lower than stoichiometric ZrC (4.696 Å)[144]. Both SAED patterns (Figure 4.9c and Figure 4.10c) show double diffraction and are typical of epitaxy [146] with the weaker spots most likely being due to the outer layer and the main diffraction pattern coming from the bulk of the particle. It can also be seen from the high resolution images (figures Figure 4.9b) that there is registry between the lattice fringes in the core and rim of the particle. The lattice constants for ZrC and ZrN are within 2.6% of each other and both crystals are cubic ($Fm\bar{3}m$) so distinguishing by electron diffraction is difficult. The double diffraction spots seen in the SAED patterns (Figure 4.9c and Figure 4.10c) may be due to diffraction from a second phase of which two scenarios may be possible;

- The streaks in the SAED pattern may arise from the defects present in this outer layer of ZrC that has reduced C content, which would produce an outer layer of non-stoichiometric ZrC_{1-x} which has been reported to have a slightly

larger lattice cell for stoichiometries of $ZrC_{0.8-0.95}$.[67]

- A ZrC-rich or ZrC_xN_y phase on top of a bulk ZrN rich particle, consistent as the ZrC-rich external layer would have a larger lattice parameter than the ZrN-rich bulk phase, suggesting the ZrN-rich particles may grow with higher C content at the surface.

The streaking in Figure 4.9c could arise from deformation and strain effects in the lattice such as modification of the unit cell parameter via carbon removal from the ZrC lattice and increasing vacancy defects and nitrogen content. However, in Figure 4.9c a halo connecting the streaks can be discerned, which could be due to the outer layer having both crystalline and amorphous regions observed in the HRTEM image (Figure 4.9b). Polycrystalline regions which indexed with ZrN were also observed via BF-TEM (Figure 4.11).

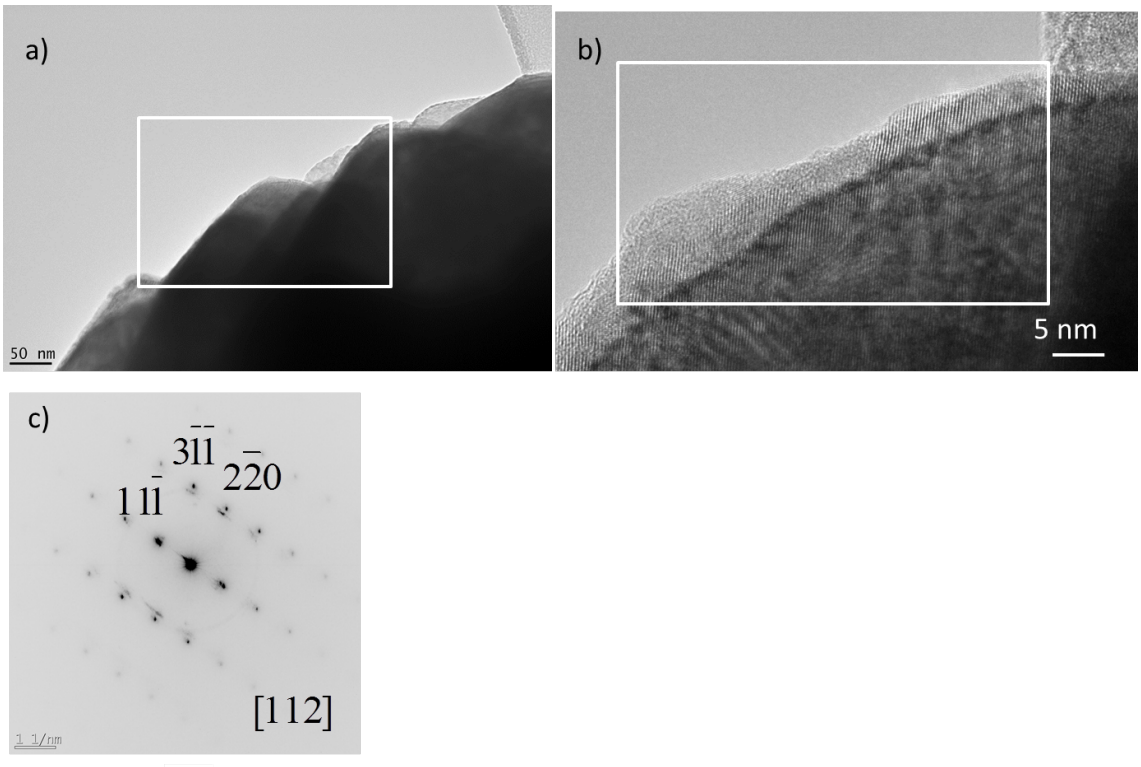


Figure 4.9: a) BF-TEM image of $ZrC_{0.9}$ after nitridation iteration 2 (dwell time 8h, dwell temperature 1873K) $ZrC_{0.67}N_{0.33}$, b) higher magnification showing external layer, c) SADP of area shown in b

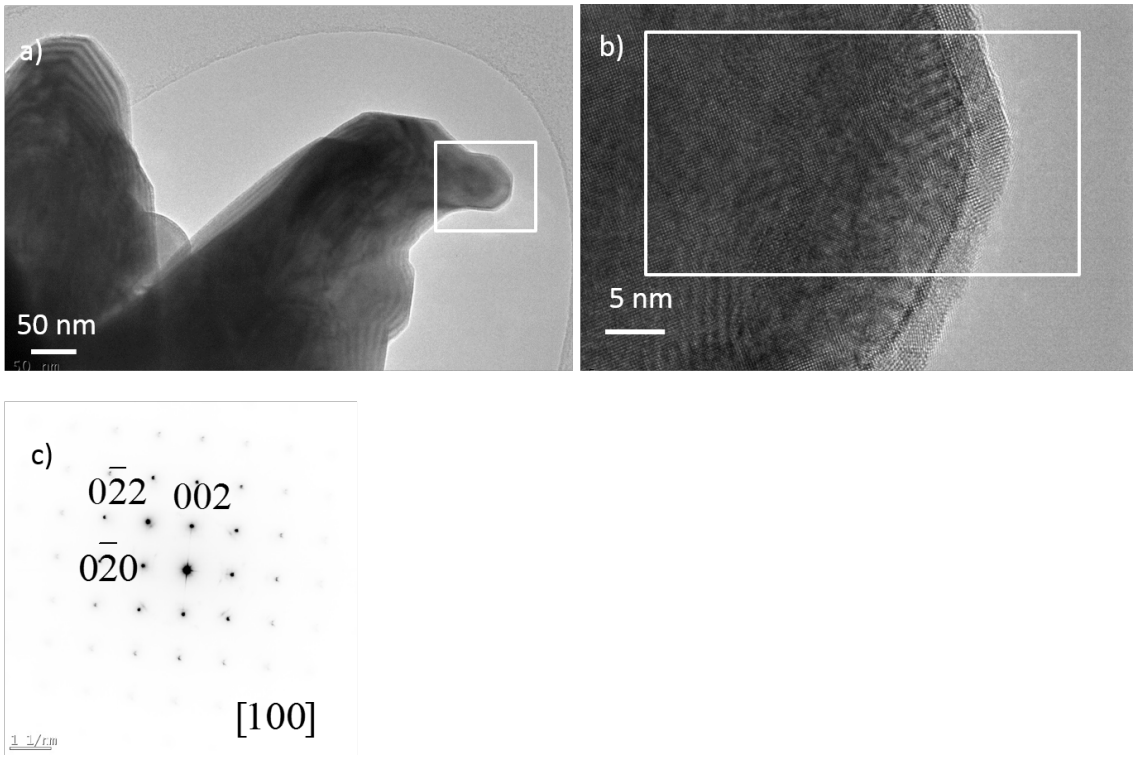


Figure 4.10: a) BF-TEM image of $ZrC_{0.9}$ after nitridation (dwell time 8h, dwell temperature 1873K) $ZrC_{0.67}N_{0.33}$,b) higher magnification image showing external layer, c) SADP of area shown in b

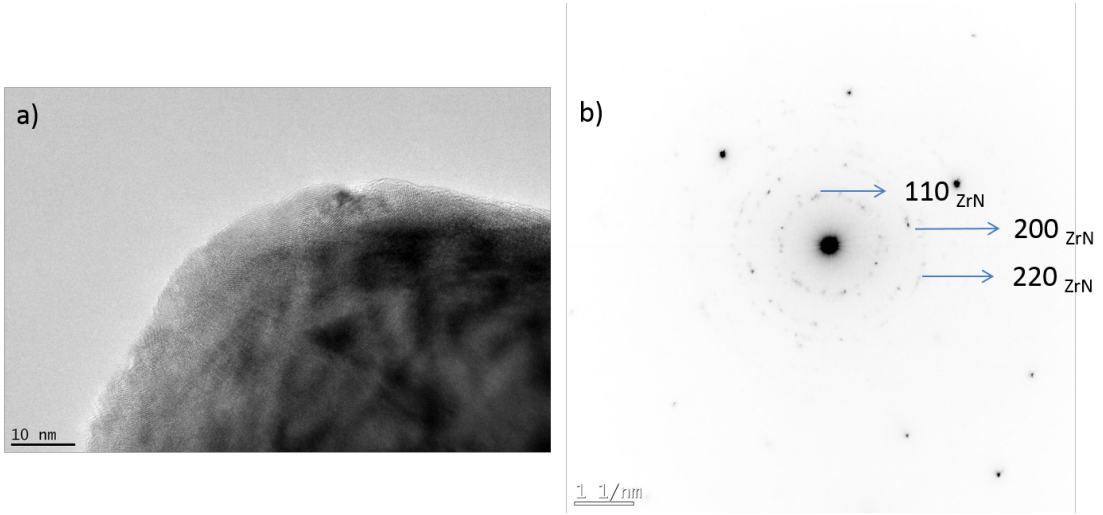


Figure 4.11: a) BF-TEM image of $ZrC_{0.9}$ after nitridation (dwell time 8h, dwell temperature 1873K) $ZrC_{0.67}N_{0.33}$, b) SADP of area shown in a

The ledges and terraces may indicate the removal of carbon from the ZrC lattice in a uniform direction, which may be the result of planar defects and the formation of ZrC_{1-x}. Different rates of crystal growth in a given direction can be described due to the preference in minimisation of high energy surfaces (i.e. surfaces with a larger number of interactions) over surfaces with low energy (fewer available interactions). The observation of terrace-ledge-kink mechanism is typical of crystal growth or dissolution.[147] In this mechanism three types of faces are seen; flat, stepped and kinked. For a cubic system crystals can be imagined as cubes whereby those in the flat face have 5 bonds with other crystals, stepped faces have crystals with 4 bonds and kink face crystals have 3 bonds (face types depicted in Figure 4.12). From this bonding order it can be seen that in the dissolution, the removal of a crystal at the kinked face will be easier than crystals at the stepped face, with the most difficult to remove being crystals in the flat face, this gives rise to the structures observed in the SEI micrographs of nitrided powders (Figure 4.8a).

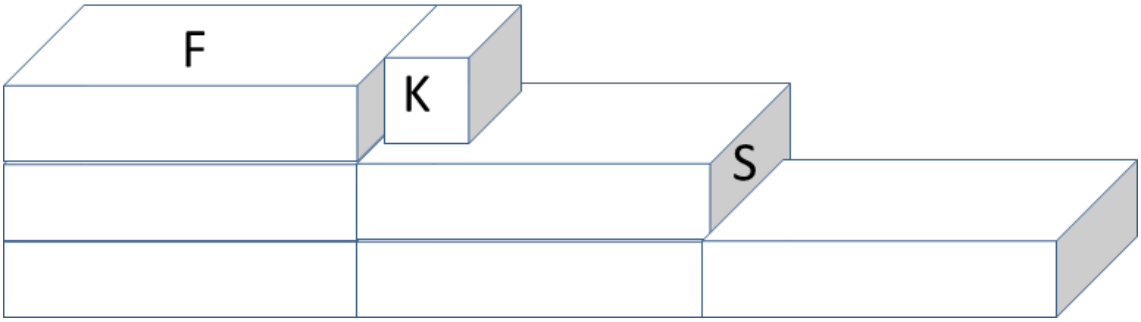


Figure 4.12: Types of crystal surfaces, F - flat face, S - stepped face and K - kinked face, according to TLK formation [147]

High resolution SEI of the as-reacted powder from iteration 4 of $ZrC_{0.9}$ and $ZrC_{1.00}$ are shown in Figure 4.13 and Figure 4.14 and had stoichiometries of $ZrC_{0.43}N_{0.52}$ and $ZrC_{0.25}N_{0.7}$ respectively (Table 4.3). Decreased numbers of ledges can be seen in the powders as reaction proceeds, compared to the powder reacted for shorter times (Figure 4.8). The ledges may be evidence of crystal defects arising from the removal of carbon from the ZrC lattice similar to observations made by David et al.[36] on the zirconia system. Nucleation of ZrC_xN_y or ZrN particles may occur on the surface of the ZrC particles either from evaporation-condensation of $Zr_{(g)}$ and $HCN_{(g)}$ or the mass diffusion of Zr to the ZrC particle surface followed by reaction with $HCN_{(g)}$ to form a carbonitride particle.

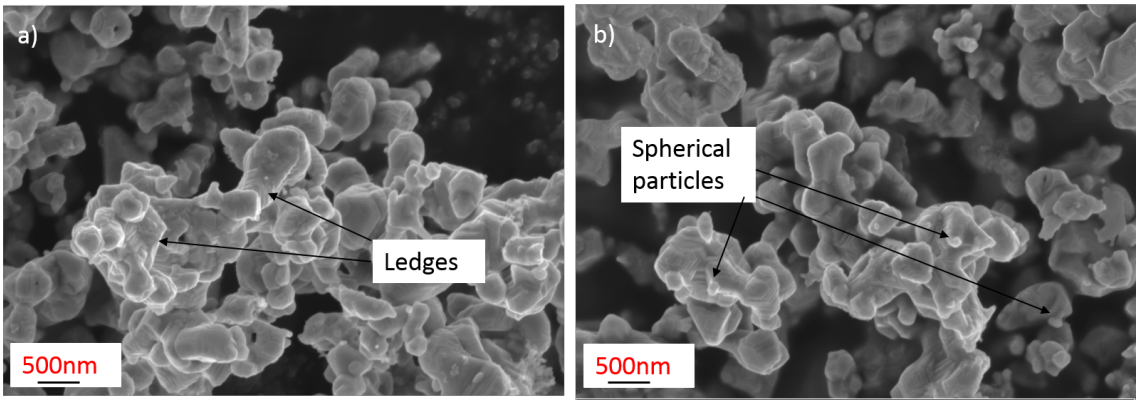


Figure 4.13: SEI of nitrided powders from iteration 4, starting composition $ZrC_{0.9}$ (dwell time 24h, dwell temperature 1800K) $ZrC_{0.43}N_{0.52}$, a) shows regions of ledge and terraces, b) reveals small spherical particles

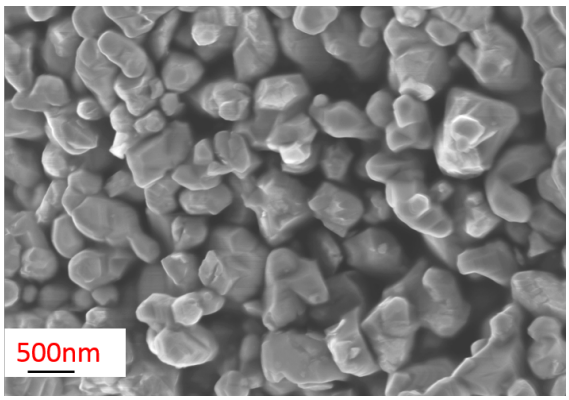


Figure 4.14: SEI of nitrided powders from iteration 4, starting composition $ZrC_{1.00}$ (dwell time 24h, dwell temperature 1800K) $ZrC_{0.25}N_{0.7}$

From this advanced stage of reaction it would be expected, if it is indeed a ZrN layer observed in the TEM of iteration 2 (Figure 4.9 and Figure 4.10) that it should be thicker. However, TEM (Figure 4.15 and Figure 4.16) of the as-reacted powders from iteration 5, which had a stoichiometry of $ZrC_{0.3}N_{0.65}$ reveal the layer on the surface is still around 5 nm thick, showing no change in the thickness of this external layer. The additional diffraction spots observed in the early stages of the reaction (Figure 4.9 and Figure 4.10) are not present at this late stage of reaction, consistent with the XRD patterns indicating it is a pure bulk single phase. However, ledges were also observed in the TEM image (Figure 4.15) that indexed well with ZrC, indicating some ZrC remains. Indexing of the SAED pattern (Figure 4.16c) is consistent with

ZrN indicating the the small spherical particle (∼400 nm) in Figure 4.16a, which is similar to those observed in the SEIs (Figure 4.8b and Figure 4.13b) is nitrogen rich.

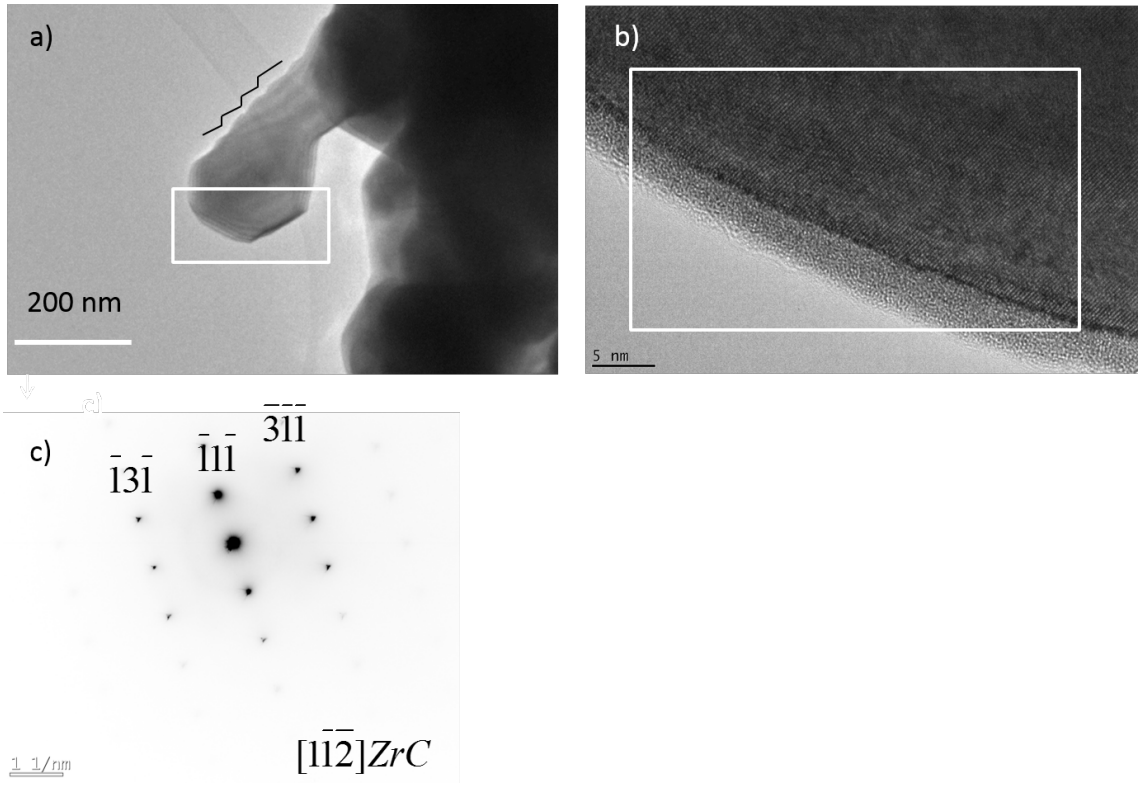


Figure 4.15: a) BF-TEM image of powder from iteration 5, nitridation of $ZrC_{0.9}$ (dwell time 24h, dwell temperature 1873K) $ZrC_{0.3}N_{0.65}$ b) higher magnification showing external layer, c) SADP of area shown in b

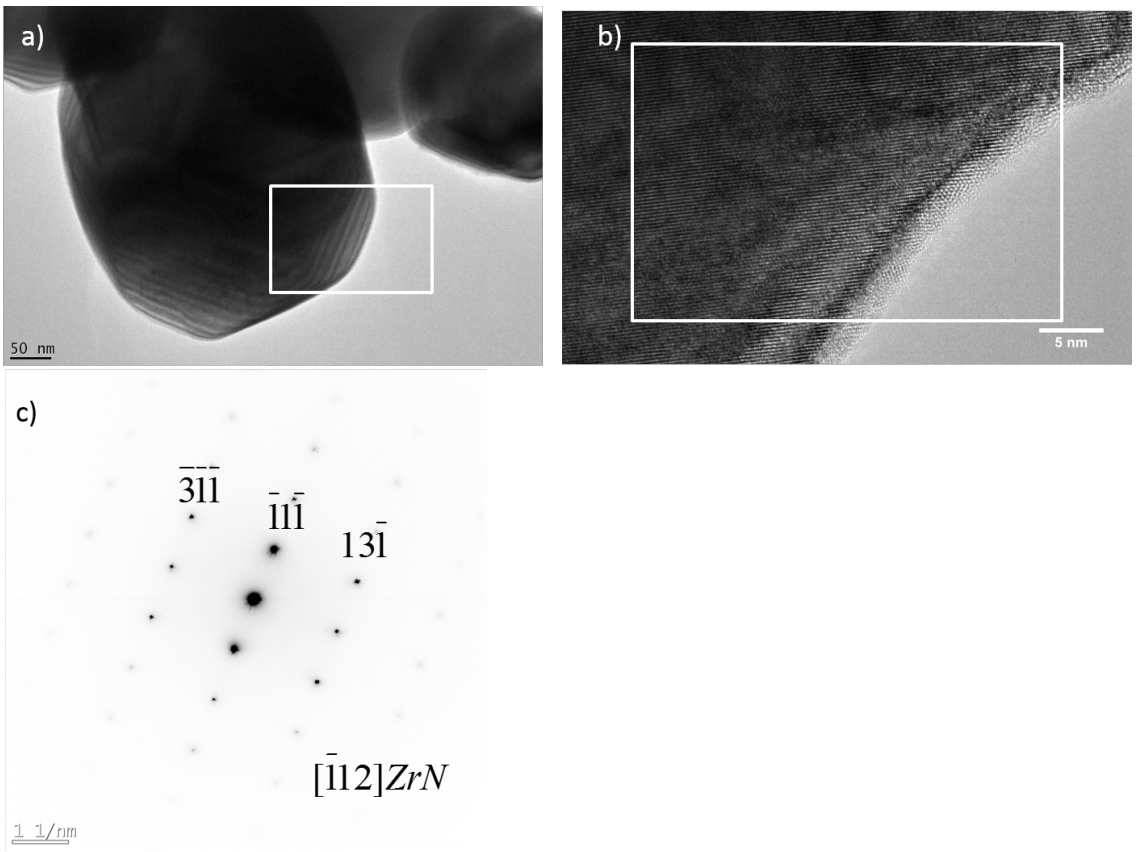


Figure 4.16: a) BF-TEM image of powder from iteration 5 - nitridation of $ZrC_{0.9}$ (dwell time 24h, dwell temperature 1873K) $ZrC_{0.3}N_{0.65}$, b) higher magnification showing external layer, c) SADP of area shown in b

4.1.3 Alteration of Nitridation Parameters

A one step carbothermic reduction-nitridation was performed with a ZrO_2+ C (with a C/Zr mole ratio of 3) sample reacted under flowing nitrogen gas with no hydrogen doping (dwell time 4 h, dwell temperature 1800 K) in a graphite furnace. Combustion analysis of the powders revealed the carbon content after reaction in wt% carbon was 11.39 ±0.21 %, corresponding to a stoichiometry of $ZrC_{0.98}$ and XRD (Figure 4.17) revealed a single phase with a lattice parameter of 4.655 Å (4.696 Å for ZrC,[144] 4.579 Å for ZrN[137]) powder.

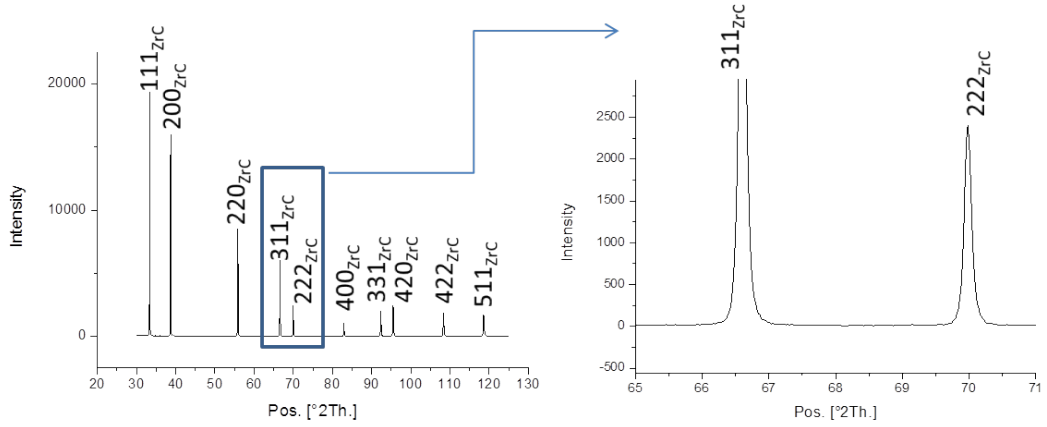


Figure 4.17: XRD of powder from one step carbothermic reduction-nitridation reaction (dwell temperature 1873 K, dwell time 4h)

The effects of the amount of hydrogen doping of the nitrogen gas were investigated by performing nitridation reactions in 0%, 1% and 10% hydrogen-nitrogen atmospheres, $ZrC_{1.00}$ powders were nitrided in a molybdenum furnace at 1873 K for 2 h (+50 K/min) and cooled rapidly to RT ($\sim$ 30 mins). Figure 4.18 shows XRD of the resulting powders and reveals that the hydrogen doping of the atmosphere causes much more nitridation than in the samples nitrided in a nitrogen only atmosphere. XRD reveals that there is little difference between the powders reacted using 1% or 10% hydrogen doping (Figure 4.18) with both forming a biphasic powder with two main peak components. Figure 4.18 reveals that the relative height of the peak components changes concomitantly with decrease of the ZrC peaks and the increase in intensity of the ZrN peaks. Chemical analyses by the oxidation technique revealed a similar stoichiometries of $ZrC_{0.58}N_{0.37}$, $ZrC_{0.6}N_{0.35}$ for the powders reacted under the 1% and 10% hydrogen doped atmospheres respectively .

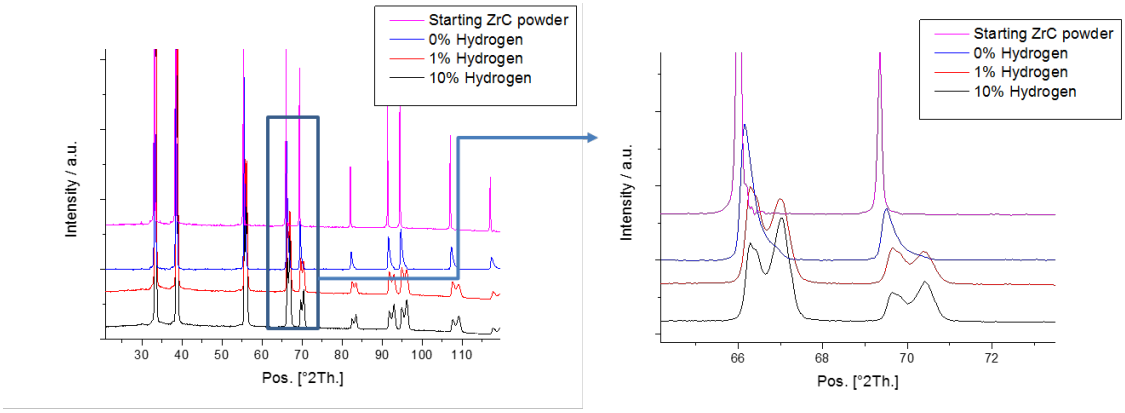


Figure 4.18: XRD of powders reacted in 0, 1 and 10% hydrogen doped nitrogen atmospheres for 2h at 1873 K

Figure 4.19 shows the change in wt% carbon as the reaction proceeds for the two different starting compositions using combustion analysis. Again it can be seen that the samples with higher amounts of carbon (sample name 1Zr-3C, stoichiometry $ZrC_{1.00}$) undergo increased nitridation compared to the samples with less initial carbon content. The rate of carbon loss is higher from 0-8 h than it is for 8-24 h reaction time, indicating the reaction rate slows as it proceeds. However, the higher wt% C of the 1Zr-3C sample (12.35 wt%) is higher than the theoretical wt % for stoichiometric ZrC (11.6 wt%) and this may be due to free carbon present in the sample. The presence of free carbon would rapidly form hydrocarbons during the initial part of nitridation and so could be a possible explanation for the increased loss of carbon shown in Figure 4.19.

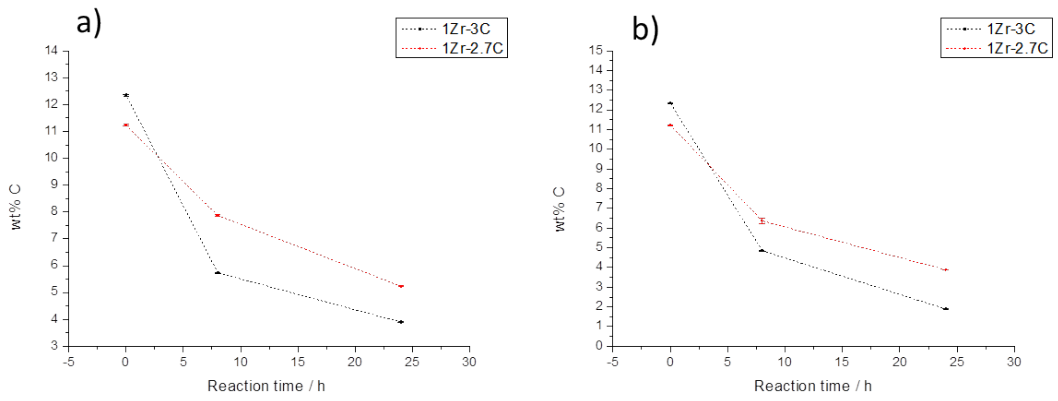


Figure 4.19: Change in wt% carbon as a function of time for nitridation reaction a) reaction temperature 1800 K b) reaction temperature 1873 K (lines to guide eyes only)

To further investigate the observations seen in the decrease of reaction rate as reaction time increases the nitridation was considered to occur in two parts; the first is the destabilisation of ZrC to non-stoichiometric ZrC_{1-x} by the reaction with H_2 and the second the diffusion of N_2 into the particle.

To verify this hypothesis samples from the $ZrC_{1.0}$ batch were nitrided in a molybdenum furnace at 1873K for 2 and 4 h (+50 K/min) under 10% H_2/N_2 atmosphere and cooled rapidly to RT ($\sim$ 30 mins). High-angle excerpts of X-ray diffractograms of the powders from the reactions are shown in Figure 4.20, along with the starting $ZrC_{1.0}$ powder. It can be seen that again 2 main phases form with two main components for each reflection. The intensity of the two maxima change respectively with reaction time and the peaks shift to higher 2θ corresponding to decrease in lattice parameter which is consistent with the change from ZrC towards ZrN. Table 4.4 reveals there is a higher amount of nitrogen in the powders reacted for 4 h as compared to powders reacted for 2 h.

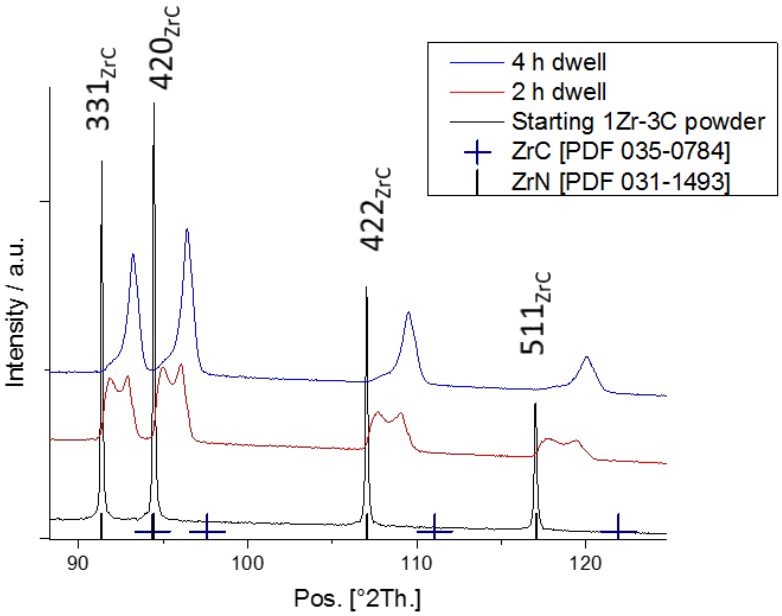


Figure 4.20: XRD of $ZrC_{1.0}$ powder reacted for 2-4 h under 10% H_2-N_2 [136, 137]

Starting sample	Dwell time / h	Dwell temperature / K	Atmosphere	at% C	at % N	Stoichiometry
$ZrC_{1.0}$	2	1873	10% H_2/ N_2	16.62 ±0.30	32.84 ±0.13	$ZrC_{0.67}N_{0.33}$
$ZrC_{1.0}$	4	1873	10% H_2/ N_2	29.28 ±0.44	20.25 ±0.28	$ZrC_{0.41}N_{0.59}$
$ZrC_{0.67}N_{0.33}$	2	1873	Vacuum	17.45 ±0.40	30.29 ±0.49	$ZrC_{0.61}N_{0.35}$

Table 4.4: Chemical analyses of reacted powders using oxidation technique

Figure 4.21 shows the resolution (using Gaussian fitting, as described in section 3.3) of the peaks into their separate components, which match well with the existence of two separate phases. Although the peak resolution fitted well with two separate peaks suggesting ZrC and ZrN phases, if the mechanism proceeds via the removal of carbon leaving a carbon deficient ZrC_{1-x} region the diffusion of nitrogen into those vacancies would be fast as the two atoms are similar in size and mass, and so the

existence of a ZrC_xN_y reaction phase at the ZrC rich -ZrN rich interface is likely, however this is likely to be missed by XRD.

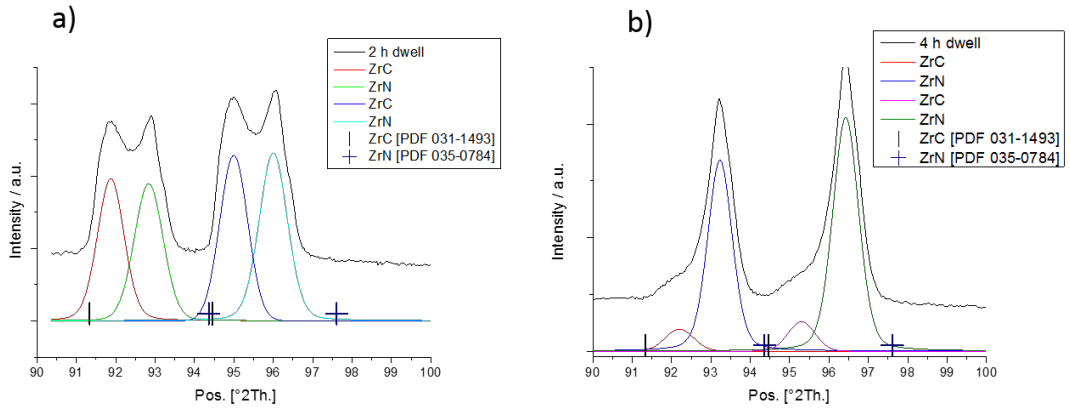


Figure 4.21: Peak resolution of XRD patterns from Figure 4.20, a) peak resolution of 2 h nitridation, b) peak resolution of 4 h nitridation. Baselines in both graphs indicate no unresolved peaks

FIB-SIMS was attempted on the particles from the above reactions and the SEI obtained are shown in Figure 4.22 and Figure 4.23. It can be seen from the micrographs that the powders are agglomerations of sub-micron powders immediately after reaction, and so, SIMS would not be an effective method for characterisation of the particles due to their nm size.

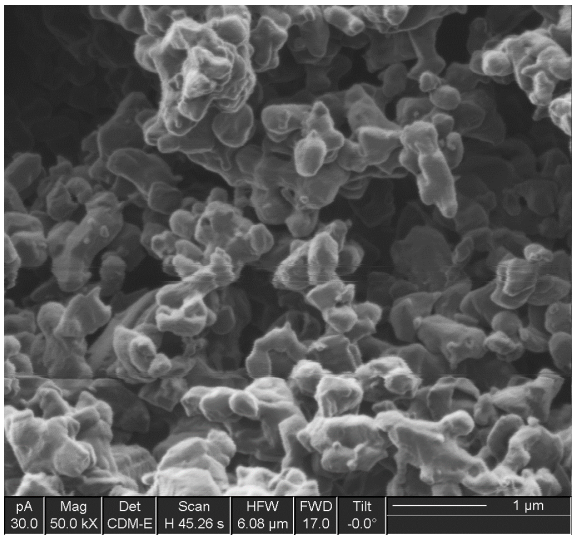


Figure 4.22: SEI of powder after 2 h nitridation reaction at 1873 K

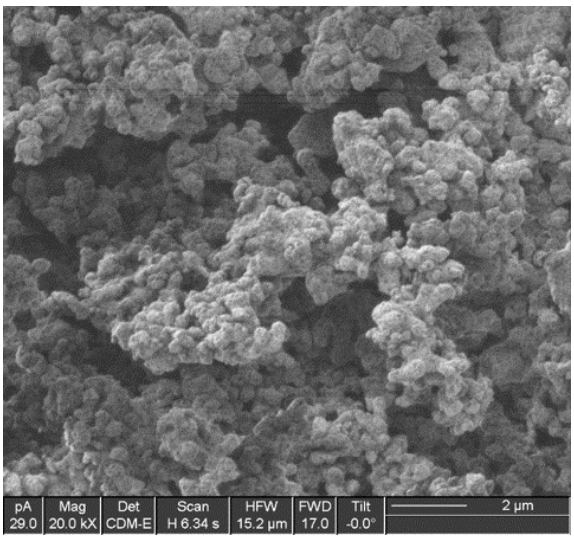


Figure 4.23: SEI of powder after 4 h nitridation reaction 1873 K

To investigate the nature of the mixed phase formed during nitridation and the absence of formation of a solid solution, powders from the 2 hour nitridation were then annealed in vacuum (10^{-4} Pa) for 1 and 2 h at 1873 K (+50 K/min) and cooled rapidly to RT ($\sim$ 30 mins). XRD (Figure 4.24) reveals that the two-phase powder from nitridation has become single phase indicating formation of a solid solution which is to be expected from the phase diagram (Figure 2.14) by Binder at al. [47], although the asymmetric peaks still suggests the presence of a minor phase. This solid solution appears to form rapidly with no change between the 1 and 2 h annealing reactions suggesting that during the nitridation reaction the uniformity of carbon removal and nitride growth results in little mixing of carbon and nitrogen.

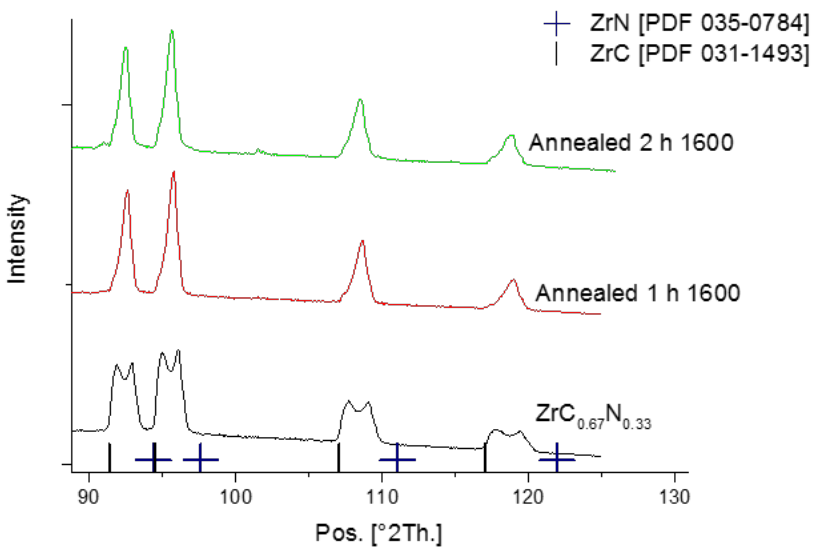


Figure 4.24: XRD pattern of $ZrC_{0.67}N_{0.33}$ powder before and after annealing under vacuum (10^{-4} Pa) at 1873 K for 1 and 2 h

4.2 Discussion

4.2.1 Introduction

The following section will draw together the experimental results from the fabrication of the ZrC_xN_y powders and by comparison with previous literature a mechanism for the nitridation of ZrC will be presented (Figure 4.25).

The carbothermic reduction of ZrO_2 achieved ZrC indicated to be single phase by XRD (Figure 4.3) and as characterised by elemental analysis of C and N quantities using oxidation and C N and O by combustion analysis (Table 4.1 and Table 4.2), with the remaining balance being attributed to Zr. Reducing the amount of carbon in the initial carbothermic reduction reactions resulted in a decreased amount of carbon in the product indicating substoichiometric ZrC_{1-x} and was consistent with the change in lattice parameter observed. Oxygen analysis revealed 2-3 at% contamination of the powders and so it is possible that a ZrO_xC_y phase was present due to incomplete carbothermic reduction.

The observation of an external layer shell on a particle core by TEM and the ex-

istence of a composite phase after reaction is evidence for a mechanism similar to that of Mukerjee et al. [29] for the 1 step carbothermal reduction-nitridation of UO_2. However, this external shell layer does not change in size in this work as the reaction proceeds and therefore cannot be due to the diffusion of nitrogen in the carbide particle. Mukerjee et al. [29] suggest after the formation of a carbonitride shell on the surface of the UO_2 particle, the free carbon then diffuses to the reaction interface where it is removed by reaction with hydrogen to form methane, and propagates until a particle of UN exists.

4.2.2 Destabilisation of ZrC

From observations of ledge formation and growth of small nitrogen-rich particles (∼500 nm) at the surface of bulk particles, the mechanism of nitridation could be similar to the mechanism of carbothermal reduction of ZrO_2 to ZrC proposed by David et al. [36] Following the carbothermal reduction step, the particles will be small ($\leq 1\mu m$) agglomerates derived from the nucleation of $Zr_{(g)}$ and free carbon. During the nitridation ZrC is destabilised to the substoichiometric carbide, leading to the formation of ledges and terraces observed by SEI (Figure 4.8). The removal of carbon leads to the formation of $HCN_{(g)}$ as observed previously by Bardelle and Warin [30] in the carbothermic reduction-nitridation of UO_2 according to Equation 4.1 and it was calculated to be the third most abundant gas under the reaction conditions here using FactSage software (Table 4.5, ver. 6.2 at conditions of 1873 K under 101.325 kPa). The shell layer observed on the ledge particles via TEM (Figure 4.15) could correspond to an outer layer of substoichiometric ZrC_{1-x}.

Species (g)	Mole fraction / 10^{-2}
N_2	89.311
H_2	10.501
H-C-N	0.1678
H	0.0120
H-N-C	0.0058
CH_4	0.0011
C_2H_2	0.0009

Table 4.5: Mole fractions of gaseous species present during nitridation of ZrC powder at 1873 K under flowing H_2(10%) - N_2 gas calculated using FactSage

$$ZrC_{(s)} + \frac{x}{2}H_{2(g)} + \frac{x}{2}N_{2(g)} \longrightarrow ZrC_{1-x(s)} + xHCN_{(g)} \tag{4.1}$$

The step is shown in **step 1** of Figure 4.25, whereby removal of carbon results in the ledges observed by SEM (Figure 4.8) and TEM (Figure 4.15). This creates the ledge-terrace surfaces with crystals being more easily removed from this surface than the flat surface at the other side of the particle. The generation of substoichiometric ZrC_{1-x} external ledges is shown in part 2 of Figure 4.25 and agrees well with the SAED shown in Figure 4.9c of these external layers that indexed well with ZrC but has a smaller lattice parameter of 4.678 Å than stoichiometric ZrC (4.696 Å [144]) indicating it is substoichiometric.

4.2.3 Nucleation and growth of ZrN rich phase

Nucleation of ZrC_xN_y (**step 2** in Figure 4.25) then occurs by either evaporation-condensation of $Zr_{(g)}$ and $HCN_{(g)}$ at the surface of the ZrC particle, although this is unlikely due to the high boiling point of Zr (around 4500 K) resulting in low amounts of $Zr_{(g)}$. More likely nucleation occurs at the surface of the $ZrC_{1-x(s)}$ particle from reaction of Zr with $HCN_{(g)}$, shown in Equation 4.2 and proceeds by surface diffusion of Zr to the nucleation site.

$$Zr_{(s/g)} + xHCN_{(g)} \longrightarrow ZrC_{x/2}N_{x(s)} + C_{x/2}H_{x(g)} \tag{4.2}$$

ZrC_xN_y particles then grow by further migration of Zr to the reaction layer and condensation of $HCN_{(g)}$. An external layer is then formed on the ZrC_xN_y particle as carbon diffuses to the reaction layer to form more $HCN_{(g)}$ leading to a carbon-rich external layer, and a nitrogen-rich core (Equation 4.3, **step 3 and 4** in Figure 4.25). This is consistent with the additional diffraction spots in SAED patterns indicating a minor phase with an increased lattice parameter in epitaxy with the bulk phase (Figure 4.9d and Figure 4.10c) and XRD measurements where two monolithic phases and a range of mixed carbonitride phases are observed.

$$ZrC_xN_{y(s)} + \frac{z}{2}H_{2(g)} + \frac{z}{2}N_{2(g)} \longrightarrow ZrC_{x-z}N_{y(s)} + zHCN_{(g)} \tag{4.3}$$

The increased rate of reaction with higher initial carbon content would then be due to the increased rate of formation of $HCN_{(g)}$ which is a key reactive agent in

this proposed mechanism. The reaction continues by further diffusion of carbon to the reaction layer leading to removal of carbon at the surface until a core of ZrN exists. These steps are consistent with XRD (Figure 4.6 and Figure 4.7) whereby peak components of monolithic phases of ZrC and ZrN exist in the early stage of reaction (up to 8h, 1800K) indicative of a ZrC-rich particle and ZrN-rich phases.

4.2.4 Removal of carbon

In the later reactions (>24 h, 1800 K) no monolithic ZrC exists indicating it has all been consumed and the remaining particles are ZrN with an external shell of ZrC_xN_y, shown in **step 5** of the mechanism in Figure 4.25, similar to the mechanism of nitridation of SiO_2.[37, 38] The external carbon-containing layer now exists as a solid solution with the nitride, observed in XRD measurements (Figure 4.6) by the asymmetry of the peak being caused by a minor phase that is very close in lattice size to the main phase but all ZrC-rich phase has been removed, observed by the existence of only one peak in the XRD. Diffusion of this carbon to the surface may be slow and could introduce the rate limiting step, meaning that the rate of reaction slows from **step 3** in Figure 4.25. Another possibility is that as the ZrC particle is fully consumed in **step 5**, the partial pressure of $HCN_{(g)}$ will decrease and the mechanism of the removal of carbon may change, this may reduce the rate of decarburisation which would also decrease the rate of reaction with time (Figure 4.19).

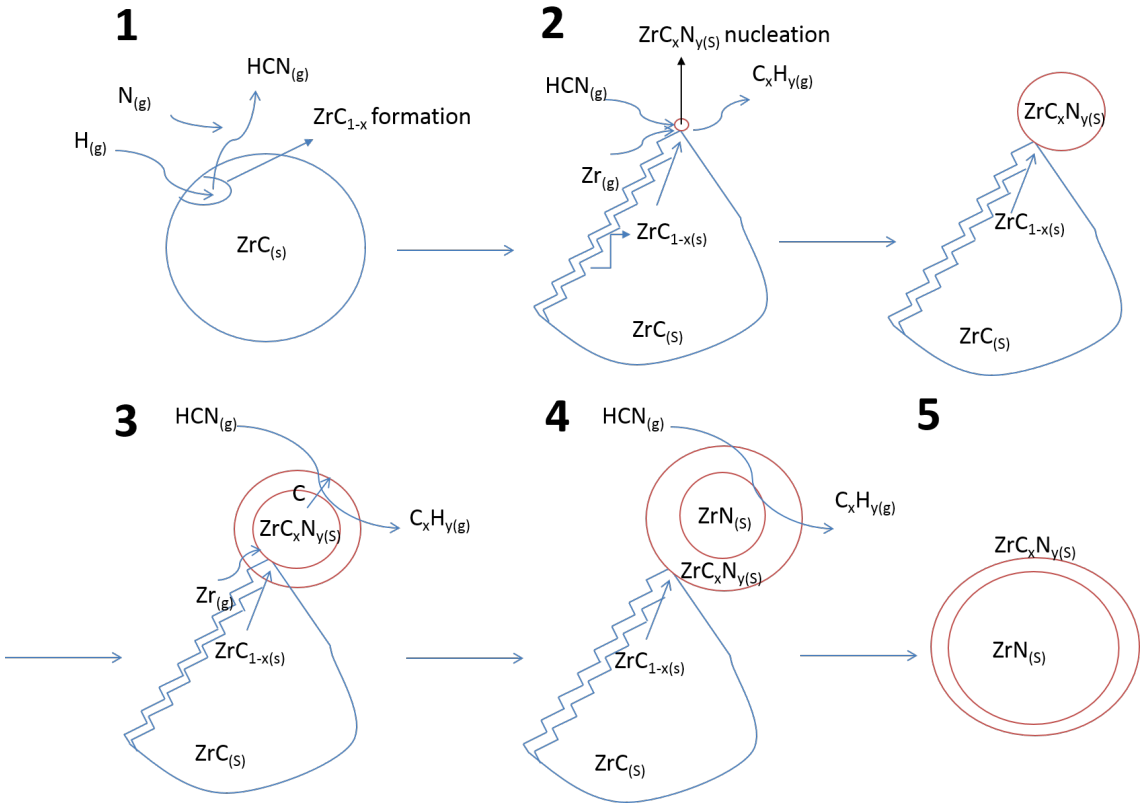


Figure 4.25: Schematic diagram of the mechanism of nitridation of ZrC particles

4.2.5 Reaction parameters

Reaction parameters of the nitridation of the ZrC powders were assessed with wt% C, dwell temperature, dwell time and $\%H_2$ doping of nitrogen atmosphere all having an observable effect on the rate. Higher dwell times and dwell temperatures lead to increased nitridation. Increasing wt% C also resulted in an increase in the rate of nitridation of UO_2 as reported by Nakagawa et al. [32] who observed formation of CH_4 during nitridation of UC and CeC_2 under flowing NH_3 stating that the formation of CH_4 was an equilibrium reaction and by increasing flow the equilibrium was pushed to the right, this could also be applied to the formation of HCN.

Another indication that the mechanism occurs by growth of a ZrN-rich phase and removal of the ZrC phase can be seen by the rapid formation of the solid solution during annealing under vacuum shown in Figure 4.24. After 1 h the mixed phase has formed more of a solid solution, however a slight minor phase remains. Also by resolving the XRD peaks for the mixed phases it can be seen the two phase mixture

can be well separated into two, and only two, components shown in Figure 4.21. This suggests that during nitridation the removal of carbon and the growth of the nitride phase must occur in uniform directions that does not allow mixing of the two phases and inhibits formation of a solid solution during nitridation which appears to be rapid under annealing conditions.

5 Ceramic Production

This chapter describes the optimisation of densification of the ceramics from commercial ZrC and ZrN powders using spark plasma sintering (SPS) and hot pressing (HP) with achievable densities and resulting microstructure being discussed. Densification of the ZrC_xN_y powders produced as described in chapter 4 is presented and the effect of stoichiometry on achievable density and microstructure discussed, along with microscopy to characterise the ceramic microstructure to aid interpretation of the sintering mechanisms.

5.1 Densification

5.1.1 Commercially-available ZrC and ZrN

Initial densification experiments examined the benefits of using SPS and HP for commercially-available powders. XRD patterns of commercially available ZrN and ZrC powders are shown in Figure 5.1 revealing they are both single-phase cubic crystalline materials as determined within the limits of XRD detection. Commercially-available powders of ZrN are produced via the carbothermic reduction-nitridation route, or the hydrogenation of zirconium ingot and then the nitridation of zirconium hydride and so formation of phases contaminated oxygen or hydrogen is possible.

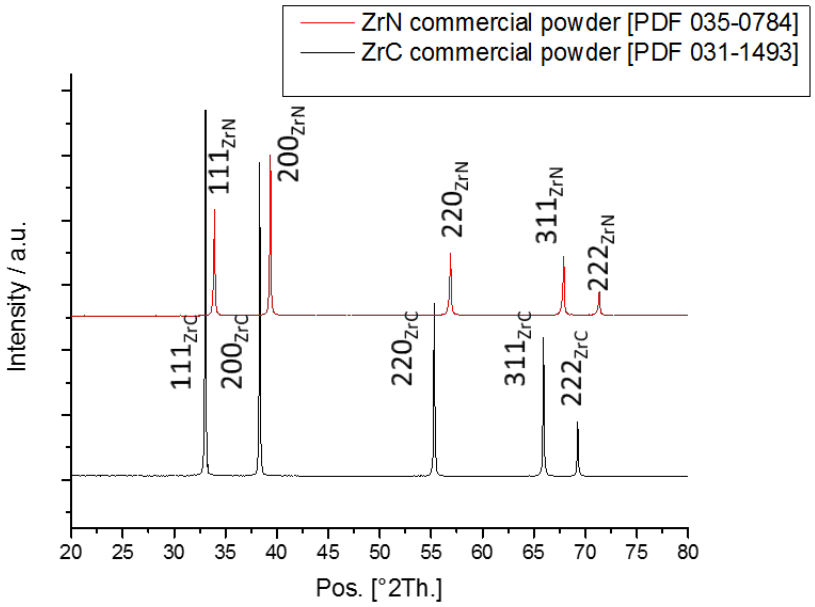


Figure 5.1: XRD pattern of commercially-available ZrC [136] and ZrN [137] powder

Chemical analyses were performed on the powders to quantify their chemical purity using the oxidation and combustion technique (Table 5.1 and Table 5.2). Table 5.1 indicates the carbide has a stoichiometry of $ZrC_{0.9}$ with nitrogen contamination, however from Table 4.1 the as-fabricated ZrC samples also contain similar amounts of nitrogen which may arise from an error with the instrument due to air trapped between the particles when the sample is packed in the tin crucible (as described in subsubsection 3.1.1.3). Chemical analysis by the combustion technique in Table 5.2

shows there to be negligible nitrogen content in the commercial ZrC sample however, and the material is stoichiometric. The commercially available nitride is substoichiometric with both techniques agreeing well, however, more nitrogen was detected by the oxidation technique although this is consistent with the observation of about 2.3 at% N being recorded in ZrC samples by the same technique, strengthening the hypothesis that N detected by oxidation technique comes from trapped air.

Sample	at% C	at% N	Stoichiometry	a / Å
ZrC commercial	44.67±3.24	2.35 ±0.44	$ZrC_{0.89}$	4.696
ZrN commercial	0.16 ±0.04	43.72 ±0.28	$ZrN_{0.88}$	4.577

Table 5.1: Carbon and nitrogen analysis of commercial powders using the oxidation technique

Sample	at% C	at% N	at% O	Stoichiometry
ZrC commercial	50.49 ±1.04	0.03 ±0.00	1.90 ±0.03	$ZrC_{1.02}$
ZrN commercial	0.16 ±0.01	43.56 ±0.20	2.73 ±0.03	$ZrN_{0.82}$

Table 5.2: Carbon, nitrogen and oxygen analysis of commercial powders using the combustion technique

SPS has been increasingly used to densify carbides and nitrides due to their low sinterability arising from strong covalent bonds.[58, 101, 106, 127, 148] SPS was examined for the densification of carbides and nitrides in this work, optimising the sintering program with samples of commercially-available TiN due to this sintering poorly after initial tests. After optimisation for TiN the same sintering programs were used in the densification of commercially-available ZrN and ZrC powders shown in Table 5.3 (forming dense samples ($\geq$95%), it should be noted that HP was carried out at 100 K less that SPS and so a direct comparison between sintering programes is not possible. The increase in density between the ZrC and ZrN samples may be due to the difference in starting powder particle size ($\leq$5 μm and 1-2 μm respectively). Another reason for the denser ZrN samples is the strength of the covalent bonds in the nitride being weaker than those in the carbide. This reduction in bond strength will increase nitrogen diffusion through the sample. Theoretical densities of ZrN and ZrC are quoted as 7.09 and 6.73 g/cm^{-3} from the manufacturers. Theoretical

densities were also calculated from Equation 5.1, where ρ_{th} (gcm^{-3}) is the theoretical density, FW ($gmol^{-1}$) is the formula weight of the sample, a (cm^3) is the lattice parameter and N_{Av} is Avogadro's number (6.02×10^{23} mol^{-1}), $4FW$ corresponds to the molecular weight of the unit cell (6 face centred atoms + 8 corner atoms on the metal lattice and 1 body centered and 12 edge centered atoms on the non-metal lattice). Using Equation 5.1 the densities for ZrN and ZrC are 7.30 and 6.62 gcm^{-3} respectively. Percentage theoretical densities are here on presented from the theoretical densities calculated using Equation 5.1 and not from the manufacturer's values.

$$\rho_{th} = \frac{4FW}{a^3 N_{Av}} \tag{5.1}$$

Sample	Dwell temperature/ K	Dwell time/ min	Pressure/ MPa	Density / g cm^{-3}	%TD	Average grain size / μm
SPS-TiN-1	2073	8	50	4.36±0.02	-	-
SPS-TiN-2	2173	10	60	4.70±0.04	-	-
SPS-TiN-3	2373	10	50	4.88±0.05	-	-
SPS-ZrN-1	2373	10	50	7.13±0.01	97.7±0.1	~ 35
SPS-ZrC-1	2373	10	50	6.39±0.04	96.5±0.6	~ 15

Table 5.3: SPS parameters and bulk properties of ceramics

Sample	Dwell time/ min	Pressure/ MPa	Density / g cm^{-3}	%TD	Average grain size/ μm
HP-ZrN-1	60	50	7.00± 0.05	95.5±0.6	∼ 100
HP-ZrN-2	60	50	7.07± 0.01	96.8±0.1	-
HP-ZrC-1	60	50	6.20± 0.03	93.6±0.5	∼ 5
HP-ZrC-2	60	50	6.15± 0.02	93.0±0.3	-

Table 5.4: HP sintering (dwell temperature 2273 K) program and bulk properties of ceramics produced

SEIs of the ZrC and ZrN samples are shown in Figure 5.2 and Figure 5.3. The SPS-ZrN-1 sample was thermally etched at 1673 K for 30 min in vacuum (10^{-6} mbar, 10^{-4} Pa and ≤0.001 ppb O_2) to reveal grain boundaries as the materials are resistant to chemical etching. The thermal etching did reveal grain boundaries, however, grain boundaries were contaminated either from the residual acids from chemical etching or oxygen in the furnace or oxygen impurities that were also in the powder. Thermal annealing may also have resulted in grain growth and the debris at grain boundaries may be material that has been forced from the grains enveloping other grains, which may appear larger than they were after SPS. Due to the issue with chemical etching being ineffective and thermal etching possibly altering the surface of the materials, BSE imaging was used, generating contrast from different grain-electron beam orientations (Figure 3.3). The grains of the commercial ZrC in Figure 5.3 are much smaller than in the ZrN samples produced by SPS showing that the carbide undergoes little grain growth during extended sintering times. This again will be due to the slow diffusion of material during the sintering process caused by strong covalent bonds.

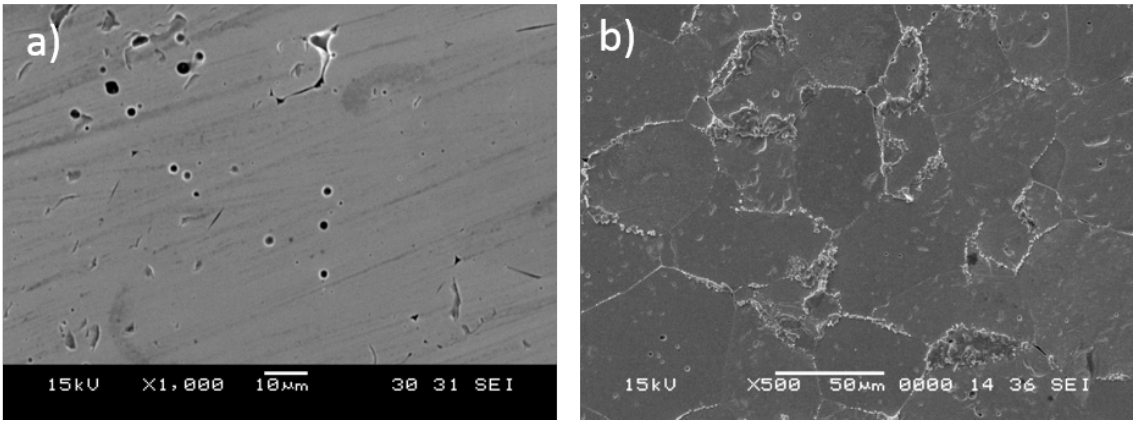


Figure 5.2: SEIs of SPS-ZrN-1 (dwell time 10 min, dwell temperature 2373 K, 50 MPa) a) after polishing, b) after thermal etching

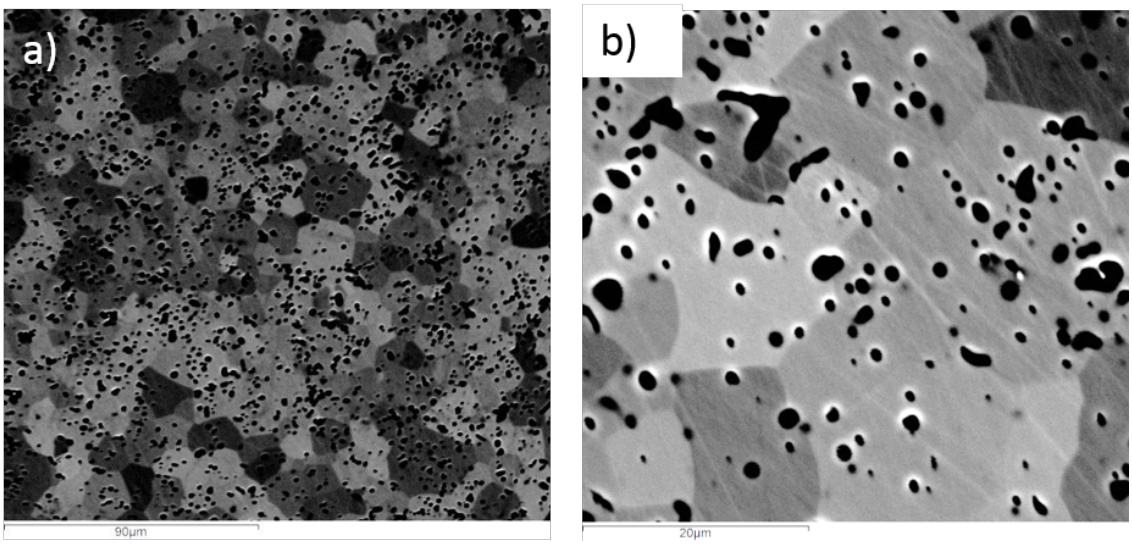


Figure 5.3: BSE images of polished, unetched SPS-ZrC-1 (dwell time 12 min, dwell temperature 2373 K, 50 MPa) a) low magnification to show grain boundary size distribution, b) higher magnification showing pore distribution

HP was also used to produce sintered samples of ZrC and ZrN from commercially-available powders. HP is similar to SPS in the sense that the same amount of uniaxial pressure can be applied and sintering temperatures used. However, the longer times required to achieve the dwell temperature and the longer dwell times give rise to much longer sintering programs compared to SPS which results in much larger grain sizes (10-100 μm by HP compared with around 1-10 μm by SPS). HP uses radiation heating of an enclosed furnace to achieve dwell temperature compared

to the pulsed Joule heating in SPS meaning the samples are not subject to any possible sintering effects from the current passing through the sample generating hot spots from resistance (section 3.2). BSE images of the hot pressed commercially available powders are shown in Figure 5.4 and Figure 5.5 with the density's and bulk properties presented in Table 5.4.

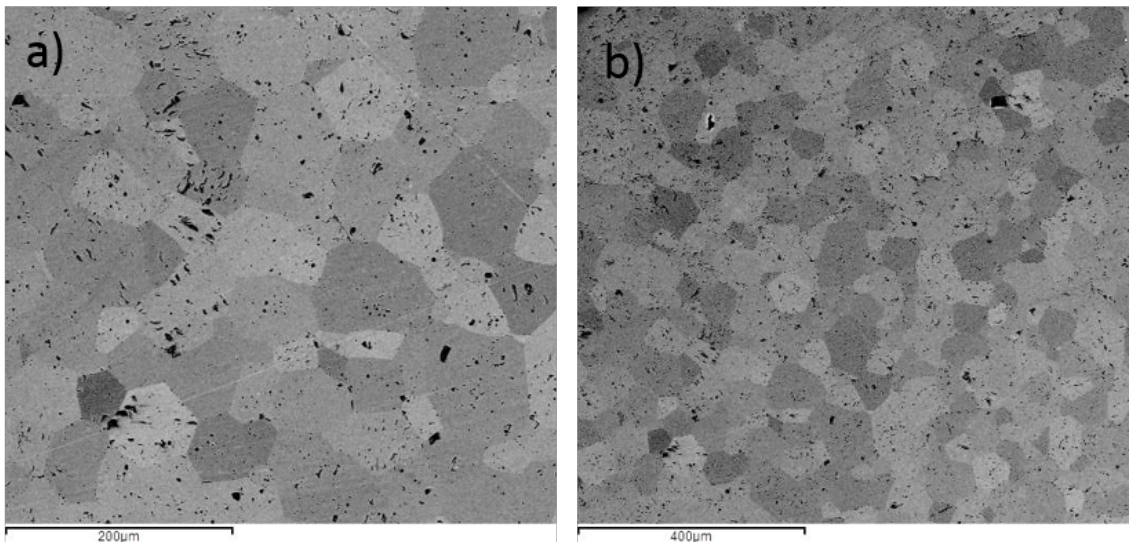


Figure 5.4: BSE image of polished, unetched HP-ZrN-1 (dwell time 60 min, dwell temperature 2273 K, 50 MPa, a) higher magnification, b) lower magnification

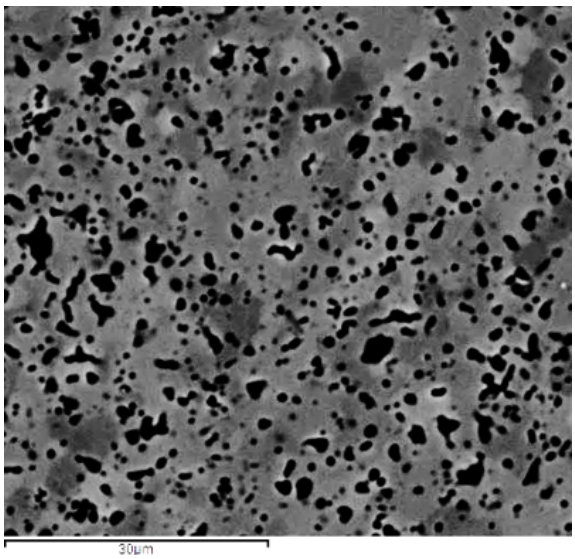


Figure 5.5: BSE image of polished, unetched HP-ZrC-1 (dwell time 60 min, dwell temperature 2273 K, 50 MPa)

Both methods of sintering achieved similar levels of densification with all samples having ≥90% TD. With similar densities being achieved by both methods, HP'ing was chosen as the densification route to fabricate ZrC_xN_y ceramics due to problems with bonding to the graphite die observed in the SPS, which was not observed in the HP. The rapid Joule heating and electric current passing through the materials during SPS may have caused the formation of high temperature regions above the measured pyrometer temperature. Chemical analyses of the commercial ZrN powder revealed it contained 43.11 at% N which is approaching the metal-rich liquid phase boundary (Figure 2.13) at the sintering temperature. Alternatively impurities such as the oxygen may form a tertiary or quaternary phase which forms a liquid which will eventually weld the pellet to the graphite die.

5.1.2 As-Fabricated ZrC_xN_y Powders

Powders from the nitridation reaction were milled as described in subsubsection 3.1.1.2 to minimise particle size and break up agglomerates to favour densification. The sample from the longest reaction time, ZrCN-4, was repeated in duplicate to ensure thermal analyses for the highest nitrogen-containing sample was repeatable (duplicate sample name- ZrCN-4-D, see Table 5.5). Particle size measurements were made via SEM as opposed to laser diffraction. Laser diffractometers measure the distribution of particle sizes by measuring the amount of diffraction caused to the laser beam as the particles pass through the beam in a flowing tube. Unfortunately, due to the hydrophobic nature of the powder, the particles would line the plastic tubing of the equipment thus reducing the reliability of the results. SEI of the milled ZrC_xN_y powders (Figure 5.6a-d) reveal that all particles are ≤10 μm.

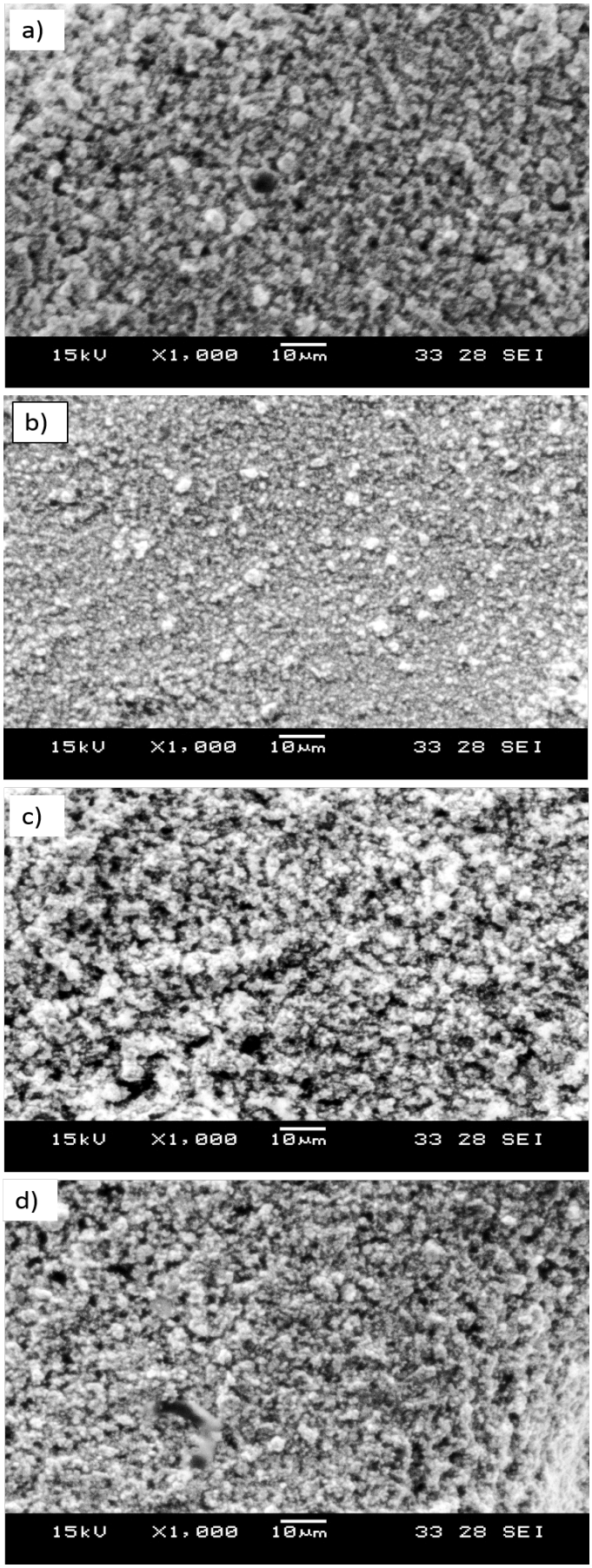


Figure 5.6: SEI of ZrC_xN_y powders after milling a) $ZrC_{0.55}N_{0.4}$ b) $ZrC_{0.4}N_{0.55}$ c) $ZrC_{0.33}N_{0.6}$ and d) $ZrC_{0.12}N_{0.78}$.

ZrC_xN_y powders were densified using HP and the bulk properties, microstructure and stoichiometries characterised. Chemical analyses were performed on crushed samples of the pellets to ascertain stoichiometry and any impurities in the samples. Table 5.5 shows that the at% of C and N agree well with Table 4.3 indicating little change in carbon and nitrogen content during sintering showing negligible carbon ingress from the graphite foil and die. The increase in oxygen content with sintering time suggests the material might have undergone some oxidation during nitridation but is most probably associated with contamination from crushing the pellets and grinding in air before chemical analysis.

Sample	at% C	at% N	at% O	Stoichiometry	[C] / [C]+[N]
ZrCN-1[1a]	20.64 ± 0.34	26.96 ±0.41	3.43 ± 0.10	$ZrC_{0.4}N_{0.55}$ $O_{0.06}$	0.42
ZrCN-2[1a]	27.50 ± 0.48	20.25 ±0.48	2.65 ±0.09	$ZrC_{0.54}N_{0.4}$ $O_{0.04}$	0.57
ZrCN-3[1a]	16.54 ±0.30	29.90 ±0.55	4.83 ±0.16	$ZrC_{0.33}N_{0.6}$ $O_{0.08}$	0.32
ZrCN-4[1a]	8.21 ±0.13	40.01 ± 0.18	2.20 ±0.08	$ZrC_{0.16}N_{0.80}O_{0.04}$	0.16
ZrCN-4[2b]	6.55 ±0.05	41.03 ±0.39	-	$ZrC_{0.12}N_{0.78}$	0.13
ZrCN-4-D[2b]	6.75 ±0.23	41.23 ± 0.31	-	$ZrC_{0.13}N_{0.83}$	0.14

Table 5.5: Carbon, nitrogen and oxygen chemical analysis of nitrided powders [1)] Crushed pellet analysed, [2)] Powder analysed, [a)] combustion analysis results [b)] oxidation analysis results

As compared to excerpts of XRD patterns of ZrC_xN_y powders (Figure 5.7), XRD of ceramic pellets (Figure 5.8) revealed sharper single peaks and more highly crystalline phases, revealing that during sintering a solid solution is formed and the crystallinity has improved definitively. The formation of a solid solution is an effect of the sintering/annealing reducing the residual strain in the lattice and allowing diffusion of the nitrogen throughout it. It is important to note that if the XRD had been performed on the pellet only, then the solid solution may have been mistaken for a pure single phase with a slight deviation from lattice parameter. Account must be taken of changes from powders to dense ceramics in the fabrication of non-oxides via the carbothermic reduction-nitridation route. Lattice parameters calculated from

the XRD pattern of the ceramics (Figure 5.8) show a decrease with increasing nitrogen content. Plotting lattice parameter (Figure 5.9) as a function of [C]/[C]+[N] (where [C] and [N] are the x and y stoichiometry values respectively of the ZrC_xN_y phases) with published values of ZrC and ZrN lattice parameter gives good correlation showing agreement between the chemical analysis and XRD data [137, 144] and also confirms the existence of a complete ZrC_xN_{1-x} phase respecting Vegards law.

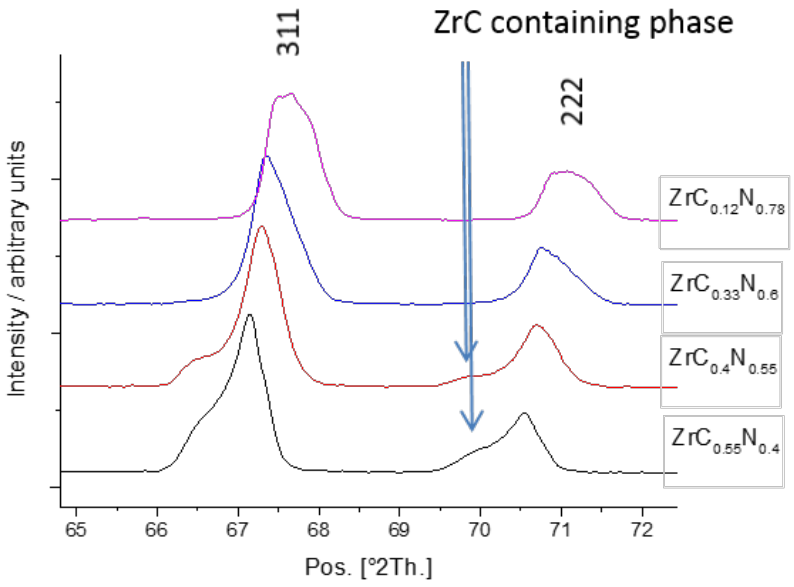


Figure 5.7: Excerpts of XRD patterns of ZrC_xN_y powders before sintering

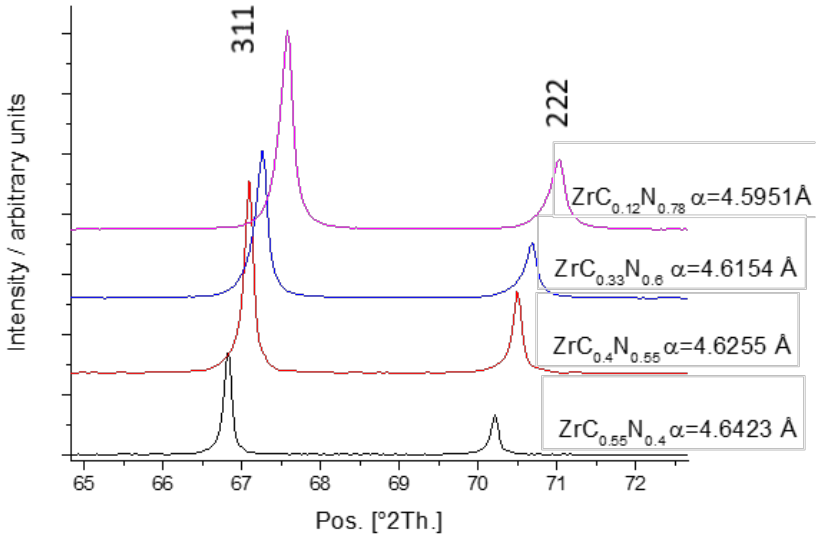


Figure 5.8: Excerpts of XRD patterns of ZrC_xN_y after sintering at 2273 K for 1 hour under 50 MPa uniaxial pressure

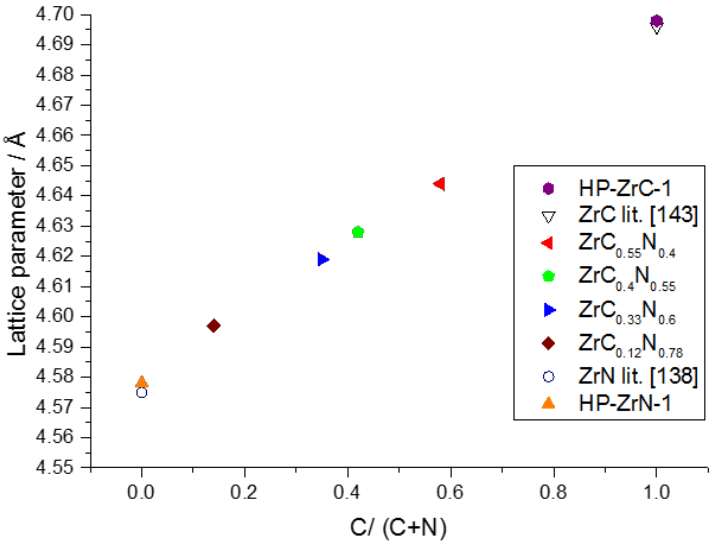


Figure 5.9: Lattice parameters of ZrC, ZrN and ZrC_xN_y ceramics as a function of [C]/[C]+[N] with literature values of ZrC and ZrN [137, 144]

Distinct colour changes were observed in the pellets produced from the ZrC_xN_y

phase (Figure 5.10). As nitrogen content increases the samples become lighter changing from a grey colour through orange and red to yellow-gold, as previously observed by Lengauer.[41] SEI and BSE images of the ZrC_xN_y ceramics are shown in Figure 5.11-Figure 5.14 along with bulk properties in Table 5.6. The carbonitrides have a higher density than the ZrC pellets derived from commercial powders produced by either HP or SPS. The density of the ZrC_xN_y phases increases with increasing nitrogen content, from around 6.90 g/cm^3 to 7.06 g/cm^3 and is expected as the carbonitrides should have intermediate density values between ZrC and ZrN, although substoichiometry and oxygen impurities will cause a deviation from densities predicted by the rule of mixtures. The increased diffusion of nitrogen may explain the increased density of the nitride and carbonitrides over the carbide. The difference in grain size between the two samples of commercial ZrN and ZrC is most likely due to the nitride undergoing more grain growth during the 1 h dwell (Table 5.4). Grain growth is driven by the reduction of grain boundary area (regions of high energy). Figure 5.11 shows the surface microstructure of the pellet produced from the zirconium carbonitride phase $ZrC_{0.55}N_{0.4}$, less grain growth is observed than in the nitride, however, the carbonitrides contains larger grains (∼10-30 μm) than the carbide (∼5 μm), and this may also be an effect of the increased diffusion of nitrogen. The sample is also fully dense with no porosity observed by SEM, evidence that the nitrogen content has had a positive impact on the sinterability of ZrC.

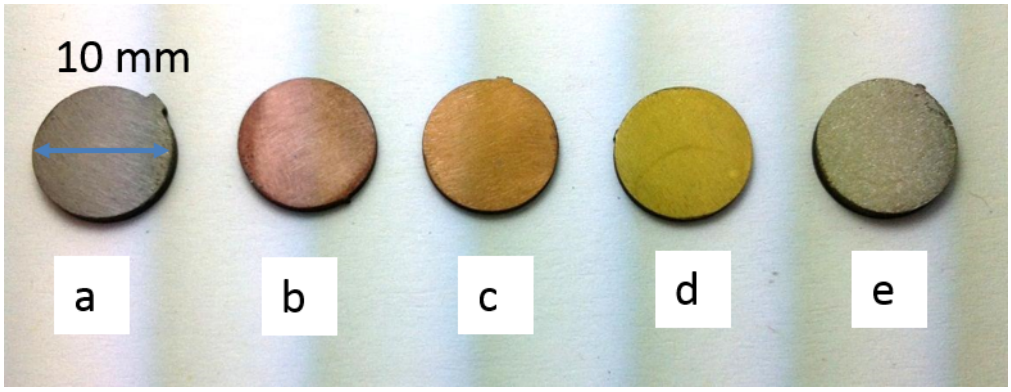


Figure 5.10: Photograph of 10 mm ceramic pellets a) commercial ZrC, b) $ZrC_{0.4}N_{0.55}$, c) $ZrC_{0.33}N_{0.6}$, d) $ZrC_{0.12}N_{0.78}$ and e) commercial ZrN

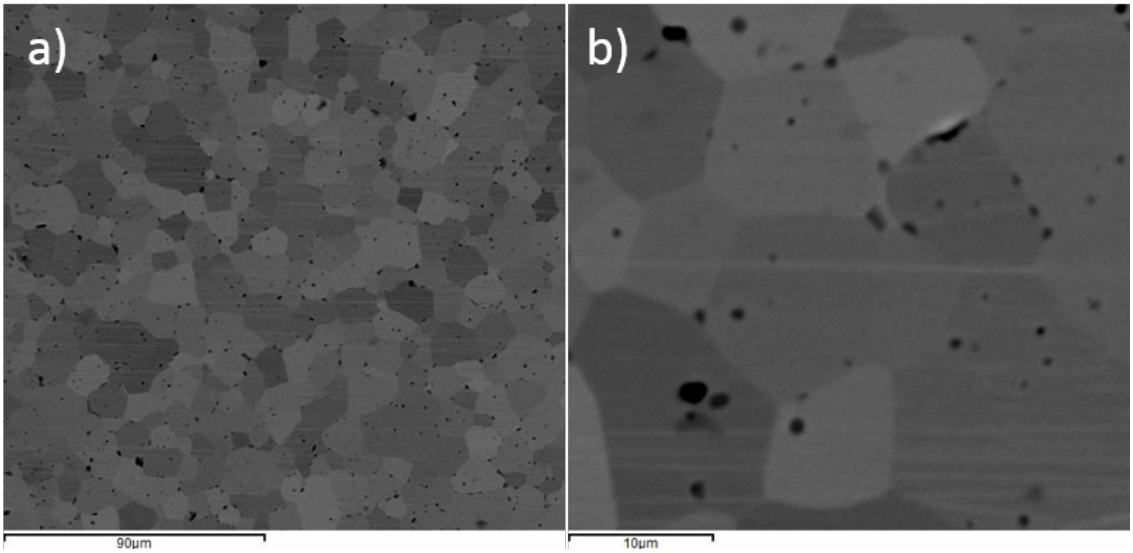


Figure 5.11: BS electron images of $ZrC_{0.55}N_{0.4}$ ceramic pellet, a) low magnification revealing uniform density and grain size, b) higher magnification showing more detailed grain boundaries (line features due to residual scratches)

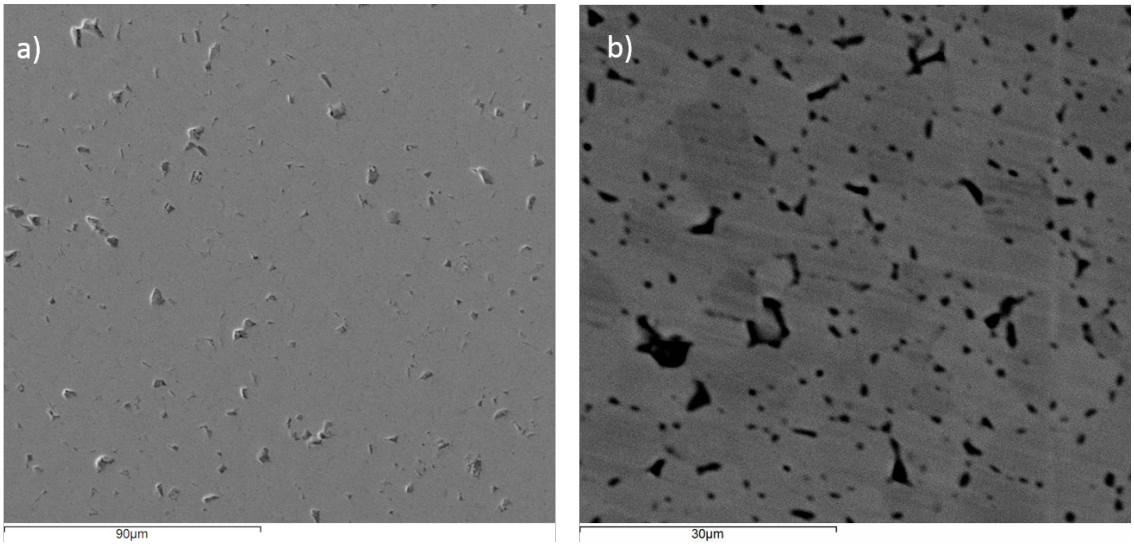


Figure 5.12: SEM images of $ZrC_{0.4}N_{0.55}$, a) SEI revealing surface microstructure, b) BSE image which reveals grains and pore distribution in bulk (line features due to residual scratches)

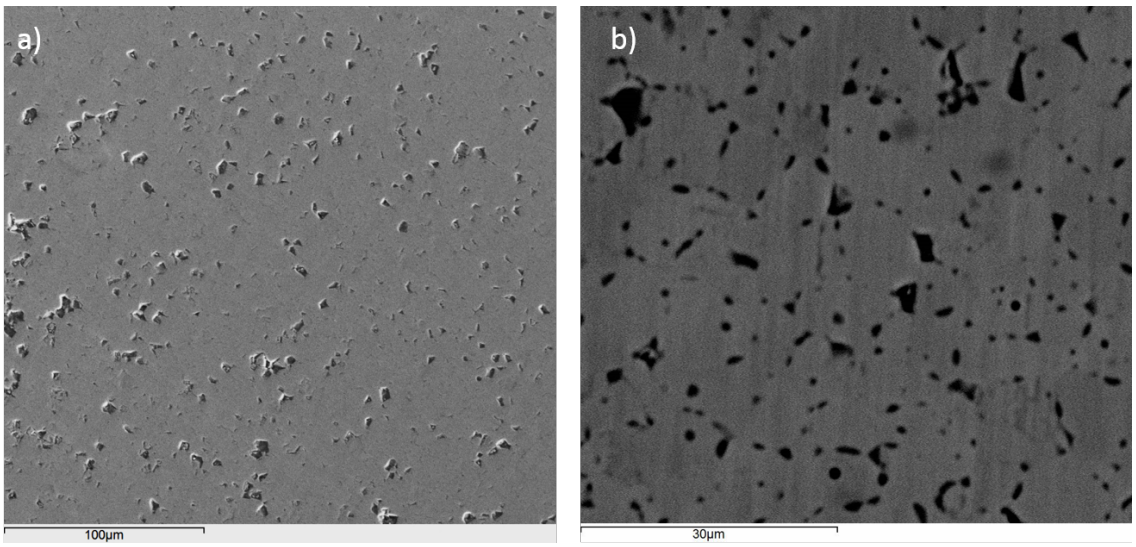


Figure 5.13: SEM images of $ZrC_{0.33}N_{0.6}$, a) SEI revealing surface microstructure, b) BSE image which reveals grains and pore distribution in bulk

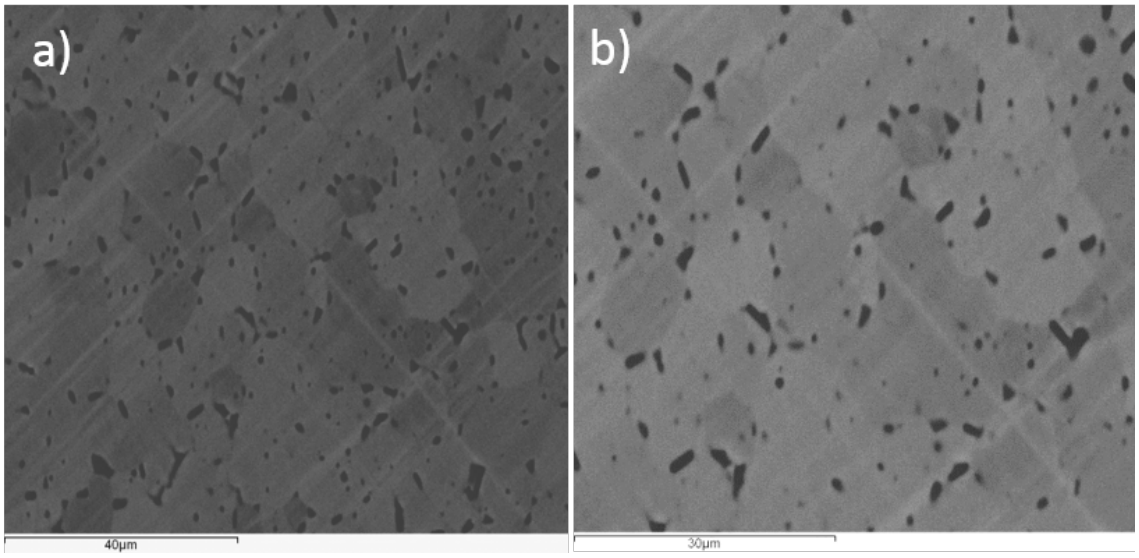


Figure 5.14: BS electron images of $ZrC_{0.12}N_{0.78}$ ceramic pellet, a) BSE image revealing bulk grain sizes, b) BSE image at higher magnification showing more detailed grain boundaries (line features due to residual scratches)

Sample	Stoichiometry	Density / g cm^{-3}	%TD	Grain size / μm	a/ Å	Theoretical density / g cm^{-3}
ZrCN-1	$ZrC_{0.55}N_{0.4}$ [a]	6.90 ±0.01	≤ 99% [c]	10-30 [c]	4.6443	6.87
ZrCN-2	$ZrC_{0.4}N_{0.55}$ [a]	6.80 ±0.01	≤ 95% [c]	∼ 10 [c]	4.6281	6.96
ZrCN-3	$ZrC_{0.33}N_{0.6}$ [a]	6.85 ±0.07	≤ 95% [c]	∼ 10 [c]	4.6189	7.00
ZrCN-4	$ZrC_{0.12}N_{0.78}$ [b]	7.06 ±0.04	≤ 97% [c]	10-30 [c]	4.5971	7.14
ZrCN-4-D	$ZrC_{0.13}N_{0.83}$ [b]	7.15 ±0.10	≃100%	-	4.6026	7.15

Table 5.6: Bulk properties of hot pressed ceramic pellets, [a]- Determined from combustion analysis [b]- Determined from oxidation analysis [c]- Measured by SEM

Figure 5.15a shows the HRTEM of a grain boundary in the $ZrC_{0.12}N_{0.78}$ ceramic revealing no amorphous phase at the boundary. The SAED pattern shown in Figure 5.15b also reveals a crystalline single phase. With no amorphous phase providing evidence for liquid phase formation during sintering both ZrC and ZrN's primary diffusion mechanism will be solid state sintering.

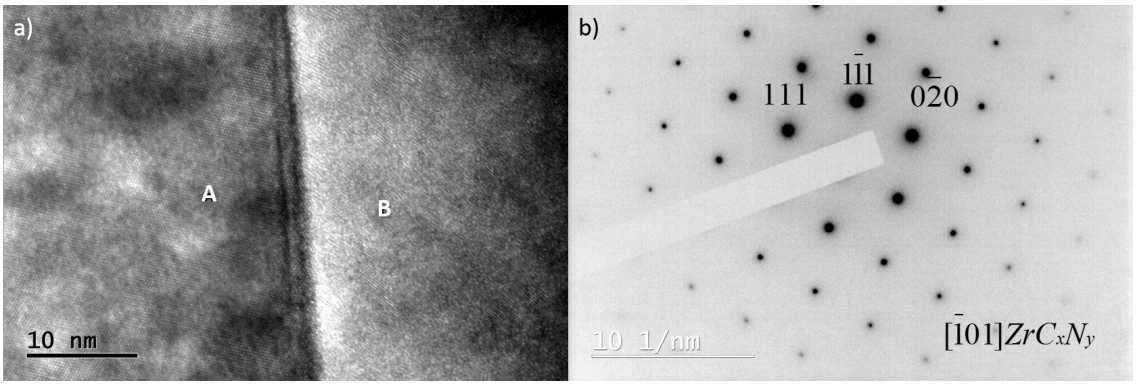


Figure 5.15: a) HRTEM image of grain boundary in $ZrC_{0.12}N_{0.78}$ ceramic showing crystalline lattice fringes in both grains, b) SAED pattern of grain A showing a cubic single phase

5.2 Discussion

SPS and HP of powders yielded higher than 90% dense ceramics for the monolithic and mixed phase powders, with almost theoretically dense ceramics produced for the carbonitrides and monolithic ZrN (Table 5.3, Table 5.4 and Table 5.6). For SPS practical limits of temperature and pressing affected the achievable density of commercial ZrC however the use of identical sintering parameters for all phases allowed for direct comparison between the ceramics. The carbide is more difficult to sinter than ZrN due to stronger covalent bonds. This improved sintering of the carbonitrides could provide a way to achieve high density ZrC-rich ceramics if the effect is observed at low wt% N.[41]

Several authors note the difficulty of sintering carbides and nitrides and propose the need for high heating rates via SPS or sintering additives to achieve densities above 80% TD.[58, 65, 91, 101] In comparison with the densities achieved in this work, monolithic ZrC and ZrN ceramics derived from commercial powders could both be produced $\geq$ 90%TD using either SPS or HP, and the ZrC_xN_y powders achieved higher than 95% TD . Although porosity does reduce some mechanical and thermal properties nuclear fuels have historically been produced with some porosity ($\sim$ 10%) to allow the collection of fission gases and reduce swelling from radiation damage. Currently, no reference value or ideal density of fuel exists for next generation fuel materials. High density will ensure efficient transport of heat to the coolant, however, some porosity will be needed to compensate for the accumulation of fission gases in the material in-pile.

Although SPS and HP achieved similar densities for the ZrN samples a factor that will need to be considered in the large scale manufacturing of nuclear fuel is the processing time. Currently, UO_2 pellets can be batch sintered by pressureless sintering of green bodies, however, using pressure assisted techniques requires much longer times. The advantage of the rapid heating, dwell and cooling times in an SPS sintering program would aid the commercial manufacture of non-oxide fuel materials in the nuclear industry as opposed to the longer times needed with HP'ing. Other considerations to take into account when manufacturing larger pellets and machining smaller pellets would be the amount of fissionable mass allowed per unit volume due to criticality risks and radiotoxic dust production.

Complete solid solutions of the carbonitrides were also observed post sintering, as opposed to the as-reacted powders which were a composite material. The high

temperatures and pressures achieved during sintering would result in the diffusion of carbon and nitrogen. Lattice parameters of the carbonitride solid solution were consistent with Vegards law, with lattice size decreasing linearly with increasing nitrogen content.[58, 65] It is important to note that if the XRD had been performed on the pellet only, then the solid solution may have been mistaken for a close to monolithic phase with a slight deviation from lattice parameter. Account must be taken of changes from powders to dense ceramics in the fabrication of non-oxides via the carbothermic reduction-nitridation route.

6 Thermophysical Characterisation

This chapter describes the thermal and electrical characterisation of the ceramics sintered as described in the previous chapter. The analysis focused on thermal diffusion, heat conductivity, heat capacity and thermal expansion. The experimentally-obtained thermal conductivity of the ZrC and ZrN ceramics derived from commercially-available powders produced by SPS and HP are presented. The thermophysical properties of as-fabricated ZrC_xN_y ceramics presented in the previous chapter are discussed as a function of stoichiometry. The contributions of heat transfer in the ceramics was investigated experimentally by measuring their electrical conductivities allowing the origin and dominant mechanisms of thermal conductivity to be determined.

6.1 Results

6.1.1 Thermal Properties

6.1.1.1 Thermal Diffusivity

Thermal diffusivities of the ceramics were characterised by the laser flash technique as described in section 3.6. Figure 6.1 shows the thermal diffusivity of the ceramics produced from commercially-available ZrC and ZrN by HP and SPS. There is a notable variation with the ZrC samples, however this can be explained as the HP-ZrC-1 sample has around 8 vol% porosity, whereas the HP-ZrC-2 and SPS-ZrC1 have around 4-5 vol% porosity. The ZrN samples have similar thermal diffusivity behaviour up to 1600 K then the 3 samples differ at high temperature. A decrease in thermal diffusion is expected for ceramics at high temperature as phonon conduction decreases due to scattering effects from anharmonic lattice vibrations. However, for non-oxides thermal diffusion can arise from electrical conduction of heat,

as in metals, which increases with increasing temperature and may explain the increased thermal diffusivity of the SPS-ZrN-1 and HP-ZrN-2 samples. The decrease in thermal diffusivity in the HP-ZrN-1 sample may be due to the decreased density or increased impurities such as oxygen or vacancies. The thermal diffusivity of ZrN also shows no change as a function of grain size, with the SPS prepared sample having grains of around 30 μm and the HP samples with grain sizes of around 100 μm, which agrees well with Lee et al.'s [99] observation that grain boundary scattering of phonons is observable in the nanostructure and not the microstructure, meaning that point defects or impurities will have a greater effect on the mean free path of the phonons at lower temperatures.

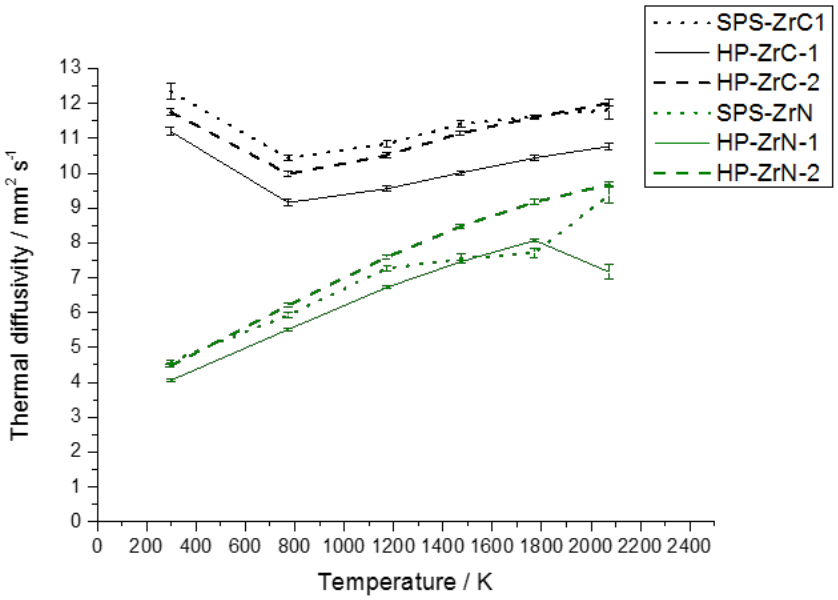


Figure 6.1: Thermal diffusivity of ZrC and ZrN ceramics derived from commercially-available powders by SPS and HP

Thermal diffusivities of the ZrC_xN_y ceramics were all higher than the ceramics prepared from the commercially-available ZrC and ZrN powders and also showed an increase in thermal diffusivity with nitrogen content (Figure 6.2). The decreased thermal diffusivity of the $ZrC_{0.33}N_{0.6}$ sample is due to increased porosity compared to the other carbonitride samples. All of the ZrC_xN_y ceramics show the same trends with a decrease in thermal diffusivity in the 300-800 K range, similar to the ZrC ceramic from commercial powders, then a plateau region up to 1800 K and finally a decrease at higher temperatures.

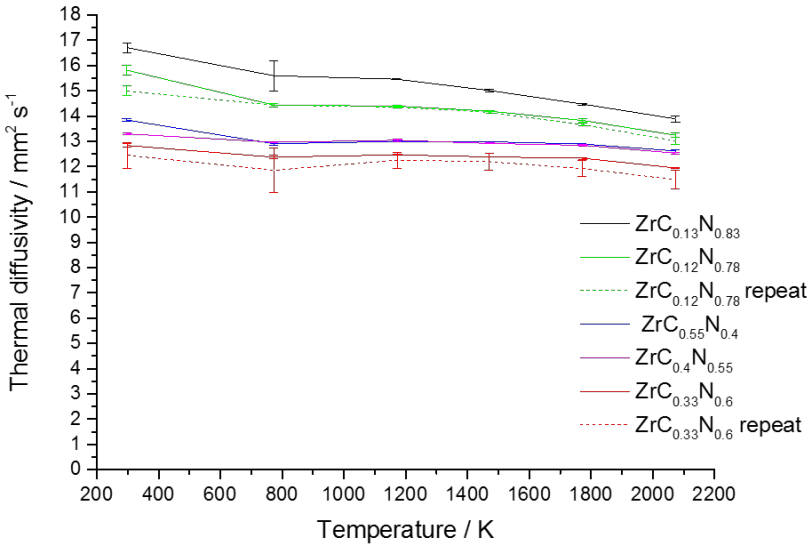


Figure 6.2: Thermal diffusivity as a function of temperature for ZrC_xN_y ceramics

6.1.1.2 Heat Capacity

Heat capacity (C_p) measurements were made on the ceramics using DSC (Figure 6.3), as described in section 3.6. C_p increased with nitrogen content by a small amount as is to be expected as the nitrides weaker bond has a larger amount of energy levels over which to oscillate due to it being less stiff. The experimentally obtained C_p values also match well with the C_p values calculated from NIST values from monolithic ZrC and ZrN using the rules of mixtures (Figure 3.8) with C_p increasing slightly with increase in nitrogen content and are in the range of C_p presented in Figure 2.15, Figure 2.16 and Figure 2.17. However, values calculated from the rule of mixtures show regions where calculated C_p values are lower than monolithic ZrC and ZrN due to the samples stoichiometry not being equal to 1 (ZrC_xN_y, $x+y<1$).

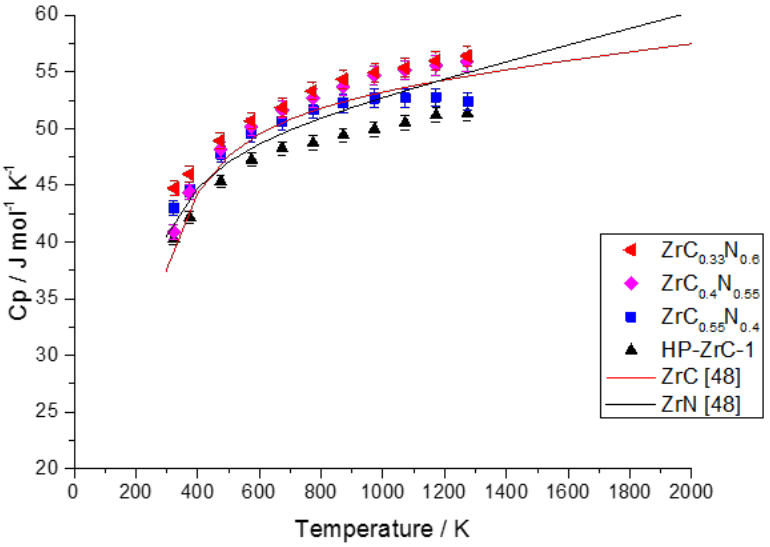


Figure 6.3: Heat capacity as a function of temperature of ZrC ceramic produced from commercially-available powder and ZrC_xN_y ceramics compared to literature values [48]

6.1.1.3 Thermal Expansion

Increase in lattice parameter as a function of temperature (Figure 6.4) was determined using HT-XRD and the linear coefficients of thermal expansion for the materials calculated using Equation 3.6. Figure 6.4 reveals that the increase in lattice parameter to 1273 K for all materials is $\leq$ 0.01 Å, corresponding to the CTEs of the materials all being $\leq 5 \times 10^{-6}K^{-1}$(Figure 6.5), which are lower than the CTE's of 2-8 $\times$ $10^{-6}K^{-1}$ shown in subsubsection 2.2.3.5 over the same temperature range. Change in density of these materials at higher temperature can therefore be considered negligible as the errors associated with the density measurements are far greater than the error associated with change in density. Thermal expansions between inert phases and fissile phases in inert matrix fuels will also have to be close, to avoid stresses generated by thermal expansion mismatch. A lower thermal expansion of the inert matrix compared to the fissile phase may be desirable so as stresses on cooling occur at the fissile-inert interface and not in the inert matrix, which could lead to failure of the inert matrix barrier. However, thermal expansion of uranium and plutonium carbide and nitride materials are higher with UN and PuN having CTEs of 7-9 $\times$ $10^{-6}K^{-1}$ and 10-13 $\times$ $10^{-6}K^{-1}$[149] respectively over the same temperature range

and UC, PuC and mixed carbides in the range of 10-15 $\times$ $10^{-6}K^{-1}$.[7, 150] In this case, a (U, Zr)N fuel material may be the best option to avoid thermal expansion mismatch as their CTE's are closer than the carbides.

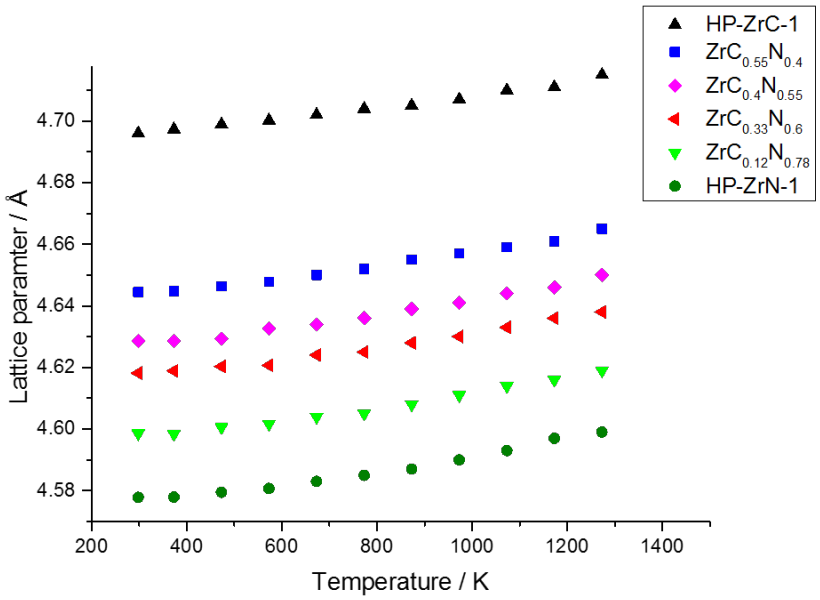


Figure 6.4: Lattice parameter as a function of temperature for ZrC_xN_y ceramics ZrC and ZrN ceramics derived from commercially-available powders

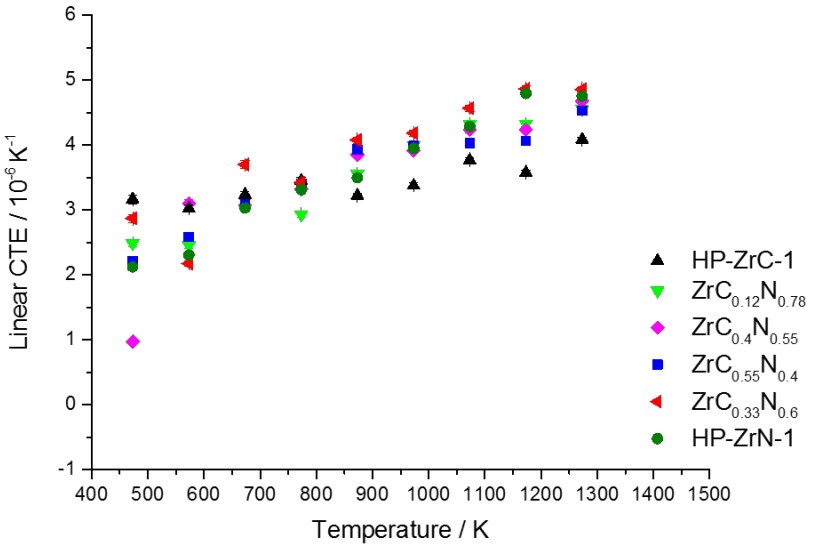


Figure 6.5: Linear CTE's as a function of temperature (L_0 298 K) for ZrC_xN_y ceramics and ZrC and ZrN ceramics derived from commercially-available powders (errors are smaller than symbols)

6.1.1.4 Thermal Conductivity

Thermal conductivities of the ZrC and ZrN pellets matched well with previous work (Figure 2.18 and Figure 2.19) [41, 54, 56, 57, 59, 62]. The increased thermal conductivity of the ZrN ceramics produced from commercially-available powders in this work is probably due to them being fully dense as compared to literature values (Figure 2.19) which report porous samples (7-30 vol% porosity). Thermal conductivities in Figure 6.6 are corrected for samples with 100% TD using density values from Table 5.3 and Table 5.4.

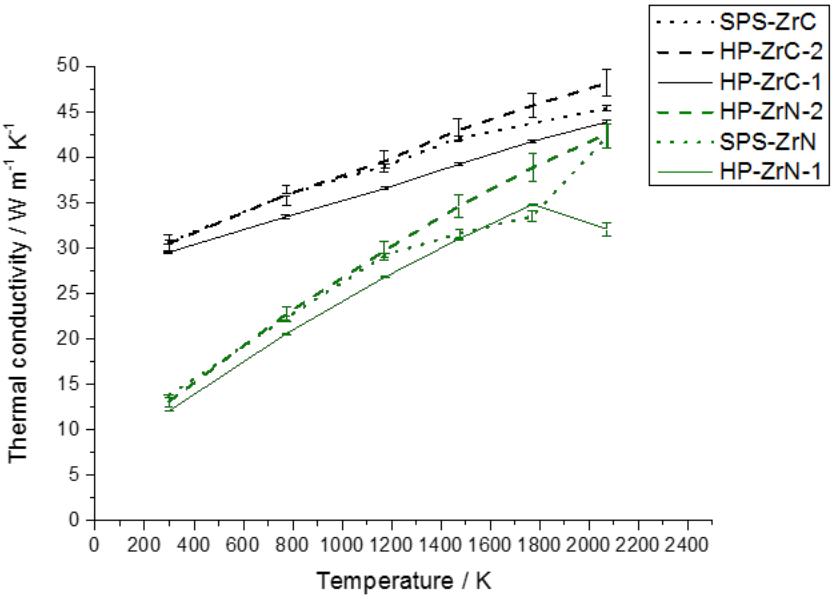


Figure 6.6: Thermal conductivities as a function of temperature of HP and SPS for ceramic samples made from commercially available powders (corrected for porosity using Equation 2.15)

Figure 6.7 reveals a higher thermal conductivity for all ZrC_xN_y phases compared to the ceramics produced using commercial ZrC and ZrN. An increase of around a third can be seen between $ZrC_{0.12}N_{0.78}$ and ZrC, and roughly a 4-fold increase compared with ZrN ceramics produced from commercially-available powders respectively at RT. This difference between the ZrC_xN_y phases and the ZrC ceramics can be attributed to the fact that the thermal conductivity is proportional to density and thermal diffusivity. Heat capacities for the materials are similar, however the ZrC_xN_y phases have a higher thermal diffusivity than the ZrC ceramics produced from commercially-available powders and a density similar to ZrN so that the resultant thermal conductivity data is not a mixture of the two monolithic materials, but higher than them.

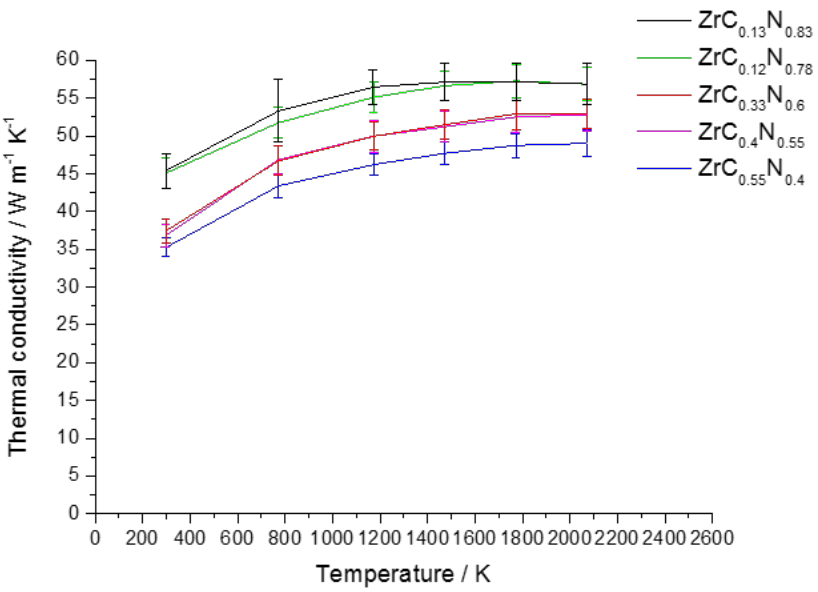


Figure 6.7: Thermal conductivities as a function of temperature of ZrC_xN_y ceramics (corrected for porosity using Equation 2.15)

6.1.2 Electrical Properties

Electrical conductivity was measured using 4-point DC to determine the electronic contribution to the thermal conductivity to fully characterize the mechanism of thermal conductivity in these ceramics. Figure 6.8 shows the electrical conductivity decreases with temperature but increases with increasing nitrogen content, although the ZrN ceramic produced from commercial powder is far lower than the fabricated ZrC_xN_y ceramics. Data for some samples were not obtainable at high temperature as the voltmeter would read non-zero values when there was no current being applied due to high temperature oxidation of samples with higher N contents. The trend of decreasing electrical conductivity with temperature indicates metallic behaviour. Electrical conductivity decreases as scattering from collisions with phonons and other electrons increases. However, the heat transferred by the electrons can also increase as the average velocity of the electrons increases with increasing temperature. The electronic contribution, K_{el} of the total thermal conductivity was calculated using Equation 2.17 and is shown Figure 6.9 showing an increase in the electrical contribution to thermal conductivity with temperature.

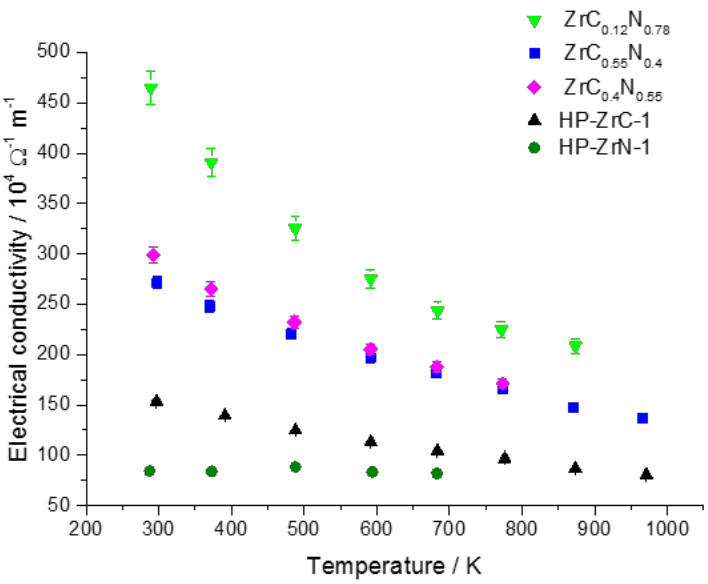


Figure 6.8: Temperature dependence of electrical conductivity of ZrC, ZrN ceramics produced from commercially available powders and ZrC_xN_y ceramics produced from as-fabricated powders

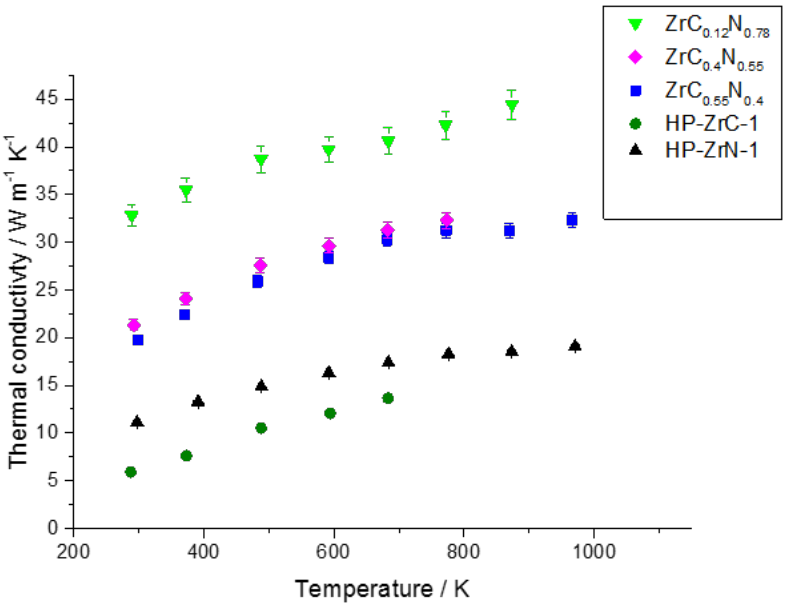


Figure 6.9: Temperature dependence of the electrical contribution to thermal conductivity (K_{el}) of ZrC, ZrN ceramics produced from commercially available powders and ZrC_xN_y ceramics produced from as-fabricated powders

The relationship between the lattice and electronic contributions to thermal conductivity can be realised (using Equation 2.16 to calculate K_{lat}) and is shown in Figure 6.10. The percentage of the thermal conductivity at room temperature that comes from electrical conductivity (Figure 6.10) shows that the dominant mechanism for thermal conduction in samples with higher nitrogen content is via electron heat transfer (K_{el}). Nitrogen's extra electron in its 2p orbital which would occupy an antibonding orbital located above the Fermi energy, leading to increased electrical conductivity and agrees with Lengauer.[41] The reduced electrical contribution to thermal conductivity in the ZrN ceramic produced from commercially-available powders may be due to vacancy concentration as the powder was determined to be more substoichiometric by chemical analysis as compared to the as-fabricated ZrC_xN_y powders (Table 5.1 and Table 5.2). It should be noted that the estimation of K_{el} assumes the Lorenz number and its use in Equation 2.19 is appropriate for use in these materials.

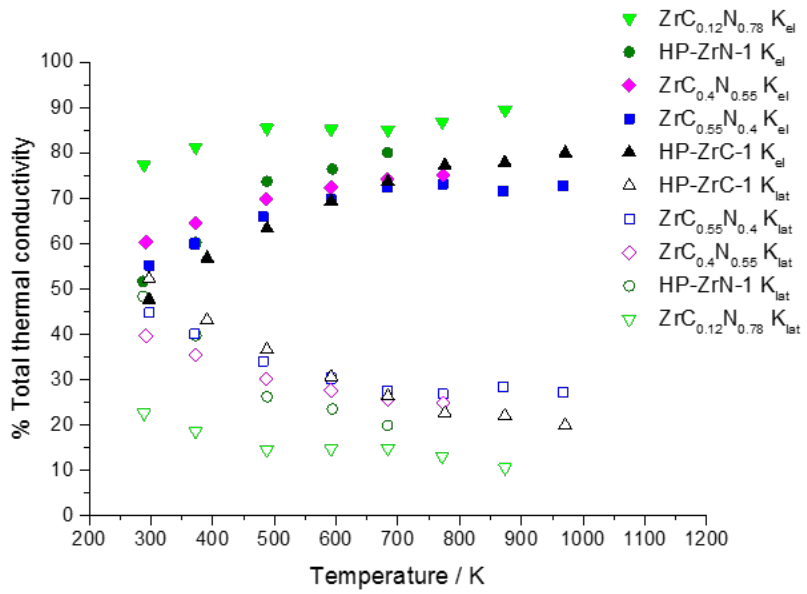


Figure 6.10: Temperature dependence of electrical and phonon contribution to thermal conductivities of ZrC_xN_y ceramics produced from as-fabricated powders

The decrease in lattice contribution to thermal conductivity is as expected for a ceramic material. Lattice vibrational (phonon) energy is another mechanism by which heat transfer can occur in a material. Each lattice vibrates at a quantised energy level and in doing so has a heat capacity, this vibrational energy can then traverse to other lattice vibrational modes at the same energy level and thus conduct heat. At low temperatures the mean free path of phonons is governed mostly by the size of the crystals or point defects, whereas at higher temperatures phonon-phonon scattering governs the mean free path due to anharmonic atomic vibrations. The frequency of vibrations of a linear row of atoms can be described by Equation 6.1, where ω is the frequency, k is the force constant, M is the mass of atoms in a linear chain, q is the wave number and α is the distance the atoms are apart.[142]

$$\omega = 2\sqrt{\frac{k}{M}} \mid sin(q\alpha/2 \mid \tag{6.1}$$

From this equation it can be seen that frequency, and therefore energy of lattice vibrations is proportional to k, which describes the stiffness of the 'spring' in the oscillation, which in this case is the lattice bonds. Thus, lattice vibrations in the carbide will be higher than the nitride due to the increased stiffness of the bond,

arising from the increased bond strength as compared to the nitride. Figure 6.10 shows that as carbon content decreases, lattice thermal conductivity (K_{lat}) decreases as well with the more dominant mechanism shifting to electron conductivity. At RT the electronic contribution of thermal conductivity for ZrC ceramic produced from commercially available powders is around 46% with the remaining 54% arising from lattice conductivity as opposed to the $ZrC_{012}N_{0.78}$ ceramic where around 77% of the total thermal conductivity comes from the electronic contribution.

6.2 Discussion

6.2.1 Thermal Properties

The thermal conductivities of both ZrC and ZrN have been reported in the literature [41, 54, 56, 57, 62–66, 151] (discussed in chapter 2, subsubsection 2.2.3.3) with the majority of work occurring in the 1960's and within the last 5-10 years due to the renewed interest in non-oxide materials as potential materials for nuclear fuel cladding material and inert matrices. With regards to the nitride the vast majority of thermophysical characterisation has been performed on commercially-available powders. Due to the evolution of processing routes, such as HP and SPS the achievable densities have improved the scatter in literature which was due to porosity, however it was found that a larger degree of scatter stems from differences in stoichiometry and purity of the samples. ZrC ceramics produced from commercially-available powders all showed a similar range of thermal conductivity values when corrected to 100% TD consistent with literature values.[62–64] This work has also shown that samples produced from commercially-available ZrN powder have thermal conductivities in the range of 10-38 $Wm^{-1}K^{-1}$ over the temperature range of 298-2073K for near TD samples with varying grain sizes. These results for the commercially-available nitride agree well with the majority of published experimental data (Figure 2.19) with the exception of Basini et al., Adachi et al. and Muta et al.[54, 56–59, 66]. Basini et al.'s [56] results for a 70% TD sample were corrected to the range of 33-36 $Wm^{-1}K^{-1}$ over the same temperature range, however correction of thermal conductivity of a sample with 30% porosity may not be appropriate using the Maxwell-Euken equation. Adachi et al.[66] produced ZrN samples of 82.2% and 91.3% TD by SPS at 1873 K which is around 400 K lower than the sintering temperature used in this work. These values were corrected using the Maxwell-Euken (Equation 2.15) equation and were in the range of 32-45 $Wm^{-1}K^{-1}$ for the 82.2% TD sample and 37-53 $Wm^{-1}K^{-1}$ for the 91.3% TD, still showing disagreement between the two samples after correction for porosity. Muta et al.[58] also measured the thermal conductivity of ZrN ceramics prepared by SPS to be in the range of 34-45 $Wm^{-1}K^{-1}$ between 298-1600 K for samples corrected to 100% TD. These estimates however are lower than the results obtained from the ZrC_xN_y after correction to fully dense samples in this work which have a thermal conductivity of 35-45 $Wm^{-1}K^{-1}$ at room temperature. With the increasing trend of thermal conductivity with increasing nitrogen

content observed in this work it would be expected that for pure ZrN samples the thermal conductivity would be even higher, in the region of ∼45-50 $Wm^{-1}K^{-1}$ at room temperature.

Another cause of scatter in the thermal conductivity values in the literature could arise from stoichiometries and purity of the powders which are rarely reported. The chemical analyses performed on the crushed ceramics in this work showed a non-negligible amount of oxygen in the samples, with wt% of oxygen in the samples (Table 5.5) from $\sim 2-5$ at% O. The increase in oxygen wt% is also observed with the increase in reaction time of the samples is likely due to the purity of the gas used during the reaction or may be due to contamination from the alumina crucible or mulite in the tube furnace. Samples with higher nitrogen content are also theoretically susceptible to oxidation arising from the weaker Zr-N bond as compared to ZrC, so as nitrogen content increases in the ceramic the probability of oxidation during crushing for chemical analysis increases. Values of thermal conductivity would be negatively affected if oxygen content arises during processing due to the increased scattering of both phonons and electrons. Vacancy defects also cause scattering of electron and phonons, resulting in decreased thermal conductivity. ZrC_xN_y phases presented in this work all contain a non-stoichiometric phase, whereby $x + y < 1$, this may also have a negative effect on the thermal conductivities of the samples and may explain the reason for the $ZrC_{0.33}N_{0.6}$ only showing a small increase in thermal conductivity as compared to the $ZrC_{0.4}N_{0.55}$ sample (Figure 6.7). Adachi et al.[65] attributed the decreased thermal conductivity of the samples to porosity and nitrogen content reporting a stoichiometry of $ZrN_{0.935}$, although chemical analysis was determined by EDS. Thermal conductivity of non-stoichiometric ZrN has not been reported in the literature, probably due to the difficulty in fabricating samples with only N vacancies with no carbon or oxygen impurities. Fabrication of non-stoichiometric ZrN is mainly achieved by chemical or vapour deposition techniques or sputtering.[152–155] The effect of substoichiometry on the thermal properties of ZrC has been studied however, showing a steep drop in thermal conductivity with increased vacancy concentration (Figure 6.11).[71, 156, 157]

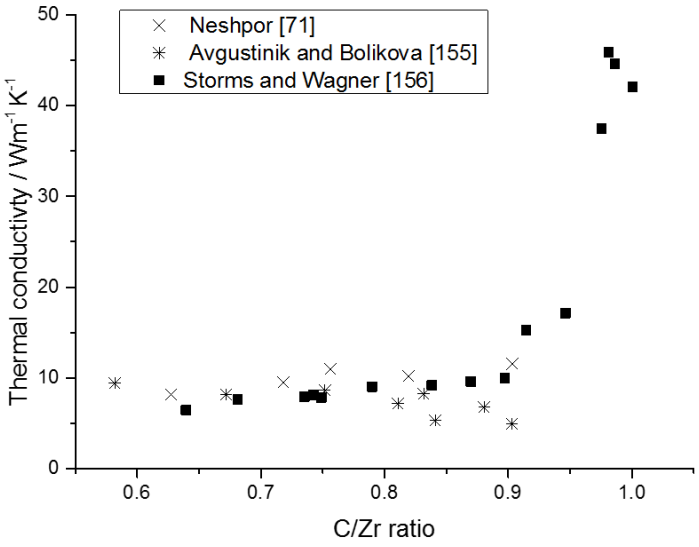


Figure 6.11: Thermal conductivity as a function of stoichiometry for ZrC [71, 156, 157]

In the case of ZrC there is a strong relationship between substoichiometry and thermal conductivity with values falling to around 10 $Wm^{-1}K^{-1}$ for samples of $ZrC_{0.9}$ with further reduction of carbon content causing no further significant degradation in thermal conductivity. Increasing vacancy concentration in these interstitial carbides and nitrides would cause increased scattering of both phonons and electrons meaning that ZrN may show a similar effect to ZrC_x manifesting as a large decrease in thermal conductivity at around $ZrN_{0.9}$. The chemical analyses results obtained for commercial ZrN samples in this work showed a nitrogen content of around $ZrN_{0.82}$ (Table 5.2) agreed well with the majority of thermal conductivity data in the literature,[54, 56, 57] meaning the poor thermal properties of ZrN ceramics produced from commercially-available powders may be due to it being substoichiometric .

6.2.2 Electrical properties

Electrical conductivity values of ZrC and ZrN ceramics made from commercially-available powders and the ZrC_xN_y ceramics derived from as-fabricated powders were assessed, to determine the contribution of electrical conduction to thermal conduct-

ivity. The results indicate a poor electrical conductivity of the ZrN ceramic made from commercial powder with a constant value of 80 $\times$ 10^4 $\Omega^{-1}m^{-1}$ across a temperature range of 298-700 K. However, the results for the ZrC ceramic made from commercially-available powder were higher, with a room temperature electrical conductivity of 150 $\times$ 10^4 Ω^{-1}m^{-1}, decreasing to around 80 $\times$ 10^4 $\Omega^{-1}m^{-1}$at 973 K, matching well with literature values.[62, 71] Few values of electrical conductivity have been reported for ZrN in the open literature. Adachi et al.[66] reported the electrical conductivity of commercially-available samples to be 200 $\times$ 10^4 $\Omega^{-1}m^{-1}$for their 82.3% dense samples and 240 $\times$ 10^4 $\Omega^{-1}m^{-1}$ for the 91.3% dense sample at room temperature. These values were corrected to 100% TD using the Maxwell-Euken equation, estimating an electrical conductivity of 300 $\times$ 10^4 $\Omega^{-1}m^{-1}$ decreasing to 150 10^4 $\Omega^{-1}m^{-1}$over the temperature range 298-100 K. Samples in the present work showed that increasing nitrogen content increased thermal conductivity, reaching a maximum of 450 $\times$ 10^4 $\Omega^{-1}m^{-1}$for $ZrC_{0.12}N_{0.78}$ at room temperature, decreasing to around 200 $\times$ 10^4 $\Omega^{-1}m^{-1}$ at 873 K. The values are in good agreement with those estimated by Samsanov [72], but lower than those measured by Petrova et al. [74] (Figure 2.21) who reported stoichiometric samples of $ZrN_{0.97-1.00}$. The decrease may be due to the samples still containing carbon, or the presence of vacancies. The results for the carbonitrides were also in good agreement with Lengauer et al. [60] whose results showed an increase in room temperature electrical conductivity with nitrogen content to around 450 $\times$ 10^4 $\Omega^{-1}m^{-1}$for a sample with [C]/[C+N] ratio of 0.11, which matches well with the [C]/[C+N] ratio of $ZrC_{0.12}N_{0.78}$. It can also be seen from Figure 6.8 that the samples RT electrical conductivity increase relatively with nitrogen content as the $ZrC_{0.55}N_{0.4}$ and the $ZrC_{0.4}N_{0.55}$ samples are roughly double the ZrC ceramic produced from commercially-available powder.

The low values of electrical conductivity of ZrN made from commercially-available powders may again be due to the vacancy content of the material, causing scattering of electrons. However, as with thermal conductivity, no data exists for the relationship of electrical conductivity of ZrN_x as a function of x. ZrC_x has been shown to have a strong relationship between C/Zr ratio and electrical conductivity, similar to the thermal conductivity, with a large drop off in electrical conductivity at low vacancy concentrations and then little effect with increasing vacancy concentration, shown in Figure 6.12.[71, 72, 157] Again if ZrN has a similar relationship, then the samples of $ZrN_{0.82}$ made from commercial powders measured in this work would agree well with this trend.

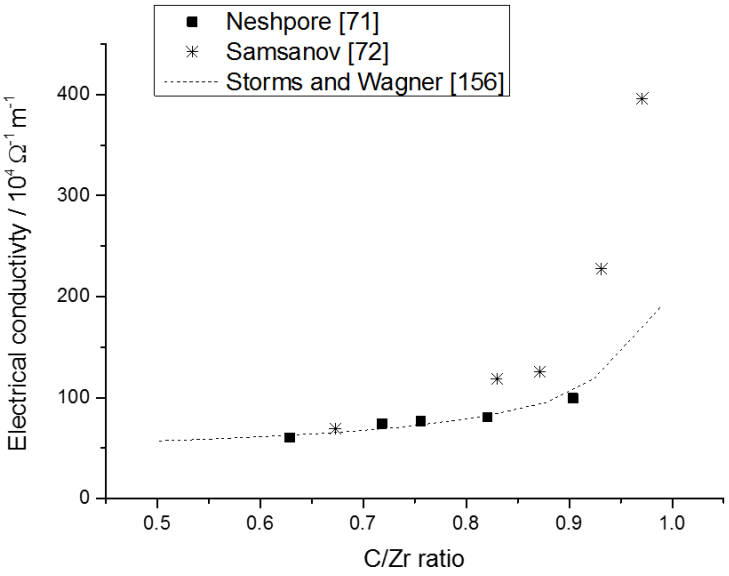


Figure 6.12: Room temperature electrical conductivity of ZrC as a function of C/Zr ratio[71, 72, 157]

Andrievskii et al. [126] also characterised the electrical conductivity of $ZrC_{0.7}$ and $ZrC_{0.94}$ samples finding that the $ZrC_{0.7}$ sample had an electrical conductivity around 3 times lower than that of the $ZrC_{0.94}$ sample.

6.3 Outlook

Thermal conductivity is a crucial property to consider in the selection of next generation materials for use as fuel cladding or inert matrix materials. This work has assessed and characterised the effect of stoichiometry and purity from the commercially favoured carbothermal reduction-nitridation process on the thermal and electrical properties of ZrC_xN_y ceramics as a function of stoichiometry. These results have also been compared these to results from ceramics of ZrC and ZrN made from commercially-available powders.

Zirconium carbide and nitride have both been evaluated in several recent reports, however, scatter in the data from the less studied ZrN system has lead to the reviews finding the carbide to be superior to the nitride in terms of thermal conductivity, with some reports quoting the room temperature values of ZrN as low as 10 $Wm^{-1}K^{-1}$.[15, 158] However, this work has shown that thermal conductivity increases with nitrogen content to values around 4 times higher than ZrC. These values all satisfy the suggested minimum thermal conductivity values reported by Meyer at al.[12], however, an inert matrix with a higher thermal conductivity would increase efficiency of heat transfer to the coolant and increase the overall thermal conductivity of the fissile phases which have lower thermal conductivities than ZrN (see Table 2.3). IMFs using nitrides (such as (U,Zr)N) may also be a better choice than carbide based IMFs due to ZrN having a similar CTE to the actinide nitrides,[7, 149, 150] therefore avoiding stresses during reactor operation due to thermal expansion mismatch.

7 Oxidation Behaviour

Oxidation behaviour of ZrN will be important especially in accident scenarios such as a loss of coolant accident (LOCA). Preliminary results from the oxidation study of bulk ZrN samples are presented in this chapter. Rate kinetics of the oxidation reaction were studied and oxide scale characterisation performed to develop an understanding oxidation mechanism. Oxidation of ZrC was not performed in this study due to it being well reported in the literature.[67, 93, 114–116]

7.1 Results

7.1.1 Oxidation Behaviour and Kinetics

HT-XRD detected onset of oxidation around 773 K with monoclinic ZrO_2 peaks becoming visible (Figure 7.1). No tetragonal or cubic oxide polymorph was observed for the powders oxidised to 1023 K, although this would be expected as these are both high temperature polymorphs. However, this is not consistent with results from Krusin-Elbaum and Wittmer [111] and a reason may be that the authors used glancing angle XRD which is more sensitive in the detection of thin layers. The chamber window of the furnace used also reduces the chance of seeing a minor phase with a low intensity as this will cause scattering of X-rays.

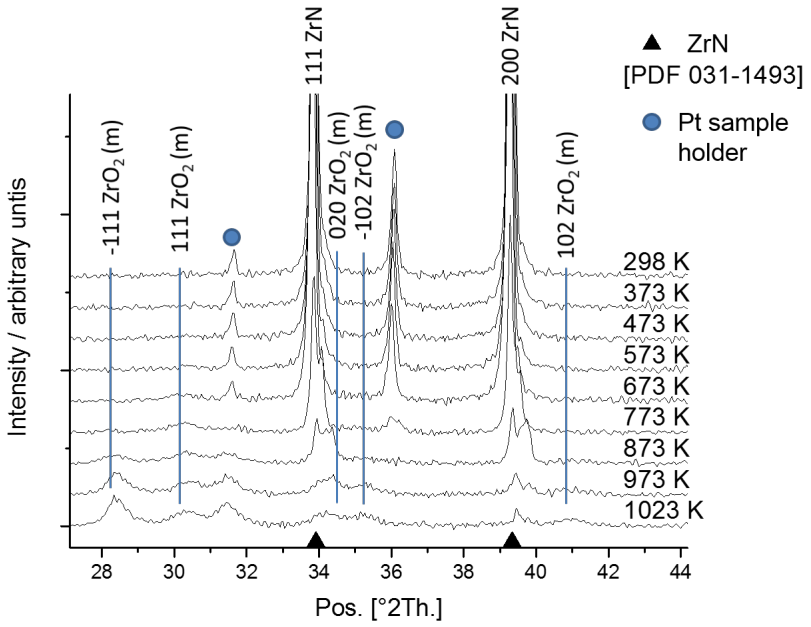


Figure 7.1: HT-XRD of ZrN powder with scans at every 100 K to 1023 K under static air indexed using PDF 001-075 [133] and PDF 031-1493 [137]

An excerpt of the (200)ZrN reflection is shown in Figure 7.2 which reveals the destabilisation of the ZrN peak with temperature. It can be seen that initially the position of the peak shifts to lower 2θ which corresponds to thermal expansion, up until 673 K beyond which point the peak shifts to higher 2θ indicating a decrease in lattice size. It can also be seen that the peak splits into two main components indicative of a two-or multi-phase system. A decrease in lattice size could be attributed to the removal of nitrogen from the lattice, as the interstitial sites that were previously occupied by nitrogen are now empty and the lattice can contract. Incorporation of oxygen into the ZrN lattice could also cause a decrease in lattice size as oxygen is more electronegative than nitrogen so the Zr-O bond would be shorter. This trend would be observed as long as only a ZrO_xN_{1-x} phase exists as once the stoichiometry ≥ 1 then the lattice would begin to expand. Gendre et al. [145] showed that lattice size of the cubic ZrC lattice decreased with increasing oxygen content up to a stoichiometry of $ZrC_{0.79}O_{0.13}$. Beyond this content of oxygen a second ZrO_2 phase was observed. Both of these mechanisms are consistent with the observation that the reflections contain two major components, indicating either;

formation of substoichiometric ZrN_{1-x} phases on top of the bulk ZrN or more likely a ZrO_xN_{1-x} at the ZrN_{1-x} particle surface.

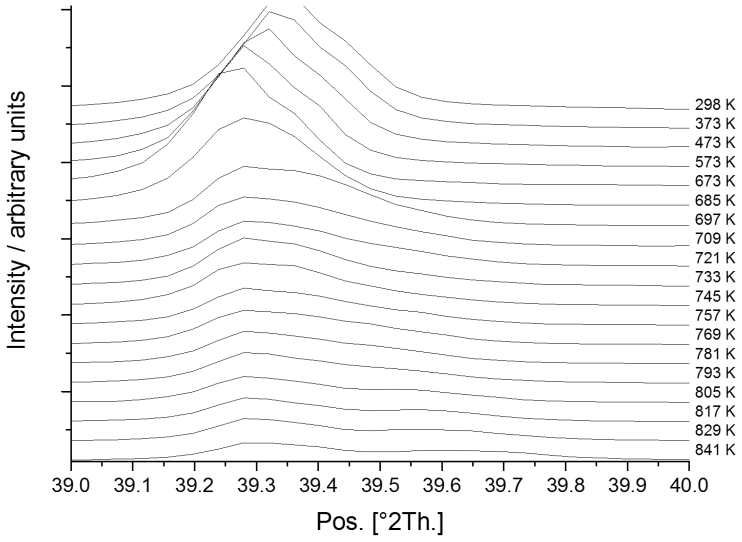


Figure 7.2: Excerpt of HT-XRD showing destabilisation of ZrN with temperature

A typical TGA-DTA result of the oxidation of the dense ceramic samples is shown in Figure 7.3, revealing the onset of oxidation around 763 K which agrees well with the HT-XRD measurements showing oxide peak formation at 773 K (Figure 7.1). The rapid gain of mass at the onset temperature of 763 K is consistent with the gain of oxygen initially and suggests the peak splitting in Figure 7.2 is due to formation of oxynitride phases not ZrN_{1-x} phases.

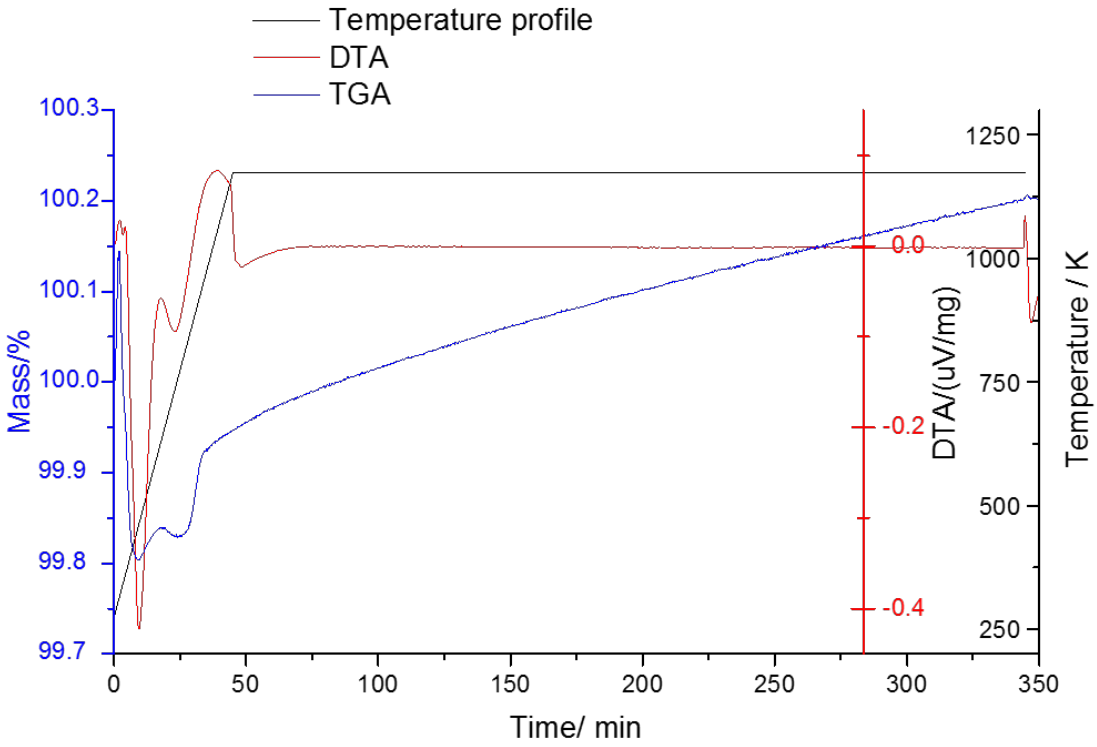


Figure 7.3: TGA-DTA results of isothermal oxidation of ZrN sample at 1173 K

The change in weight of the samples normalised for surface area as a function of time for each oxidation temperature is shown in Figure 7.4. It can be seen that the samples oxidised at 973 and 1073 K underwent more oxidation than the samples at 1173 and 1273 K indicating a change in oxidation mechanism between the lower and higher oxidation temperatures. The sample oxidised at 1373 K for 5 h showed the highest gain in weight after normalisation for surface area. From Figure 7.4 it can also be seen that the curves show parabolic rate behaviour with samples having R^2 values $\leq$0.99 according to a plot of Equation 3.12, except for the sample oxidised at 1273 K for 5 h which did fit well with linear kinetics. Plotting the square of the change in weight normalised for surface area against time (Figure 7.5) revealed a good fit according to Equation 3.13 with each fit having an R^2 value $\geq$0.99, except for the sample oxidised at 1273 K for 5 h which fit better with a linear kinetics (R^2 value of 0.9947 in Figure 7.4). Observation of parabolic rate behaviours is consistent with oxygen diffusion through the advancing oxide scale becoming the rate limiting step and agrees with Krusin-Elbaum and Wittmer [111] and Panjan et al. [112]

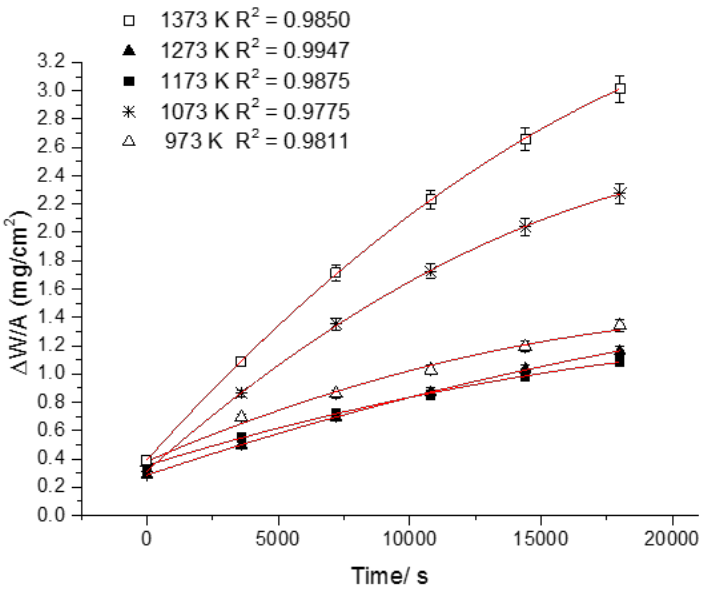


Figure 7.4: Change in mass (ΔW) per unit surface area (A) as a function of time for each oxidation temperature

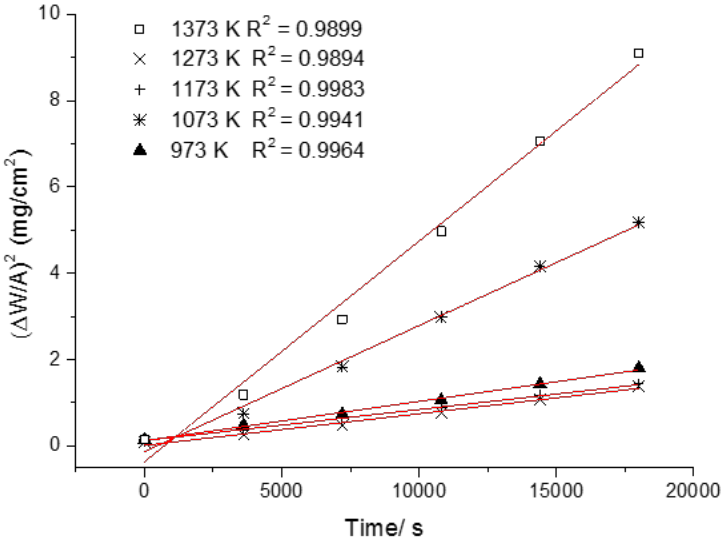


Figure 7.5: Square of the change in mass per unit surface area as a function of time for each oxidation temperature

The rate constants, k_p calculated using Equation 3.13 are shown in Figure 7.6 which, as Figure 7.4 displays a rapid increase in the rate between 973 and 1073 K. This is followed by a large decrease in rate of oxidation at 1173 K and then no significant change for the sample oxidised at 1273 K, after which there is around a 10 fold increase in the rate of oxidation for the sample oxidised at 1373 K for 5 h.

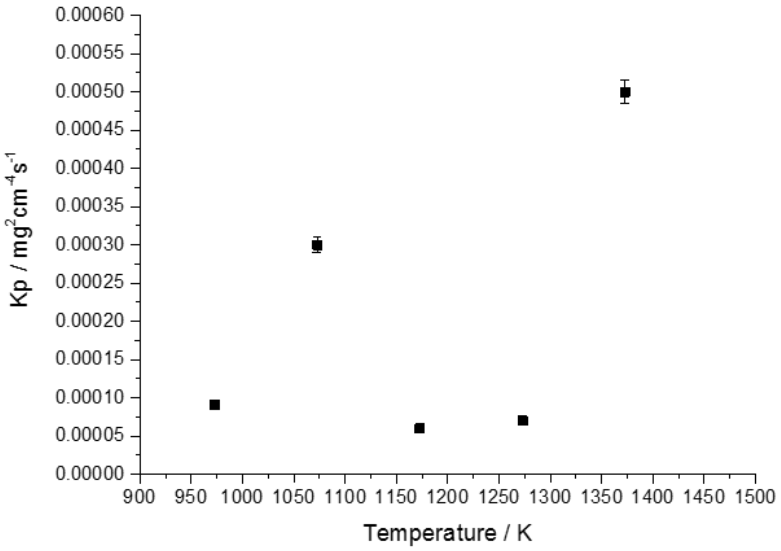


Figure 7.6: Parabolic rate constants (k_p) as a function of temperature

7.1.2 Oxidation Layer Characterisation

The sample oxidised at 973 K for 5 h showed a very brittle, porous white coloured outer layer that spalled off and was visible in the TGA crucible as loose powder. The SEI of the cross section of this sample is shown in Figure 7.7a and shows a very fragmented, cracked outer layer that was determined to be zirconium oxide by EDS analysis. Figure 7.7b shows the grains near the surface of the bulk have been revealed which may be due to either oxygen diffusion along the grain boundaries or intergranular stresses imposed by the advancing oxide layer.

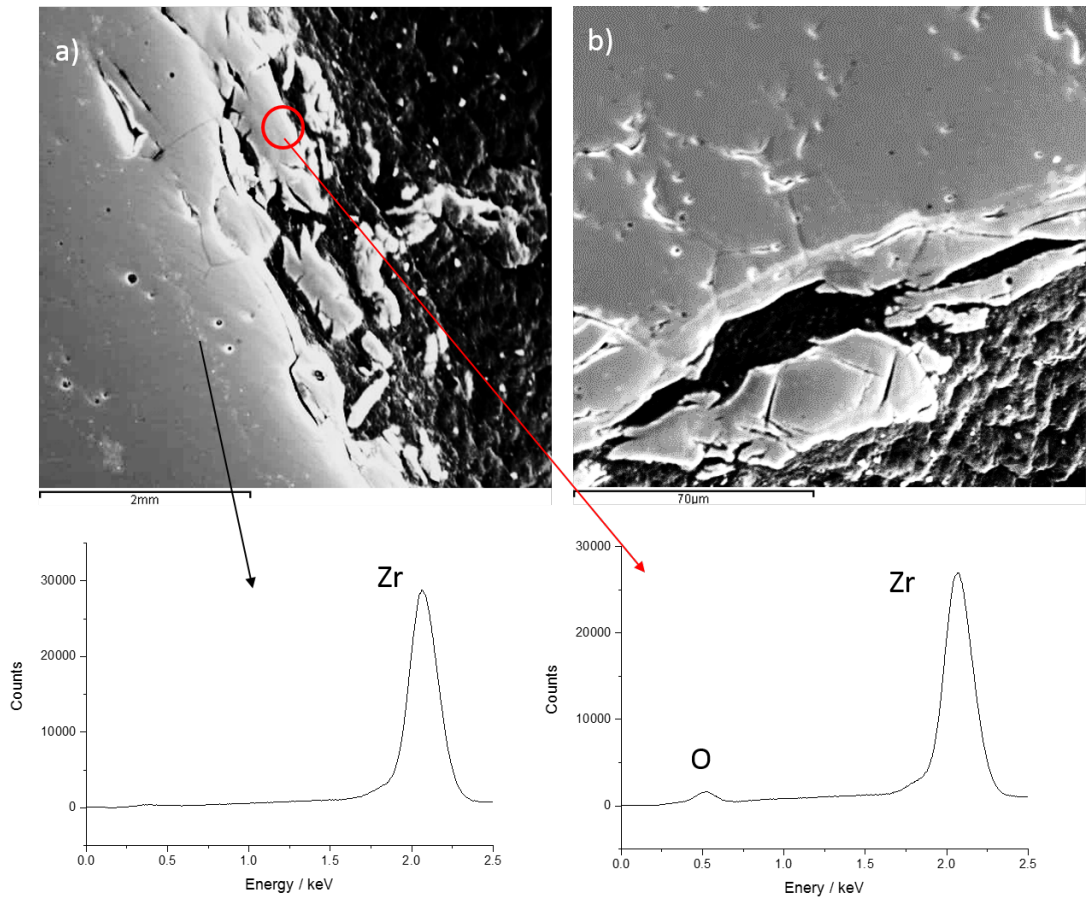


Figure 7.7: SEIs of oxide layer of ZrN sample heated to 973 K for 5 h, a) shows fragmented oxide layer, b) shows grains revealed near to oxide layer

Figure 7.8 shows the oxide layer of the ZrN sample oxidised at 1073 K, again the outer layer (circled in Figure 7.8b) was determined to be oxide by EDX analysis. A cracked and porous layer is observed in both Figure 7.8a and b. Cracks in the bulk of the sample can be observed in Figure 7.8a and from the SEI it appears the layer consists of mixed phases, with a large variance in contrast in the layer. The cracks in Figure 7.8a may arise during the isothermal oxidation from stresses on the bulk grains from oxidation or due to stresses associated with the molar volume change from ZrN to ZrO_2. Cracking may also occur on cooling is a higher temperature ZrO_2 polymorph is formed during oxidation the associated transformations from either cubic or tetragonal to monoclinic would result in a volume change.

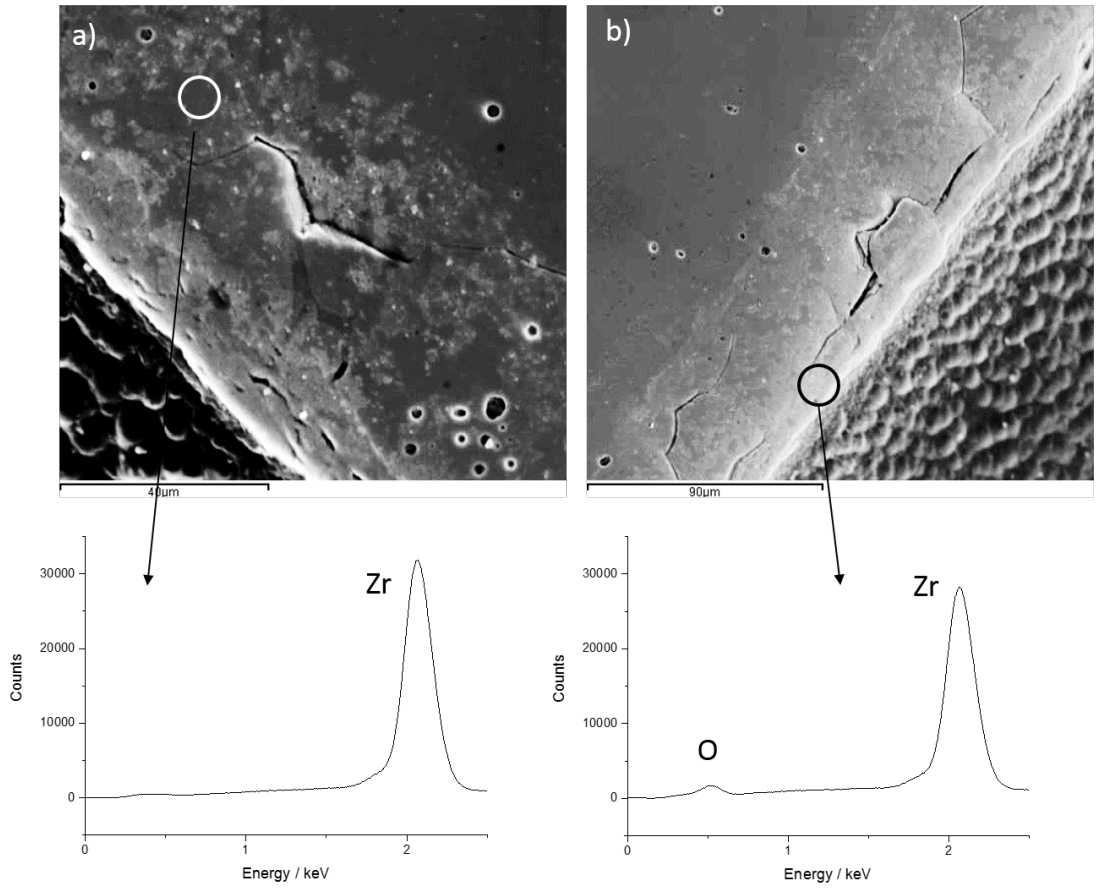


Figure 7.8: SEIs of oxide layer of ZrN sample heated to 1073 K for 5 h, a) shows cracks present in bulk ZrN, b) shows cracks in oxide layer

As observed in Figure 7.5 and Figure 7.6 the rate of oxidation of the sample oxidised at 1173 K was significantly lower than at 973 and 1073 K. This can also be observed in Figure 7.9, as the oxide layer is thinner ($\sim$15 μm) than the oxide layer seen in Figure 7.8 ($\sim$40 μm). It can also be seen from Figure 7.9 that the oxide layer is dense and there are large numbers of cracks in the outer oxide layer. No powder was observed in the crucibles after oxidation indicating a adhesive oxide layer. A thin ($\leq$1 μm) layer between the outer layer and the bulk is also seen. EDS of the area shown in Figure 7.9b revealed no oxygen or nitrogen. In Figure 7.9a a region can be seen where this intermediate layer breaks and the outer layer has advanced further into the bulk. From both SEIs of the sample in Figure 7.9 no grains are visible in the ZrN bulk unlike the other two samples at 973 and 1073 K suggesting either stresses on the ZrN grains have been relieved, or oxygen diffusion into the bulk via grain boundary diffusion has been slowed.

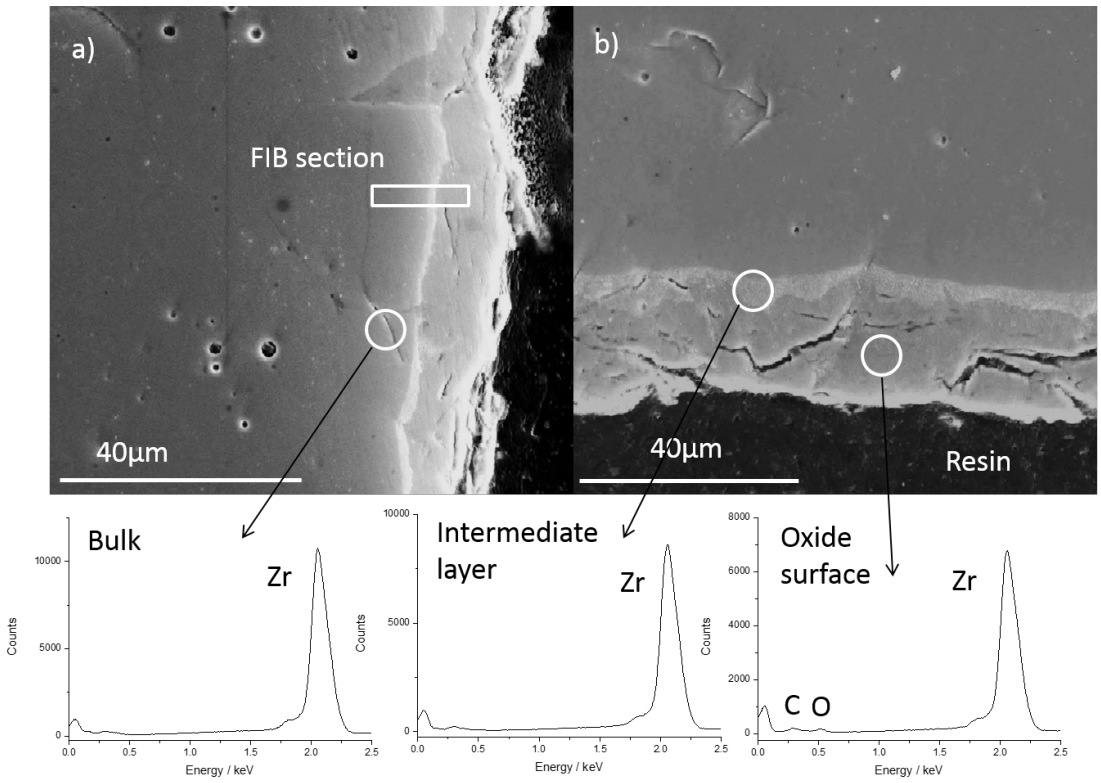


Figure 7.9: SEIs of oxide layer of ZrN sample heated to 1173 K for 5 h, a) shows region of where intermediate layer is penetrated by oxide scale (rectangle shows FIB section) b) shows cracks in the oxide layer

Similar to Figure 7.9 (1173 K 5 h) the SEIs of the sample oxidised at 1273 K reveal a dense outer layer of oxide shown in Figure 7.10 that contains larger number of cracks. However in this sample no intermediate layer is observed and grains in the bulk of the ZrN sample are clearly visible which may indicate higher intergranular stresses in the bulk or increased rate of oxygen diffusion via grain boundaries compared to oxidation at 1173 K for 5 h (Figure 7.9).

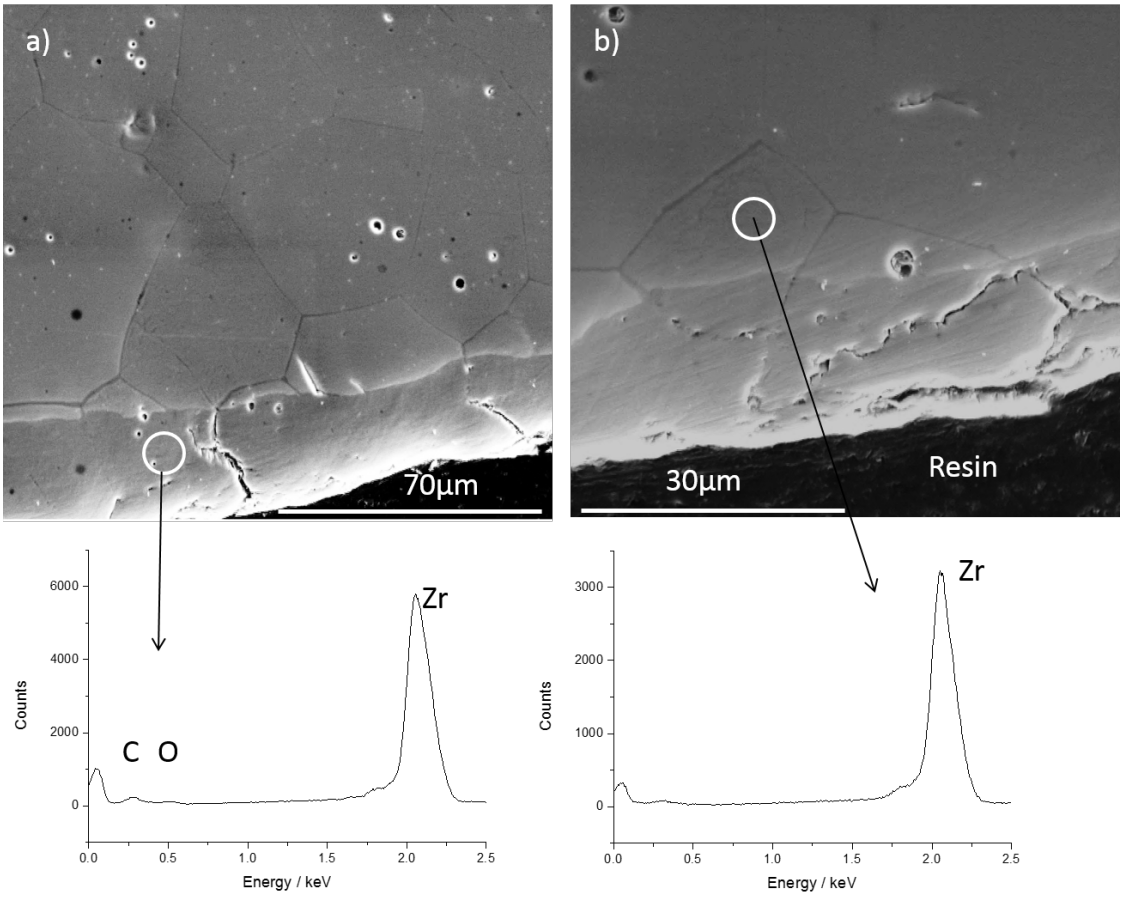


Figure 7.10: SEIs of oxide layer of ZrN sample heated to 1273 K for 5 h, a) shows region where grains revealed deep into bulk, b) shows cracks in oxide scale and region of EDS from grain in the bulk

SEIs of the sample oxidised at 1373 K for 5 h showed extensive grain boundary oxidation of the ZrN grains, shown in Figure 7.11. Although oxygen diffusion will be limited through the dense oxide scales observed for the samples oxidised at 1173 and 1273 K for 5 h, the diffusion rate will increase with temperature. At this higher temperature of 1373 K the protective nature of the dense oxide scale begins to fail and increased grain boundary oxidation can be seen in Figure 7.11a and b compared to the little amount of oxidation of the grain boundaries in the sample oxidised at 1273 K for 5 h (Figure 7.10a and b). The oxide scale of the sample oxidised at 1373 K for 5 h also showed large numbers of cracks and was brittle, spalling away on handling of the sample, which can be seen from the fragments in Figure 7.11a and b. XRD of the sample after oxidation shown in Figure 7.12 reveals monoclinic ZrO_2

and ZrN. This spalling of the oxide scale would also reduce the diffusion length of oxygen into the bulk, resulting in increased oxidation.

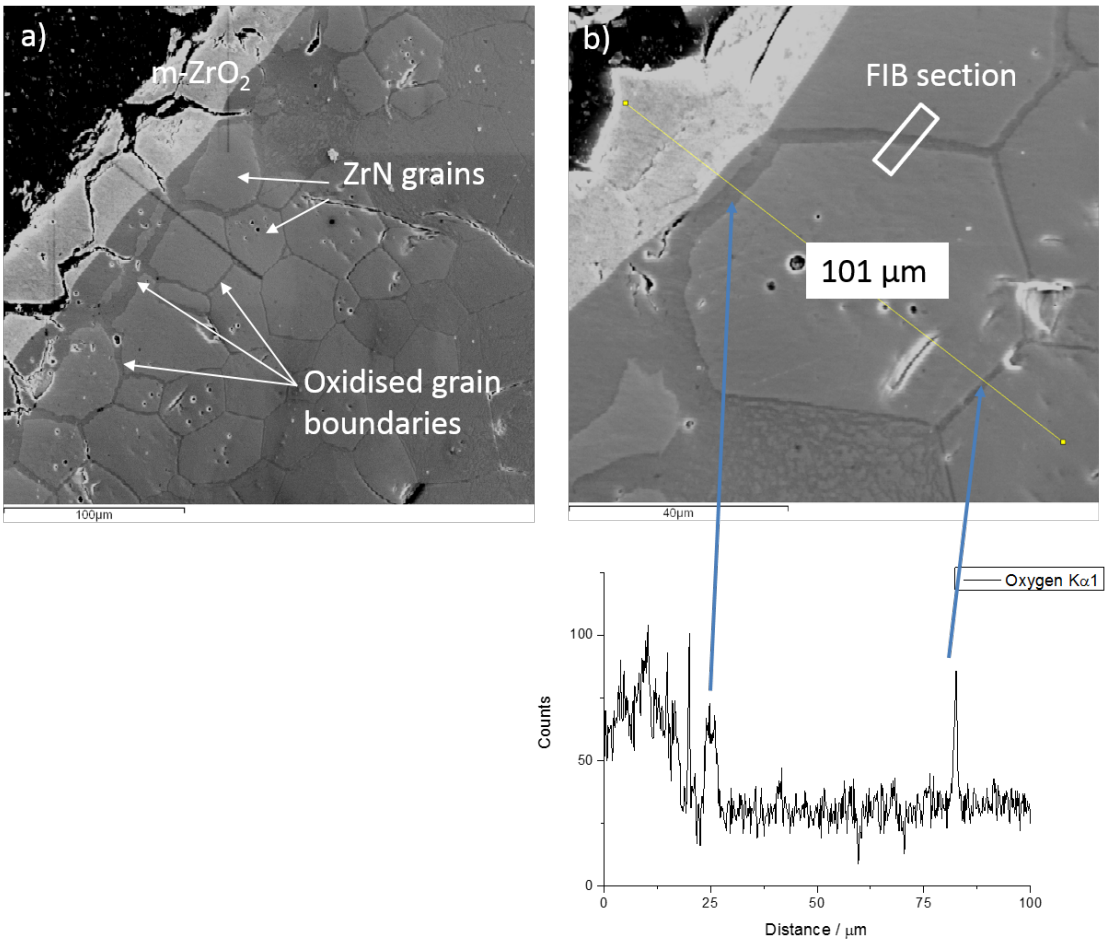


Figure 7.11: SEIs of oxide layer of ZrN sample heated to 1373 K for 5 h, a) shows depth of oxidation of grain boundaries into the ZrN bulk, b) shows ZrN grain close to oxide scale with oxygen content in grain boundaries (area shown in rectangle represents FIB section)

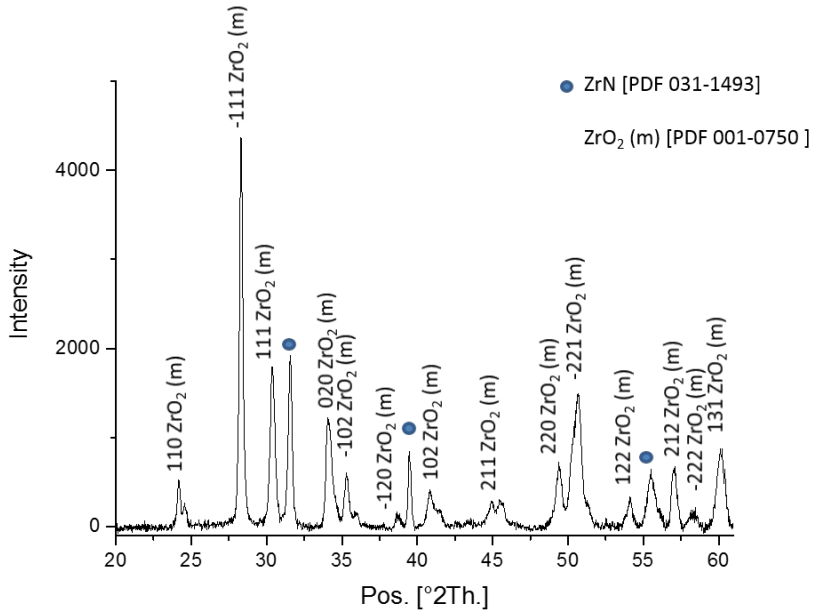


Figure 7.12: XRD of ZrN sample oxidised at 1373 K for 5 h revealing ZrN and monoclinic ZrO_2 [133, 137]

BF-TEM of the sample oxidised at 1173 K is shown in Figure 7.13. Figure 7.13a shows the FIB section of the sample which was made of the intermediate layer seen in Figure 7.9a and b. The SADP of the bulk ZrN grain is shown in Figure 7.13b and shows a cubic material that indexed well with the [100]ZrN zone axis. The lattice parameter calculated from the SADP in Figure 7.13b of 4.400 ± 0.088 Å however is smaller than the literature value of ZrN of 4.597 Å[137]. The decrease in lattice parameter may be again due to nitrogen removal from the lattice or incorporation of oxygen and is consistent with the HT-XRD results (Figure 7.2). The SADP of the intermediate layer (Figure 7.13c) indexed well with ZrO_2 and had a calculated lattice size of 4.877 ± 0.098 Å. Distinguishing between tetragonal and cubic ZrO_2 can be difficult due to similar lattice dimensions in the a and b directions. However, the SADP in Figure 7.13d indexed well with the [103]c-ZrO_2 zone axis as the ratio of the (311)/(002) d-spacings (1.678 ± 0.034) matches well with the cubic pattern (1.658) as opposed to the ratio of 1.728 in the tetragonal [103]t-ZrO_2 zone axis. The lattice parameter calculated from Figure 7.13d was determined to be 4.938 ± 0.99 Å, which, although similar to the lattice parameter calculated from the SADP in

Figure 7.13c is lower than the literature value of 5.090 Å of c-ZrO_2.[135] The decrease in lattice size may arise from oxygen vacancies and/or nitrogen impurities creating oxygen vacancies. Forbidden reflections were observed in both SADPs (Figure 7.13c and d) and are generally attributed to superlattice reflections, which are present because the material is ordered in such a way that reduces the symmetry of the lattice.

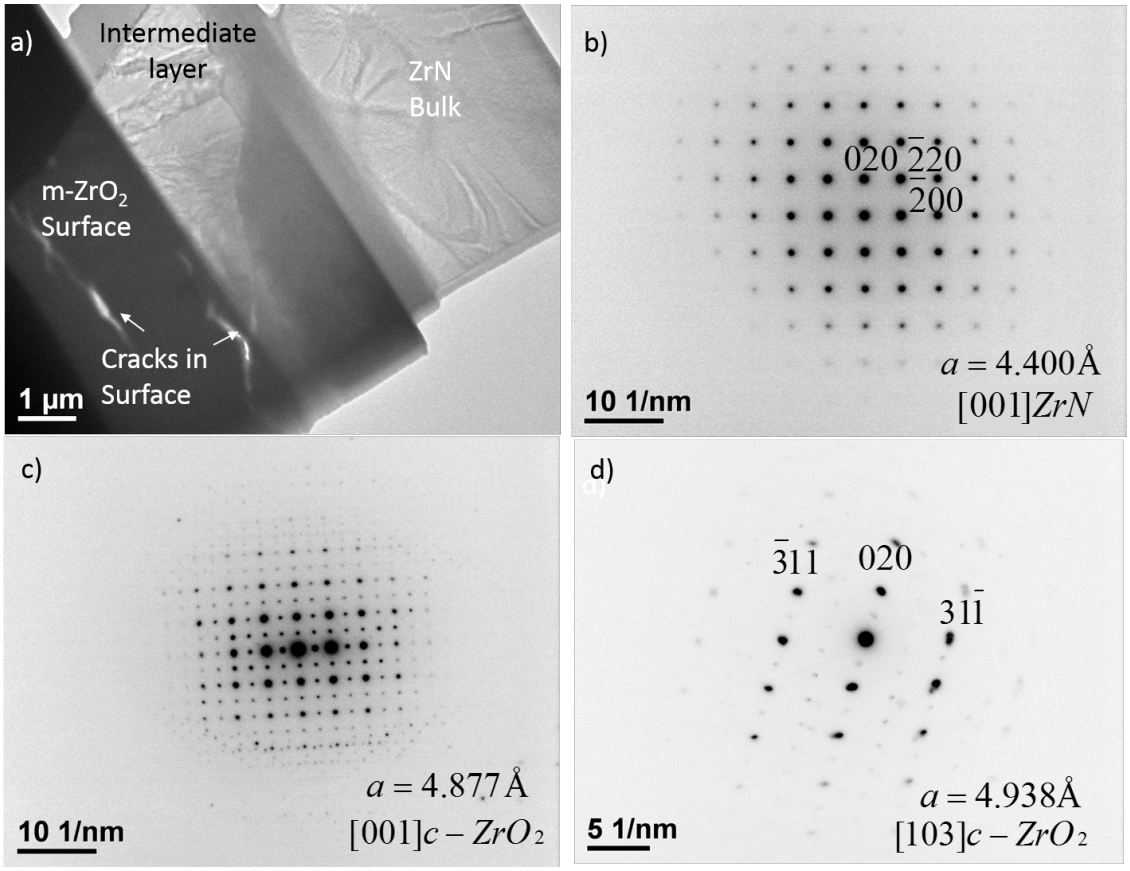


Figure 7.13: a) TEM image of FIB section (area represented by rectangle in Figure 7.9a), taken from intermediate layer of sample oxidised at 1173 K for 5 h, b) [001]ZrN SADP of bulk region, c and d) [001] and [103] c-ZrO_2 SADP patterns of intermediate layer grains

The BF-TEM image in Figure 7.14a reveals a FIB section of a grain boundary from the sample oxidised at 1373 K for 5 h (shown in Figure 7.11). It can be seen the material between the ZrN grains consists of sub-micron grains which were indexed as the [1$\bar{1}$1]c-ZrO_2 zone axis similar to the intermediate layer observed in Figure 7.9 and Figure 7.13 and had a calculated lattice parameter of 4.850 ± 0.097 Å. Forbidden reflections are seen again in Figure 7.14b indicating an ordered structure. Cracking

can also be observed in Figure 7.14a which would lead to the generation of channels and pores which would allow further ingress of oxygen.

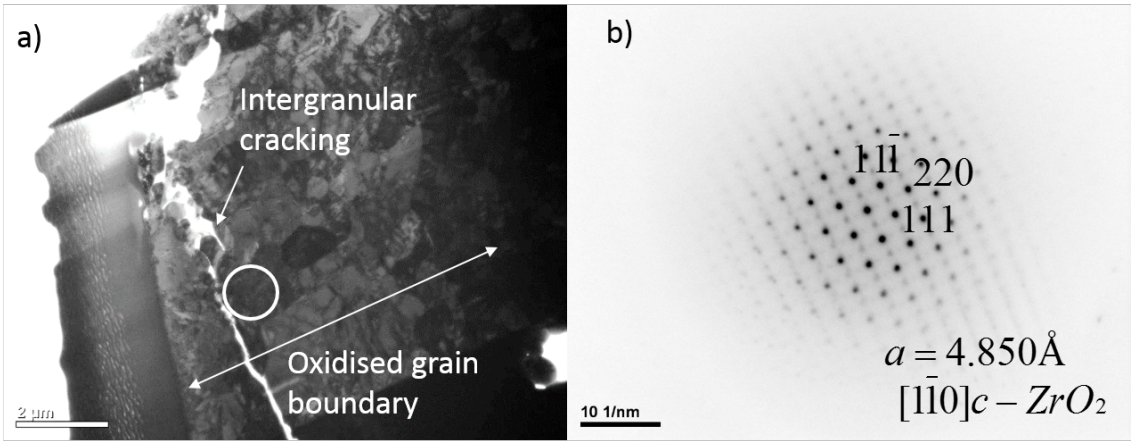


Figure 7.14: a) BF-TEM image of FIB section (area represented by rectangle in Figure 7.11b) taken from grain boundary of sample oxidised at 1373 K for 5 h, b) $[1\bar{1}0]$c-ZrO_2 SADP of area indicated by circle

Three oxynitride polymorphs have been reported by Gilles et al.[159]: Zr_2ON_2, $Zr_7O_8N_4$ and $Zr_7O_{11}N_2$ which are designated γ, β and β' respectively shown in the ternary phase diagram in Figure 7.15. The β and β' have rhombohedral superstructures of the fluorite structure and the γ-phase has the cubic bixbyite structure.[160] Similar forbidden reflections and stabilisation of a c-ZrO_2 similar phase by the addition of ZrN were made by Van Tendeloo and Thomas.[161] The authors state that the vacancies introduced by replacing oxygen with nitrogen ordered along one of the three fold axes lowering the symmetry of a rhombohedral β-phase, which is closely related to the cubic fluorite structure thus allowing the forbidden reflections. Although the SADPs indexed with c-ZrO_2 in this work, a similar distortion of the β or β' phase (resulting in a similar cubic fluorite structure) may be occurring in this work similar to that reported by Van Tendeloo and Thomas. [161]

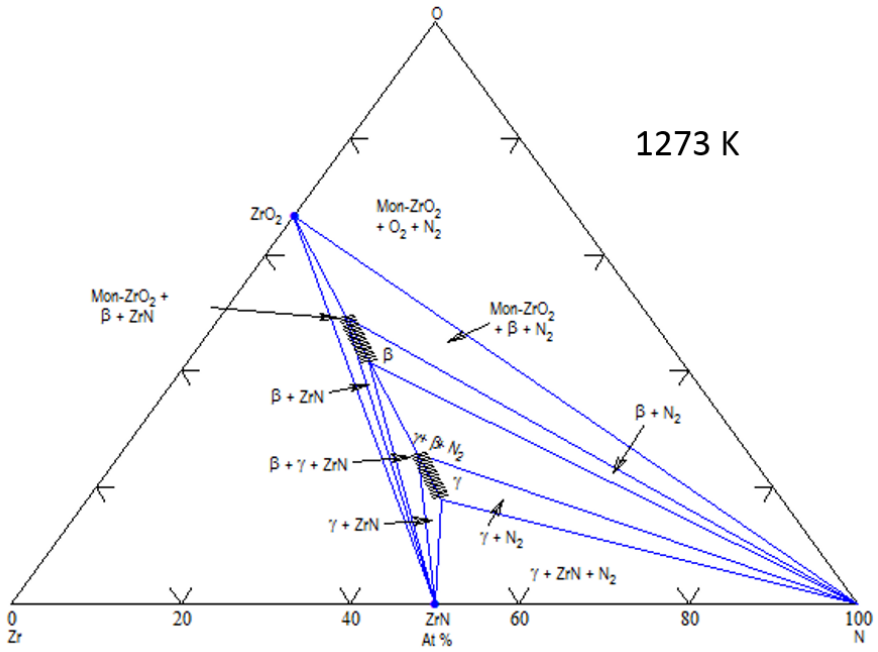


Figure 7.15: Phase diagram for the Zr-N-O system at 1273 K [159]

7.2 Discussion

The observed decrease in rate of oxidation between 1073 and 1173 K along with the difference in morphology of the oxidation layer cross sections (e.g.Figure 7.8 compared to Figure 7.9) suggest the mechanism of oxidation changes with temperature. At temperatures up to 1073 K a porous oxidation layer forms, readily allowing oxygen diffusion through pores and voids and nitrogen (or NO_x species) diffusion out of the sample. The increase in oxidation rate (Figure 7.6) is consistent with the porous microstructure of the oxide layers (Figure 7.7 and Figure 7.8). At oxidation temperatures of 1173 K and 1273 K a dense intermediate oxide layer forms which inhibits the diffusion of oxygen and therefore the rate of oxidation. This dense layer is revealed to be c-ZrO_2 by TEM analysis of the intermediate layer (Figure 7.13). As the sample cools the oxide layer transforms to the monoclinic polymorph creating the cracks present in the dense ZrO_2 phase at the surface (Figure 7.9 and Figure 7.10) due to the volume change associated with the phase transformation. This would mean the protective nature of this oxide layer may last at prolonged oxidation times, however, not against thermal cycling, where cracks will form creating channels for oxygen diffusion. At the higher temperatures of 1273 K grain boundaries in the bulk have become visible (Figure 7.10) indicative of early stages of oxidation and at 1373 K the SEIs reveal extensive grain boundary oxidation of the sample (Figure 7.11). This failure of the protective dense layer can be attributed to the increased diffusion of oxygen at higher temperatures.

Shimada and Ishi [114] describe a change in mechanism of oxidation of ZrC with increasing temperature. At higher temperatures ($\geq$743 K) small sub-micron c-ZrO_2 crystals nucleate from the amorphous ZrO_2 + C layer and this forms a compact dense layer which becomes the rate determining step for oxygen diffusion. However, at longer oxidation times the small crystallites grow and the volume expansion causes intergranular fracture providing paths for oxygen diffusion in and CO_2 diffusion out. Berkowitz-Mattuck [162] observed that oxidation of ZrC at $\leq$1470 K resulted in porous m-ZrO_2 which fractured due to intergranular oxidation. However, above 1470 K a denser ZrO_2 layer formed, slowing diffusion of oxygen to the bulk, attributed to sintering effects on the oxide layer. From the observation of a thin ($\leq$1 μm) c-ZrO_2 layer in the ZrN samples in this work (Figure 7.9) and small grains ($\leq 1\mu$m) observed by TEM (Figure 7.13) a similar rate limiting step can be expected for ZrN. The observations of denser outer layers of ZrO_2 between the samples oxidised

at 973 and 1073 K (Figure 7.7 and Figure 7.8) and those oxidised at 1173 and 1273 K (Figure 7.9 and Figure 7.10) agree well with observation by Berkowitz-Mattuck [162] and a sintering step may be occurring resulting in this dense, partially protective layer. The formation of dense scales of ZrO_2 have been proposed to provide effective oxidation resistance in ZrB_2-SiC [163] and ZrC-SiC [164] composites.

Two proposed mechanisms for the low temperature ($\leq$1073 K) and higher temperature ($\geq$1173 K) oxidation of ZrN in this work are given in Figure 7.16. The oxidation mechanism at temperatures $\leq$1073 K can be described in several steps, initially oxygen diffusion through the surface ZrN grain boundaries results in a ZrO_xN_y phase which then forms m-ZrO_2. Stresses from the m-ZrO_2 grains between the ZrN grains results in intergranular fracture and the creation of a porous oxide layer as observed in Figure 7.7, similar to the observation by Berkowitz-Mattuck.[162] Figure 7.8 also reveals lighter regions in the bulk of the ZrN which correspond to oxygen rich area's formed from ingress of oxygen via pores and channels from intergranular fracture. Oxidation of ZrN at higher temperatures, however, proceeds by the formation of a high temperature c-ZrO_2 polymorph comprised of submicron grains. This high temperature polymorph is stabilised by the substitution of oxygen with nitrogen forming oxygen vacancies. As the oxidation of ZrN is exothermic (Figure 7.3), it can be envisaged the local temperature at the interface is higher than the oxidation temperature and gives rise to sintering of the small c-ZrO_2 crystals, however this local increase in temperature cannot be estimated. This dense oxide layer inhibits oxygen's ingress and therefore rate of oxidation. However, from Figure 7.10, grains close to the surface/oxide layer are becoming visible indicative of oxygen diffusion via grain boundary diffusion and at the higher oxidation temperature of 1373 K (Figure 7.11) extensive oxidation of the ZrN grains is observed indicating this protective layer fails as diffusion rates increase. It is envisaged at higher oxidation temperatures and times that the rate of oxidation will increase as the c-ZrO_2 crystallites grow and exert intergranular stresses causing channels to form between grain boundaries which is observed in Figure 7.14 as intergranular cracking, allowing further ingress of oxygen. This c-ZrO_2 polymorph transforms to monoclinic at regions near the surface where nitrogen content is lower or at lower temperatures resulting in the cracks present in the oxide layers in Figure 7.9 and Figure 7.10 which are due to the associated volume change.

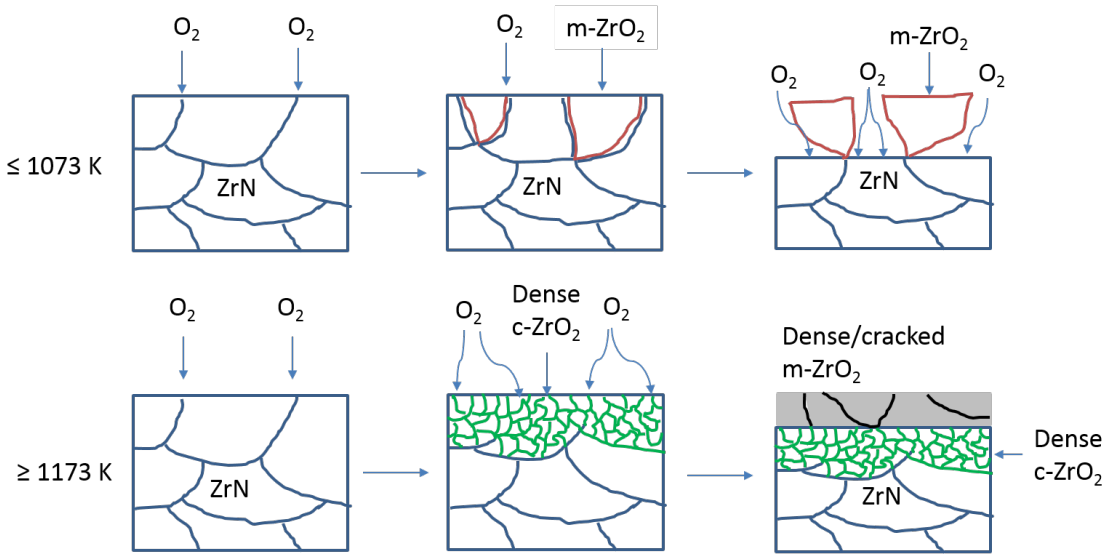


Figure 7.16: Schematic diagram of proposed mechanisms of oxidation of ZrN at low and higher temperatures

8 Conclusions and Further Work

The processing route and fabrication of ZrN from ZrO_2 using the established carbothermal reduction-nitridation technique has been studied with the focus largely on the nitridation step of ZrC_x compositions. The rate of nitridation was increased with increasing dwell times and dwell temperatures of the nitridation reaction. However, even after long reaction times (24 h) all samples still contained carbon impurities and preliminary analysis of nitridation progress as a function of time indicates a reduction in rate with reaction time although a more comprehensive study of rate kinetics study is needed. Mechanistic studies presented in chapter 4 combined results from XRD, SEM and TEM and showed the nitridation of the ZrC powders occurs in two steps. Initially carbon is removed from the ZrC lattice by reaction with $H_{2(g)}$, resulting in the formation of the $HCN_{(g)}$ reactive species as reported previously [30] (step 1 in Figure 4.25). Increasing carbon content of the ZrC_x composition also resulted in an increased rate of nitridation which is attributed to the formation of a higher amounts of reactive $HCN_{(g)}$ species. Nucleation of a nitrogen-containing species then occurs by either condensation of $HCN_{(g)}$ with $Zr_{(g)}$ formed via the removal of C from the Zr lattice, or more likely the condensation of $HCN_{(g)}$ at a Zr-rich (C-deficient) region of the starting ZrC particle (step 2 in Figure 4.25). XRD of nitrided powders all showed a mixed phase containing two main components corresponding to a ZrC-rich and ZrN-rich phases. Annealing experiments in vacuum of the mixed phases showed formation of a solid solution was rapid ($\leq$ 1h, 1873 K), indicating during the nitridation reaction there is little to no mixing of the phases.

The kinetics and rate of reaction require a more detailed study by a comprehensive rate study using TGA/DTA with evolved gas analysis to further confirm the mechanism proposed in this work. The process used in this work was able to produce high N content ZrC_xN_y samples, however, complete carbon removal was not achieved in reasonable times ($\leq$ 24 h) and a kinetic study would contribute to the evaluation of the process route to give a best practice process. The work in this thesis also aimed to study the fabrication of ZrN from ZrO_2 as a simulant system for UN or PuN sys-

tems and the experimental parameters and studies performed in this work should be applied to those actinide systems. Kinetic studies of the carbothermic reduction-nitridation of uranium and plutonium oxides have been performed [30–32] but an experimental assessment of the powders during the reaction is still lacking and the use of high resolution SEM and TEM techniques used in this thesis and other works [36, 38] should be performed to greater understand the role of the morphology of the powders during the reaction as to further develop mechanisms for actinide nitride fabrication using the carbothermic reduction-nitridation route.

SPS and HP densification techniques were used in the production of ceramic samples from commercially-available ZrC and ZrN powders and the as-fabricated ZrC_xN_y powders as discussed in chapter 5. Both sintering techniques achieved high densification of the commercial powders, $\geq$90% TD, however the carbide sintered poorly compared to the nitride in both techniques. The increased densification of the nitride over the carbide can be attributed to the increased diffusion coefficent of nitrogen allowing increased mass transport during the sintering step. XRD analysis of the mixed ZrC_xN_y showed the samples had formed highly crystalline solid solutions during sintering and calculated lattice parameters obeyed Vegards law. ZrC_xN_y samples all showed better densification compared to commercially-available ZrC powders showing the nitrogen content has a positive impact on the sinterability of ZrC-containing ceramics. Pressure assisted techniques such as HP and SPS have shown good consolidation of ZrC_xN_y and ZrN, achieving >95% TD. Nevertheless, these techniques suffer from poor scalability. Even with the fast heating rates (100 K/min) and short dwell times (10-15 mins) of SPS, compared with traditional cold pressing and sintering (several hours), much longer processing times are needed because it is not a batch process. A material that could be consolidated by conventional techniques — such as ZrN doped with metallic Zr — would be of interest. A change in sintering mechanism may result from doping ZrN with Zr metal as the defect concentration would increase,[100] or if the phases produced at the sintering temperature approach the metal-rich liquidus around 2273 K (shown in Figure 8.1) liquid phase sintering may aid densification. The resulting $\sigma - ZrN_x$ and $\alpha - Zr$ biphasic material would still meet the melting temperature requirements of GFR fuel materials of $\geq$2200 K.[12] In addition to studying sintering behaviour, the effect of the Zr second phases on the thermal conductivity and mechanical properties would need to be investigated.

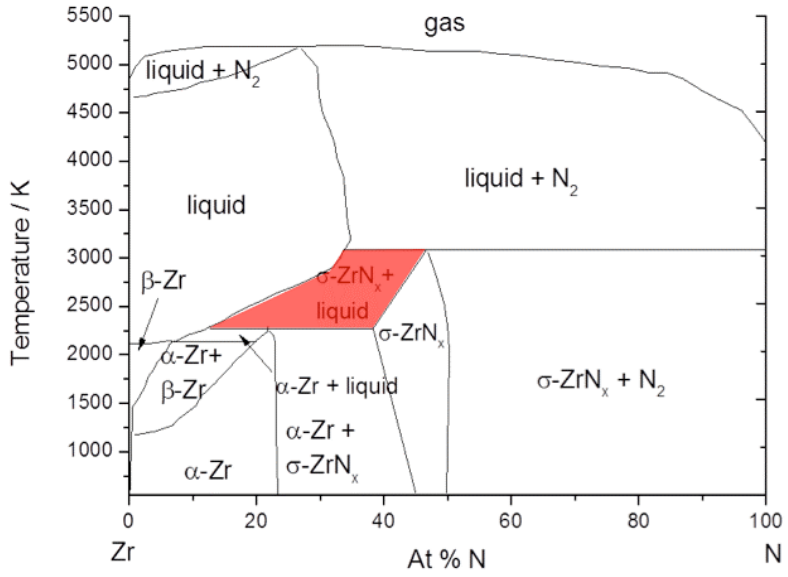


Figure 8.1: Zr-N phase diagram,[44] highlighting metal rich liquidus sintering region

Thermal conductivities of the ZrC_xN_y ceramics presented in chapter 6 were all higher than the ceramics produced from commercially-available powders and are in the range of 35-43 W $m^{-1}K^{-1}$at RT and increased with increasing nitrogen content. Thermal conductivities also increased with temperature for all samples. However, the RT thermal conductivity of the ZrN ceramics made from commercially-available powders of around 10 $Wm^{-1}K^{-1}$ were far inferior to the carbonitrides produced in this work. Electrical conductivities of the samples were measured, showing the ZrC_xN_y ceramics had electrical conductivities in the range of 250-450 $\times 10^4$ $\Omega^{-1}m^{-1}$at RT, with the higher nitrogen-containing samples having increased electrical conductivities. This is again higher than the electrical conductivity of the ZrN sample made from commercially-available powders, which had a RT electrical conductivity of around 50×10^4 $\Omega^{-1}m^{-1}$. The decreased thermal and electrical conductivities of the $ZrN_{0.82}$ samples produced from commercially-available powders is attributed to the large concentrations of vacancies as determined from chemical analysis (chapter 5) causing increased phonon and electron scattering. The ZrC_xN_y ceramics produced in this work had a lower concentration of vacancies, with $x + y \approx 0.95$ and it has been shown that a sharp decrease in thermal and electrical

properties in ZrC is observed at a stoichiometry around $ZrC_{0.9}$ (Figure 6.11 and Figure 6.12) Electrical conductivities of all samples decreased with temperature, indicating metallic behaviours. Calculating the electrical contribution to thermal conductivity, k_{el}, showed this increased with nitrogen content concomitantly with a decrease in lattice contribution, k_{lat}, to thermal conductivity. This was attributed to the extra electron possessed by nitrogen occupying a higher energy level antibonding orbital. This occupation of higher energy orbitals shifts the Fermi level of the nitride to a region with a higher DOS [1, 41] meaning that increased promotion to the conductance band of the nitride is possible and therefore heat conduction by those electrons. The decrease in lattice conductivity with nitrogen content can be explained as the weaker Zr-N bond is less stiff than the Zr-C bond, meaning it can oscillate over a wider range of energies. This was observed experimentally by measurement of C_p of the materials which increased with increasing nitrogen content. This larger range of bond oscillation will increase the anharmonicity of the lattice vibrations which creates phonon and electron scattering points. From these observations a trend was observed in the ZrC_xN_y ceramics whereby the main mechanism of thermal conductivity shifts from k_{lat} to k_{el}.

As candidates for inert matrix fuels ZrC and ZrN are often directly compared, with the thermal conductivity of ZrC often reported to be far superior to that of ZrN. The nitride is often quoted as having a RT thermal conductivity of around 10 $Wm^{-1}K^{-1}$[15, 158], similar to the values obtained in this work for commercially-available ZrN ceramics. However, this work has shown that thermal conductivity increases with increasing nitrogen content which is to be expected theoretically.[1, 41] Therefore with regards to thermal conductivity ZrN has been shown to be far superior to ZrC in this work and this should be taken into account when comparing the candidates for use in IMF. The added expense of fabricating nitride fuels with ^{15}N as to avoid ^{14}C production (Equation 2.4) may be cost-effective due to this increased thermal conductivity and therefore increased heat transfer efficiency. A carbonitride phase may also be desirable for an inert matrix fuel as it may combine the benefits of both phases, such as the good fission product retention of ZrC [67] along with the easier densification, compatibility with current reprocessing techniques and improved radiation damage tolerance of the nitride.[6, 123]

Radiation damage on materials is another key aspect which needs to be understood before materials can be used in core. Candidates for inert matrix fuels have received initial studies on the effects of radiation damage to their microstructure and mech-

anical properties.[123, 124, 126, 130] This work has shown that a stoichiometric, pure phase of ZrN would be far superior in thermal conductivity to ZrC (chapter 6) and previous ZrN samples produced from commercially-available powders. Damage from radiation in the reactor core will lead to the formation of point defects and degradation of thermal properties of fuel materials during service. It is therefore important to predict damage evolution over the reactor lifetime, i.e. up to 10's displacements per atom (dpa).[12] Despite this, only relatively minor irradiation doses have been studied examining microstructural evolution and radiation hardening properties up to 1.8 dpa.[122, 123] A higher dose study, using the 5 MV tandem accelerator at The Dalton Cumbria Facility (DCF) to irradiate samples with protons could be envisaged. A study irradiating TEM samples and thin (~100 μm) pellets (10 mm diameter) for thermal conductivity could be pursued, combining results from the evolution of microstructure (such as defects) with the change in thermal conductivity.

Under the context of a severe accident situation, such as a LOCA, preliminary oxidation studies of commercially-available ZrN powders and ceramics produced from the powders were performed to fill a lack of reported oxidation behaviour of the nitride compared to the carbide. All samples showed parabolic rate behaviour, indicative of a rate limiting step which is attributed to the increased length of diffusion of oxygen through the advancing oxide scale. The onset of oxidation under air was determined by HT-XRD and TGA-DTA to be around 773 K which is comparable with the onset of oxidation of the carbide.[93] An initial increase in rate of oxidation with temperature to 1073 K was observed, however, at 1173 K the rate of oxidation decreases and remains similar for the sample oxidised at 1273 K. The decrease in oxidation rate was observed along with the formation of both an intermediate layer between the bulk ZrN and the ZrO_2 layer and the formation of a dense oxide scale which provides an effective diffusion barrier to oxygen. The intermediate layer was determined to be high temperature c-ZrO_2 phase by TEM similar to the reported formation of a dense ZrO_2 protective layer during oxidation of ZrC [114]. TEM observations also revealed superlattice reflections in the c-ZrO_2 which arise from the stabilisation of the high temperature oxide phase by replacement of oxygen with nitrogen, which creates ordered oxygen vacancies.[161] However, the protective nature of the dense ZrO_2 layer fails at higher temperature (1373 K) due to increased rate of oxygen diffusion through the oxide scale. This failure mechanism would probably occur at longer oxidation times at 1173 K and 1273 K due to

oxygen diffusion through the layer increasing as a function of time. This protective behaviour observed for samples oxidised at 1173 and 1273 K needs to be assessed further with more complete study incorporating different oxidising atmosphere and longer isothermal dwells. The oxidation behaviour of the ZrC_xN_y ceramics from the as-fabricated powders in this work or ZrN_{1-x} would also be of interest as vacancy concentration may adversely affect oxidation behaviour.

References

[1] H. O. Pierson. *4 - Carbides of Group IV: Titanium, Zirconium, and Hafnium Carbides*, pages 55–80. William Andrew Publishing, New Jersey, USA, 1996.

[2] A Technology Roadmap for Generation IV Nuclear Energy Systems. Report, USDOE, 2002.

[3] R. Fielding. Report on Feasibility Assessment of GFR Fuel Concepts. Report, Argonne National Laboratory, 2004.

[4] W. E. Lee, M. Gilbert, S. T. Murphy, and R. W. Grimes. Opportunities for advanced ceramics and composites in the nuclear sector. *Journal of the American Ceramic Society*, 96(7):2005–2030, 2013.

[5] G. Van-Goethem. Nuclear fission, today and tomorrow: From renaissance to technological breakthrough (Generation IV). *Journal of Pressure Vessel Technology*, 133(4):044001, 2011.

[6] Y. Arai. *3.02 - Nitride Fuel*, volume 3 of *Comprehensive Nuclear Materials, R. J. M. Konings (ed.)*, pages 41–54. Elsevier, Oxford, UK, 2012.

[7] A. K. Sengupta, R. Agarwal, and H. S. Kamath. *3.03 - Carbide Fuel*, volume 2 of *Comprehensive Nuclear Materials, R. J. M. Konings (ed.)*, pages 55–86. Elsevier, Oxford, UK, 2012.

[8] W. E. Lee, E. Giorgi, R. Harrison, A. Maitre, and O. Rapaud. *Ultra-High Temperature Ceramics: Materials for Extreme Environment Applications*, chapter 15 Nuclear Applications for Ultra-High Temperature Ceramics and MAX Phases, pages 391–415. John Wiley & Sons, Inc, New Jersey, USA, 2014.

[9] T. D. Newton and P. J. Smith. Flexibility of the Gas Cooled Fast Reactor to Meet the Requirements of the 21st Century. Report, Serco Assurance.

[10] E. Parma, S. Wright, M. Vernon, D. Fleming, G. Rochau, A. Suo-Anttila, A. Rashdan, and P. Tsvetkov. Supercritical CO_2 Direct Cycle Gas Fast Reactor (SC-GFR) Concept. Report, Sandia National Laboratories, 2011.

[11] Status of Minor Actinide Fuel Development. Report NF-T-4.6, International Atomic Energy Agency (IAEA), 2009.

[12] M. K. Meyer, R. Fielding, and J. Gan. Fuel development for gas-cooled fast reactors. *Journal of Nuclear Materials*, 371(13):281–287, 2007.

[13] E. A. C. Neeft, K. Bakker, R. P. C. Schram, R. Conrad, and R. J. M. Konings. The EFTTRA-T3 irradiation experiment on inert matrix fuels. *Journal of Nuclear Materials*, 320(1-2):106–116, 2003.

[14] N. Nitani, K. Kuramoto, T. Yamashita, Y. Nihei, and Y. Kimura. In-pile irradiation of rock-like oxide fuels. *Journal of Nuclear Materials*, 319:102–107, 2003.

[15] P. A. Demkowicz, K. Wright, J. Gan, D. A. Petti, T. Allen, and J. Blanchard. Evaluation of Alternate Materials for Coated Particle Fuels for the Gas-Cooled Fast Reactor. Report, Idaho National Laboratory (INL), 2006.

[16] Development Status of Metallic Dispersion and Non-Oxide Advanced and Alternative Fuels for Power and Research Reactors. Report IAEA-TECDOC-1374, International Atomic Energy Agency (IAEA), 2003.

[17] N. Chauvin, R. J. M. Konings, and H. Matzke. Optimisation of inert matrix fuel concepts for americium transmutation. *Journal of Nuclear Materials*, 274(1-2):105–111, 1999.

[18] H. O. Pierson. *Handbook of Chemical Vapour Deposition, Principles, Technology and Applications*. Noyes Publications, New Jersey, USA, 1992.

[19] A. Slaga. *Chemical Vapour Deposition of Porous Silicon Carbide Onto Ceramic Microspheres Using a Fluidised Bed Reactor*. Masters thesis, Purdue University, IN, USA, 2006.

[20] A. Nosek, J. Conzen, H. Doescher, C. Martin, and J. Blanchard. Thermomechanics of candidate coatings for advanced gas reactor fuels. *Journal of Nuclear Materials*, 371(1-3):288–303, 2007.

[21] M. Salvatores and G. Palmiotti. Radioactive waste partitioning and transmutation within advanced fuel cycles: Achievements and challenges. *Progress in Particle and Nuclear Physics*, 66(1):144–166, 2011.

[22] J. Li, Z. Y. Fu, W. M. Wang, H. Wang, S. H. Lee, and K. Niihara. Preparation of ZrC by self-propagating high-temperature synthesis. *Ceramics International*, 36(5):1681–1686, 2010.

[23] J. Russias, S. Cardinal, C. Esnouf, G. Fantozzi, and K. Bienvenu. Hot pressed titanium nitride obtained from SHS starting powders: Influence of a pre-sintering heat-treatment of the starting powders on the densification process. *Journal of the European Ceramic Society*, 27(1):327–335, 2007.

[24] H. Berndt, A. Q. Zeng, H. R. Stock, and P. Mayr. Zirconium carbonitride films produced by plasma-assisted metal organic chemical vapour deposition. *Surface and Coatings Technology*, Part 1(7475):369–374, 1995.

[25] C. Hsin-Tien and H. Cheng-Chung. Low-pressure chemical vapor deposition of titanium and zirconium carbonitride thin films from $M(NEt_2)_4$ (M = Ti and Zr). *Materials Letters*, 16(4):194–199, 1993.

[26] I. A. Khan, S. Jabbar, T. Hussain, M. Hassan, R. Ahmad, M. Zakaullah, and R. S. Rawat. Deposition of zirconium carbonitride composite films using ion and electron beams emitted from plasma focus device. *Nuclear Instruments and Methods in Physics Research Section B: Beam Interactions with Materials and Atoms*, 268(13):2228–2234, 2010.

[27] K. Minato, M. Akabori, M. Takano, Y. Arai, K. Nakajima, A. Itoh, and T. Ogawa. Fabrication of nitride fuels for transmutation of minor actinides. *Journal of Nuclear Materials*, 320(12):18–24, 2003.

[28] G. Pautasso, K. Richter, and C. Sari. Investigation of the reaction $UO_2 + PuO_2 + C + N_2$ by thermogravimetry. *Journal of Nuclear Materials*, 158(0):12–18, 1988.

[29] S. K. Mukerjee, J. V. Dehadraya, V. N. Vaidya, and D. D. Sood. Kinetics of the carbothermic synthesis of uranium mononitride microspheres. *Journal of Nuclear Materials*, 185(1):39–49, 1991.

[30] P. Bardelle and D. Warin. Mechanism and kinetics of the uranium-plutonium mononitride synthesis. *Journal of Nuclear Materials*, 188(0):36–42, 1992.

[31] S. K. Mukerjee, J. V. Dehadraya, V. N. Vaidya, and D. D. Sood. Kinetic study of the carbothermic synthesis of uranium monocarbide microspheres. *Journal of Nuclear Materials*, 172(1):37–46, 1990.

[32] T. Nakagawa, H. Matsuoka, M. Sawa, M. Hirota, M. Miyake, and M. Katsura. Formation of uranium and cerium nitrides by the reaction of carbides with NH_3 and N_2/H_2 stream. *Journal of Nuclear Materials*, 247:127–130, 1997.

[33] M. Streit, F. Ingold, M. Pouchon, L. J. Gauckler, and J. P. Ottaviani. Zirconium nitride as inert matrix for fast systems. *Journal of Nuclear Materials*, 319:51–58, 2003.

[34] M. Streit. *Fabrication and Characterisation of (Pu,Zr)N fuels.* Doctorate thesis, University of Basle, Switzerland, 2004.

[35] L. M. Berger, W. Gruner, E. Langholf, and S. Stolle. On the mechanism of carbothermal reduction processes of TiO_2 and ZrO_2. *International Journal of Refractory Metals and Hard Materials*, 17(1-3):235–243, 1999.

[36] J. David, G. Trolliard, M. Gendre, and A. Maitre. TEM study of the reaction mechanisms involved in the carbothermal reduction of zirconia. *Journal of the European Ceramic Society*, 33(1):165–179, 2013.

[37] A. W. Weimer, G. A. Eisman, D. W. Susnitzky, D. R. Beaman, and J. W. McCoy. Mechanism and kinetics of the carbothermal nitridation synthesis of alpha-silicon nitride. *Journal of the American Ceramic Society*, 80(11):2853–2863, 1997.

[38] A. Ortega, M. D. Alcala, and C. Real. Carbothermal synthesis of silicon nitride (Si_3N_4): Kinetics and diffusion mechanism. *Journal of Materials Processing Technology*, 195(13):224–231, 2008.

[39] A. R. West. *Basic Solid State Chemistry.* Wiley, New York, USA, 1988.

[40] W. S. Williams. Physics of transition metal carbides. *Materials Science and Engineering: A*, 105–106, Part 1(0):1–10, 1988.

[41] W. Lengauer. *Transition Metal Carbides, Nitrides, and Carbonitrides*, pages 202–252. Wiley-VCH Verlag GmbH, Weinheiin, Germany, 2008.

[42] K. Schwarz, H. Ripplinger, and A. Neckel. Energy band structure and X-ray emission spectra of ZrC and ZrN. *Zeitschrift fur Physik B Condensed Matter*, 48(1):79–87, 1982.

[43] A. Fernandez Guillermet. Analysis of thermochemical properties and phase stability in the zirconium-carbon system. *Journal of Alloys and Compounds*, 217(1):69–89, 1995.

[44] L. Gribaudo, D. Arias, and J. Abriata. The N-Zr (nitrogen-zirconium) system. *Journal of Phase Equilibria*, 15(4):441–449, 1994.

[45] X. Ma, C. Li, K. Bai, P. Wu, and W. Zhang. Thermodynamic assessment of the ZrN system. *Journal of Alloys and Compounds*, 373(1-2):194–201, 2004.

[46] M. A. Eron'yan, R. G. Avarbeh, and T. A. Nikol'skaya. Temperature dependence of zirconium nitride congruent melting. *Zhurnal Prikladnoj Khimii*, 46(2):428, 1973.

[47] S. Binder, W. Lengauer, P. Ettmayer, J. Bauer, J. Debuigne, and M. Bohn. Phase equilibria in the systems TiCN, ZrCN and HCN. *Journal of Alloys and Compounds*, 217(1):128 – 136, 1995.

[48] M. W. Chase. NIST-JANAF Themochemical Tables, Fourth Edition. *J. Phys. Chem. Ref. Data,*, Monograph 9:1–1951, 1998.

[49] L. E. Toth. *Transition Metal Carbides and Nitrides*, volume 7 of *Refractory Materials*. Academic Press, New York, USA and London, UK, 1971.

[50] E. Grigore, C. Ruset, X. Li, and H. Dong. Zirconium carbonitride films deposited by combined magnetron sputtering and ion implantation (CMSII). *Surface and Coatings Technology*, 204(1213):1889–1892, 2010.

[51] C. B. Alcock, K. T. Jacon, and S. Zador. Zirconium, physicochemical properties of its compounds and alloys. Report, International Atomic Energy Agency, 1976.

[52] R. Hultgren, P. R. Desai, D. T. Hawkins, M. Gleiser, and K. K. Kelley. *Selected Values of Thermodynamic Properties of Binary Alloys*. American Society for Metals, Ohio, USA, 1973.

[53] L. S. Levinson. High temperature heat contents of TiC and ZrC. *Journal of Chemical Physics*, 42(8):2891–2892, 1965.

[54] D. S. Neel, S. Oglesby, and C. D. Pears. *The thermal properties of thirteen solid materials to 5000°F for their destruction temperatures*. WAAD technical documentary reportno. 60-924. Directorate of Materials and Processes, Aeronautical Systems Division, Air Force Systems Command, Ohio, USA, 1962. (Birmingham, AL.) "Project no. 7360, Task no. 73603." Prepared under Contract no. AF 33 (616)-6312, by the Southern Research Institute, Birmingham, Alabama.

[55] E. K. Storms and J. Griffin. The vapourisation behaviour of the defect carbides. Part IV: The Zr-C system. *High Temperature Science*, 5:423, 1973.

[56] V. Basini, J. P. Ottaviani, J. C. Richaud, M. Streit, and F. Ingold. Experimental assessment of thermophysical properties of (Pu,Zr)N. *Journal of Nuclear Materials*, 344(1-3):186–190, 2005.

[57] J. C. Hedge, J. W. Kopec, C. Kostenko, and J. L. Lang. Thermal properties of refractory alloys. *US Air Force Report ASD-TDR*, pages 63–597, 1963.

[58] H. Muta, K. Kurosaki, M. Uno, and S. Yamanaka. Thermophysical properties of several nitrides prepared by spark plasma sintering. *Journal of Nuclear Materials*, 389(1):186–190, 2009.

[59] A. Ciriello, V. V. Rondinella, D. Staicu, J. Somers, O. Benes, R. Jardin, D. Bouxire, F. Wastin, and E. Colineau. Thermophysical characterization of ZrN and (Zr,Pu)N. *Journal of Alloys and Compounds*, 473(1-2):265–271, 2009.

[60] W. Lengauer, S. Binder, K. Aigner, P. Ettmayer, A. Guillou, J. Debuigne, and G. Groboth. Solid state properties of group IVb carbonitrides. *Journal of Alloys and Compounds*, 217(1):137–147, 1995.

[61] Y. Arai, Y. Okamoto, and Y. Suzuki. Thermal conductivity of neptunium mononitride from 740 to 1600 K. *Journal of Nuclear Materials*, 211(3):248–250, 1994.

[62] R. E. Taylor and J. Morreale. Thermal conductivity of titanium carbide, zirconium carbide, and titanium nitride at high temperatures. *Journal of the American Ceramic Society*, 47(2):69–73, 1964.

[63] L. N. Grossman. High-temperature thermophysical properties of zirconium carbide. *Journal of the American Ceramic Society*, 48(5):236–242, 1965.

[64] B. H. Morrison and L. L. Strugess. The thermal deiffusivity and conductivty of zirconium carbide from 100 to 2500 K . *Revue Internationale des Hautes Temperatures et des Refractories*, 7(4):351, 1970.

[65] J. Adachi, K. Kurosaki, M. Uno, and S. Yamanaka. Thermal and electrical properties of zirconium nitride. *Journal of Alloys and Compounds*, 399(12):242–244, 2005.

[66] J. Adachi, K. Kurosaki, M. Uno, and S. Yamanaka. Effect of porosity on thermal and electrical properties of polycrystalline bulk ZrN prepared by spark plasma sintering. *Journal of Alloys and Compounds*, 432(12):7–10, 2007.

[67] H. F. Jackson and W. E. Lee. *2.13 - Properties and Characteristics of ZrC*, volume 2 of *Comprehensive Nuclear Materials, R. J. M. Konings (ed.)*, pages 339–372. Elsevier, Oxford, UK, 2012.

[68] H. F. Jackson. *Thermophysical Properties and Thermodynamic Stability of Zirconium Carbide as a function of Non-Stoichiometry.* PhD thesis, Imperial College London, 2012.

[69] R. G. Sharma, M. S. R. Chari, and D. K. Reddy. The electronic lorenz number in transition metals at high temperatures. *Journal of Physics F: Metal Physics*, 16(5):603, 1986.

[70] P. E. D. Morgan. Wiedemann-Franz-Lorenz Relation in Metallic Conducting Ceramics. *Journal of the American Ceramic Society*, 58(7-8):349–349, 1975.

[71] V. S. Neshpor, V. S. Davydov, B. G. Ermakov, and B. V. Mogilevich. Some properties of pyrolytic carbides and nitrides of group IV metals. *Powder Metallurgy and Metal Ceramics*, 6(2):135, 1967.

[72] G. V. Samsonov, I. B. Paderno, and A. D. Panasiuk. Electrical and physical properties of the defined compounds and homogeneity fields of the transition metal carbides of groups IV and V up to 2500°C. *Revue Internationale des Hautes Temperatures et des Refractaires*, 3(2):179, 1966.

[73] G. V. Samsonov. *Nitrides (in Russian).* Naukova Dumka, Kiev, Ukraine, 1969.

[74] I. I. Petrova, V. A. Petrov, B. G. Ermakov, and V. V. Sokolov. Specific electrical resistance of zirconium and hafnium nitrides. *High temperature (In Russian)*, 10:1007–1012, 1972.

[75] A. C. Lawson, D. P. Butt, J. W. Richaud, and J. Li. Thermal expansion and atomic vibrations of zirconium carbide to 1600 K. *Philosophical Magazine*, 87(1-6):2507, 2007.

[76] K. Aigner, W. Lengauer, D. Rafaja, and P. Ettmayer. Lattice parameters and thermal expansion of Ti(C_xN_{1-x}), Zr(C_xN_{1-x}), Hf(C_xN_{1-x}) and TiN_{1-x} from 298 to 1473 K as investigated by high-temperature X-ray diffraction. *Journal of Alloys and Compounds*, 215(1-2):121–126, 1994.

[77] M. Takano, M. Akabori, Y. Arai, and K. Minato. Thermal expansion of TRU nitride solid solutions as fuel materials for transmutation of minor actinides. *Journal of Nuclear Materials*, 389(1):89 – 92, 2009.

[78] B. A. Fridlender and V. S. Neshpor. Thermal expansion of the carbides of group IV-VI Metals (Transition Class). *High temperature*, 14(5):847, 1976.

[79] Y-C. Chieh, W-Z. Lo, and F-H. Lu. Microstructure evolution of ZrN films annealed in vacuum. *Surface and Coatings Technology*, 200(10):3336–3340, 2006.

[80] C. J. Tavares, L. Rebouta, M. Andritschky, and S. Ramos. Mechanical characterisation of TiN/ZrN multi-layered coatings. *Journal of Materials Processing Technology*, 92–93(0):177–183, 1999.

[81] V. Craciun, E. J. McCumiskey, M. Hanna, and C. R. Taylor. Very hard ZrC thin films grown by pulsed laser deposition. *Journal of the European Ceramic Society*, 33(1-2):2223–2226, 2013.

[82] H-M. Tung, J-H. Huang, D-G. Tsai, C-F. Ai, and G-P. Yu. Hardness and residual stress in nanocrystalline ZrN films: Effect of bias voltage and heat treatment. *Materials Science and Engineering: A*, 500(1-2):104–108, 2009.

[83] D. Craciun, G. Socol, N. Stefan, G. Dorcioman, M. Hanna, C. R. Taylor, E. Lambers, and V. Craciun. The effect of deposition atmosphere on the chemical composition of TiN and ZrN thin films grown by pulsed laser deposition. *Applied Surface Science*, 302:124–128, 2014.

[84] D. Ferro, J. V. Rau, V. Rossi Albertini, A. Generosi, R. Teghil, and S. M. Barinov. Pulsed laser deposited hard TiC, ZrC, HfC and TaC films on titanium: Hardness and an energy-dispersive X-ray diffraction study. *Surface and Coatings Technology*, 202(8):1455–1461, 2008.

[85] Y. Long, A. Javed, J. Chen, Z.-K. Chen, and X. Xiong. Phase composition, microstructure and mechanical properties of ZrC coatings produced by chemical vapor deposition. *Ceramics International*, 40(1, Part A):707–713, 2014.

[86] V. M. Baranov, V. I. Knyazev, and O. S. Korostin. The temperature dependence of the elastic constants of nonstoichiometric zirconium carbides. *Strength of Materials*, 5(9):1074–1077, 1973.

[87] G. G. Travushkin, V. I. Knyazev, V. S. Belov, and G. A. Rymashevskii. Temperature threshold of brittle failure in interstitial phases. *Strength of Materials*, 5(5):639–641, 1973.

[88] E. Torokk, A. J. Perry, L. Chollet, and W. D. Sproul. Young's modulus of TiN, TiC, ZrN and HfN. *Thin Solid Films*, 153(1-3):37–43, 1987.

[89] P. V. Zubarev, A. B. Kuraev, A. S. Maskaev, E. V. Astakhova, and A. A. Bessarabov. Stress relaxation in zirconium carbide. Report 1. Test method and stress relaxation curves. *Strength of Materials*, 26(1):63–69, 1994.

[90] N. Alexandre and M. Desmaison-Brut. Mechanical properties of hot isostatically pressed zirconium nitride materials. *Journal of Materials Science*, 28:2385–2390, 1993.

[91] J. Adachi, K. Kurosaki, M. Uno, and S. Yamanaka. Porosity influence on the mechanical properties of polycrystalline zirconium nitride ceramics. *Journal of Nuclear Materials*, 358(2-3):106–110, 2006.

[92] D. J. Green. *An Introduction to the Mechanical Properties of Ceramics*. Cambridge solid state science series. Cambridge University Press, Cambridge, UK, 1998.

[93] Y. Katoh, G. Vasudevamurthy, T. Nozawa, and L. L. Snead. Properties of zirconium carbide for nuclear fuel applications. *Journal of Nuclear Materials*, 441(1-3):718 – 742, 2013.

[94] D. L. Kohlstedt. The temperature dependence of microhardness of the transition-metal carbides. *Journal of Materials Science*, 8(6):777–786, 1973.

[95] J. Wang and L. J. Vandeperre. *Ultra-High Temperature Ceramics: Materials for Extreme Environment Applications*, chapter 10 Deformation and Hardness of UHTCs as a Function of Temperature, pages 236–266. John Wiley & Sons, Inc, New Jersy, USA, 2014.

[96] Y. Kumashiro, Y. Nagai, and H. Kato. The Vickers micro-hardness of NbC, ZrC and TaC single crystals up to 1500°C. *Journal of Materials Science Letters*, 1(2):49–52, 1982.

[97] I. V. Gridneva, Yu. V. Mil'man, G. A. Rymashevski, V. I. Trefilov, and S. I. Chugunova. Effect of temperature on the strength characteristics of zirconium carbide. *Powder mMetallurgy and Metal Ceramics*, 15(8):638–345, 1976.

[98] Y. Arai and K. Nakajima. Preparation and characterization of PuN pellets containing ZrN and TiN. *Journal of Nuclear Materials*, 281(23):244–247, 2000.

[99] Y.-J. Lee, Y.-H. Park, and T. Hinoki. Influence of grain size on thermal conductivity of SiC ceramics. *IOP (Institute of Physics) Conference Series: Materials Science and Engineering*, 18(16):162014, 2011.

[100] D. Sciti, L. Silvestroni, V. Medri, and F. Monteverde. *Ultra-High Temperature Ceramics: Materials for Extreme Environment Applications*, chapter 6 Sintering and Densification Mechanisms of Ultra-High Temperature Ceramics, pages 112–143. John Wiley & Sons, Inc, New Jersey, USA, 2014.

[101] H. J. Ryu, Y. W. Lee, S. I. Cha, and S. H. Hong. Sintering behaviour and microstructures of carbides and nitrides for the inert matrix fuel by spark plasma sintering. *Journal of Nuclear Materials*, 352(1-3):341–348, 2006.

[102] Z. A. Munir, U. Anselmi-Tamburini, and M. Ohyanagi. The effect of electric field and pressure on the synthesis and consolidation of materials: A review of the spark plasma sintering method. *Journal of Materials Science*, 41(3):763–777, 2006.

[103] D. M. Hulbert, A. Anders, J. Andersson, E. J. Lavernia, and A. K. Mukherjee. A discussion on the absence of plasma in spark plasma sintering. *Scripta Materialia*, 60(10):835–838, 2009.

[104] T. Sakai and M. Iwata. Effect of oxygen on sintering of AlN. *Journal of Materials Science*, 12(8):1659–1665, 1977.

[105] K. A. Khor, L. G. Yu, and Y. Murakoshi. Spark plasma sintering of Sm_2O_3-doped aluminum nitride. *Journal of the European Ceramic Society*, 25(7):1057–1065, 2005.

[106] T. Hollmer. *Manufacturing Methods for (U-Zr)N Fuels*. Doctorate thesis, Kungl Tekniska Hogskolan (KTH) Royal Institute of Technology, Stockholm, Sweden, 2011.

[107] M. Pukari and M. Takano. Sintering and characterization of ZrN and (Dy,Zr)N as surrogate materials for fast reactor nitride fuel. *Journal of Nuclear Materials*, 444(1-3):7–13, 2014.

[108] L. Priester. *Grain Boundaries From Theory to Engineering*. Springer, New York, USA, 2013.

[109] M. N. Rahaman. *Ceramic Processing and Sintering*. Marcel Deckker, New York, USA, 1995.

[110] Z. T. Wu, Z. B. Qi, W. F. Jiang, Z. C. Wang, and B. Liu. Influence of niobium addition on microstructure, mechanical properties and oxidation resistance of ZrN coatings. *Thin Solid Films*, 2014.

[111] L. Krusin-Elbaum and M. Wittmer. Oxidation kinetics of ZrN thin films. *Thin Solid Films*, 107(1):111 – 116, 1983.

[112] P. Panjan, B. Navinsek, A. Cvelbar, A. Zalar, and I. Milosev. Oxidation of TiN, ZrN, TiZrN, CrN, TiCrN and TiN/CrN multilayer hard coatings reactively sputtered at low temperature. *Thin Solid Films*, 281-282:298 – 301, 1996.

[113] M. Caillet, H. F. Ayedi, and J. Besson. Etude de la corrosion de revetements refractaires sur le zirconium i. Oxydation par l'oxygene de revetements de nitrure de zirconium. *Journal of the Less Common Metals*, 51(2):305 – 322, 1977.

[114] S. Shimada and T. Ishil. Oxidation kinetics of zirconium carbide at relatively low temperatures. *Journal of the American Ceramic Society*, 73(10):2804–2808, 1990.

[115] G. A. Rama Rao and V. Venugopal. Kinetics and mechanism of the oxidation of ZrC. *Journal of Alloys and Compounds*, 206(2):237 – 242, 1994.

[116] K. Tamura, T. Ogawa, and K. Fukuda. The oxidation behavior of ZrC coating and powder studied by laser Raman spectroscopy and X-ray diffraction. *Journal of Nuclear Materials*, 175(3):266 – 269, 1990.

[117] A. C. Fox and T. W. Clyne. Oxygen transport by gas permeation through the zirconia layer in plasma sprayed thermal barrier coatings. *Surface and Coatings Technology*, 184(2–3):311 – 321, 2004.

[118] S. N. Karlsdottir and J. W. Halloran. Formation of oxide scales on zirconium diboride-silicon carbide composites during oxidation: Relation of subscale recession to liquid oxide flow. *Journal of the American Ceramic Society*, 91(11):3652–3658, 2008. cited By (since 1996)19.

[119] E. Zapata-Solvas, D. D. Jayaseelan, P. M. Brown, and W. E. Lee. Effect of La_2O_3 addition on long-term oxidation kinetics of ZrB_2-SiC and HfB_2-SiC ultra-high temperature ceramics. *Journal of the European Ceramic Society*, 34(15):3535 – 3548, 2014.

[120] F. Onimus and J. L. Bechade. *4.01 - Radiation Effects in Zirconium Alloys*, volume 4 of *Comprehensive Nuclear Materials, R. J. M. Konings (ed.)*, pages 1–31. Elsevier, Oxford, UK, 2012.

[121] D. Gosset, M. Dolle, D. Simeone, G. Baldinozzi, and L. Thome. Structural evolution of zirconium carbide under ion irradiation. *Journal of Nuclear Materials*, 373(1-3):123–129, 2008.

[122] Y. Yang, C. A. Dickerson, and T. R. Allen. Radiation stability of ZrN under 2.6 MeV proton irradiation. *Journal of Nuclear Materials*, 392(2):200–205, 2009.

[123] J. Gan, Y. Yang, C. Dickson, and T. Allen. Proton irradiation study of GFR candidate ceramics. *Journal of Nuclear Materials*, 389(2):317–325, 2009.

[124] J. Gan, M. K. Meyer, R. C. Birtcher, and T. R. Allen. Microstructure evolution in ZrC irradiated with Kr ions. *ASTM International*, 3(4):358–364, 2006.

[125] A. Janse-van Vuuren, V. A. Skuratov, V. V. Uglov, J. H. Neethling, and S. V. Zlotski. Radiation tolerance of nanostructured ZrN coatings against swift heavy ion irradiation. *Journal of Nuclear Materials*, 442(1-3):507–511, 2013.

[126] R. A. Adrievskii, K. P. Vlasov, A. S. Shevchenko, A. G. Lanin, S. A. Pritchin, V. V. Klyushin, S. P. Krushin, and A. S. Maskaev. Influence of reactor irradiation on the physicomechanical properties of zirconium and hafnium carbides. *Inorganic Materials*, 14(4):530, 1978.

[127] H. F. Jackson, D. D. Jayaseelan, W. E. Lee, M. J. Reece, F. Inam, D. Manara, C. P. Casoni, F. De Bruycker, and K. Boboridis. Laser melting of spark plasma-sintered zirconium carbide: thermophysical properties of a Generation IV very high-temperature reactor material. *International Journal of Applied Ceramic Technology*, 7(3):316–326, 2010.

[128] R. A. Andrievskii, V. I. Savin, V. Y. Markin, V. T. Spravtsev, and A. S. Shevchenko. Effect of reactor irradiation on the electrical and magnetic properties of interstitial phases. *Inorganic Matierals*, 14(4):526, 1978.

[129] L. David, S. Gomes, G. Carlot, J-P Roger, C Valot, and M. Raynaud. Characterisation of thermal conductivty degradation induced by heavy ion irradiation in ceramic materials. *Journal of Physics D: Applied Physics*, 41(3):035502 (11pp), 2008.

[130] L. L. Snead, Y. Katoh, and S. Kondo. Effects of fast neutron irradiation on zirconium carbide. *Journal of Nuclear Materials*, 399(2-3):200–207, 2010.

[131] C. Jensen, M. Chirtoc, N. Horny, J. S. Antoniow, H. Pron, and H. Ban. Thermal conductivity profile determination in proton-irradiated ZrC by spatial

and frequency scanning thermal wave methods. *Journal of Applied Physics*, 114(13):–, 2013.

[132] C. W. Bale, E. Belisle, P. Chartrand, S. A. Decterov, G. Eriksson, K. Hack, I.-H. Jung, Y.-B. Kang, J. Melancon, A. D. Pelton, C. Robelin, and S. Petersen. FactSage thermochemical software and databases - recent developments. *Calphad*, 33(2):295 – 311, 2009. Tools for Computational Thermodynamics.

[133] J. D. Hanawalt, H. W. Rinn, and L. K. Frevel. Chemical analysis by X-ray diffraction. *Industrial & Engineering Chemistry Analytical Edition*, 10(9):457–512, 1938.

[134] G. Katz. X-ray diffraction powder pattern of metastable cubic ZrO_2. *Journal of the American Ceramic Society*, 54(10):531–531, 1971.

[135] P. Duwez and F. Odell. Phase relationships in the system zirconia-ceria. *Journal of the American Ceramic Society*, 33(9):274–283, 1950.

[136] M. C. Morris. Standard x-ray diffraction powder patterns; section 21: Data for 92 substances. *National Bureau of Standards (U.S.) Monograph*, 25(21):135, 1985.

[137] A. N. Christensen. A neutron diffraction investigation on single crystal of titanium carbide, titanium nitride and zirconium nitride. *Acta Chemica Scandinavica A*, 29:563–568, 1975.

[138] J. I. Goldstein, D. E. Newbury, P. Echlin, D. C. Joy, A. D. Romig Jr., C. E. Lyman, C. Fiori, and E. Lifshin. *Electron Optics*. Plenum Press, New York, USA, 1992.

[139] D. E. Newbury, D. C. Joy, P. Echlin, C. E. Fiori, and J. Goldstein. *Electron Channeling Contrast in the SEM*, book section 3, pages 87–145. Springer, New York, USA, 1986.

[140] B. Fultz and J. M. Howe. *Transmission Electron Microscopy and Diffractometry of Materials*. Spinger, Berlin, Germany, 2008.

[141] D. B. Williams and C. B. Carter. *Transmission Electron Microscopy*, volume 1. Plenum Press, New York, USA, 1996.

[142] D. T. Morelli and G. A. Slack. High lattice thermal conductivity solids. In S. L. Shinde and J. S. Goela, editors, *High Thermal Conductivity Materials*, pages 37–68. Springer, New York, USA, 2006.

[143] Y. Moriya. and A. Navrotsky. High-temperature calorimetry of zirconia: Heat capacity and thermodynamics of the monoclinic-tetragonal phase transition. *The Journal of Chemical Thermodynamics*, 38(3):211 – 223, 2006.

[144] G. W. Chinthaka Silva, A.A. Kercher, J.D. Hunn, R.C. Martin, G.E. Jellison, and H.M. Meyer. Characterization of zirconium carbides using electron microscopy, optical anisotropy, Auger depth profiles, X-ray diffraction, and electron density calculated by charge flipping method. *Journal of Solid State Chemistry*, 194(0):91–99, 2012.

[145] M. Gendre, A. Maitre, and G. Trolliard. Synthesis of zirconium oxycarbide (ZrC_xO_y) powders: Influence of stoichiometry on densification kinetics during spark plasma sintering and on mechanical properties. *Journal of the European Ceramic Society*, 31(13):2377 – 2385, 2011.

[146] H. Yanagisawa, S. Shinkai, K. Sasaki, J. Sakurai, Y. Abe, A. Sakai, and S. Zaima. Epitaxial growth of (111)ZrN thin films on (111)Si substrate by reactive sputtering and their surface morphologies. *Journal of Crystal Growth*, 297(1):80 – 86, 2006.

[147] J.-M. Gautier, E. H. Oelkers, and J. Schott. Are quartz dissolution rates proportional to B.E.T. surface areas? *Geochimica et Cosmochimica Acta*, 65(7):1059 – 1070, 2001.

[148] H. Kuwahara, N. Mazaki, M. Takahashi, T. Watanabe, X. Yang, and T. Aizawa. Mechanical properties of bulk sintered titanium nitride ceramics. *Materials Science and Engineering: A*, 319–321(0):687–691, 2001.

[149] Y. Suzuki and Y. Arai. Thermophysical and thermodynamic properties of actinide mononitrides and their solid solutions. *Journal of Alloys and Compounds*, 271-273(0):577 – 582, 1998.

[150] G. M. Nickerson and W. E. Kastenberg. Preliminary assessments of carbide fuel pins during mild overpower transients in LMFBRs. *Nuclear Engineering and Design*, 36(2):209 – 233, 1976.

[151] A. Ciriello, V. V. Rondinella, D. Staicu, and J. Somers. Thermophysical characterization of nitrides inert matrices: Preliminary results on zirconium nitride. *Journal of Nuclear Materials*, 371(1-3):129–133, 2007.

[152] H. M Benia, M. Guemmaz, G. Schmerber, A. Mosser, and J.-C Parlebas. In-

vestigations on non-stoichiometric zirconium nitrides. *Applied Surface Science*, 200(1–4):231 – 238, 2002.

[153] H. M. Benia, M. Guemmaz, G. Schmerber, A. Mosser, and J. C. Parlebas. Optical properties of non-stoichiometric sputtered zirconium nitride films. *Applied Surface Science*, 211(1–4):146 – 155, 2003.

[154] R. Lamni, E. Martinez, S. G. Springer, R. Sanjines, P. E. Schmid, and F. Levy. Optical and electronic properties of magnetron sputtered ZrN_x thin films. *Thin Solid Films*, 447–448(0):316 – 321, 2004. Proceedings of the 30th International Conference on Metallurgical Coatings and Thin Films.

[155] J. Westlinder, J. Malmstrom, G. Sjoblom, and J. Olsson. Low-resistivity ZrN_x metal gate in MOS devices. *Solid-State Electronics*, 49(8):1410 – 1413, 2005.

[156] A. I. Avgustinik and O. A. Bolikova. Relation between certain electrical and thermophysical properties of zirconium monocarbide and carbon content in the homogeneous range. *Inorganic Chemistry (USSR)*, 2(8):1230–1233, 1966.

[157] E. K. Storms and P. Wagner. Thermal conductivity of substoichiometric ZrC and NbC. *High Temperature Science*, 5(6):454–462, 1973.

[158] Gas-Cooled fast Reactor (GFR) FY04 Annual Report (accessed via www.inl.gov/technicalpublications, July 2014). Report INEEL/EXT-04-02361, Idaho National Laboaratory (INL), Idaho, USA, 2004.

[159] J. C. Gilles. Formation d'oxynitrures a partir des oxydes refractaires. *Revue internationale des Hautes Temperatures et des Refractaires*, 2(3):237–262, 1965.

[160] S. J. Clarke, C. W. Michie, and M. J. Rosseinsky. Structure of Zr_2ON_2 by neutron powder diffraction: The absence of nitride-oxide ordering. *Journal of Solid State Chemistry*, 146(2):399 – 405, 1999.

[161] G. Van Tendeloo and G. Thomas. Electron microscopy investigation of the ZrO_2-ZrN system-I. Formation of an incommensurate superstructure Zr-O-N. *Acta Metallurgica*, 31(10):1611 – 1618, 1983.

[162] J. B. Berkowitz-Mattuck. High temperature oxidation: IV . Zirconium and hafnium carbides. *Journal of The Electrochemical Society*, 114(10):1030–1033, 1967.

[163] E. Eakins, D. D. Jayaseelan, and W. E. Lee. Toward oxidation-resistant ZrB_2-SiC ultra high temperature ceramics. *Metallurgical and Materials Transactions A*, 42(4):878–887, 2011.

[164] B. Ma, W. Han, and E. Guo. Oxidation behavior of ZrC-based composites in static laboratory air up to 1300^{o}C. *International Journal of Refractory Metals and Hard Materials*, 46(0):159 – 167, 2014.